Studies on Mathematical Models for Characterizing Plume and Drift Behavior From Cooling Towers

Volume 4: Mathematical Model for Multiple-Source (Multiple-Tower) Cooling Tower Plume Dispersion

EPRI

EPRI CS-1683
Volume 4
Project 906-1
Interim Report
January 1981

Keywords:
Cooling Tower Plumes
Plume Dispersion
Multiple Plumes
Plume Model
Mathematical Model

Prepared by
Argonne National Laboratory
Argonne, Illinois

ELECTRIC POWER RESEARCH INSTITUTE

Studies on Mathematical Models for Characterizing Plume and Drift Behavior From Cooling Towers

Volume 4: Mathematical Model for Multiple-Source (Multiple-Tower) Cooling Tower Plume Dispersion

---

CS-1683, Volume 4
Research Project 906-1

Interim Report, January 1981
Work Completed, August 1980

Prepared by

ARGONNE NATIONAL LABORATORY
Division of Environmental Impact Studies
9700 South Cass Avenue
Argonne, Illinois 60439

Principal Investigators
A. J. Policastro
R. A. Carhart*
M. Wastag

*Visiting Scientist. Permanent Address: Department of Physics, University of Illinois at Chicago Circle Campus

Prepared for

Electric Power Research Institute
3412 Hillview Avenue
Palo Alto, California 94304

EPRI Project Manager
J. A. Bartz

Water Quality Control and Heat Rejection Program
Coal Combustion Systems Divisi

ORDERING INFORMATION

Requests for copies of this report should be directed to Research Reports Center (RRC), Box 50490, Palo Alto, CA 94303, (415) 965-4081. There is no charge for reports requested by EPRI member utilities and affiliates, contributing nonmembers, U.S. utility associations, U.S. government agencies (federal, state, and local), media, and foreign organizations with which EPRI has an information exchange agreement. On request, RRC will send a catalog of EPRI reports.

NOTICE

Prepared by
Argonne National Laboratory
Argonne, Illinois

ABSTRACT

This volume presents a generalization of our single source model (presented earlier in Volume 2) to multiple sources. The generalized model can treat vapor plume dispersion from any number of cooling towers in any geometrical configuration in any orientation to the direction of the wind. Important characteristics of the model include: (a) methodology of plume merging which accounts for differing plume entrainment rates during merging depending on wind direction, and (b) treatment of the effects of tower downwash from multiple towers; namely, additional entrainment and an additional pressure drag force acting vertically.

Limited calibration of the model to laboratory data was undertaken to determine two downwash coefficients. Verification of the model by comparing model predictions to new lab and field data revealed a superior performance of our model as compared to the models commonly used in environmental impact evaluation. The ANL multiple-source Model predicts visible plume height within a factor of 2 and/or visible plume length within a factor of 2 1/2 in 80% of our field data test cases. For comparison, the Orville and Slawson-Wigley Models satisfy this criterion for only 67% and 49% of the time, respectively. Additional ANL Model improvement is possible mainly through further development of the plume merging criterion.

Blank Page

EPRI PERSPECTIVE

PROJECT DESCRIPTION

Argonne National Laboratory is performing an effort to develop, improve, and validate mathematical models of cooling tower plumes. Emphasis is being placed on prediction of visible plume trajectory and deposition of saline droplet drift from the tower. Visible plumes and saline drift are environmental impacts of cooling towers that must be considered in power plant siting studies and licensing. A validated mathematical model of plume dispersion provides the industry with the tool required to make an assessment of environmental impact of the cooling tower.

This interim report, in five volumes plus an executive summary, describes results accomplished to date:

Executive Summary--Overview
Volume 1--Review of European Research
Volume 2--Single-Source Model
Volume 3--Drift Modeling of Single Sources
Volume 4--Multiple-Source Model
Volume 5--Drift Modeling of Multiple Sources

In a continuing effort, emphasis is being placed on developing a master model that is user-oriented and designed specifically for siting and licensing studies.

PROJECT OBJECTIVES

The goal of this effort is to develop, improve, and validate mathematical models of cooling tower plume dispersion for individual and clustered mechanical- and natural-draft cooling towers. The overall goal is to provide the utility planner with a tool for studies involving the environmental impact of cooling tower plumes.

PROJECT RESULTS

A model that has been developed and validated has prediction capabilities that are superior to other available mathematical models of cooling tower plume dispersion.

For example, in 77 percent of all cases of single sources that were studied, the model predicted a visible plume rise within a specified accuracy. This was the best performance among all available models (over a dozen) that were investigated.

This effort has also produced a useful review and summary of European research on cooling tower plume dispersion (Volume 1). Workshops in the fall of 1981 and in 1982 are being planned to disseminate to the industry the computer code that is being developed.

This series of volumes should be of value to utility planning engineers concerned with the impact of cooling tower plumes on plant siting.

John A. Bartz, Project Manager
Coal Combustion Systems Division

ACKNOWLEDGMENTS

The authors of this report would like to extend their appreciation to several individuals for their cooperation and assistance in responding to our numerous questions concerning the mechanical-draft field data used in this report. First, for the Gaston data, we wish to thank Professor Peter Slawson of the University of Waterloo in Waterloo, Ontario Canada and Mr. Ed Champion of Southern Company Services in Birmingham, Alabama. Second, for the Benning Road data, we wish to thank Dr. Jim Meyer of the Applied Physics Laboratory, The Johns Hopkins University in Laurel, Maryland. Dr. Meyer also provided us with visible plume outlines for each measurement date. We also appreciate the help given by Dr. Landis Kannberg of Battelle Northwest Labs who responded to our numerous questions on his MDCT lab studies. Professor Lorin Davis of Oregon State University also assisted by providing us with the Gregoric lab studies and his perspectives on that data.

We would also like to thank Dr. John Bartz of EPRI for his continued support and encouragement as technical monitor for the project. Finally, we would like to thank Dr. George McVehil for the many helpful comments and suggestions he made on a draft of this volume.

Blank Page

CONTENTS

Section		Page
1	INTRODUCTION	1-1
2	DEVELOPMENT OF ANL MULTIPLE-SOURCE PLUME MODEL	2-1
	Introduction	2-1
	Methodology of Plume Merging	2-1
	The Treatment of Downwash in the Multiple-Source Model	2-14
3	CALIBRATION OF THE ANL MULTIPLE-SOURCE PLUME MODEL	3-1
	Introduction	3-1
	Calibration of the Downwash Coefficients and Discussion of Results	3-2
4	VERIFICATION OF THE ANL MULTIPLE-SOURCE PLUME MODEL	4-1
	Introduction	4-1
	Kannberg Data	4-1
	Gregoric Data	4-9
	Field Data from Neurath and Amos	4-16
	Field Data from Benning Road	4-46
	Field Data from Gaston	4-64
	Statistics of Performance of Models Tested with the Above Field Data	4-81

Blank Page

ILLUSTRATIONS

Figure		Page
2-1	Sketch of two individual round plumes before and after merging	2-3
2-2	Sketch of a single round plume and a horizontally-oriented merged plume before and after merging; the slot and one of the half-round plumes is enlarged during merging.	2-4
2-3	Sketch of a single round plume and a vertically-oriented plume before and after merging; the slot and one of the half-round plumes is enlarged during merging.	2-4
2-4	Sketch of a single round plume and a horizontally-oriented merged plume before and after merging; only the slot portion of the merged plume is enlarged during merging.	2-4
2-5	Sketch of a single round plume and a vertically-oriented merged plume before and after merging; only the slot portion of the merged plume is enlarged during merging.	2-4
2-6	Sketch of the before (dotted curves) and after (solid line curve) merging of two horizontally-oriented merged plumes.	2-5
2-7	Sketch of the before (dotted curves) and after (solid line curve) merging of two vertically-oriented merged plumes.	2-5
2-8	Modified merged plume shape. Inner solid curve: merged plume before integration step DS. Dashed curve: merged plume configuration after completing stages 1-3 (see text). Outer solid curve: result of smoothing of merged plume after step DS has been taken following procedure from stages 1-4.	2-9
2-9	Correction Δy for the merged plume to estimate the new location of the centroid of the merged plume.	2-12
3-1	Comparison of predictions of ANL model to EDF laboratory data . . . cases D1, D2, and D3 . . . F_o = 0.65 and ALPHA = 0.25 with variation in K: (top) centerline trajectory, (bottom) centerline dilution.	3-8
3-2	Comparison of predictions of Slawson-Wigley model to EDF laboratory data . . . cases D1, D2, and D3 . . . F_o = 0.65 and ALPHA = 0.25 with variation in K: (top) centerline trajectory, (bottom) centerline dilution.	3-9

Figure		Page
3-3	Comparison of predictions of Orville model to EDF laboratory data . . . cases D1, D2, and D3 . . F_o = 0.65 and ALPHA = 0.25 with variation in K: (top) centerline trajectory, (bottom) centerline dilution.	3-10
3-4	Comparison of predictions of ANL model to EDF laboratory data . . . configuration A cases E1, E3, E5 and E7 . . . F_o = 0.8 and ALPHA = 0.25 with variation in K: (top) centerline trajectory, (bottom) centerline dilution.	3-11
3-5	Comparison of predictions of Slawson-Wigley model to EDF laboratory data . . . configuration A cases E1, E3, E5 and E7 . . . F_o = 0.8 and ALPHA = 0.25 with variation in K: (top) centerline dilution.	3-12
3-6	Comparison of predictions of Orville model to EDF laboratory data . . . configuration A cases E1, E3, E5 and E7 . . . F_o = 0.8 and ALPHA = 0.25 with variation in K: (top) centerline trajectory (bottom) centerline dilution.	3-13
3-7	Comparison of predictions of ANL model to EDF laboratory data . . . configuration B cases E2, E4, E6 and E8 . . . F_o = 0.8 and ALPHA = 0.25 with variation in K: (top) centerline trajectory, (bottom) centerline dilution.	3-14
3-8	Comparison of predictions of Slawson-Wigley model to EDF laboratory data . . . configuration B cases E2, E4, E6 and E8 . . . F_o = 0.8 and ALPHA = 0.25 with variation in K: (top) centerline trajectory, (bottom) centerline dilution.	3-15
3-9	Comparison of predictions of Orville model to EDF laboratory data . . configuration B cases E2, E4, E6 and E8 . . . F_o = 0.8 and ALPHA = 0.25 with variation in K: (top) centerline trajectory, (bottom) centerline dilution.	3-16
3-10	Comparison of predictions of ANL model to Kannberg-Onishi laboratory data . . . single tower crossflow to the wind; cases K03, K04 and K05 with variation in K: (top) centerline trajectory, (bottom) centerline dilution.	3-17
3-11	Comparison of predictions of Slawson-Wigley model to Kannberg-Onishi laboratory data . . . single tower crossflow to the wind; cases K03, K04 and K05 with variation in K: (top) centerline trajectory, (bottom) centerline dilution.	3-18
3-12	Comparison of predictions of Orville model to Kannberg-Onishi laboratory data . . . single tower crossflow to the wind; cases K03, K04 and K05 with variation in K: (top) centerline trajectory, (bottom) centerline dilution.	3-19
3-13	Comparison of predictions of ANL model to Kannberg-Onishi laboratory data . . . single tower inline to the wind; cases K012, K013 and K014 with variation in K: (top) centerline trajectory, (bottom) centerline dilution.	3-20
3-14	Comparison of prediction of Slawson-Wigley model to Kannberg-Onishi laboratory data . . . single tower inline to the wind; cases K012, K013 and K014 with variation in K: (top) centerline trajectory, (bottom) centerline dilution.	3-21

Figure | Page

3-15 Comparison of predictions of Orville model to Kannberg-Onishi laboratory data . . . single tower inline to the wind; cases KO12, KO13 and KO14 with variation in K: (top) centerline trajectory, (bottom) centerline dilution. 3-22

4-1 Comparison of predictions of ANL model to Kannberg multiple tower laboratory data . . . three towers on a line normal to the wind flow; cases K2, K3 and K4 with variation in K: (top) centerline trajectory, (bottom) centerline temperature decay. 4-3

4-2 Comparison of predictions of ANL model to Kannberg multiple tower laboratory data . . . three towers parallel to each other and crossflow to the wind; cases K10, K11 and K12 with variation in K: (top) centerline trajectory, (bottom) centerline temperature decay. 4-4

4-3 Comparison of predictions of Slawson-Wigley model to Kannberg multiple tower laboratory data . . . three towers on a line normal to the wind flow; cases K2, K3 and K4 with variation in K: (top) centerline trajectory, (bottom) centerline temperature decay. 4-5

4-4 Comparison of predictions of Slawson-Wigley model to Kannberg multiple tower laboratory data . . . three towers parallel to each other and crossflow to the wind; cases K10, K11 and K12 with variation in K: (top) centerline trajectory, (bottom) centerline temperature decay. 4-6

4-5 Comparison of predictions of Orville model to Kannberg multiple tower laboratory data . . . three towers on a line normal to the wind flow; cases K2, K3 and K4 with variation in K: (top) centerline trajectory, (bottom) centerline temperature decay. 4-7

4-6 Comparison of predictions of Orville model to Kannberg multiple tower laboratory data . . . three towers parallel to each other and crossflow to the wind; cases K10, K11 and K12 with variation in K: (top) centerline trajectory, (bottom) centerline temperature decay. 4-8

4-7 Comparison of model predictions to Gregorić laboratory data on upper edge trajectory . . . F_o = 6.0, K = 0.2 and θ = 90.0 with variation in number of towers: (top) ANL model, (bottom) Slawson-Wigley model. 4-11

4-8 (Top) Comparison of predictions of Orville model to Gregorić laboratory data on upper edge trajectory . . . F_o = 0.6, K = 0.2 and θ = 90.0 with variation in number of towers. (Bottom) Comparison of predictions of ANL model to Gregorić laboratory data on upper edge trajectory . . . F_o = 0.6, θ = 90.0 and TOWERS = 7 with variation in K. 4-12

4-9 Comparison of model predictions to Gregorić laboratory data on upper edge trajectory . . . F_o = 6.0, θ = 90.0 and TOWERS = 7 with variation in K: (top) Slawson-Wigley model, (bottom) Orville model. 4-13

4-10 Comparison of model predictions to Gregorić laboratory data on upper edge trajectory . . . F_o = 6.0, K = 0.2 and TOWERS = 7 with variation in θ: (top) ANL model, (bottom) Slawson-Wigley model. 4-14

Figure | Page

4-11 Comparison of predictions of Orville model to Gregoric laboratory data on upper edge trajectory . . . F_o = 6.0, K = 0.2 and TOWERS = 7 with variation in θ. 4-15

4-12 Comparison of predictions of KUMULUS, Orville and ANL models to observed visible plume outlines at Neurath: September 28, 1973 (1500 Hrs.). 4-26

4-13 Comparison of predictions of KUMULUS, Orville and ANL models to observed visible-plume outlines at Neurath: (top) October 4, 1974 (0030 Hrs.), (bottom) October 5, 1973 (1000 Hrs.). 4-27

4-14 Comparison of predictions of KUMULUS, Orville and ANL models to observed visible-plume outlines at Neurath: (top) December 15, 1973 (0900 Hrs.), (bottom) December 15, 1973 (1500 Hrs.). 4-28

4-15 Comparison of predictions of KUMULUS, Orville and ANL models to observed visible plume outlines at Neurath: December 15, 1973 (1130 Hrs.). 4-29

4-16 Comparison of predictions of KUMULUS, Orville and ANL models to observed visible-plume outlines at Neurath: December 16, 1973 (1130 Hrs.). 4-30

4-17 Comparison of predictions of KUMULUS, Orville and ANL models to observed visible-plume outlines at Amos: (top) December 10, 1974 (0828-1120 Hrs.), (bottom) December 12, 1974 (0800-0915 Hrs.). 4-31

4-18 Comparison of predictions of KUMULUS, Orville and ANL models to observed visible-plume outlines at Amos: December 18, 1974 (0747-0955 Hrs.). 4-32

4-19 Comparison of predictions of KUMULUS, Orville and ANL models to observed visible-plume outlines at Amos: December 29, 1974 (0749-1125 Hrs.). 4-33

4-20 Comparison of predictions of KUMULUS, Orville and ANL models to observed visible-plume outlines at Amos: January 2, 1975 (0754-1017 Hrs.). 4-34

4-21 Comparison of predictions of KUMULUS, Orville and ANL models to observed visible-plume outlines at Amos: January 4, 1975 (1033-1245 Hrs.). 4-35

4-22 Comparison of predictions of KUMULUS, Orville and ANL models to observed visible-plume outlines at Amos: (top) January 17, 1975 (0733-1112 Hrs.), (bottom) February 17, 1975 (0723-1015 Hrs.). 4-36

4-23 Comparison of predictions of KUMULUS, Orville and ANL models to observed visible-plume outlines at Amos: January 19, 1975 (0717-1034 Hrs.). 4-37

4-24 Comparison of predictions of KUMULUS, Orville and ANL models to observed visible-plume outlines at Amos: February 10, 1975 (0738-1140 Hrs.). 4-38

Figure | Page

4-25 Comparison of predictions of KUMULUS, Orville and ANL models to observed visible-plume outlines at Amos: February 18, 1975 (0728-1105 Hrs.). 4-39

4-26 Comparison of predictions of KUMULUS, Orville and ANL models to observed visible-plume outlines at Amos: February 20, 1975 (0730-0950 Hrs.). 4-40

4-27 Comparison of predictions of KUMULUS, Orville and ANL models to observed visible-plume outlines at Amos: (top) March 5, 1975 (0828-1135 Hrs.), (bottom) March 9, 1975 (0822-1132 Hrs.). 4-41

4-28 Comparison of predictions of KUMULUS, Orville and ANL models to observed visible-plume outlines at Amos: (top) January 5, 1976 (0802-0930 Hrs.), (bottom) January 9, 1976 (0927-1015 Hrs.). 4-42

4-29 Comparison of predictions of KUMULUS, Orville and ANL models to observed visible-plume outlines at Amos: January 17, 1976 (0749-1115 Hrs.). 4-43

4-30 Comparison of predictions of KUMULUS, Orville and ANL models to observed visible-plume outlines at Amos: January 18, 1976 (0755-0949 Hrs.). 4-44

4-31 Comparison of predictions of KUMULUS, Orville and ANL models to observed visible-plume outlines at Amos: January 10, 1976 (0755-0920 Hrs.). 4-45

4-32 Comparison of predictions of Slawson-Wigley, Orville and ANL models to observed visible-plume outlines at Benning Road: (top) October 31, 1973 (1110 Hrs.), (bottom) November 2, 1973 (0914 Hrs.). 4-49

4-33 Ambient profiles of measured dry-bulb temperature, wind speed and relative humidity along with associated profiles of mixing ratio and saturation deficit . . . Benning Road Case 1. 10/31/73 (1110 Hrs.). 4-50

4-34 Ambient profiles of measured dry-bulb temperature, wind speed and relative humidity along with associated profiles of mixing ratio and saturation deficit . . . Benning Road Case 2. 11/2/73 (0914 Hrs.). 4-51

4-35 Comparison of predictions of Slawson-Wigley, Orville and ANL models to observed visible-plume outlines at Benning Road: (top) November 7, 1973 (0800 Hrs.), (bottom) November 13, 1973 (1030 Hrs.). 4-52

4-36 Ambient profiles of measured dry-bulb temperature, wind speed and relative humidity along with associated profiles of mixing ratio and saturation deficit . . . Benning Road Case 3. 11/7/73 (0800 Hrs.). 4-53

4-37 Ambient profiles of measured dry-bulb temperature, wind speed and relative humidity along with associated profiles of mixing ratio and saturation deficit . . . Benning Road Case 5. 11/13/73 (1030 Hrs.). 4-54

4-38 Comparison of predictions of Slawson-Wigley, Orville and ANL models to observed visible-plume outlines at Benning Road: (top) December 14, 1973 (1151 Hrs.), (bottom) December 19, 1973 (1055 Hrs.). 4-55

Figure Page

4-39 Ambient profiles of measured dry-bulb temperature, wind speed and relative humidity along with associated profiles of mixing ratio and saturation deficit . . . Benning Road Case 6. 12/14/73 (1151 Hrs.). 4-56

4-40 Ambient profiles of measured dry-bulb temperature, wind speed and relative humidity along with associated profiles of mixing ratio and saturation deficit . . . Benning Road Case 7. 12/19/73 (1055 Hrs.). 4-57

4-41 Comparison of predictions of Slawson-Wigley, Orville and ANL models to observed visible-plume outlines at Benning Road: (top) January 22, 1974 (0900 Hrs.), (bottom) February 6, 1974 (0903 Hrs.). 4-58

4-42 Ambient profiles of measured dry-bulb temperature, wind speed and relative humidity along with associated profiles of mixing ratio and saturation deficit . . . Benning Road Case 14. 1/22/74 (0900 Hrs.). 4-59

4-43 Ambient profiles of measured dry-bulb temperature, wind speed and relative humidity along with associated profiles of mixing ratio and saturation deficit . . . Benning Road Case 16. 2/6/74 (0903 Hrs.). 4-60

4-44 Comparison of predictions of Slawson-Wigley, Orville and ANL models to observed visible-plume outlines at Benning Road: (top) February 13, 1974 (0856 Hrs.), (bottom) February 21, 1974 (0858 Hrs.). 4-61

4-45 Ambient profiles of measured dry-bulb temperature, wind speed and relative humidity along with associated profiles of mixing ratio and saturation deficit . . . Benning Road Case 18. 2/13/74 (0856 Hrs.). 4-62

4-46 Ambient profiles of measured dry-bulb temperature, wind speed and relative humidity along with associated profiles of mixing ratio and saturation deficit . . . Benning Road Case 21. 2/21/74 (0858 Hrs.). 4-63

4-47 Comparison of predictions of Slawson-Wigley, Orville and ANL models to observed visible-plume outlines at Gaston: (top) February 13, 1975 (0655-0745 Hrs.), (bottom) February 13, 1975 (0756-0818 Hrs.). 4-66

4-48 Ambient profiles of measured dry-bulb temperature, wind speed and relative humidity along with associated profiles of mixing ratio and saturation deficit . . . Gaston Case 7. 2/13/75 (0655-0745 Hrs.). 4-67

4-49 Ambient profiles of measured dry-bulb temperature, wind speed and relative humidity along with associated profiles of mixing ratio and saturation deficit . . . Gaston Case 8. 2/13/75 (0756-0818 Hrs.). 4-68

4-50 Comparison of predictions of Slawson-Wigley, Orville and ANL models to observed visible-plume outlines at Gaston: (top) February 13, 1975 (0820-0856 Hrs.), (bottom) February 14, 1975 (0851-0925 Hrs.). 4-69

4-51 Ambient profiles of measured dry-bulb temperature, wind speed and relative humidity along with associated profiles of mixing ratio and saturation deficit . . . Gaston Case 9. 2/13/75 (0820-0856 Hrs.). 4-70

Figure

Page

4-52 Ambient profiles of measured dry-bulb temperature, wind speed and relative humidity along with associated profiles of mixing ratio and saturation deficit . . . Gaston Case 10. 2/14/75 (0851-0925 Hrs.). 4-71

4-53 Comparison of predictions of Slawson-Wigley, Orville and ANL to observed visible-plume outlines at Gaston: (top) February 15, 1975 (0634-0728 Hrs.), (bottom) January 14, 1976 (0924-1018 Hrs.). 4-72

4-54 Ambient profiles of measured dry-bulb temperature, wind speed and relative humidity along with associated profiles of mixing ratio and saturation deficit . . . Gaston Case 11. 2/15/75 (0634-0728 Hrs.). 4-73

4-55 Ambient profiles of measured dry-bulb temperature, wind speed and relative humidity along with associated profiles of mixing ratio and saturation deficit . . . Gaston Case 12. 1/14/76 (0924-1018 Hrs.). 4-74

4-56 Comparison of predictions of Slawson-Wigley, Orville and ANL models to observed visible-plume outlines at Gaston: (top) January 16, 1976 (0647-0717 Hrs.), (bottom) January 16, 1976 (0719-0824 Hrs.). 4-75

4-57 Ambient profiles of measured dry-bulb temperature, wind speed and relative humidity along with associated profiles of mixing ratio and saturation deficit . . . Gaston Case 14. 1/16/76 (0647-0717 Hrs.). 4-76

4-58 Ambient profiles of measured dry-bulb temperature, wind speed and relative humidity along with associated profiles of mixing ratio and saturation deficit . . . Gaston Case 15. 1/16/76 (0719-0842 Hrs.). 4-77

4-59 Comparison of predictions of Slawson-Wigley, Orville and ANL models to observed visible-plume outlines at Gaston: (top) January 17, 1976 (0649-0755 Hrs.), (bottom) January 18, 1976 (0912-0928 Hrs.). 4-78

4-60 Ambient profiles of measured dry-bulb temperature, wind speed and relative humidity along with associated profiles of mixing ratio and saturation deficit . . . Gaston Case 16. 1/17/76 (0649-0755 Hrs.). 4-79

4-61 Ambient profiles of measured dry-bulb temperature, wind speed and relative humidity along with associated profiles of mixing ratio and saturation deficit . . . Gaston Case 20. 1/18/76 (0912-0928 Hrs.). 4-80

4-62 Comparison of ANL model predictions of visible plume length and rise to 26 sets of visible plume data for multiple-draft cooling towers at Neurath and Amos. 4-85

4-63 Comparison of ANL model predictions of visible plume length to 26 sets of visible plume data for multiple natural-draft cooling towers at Neurath and Amos. 4-86

4-64 Comparison of KUMULUS model predictions of visible plume length and rise to 26 sets of visible plume data for multiple natural-draft cooling towers at Neurath and Amos. 4-87

Figure | Page

4-65 Comparison of Orville model predictions of visible plume length and rise to 26 sets of visible plume data for multiple natural-draft cooling towers at Neurath and Amos. 4-88

4-66 Comparison of ANL model predictions of visible plume length and rise to 10 sets of visible plume data for a single mechanical-draft cooling tower at Benning Road. 4-89

4-67 Comparison of Slawson-Wigley model predictions of visible plume length and rise to 10 sets of visible plume data for a single mechanical-draft cooling tower at Benning Road. 4-90

4-68 Comparison of Orville model predictions of visible plume length and rise to 10 sets of visible plume data for a single mechanical-draft cooling tower at Benning Road. 4-91

4-69 Comparison of ANL model predictions of visible plume length and rise to 10 sets of visible plume data for multiple mechanical-draft cooling towers at Gaston. 4-92

4-70 Comparison of Slawson-Wigley model predictions of visible plume length and rise to 10 sets of visible plume data for multiple mechanical-draft cooling towers at Gaston. 4-93

4-71 Comparison of Orville model predictions of visible plume length and rise to 10 sets of visible plume data for multiple mechanical-draft cooling towers at Gaston. 4-94

4-72 Layout of the Neurath site along with magnitude and direction of the wind at tower top for each of our 7 Neurath data cases. 4-95

4-73 Layout of the Amos site along with magnitude and direction of wind at tower top for each of our 19 Amos data cases. 4-96

4-74 Layout of the Benning Road towers with wind direction at tower top for our 22 Benning Road data cases. 4-97

4-75 Layout of the Gaston towers with wind direction at tower top for our 20 Gaston data cases. 4-98

TABLES

Table		Page
3-1	Tower configurations for the EDF and Kannberg-Onishi data.	3-6
4-1	Performance statistics for eight multiple-tower models for predictions of visible-plume rise and length for Neurath and Amos.	4-99
4-2	Performance statistics for the ANL Model as compared to the Slawson-Wigley Model and the Orville Model for prediction of visible plume rise and visible plume length for the ten Benning Road data cases.	4-100
4-3	Performance statistics for the ANL Model as compared to the Slawson-Wigley Model and the Orville Model for prediction of visible plume rise and visible plume length for the ten Gaston data cases.	4-101
4-4	Tower configurations and dimensions	4-102

SUMMARY

Existing cooling-tower plume models generally suffer two important deficiencies in their treatment of plume rise from multiple sources. First, most models (all except KUMULUS) do not account for the dependence of wind direction on plume merging. Clearly, the rate of entrainment will differ depending upon the angle of merging of individual plumes. Second, most models (all except KUMULUS) do not account for the effects of tower downwash on plume dispersion under moderate to high wind conditions. It is well known that, when downwash occurs, the plume undergoes additional mixing due to interaction with an ambient air of higher turbulence level. In addition, a downward-directed pressure drag force operates. Accounting for these two tower downwash effects is crucial to the representation of the systematic behavior in the experimental data for plumes under moderate-to-high wind conditions.

This volume presents a generalization of our single-source model (presented earlier in Volume 2) to multiple sources. Our multiple-source model is developed to correct both deficiencies noted above which appear in nearly all existing models. Our model was calibrated to a limited amount of laboratory data and then verified through testing with new lab and field data.

Our merging methodology is a modification of the treatment of plume merging developed recently by Wu and Koh. The Wu-Koh method is essentially a geometric treatment in which any merged plume is assumed to be represented by a finite-length slot jet capped on each end by a half-round jet. Various criteria are presented to determine (a) exactly when two plumes have merged, (b) what their merged cross-section is in terms of half-round and finite-length slot components, and (c) the fluxes for the merged plume determined from the fluxes of the individual plumes prior to merging. The Wu-Koh merging logic provides a multiple-source logic which satisfies a few important physical characteristics, each supported by data, that we wish for any multiple-plume model:

1. predicted plumes for cases where the wind is directed in line with the towers will rise higher after merging than predicted plumes for the identical case where the wind is directed normal to a line of towers.

2. predicted plumes begin as round plumes, then merge, after which the merged plume evolves back again into a round plume.

A modification we made to the Wu-Koh merging logic now assures that all plume fluxes are conserved during merging. In the original Wu-Koh methodology, this was not generally the case.

This methodology should be contrasted with existing plume merging methodologies. The first is that (Slawson-Wigley model, for example) in which plume merging occurs at the point where the plume radius from a single tower (or cell) grows to exactly half the distance between towers or cells. The second method is the setting up of an equivalent source at the start of calculations by combining fluxes into one tower or cell and following only that one plume. The first method ignores wind direction effects. The second ignores wind direction effects as well, and additionally, ignores the dispersion of the plumes as individual entities prior to merging. The second method will yield higher plumes than will occur in the field. The two methods described above are probably not significantly wrong when towers (or cells) are located very close together and long plumes occur. One of our objectives has been to employ a more universally valid merging methodology which could successfully treat plumes from towers that are not very closely situated and can also, more accurately, treat the interaction of shorter plumes. A criterion to simplify our merging method when simplifications are warranted is the subject of future work.

In terms of tower downwash, our multiple-source model generalizes our single source model in that it accounts for the wake effects from numerous obstructions (mainly the towers themselves) whereas the single source model only accounts for the wake solely from the plume's generating source. Since the multiple source model incorporates the same plume equations as does the single plume model, the generalized model draws heavily from the single source model.

The treatment of additional entrainment due to downwash is generalized from our single source method by introducing one effective flat plate to simulate each bluff body of significance in the multiple-source configuration. The turbulence level in the wake behind each plate is then combined additively leading to the cumulative wake entrainment. Exact details of our simulation for mechanical and natural-draft cooling towers is given in Section 2.

The treatment of the downward-directed pressure drag force due to the wake of the tower is generalized in the same manner. The same philosophy is kept whereby we average the force around the plume circumference, allowing for variations in the wake characteristics across the plume diameter.

Calibration of the multiple-source model to data was accomplished to determine values of two unknown downwash coefficients. The data used were

1. EDF 2- and 4-tower lab data where experiments were run for different ambient wind speeds (2 NDCTs in crossflow to the wind, K = 1.0, 2.0, 3.0; 4 towers in both parallelepiped and diamond orientation, K = 0.5, 1.0, 2.0, 3.0), and

2. Kannberg-Onishi lab data where a single linear MDCT is in-line and, alternatively, in crossflow to the wind (K = 0.6, 1.0, and 1.5).

Overall, predictions agreed quite well with the data for trajectory and dilution for the EDF data sets. Generally, the ANL Model's predicted trajectory lay above the data for low K but showed more bending than the data for large K. Dilution predictions were fairly good over the range of data tested. The ANL Model predictions were compared to predictions of the Slawson-Wigley and Orville Models. Neither of those two models has a careful treatment of plume merging and both models ignore tower downwash effects. The Slawson-Wigley model provided satisfactory trajectory predictions but dilution predictions were generally too low. Orville model predictions were rather poor. Predicted plume trajectories rose much too steeply and dilution was greatly underpredicted. Setting up an equivalent source undoubtedly contributes to a lesser overall entrainment rate for the plumes than if they were treated individually before merging. In any case, Orville model predictions were generally poor as we would suspect from the results of our model/data comparisons for single-source lab data as seen in Volume 2. The same systematic behavior was seen for all three models in our model/data comparisons with Kannberg-Onishi lab data. The presence of tower downwash leading to more bent-over and more mixed plumes was not represented in Orville and Slawson-Wigley predictions. ANL Model predictions were quite good for the crossflow cases and satisfactory for in-line cases. ANL predicted trajectories could use greater bending with better dilution in each in-line case, however.

Verification cases for the ANL Model include model/data comparisons with the following data:

1. Kannberg multiple MDCT lab data (three towers of six cells each oriented in a straight line but in crossflow to the wind or else are located

parallel to each other in crossflow; K = 0.6, 1.1, 1.6)

2. Gregoric MDCT lab data (1, 2, 3, 5, 7 cells oriented in a straight line with ambient flow at angles 0°, 90°, 45° to the line of cells)

3. 26 field data cases from Neurath and Amos representing NDCT plumes from three towers

4. 10 field data cases from Benning Road MDCT

5. 10 field data cases from Gaston MDCT

In the model/data comparisons with the Kannberg data, an interesting and typical feature was revealed. The data indicate the greatest dilutions for the lowest K (smallest winds) at any fixed downwind distance. The Slawson-Wigley and Orville models revealed the opposite trend while the ANL Model predicted the correct trend due to our treatment of tower downwash which was ignored by the other two models. The more correct merging treatment in the ANL Model also helped provide better predictions than shown by the other models. Model/data comparisons with the Gregoric data revealed similar results as obtained from the Kannberg data. ANL Model predictions were very good for crossflow cases and satisfactory for the inline data. However, no model was successful for the $\theta = 45°$ case. Undoubtedly, the very large wake for that case is not well represented in any model including our own.

Model/data comparisons with Amos and Neurath field data revealed the ANL Model to perform best overall for existing models in terms of plume length and rise statistics. The greatest improvement shown by the ANL Model over other models relates to plume length statistics. The ANL Model could be improved in the area of its atmospheric diffusion phase formulation which would allow more accurate prediction of the very long Amos cases.

The Orville model predicted best for the Benning Road data. However, that model was calibrated to those data sets. The Orville model's poor performance with lab data indicate a lack of correct representation of plume physics in spite of the good performance with these Benning Road data. ANL Model predictions are satisfactory but we suspect that better results can be achieved through a detailed review of our methodology of choosing our plates for downwash representation for in-line cases.

The ANL Model predicted Gaston plumes very well, especially visible plume length.

Clearly, the ANL Model performs best over all the lab and field data tested. In terms of a simple statistic, the ANL Model predicts visible plume height within a factor of 2 and/or visible plume length within a factor of 2 1/2 in 80% of our field data test cases. For comparison, the Orville Model predicts within a factor of 2 on visible rise and/or 2 1/2 on visible length in 67% of our field data test cases; the Slawson-Wigley model satisfies this criterion 49% of the time.

It should be noted that the lab data and field data provide complementary information on plume physics. First, the same kinds of information are available from the lab and field data. Lab data include measurements on plume trajectories and centerline concentrations (or dilutions). That same kind of information can be inferred from the visible plume height and length obtained from the field data. There is, however, one major difference between these types of data. The lab data apply only to the "near field" where plume behavior is determined almost entirely by the hydrodynamics of interactions between the source and mean flow. The field data, on the other hand, can show "far field" effects on the visible plume as dominated by the structure of ambient turbulence in the atmosphere. In about 40% of our field data cases (Neurath, Amos, Benning Road, Gaston sites), atmospheric turbulence effects appeared to be present, as identified by the number of times the ANL predicted plume entered diffusion phase before losing visibility. In about half of those latter field cases, atmospheric turbulence (far field effects) appeared to be very important in casuing the plume to lose visibility. As one would expect, for the majority of field data cases where far field effects had only a minor influence (e.g. data where plume lost visibility in rising phase), we found that the ANL Model showed the same type of behavior as applied to both the lab and field data.

We believe that our ANL model represents the state-of-the-art based on model testing done here and in our earlier work. Model refinements could provide further improvement in the areas of (a) the merging logic, (b) the choice of plates to represent MDCT cells (especially in-line case), and (c) in our modeling of the atmospheric diffusion phase. Each of these areas is the subject of ongoing improvement work.

Section 1

INTRODUCTION

This volume generalizes the model we developed for single-source plumes from cooling towers to allow the prediction of plumes from multiple-sources. Volume 2 presented the theory, calibration, and verification of our single-source model. That single-source model predicts plumes from a single natural-draft cooling tower or a plume from a single cell of a mechanical-draft cooling tower. This present volume develops a methodology of plume merging which allows us to now handle plumes from many sources such as: multiple NDCTs, one or more linear MDCTs, circular MDCTs, or any combination thereof. Our treatment of merging accounts for differing entrainment rates that a plume experiences as it merges with a second plume, and depends on angle of merging. A description of the method is given in Section 2. An expanded treatment of tower downwash is presented also in Section 2.

Existing models employ very simple merging criterion. Those criteria are probably not significantly wrong when towers are located very close together and long plumes occur. One of our objectives has been to employ a more universally valid merging methodology which could successfully treat plumes from towers that are not very closely situated and can, more accurately, treat the interaction of shorter plumes.

As seen in Section 2, the merging methodology chosen satisfies a few important physical characteristics that we want our model to have:

1. plumes in line with the wind rise higher after merging than plumes in crosswind
2. all fluxes are conserved during merging
3. plumes begin as round plumes, then merge, after which the merged plume evolves back again into a round plume.

Model calibration was carried out (to fix only two downwash coefficients) through model/data comparisons with lab data on plumes from multiple towers.

Model verification was carried out with lab and field data from sources not used in the calibration process. We leave for future work the task of determining a criterion

which would enable us to simplify the plume merging methodology for cases where the initial sources are very close together. The model developed in this volume is the basis for the multiple-tower drift model presented in Volume 5.

Section 2

DEVELOPMENT OF ANL MULTIPLE-SOURCE PLUME MODEL

INTRODUCTION

The ANL multiple-tower plume model was developed through a straight-forward generalization of the ANL single-tower plume model. Our multiple-tower model has a number of appealing advantages over competitive multiple-tower plume models, one of which is that it can treat any number of cooling towers in any geometrical configuration in any orientation to the direction of the wind. An additional important advantage is its ability to represent certain features of multiple-source plume dispersion that have been observed in the field and laboratory. Foremost among these is the observation that plumes created from a MDCT in line with the wind rise higher than plumes from a MDCT in crossflow to the wind. Plumes in line with the wind merge rapidly combining the effects of plume buoyancy of each individual plume; in addition, there is a minimization of the effects of tower downwash for the tower in line to the wind. The best way to describe the methodology of prediction of our multiple-source model is to describe how a particular plume case is computed. The merging methodology follows the work of Wu and Koh.

METHODOLOGY OF PLUME MERGING

The computer code for the model first reads in the input data and makes any adjustments, if needed, to the coordinate system. The code will arrange a cartesian coordinate system of its own so that the X-axis is parallel to the wind direction. The X and Y coordinates of the towers are made non-negative with the most upwind tower positioned at X equal to zero. The plume from this tower is computed first where checks are made at every integration step to determine when the plume centerline X-coordinate is greater than or equal to any of the X-coordinates of the downwind towers. When this happens, the code initializes all the variables needed for the calculation of the plume from this new tower at which time one integration step is taken with the new plume. If more than one new tower is involved, the same procedure is repeated for each tower. The code follows each plume one step at a time and at each step checks are made to see if any merging (defined below) is occurring. In order to understand the method of merging, it is best to look at the

simplest merging case, that of two individual single plumes merging. These plumes may be from two NDCTs or from two cells of a MDCT.

As the two single plumes continue to move downwind, their circular cross-sections may eventually begin to touch and overlap. Simple touching (not necessarily total overlapping) of plume cross-sections is the first of two criterion for merging. A second criterion required for merging for individual round plumes is shown in Figure 2-1. The area of the trapezoid defined by lines B3, B4 and the diameters of the two half-round plumes of radii B1 and B2 must be equal to or greater than the sum of the areas of the two half-round plumes represented by the semicircular dashed lines. When our two plume system satisfies both these criteria, the plumes are ready to be merged into a single plume, defined by four variables:

1. B1 - the radius of the lowermost or leftmost half-round plume. (The left end of the plume is defined as the end closer to the X-axis.)
2. B2 - the radius of the uppermost or rightmost half-round plume.
3. A - the height of the trapezoid between the two half round plumes. (also referred to as the slot jet length).
4. ϕ - the angle between the Y-axis and the line joining the center points of the two merging plumes.

These four variables, determined at the location of merging, are used in following the merged plume from that point on. The model treats this merged plume as a new plume and continues as if there never were two individual round plumes. Conserved fluxes for the merged plume are defined from the summation of the fluxes of the previous individual plumes.

Mention must be made of the integrator step size, DS, chosen by the code in the integration of the plume equations. A potential problem occurs if both plumes are not at the same downwind location at the time of merging. As two individual plumes move downwind, the code determines DS for each plume in such a way that the merging takes place when both plumes are at approximately the same X-coordinate. At any time when merging is checked, our two plumes will have their X-coordinates within a small distance of each other. This distance was chosen as one tenth of the radius of the plume which has the smaller X-coordinate. This procedure was incorporated into the merging logic by Wu and Koh so that the merging plumes will be in the same plane as much as possible at the time of merging.

The calculation of B1, B2, A and ϕ requires that the merged plume be first classified into one of two categories: horizontal or vertical. A horizontal merged plume is

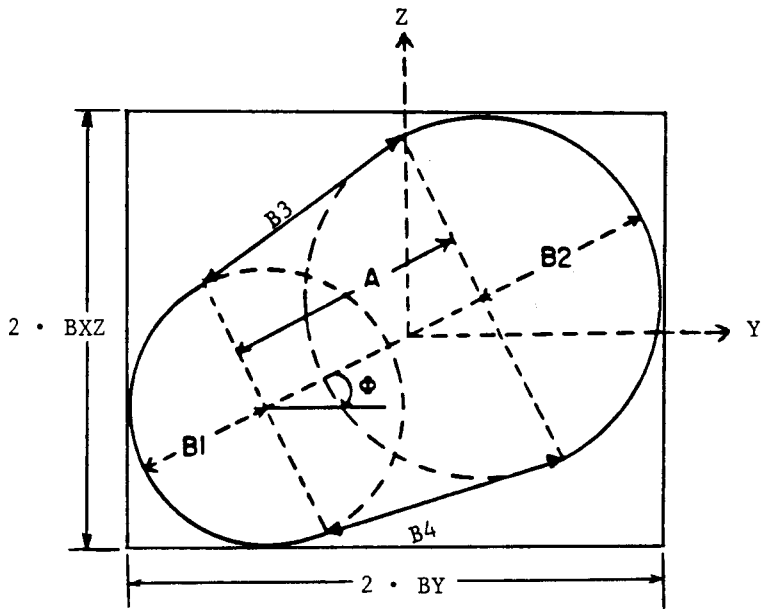

Figure 2-1. Sketch of two individual round plumes before and after merging. [Source: Wu and Koh (1).]

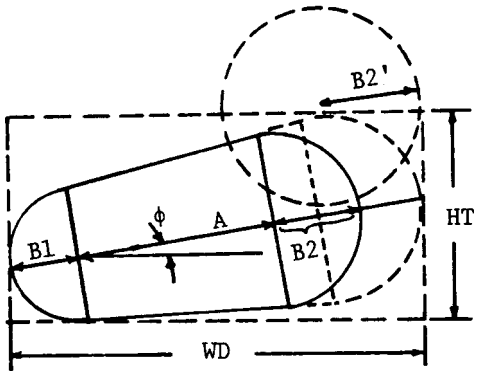

Figure 2-2. Sketch of a single round plume and a horizontally-oriented merged plume before and after merging; the slot and one of the half-round plumes is enlarged during merging. [Source: Wu and Koh (1).]

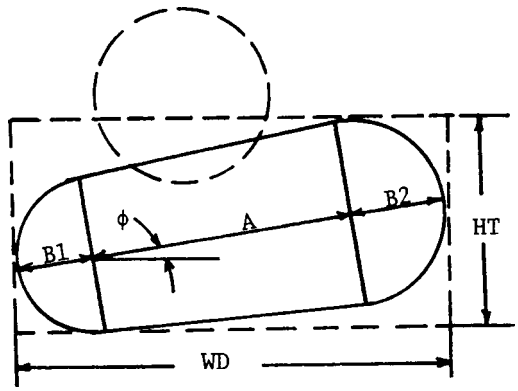

Figure 2-4. Sketch of a single round plume and a horizontally-oriented merged plume before and after merging; only the slot portion of the merged plume is enlarged during merging. [Source: Wu and Koh (1).]

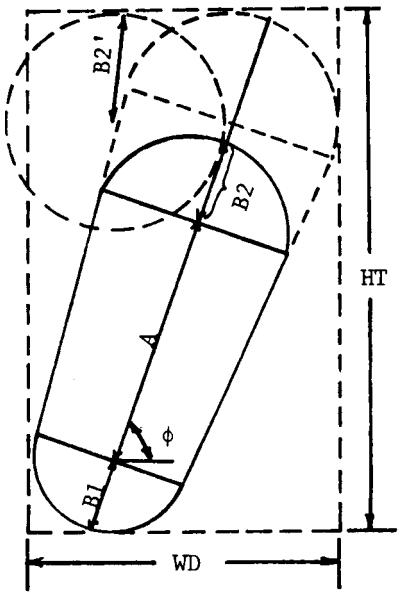

Figure 2-3. Sketch of a single round plume and a vertically-oriented plume before and after merging; the slot and one of the half-round plumes is enlarged during merging. [Source: Wu and Koh (1).]

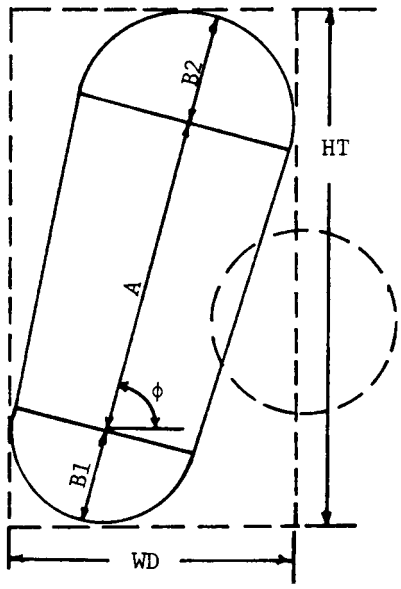

Figure 2-5. Sketch of a single round plume and a vertically-oriented merged plume before and after merging; only the slot portion of the merged plume is enlarged during merging. [Source: Wu and Koh (1).]

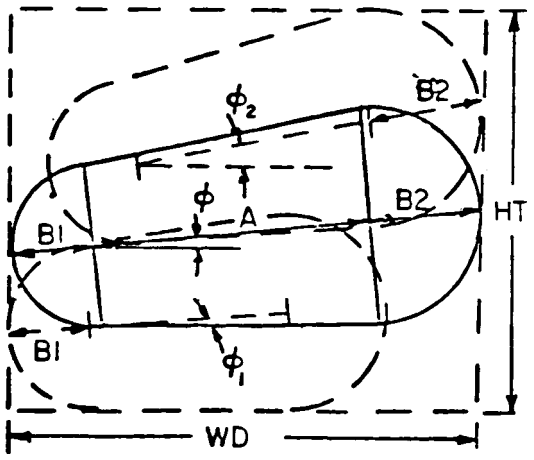

Figure 2-6. Sketch of the before (dotted curves) and after (solid line curve) merging of two horizontally-oriented merged plumes.

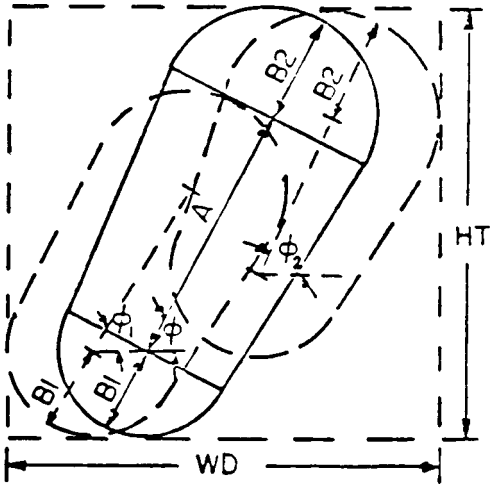

Figure 2-7. Sketch of the before (dotted curves) and after (solid line curve) merging of two vertically-oriented merged plumes.

represented by a total width, WD, of the new merged plume which is larger than the total height, HT. This can be seen in Figures 2-2, 2-4, and 2-6. Otherwise, the plume is defined to be vertical as in Figures 2-3, 2-5, and 2-7.

B1 and B2 are known at merging and ϕ is determined by simple trigonometric relations. With B1, B2 and ϕ determined, we can calculate A from the following using geometry:

For horizontal plumes:

$$A = (WD-B1-B2)/\cos\phi \qquad \cos\phi \neq 0 \qquad (2\text{-}1)$$

$$A = HT-B1-B2 \qquad \cos\phi = 0 \qquad (2\text{-}2)$$

For vertical plumes:

$$A = (HT-BL-B2)/\sin\phi \qquad \sin\phi \neq 0 \qquad (2\text{-}3)$$

$$A = WD-B1-B2 \qquad \sin\phi = 0 \qquad (2\text{-}4)$$

Merging, of course, is not always between two individual round plumes. If an individual round plume merges with a merged plume as in Figures 2-2 to 2-5, ϕ is assumed to remain unchanged from the merged plume value since Wu and Koh assume that the overall merged plume will be "dominated" by the original merged plume. If the individual round plume is merging with a merged plume as shown in Figures 2-4 and 2-5, the values for B1, B2, and A remain unchanged along with the width and height of the merged plume. The shape of this merged plume will not be altered until the next integration step. If the merging occurs as shown in Figures 2-2 and 2-3, the shape of the merged plume is altered at the moment to reflect this new merging. Since the rightmost point on the single plume (designated by the dashed line and radius B2 in Figure 2-2) is further to the right than the rightmost point of the merged plume (solid line), the half round plume with radius B2 in the merged plume will simply be replaced by the single plume with radius B2'. Subsequently, A will be recalculated to extend to the dashed line marking the right side of the trapezoid. The same applies to a vertical plume situation as shown in Figure 2-3 with the checks make on the uppermost points. One disadvantage exists of the merging logic is shown in Figures 2-2 through 2-7. As soon as any two plumes overlap (with one of them already perhaps a merged plume), the new merging is assumed to occur instantaneously. The second criterion for merging is no longer applied when one plume is already a merged plume. Another drawback is represented in Figures 2-4 and 2-5. After merging, the shape is <u>not</u> altered, only the fluxes of the merged plume are redefined. Essentially then, during merging, the single round plume is assumed to be "swallowed up" by the slot portion of the already merged plume. The reasoning for that assumption was

apparently that the original merged plume would dominate this new merging also. These two disadvantages of the merging method were corrected for in a different segment of the program which will be explained later.

Figures 2-6 and 2-7 represent merging between merged plumes. The two merging plumes represented by dashed lines in both figures will yield a merged plume represented by the solid line. Since the half round plume with radius B2 (Figure 2-6) in the topmost merged plume is to the right of the half round plume on the right of the lowest merged plume, then B2 will be the radius for the right end of the resulting merged plume. Likewise with the half round plume with radius B1 in the lowest merged plume. It is located further left than the left end of the topmost plume; therefore, B1 will be the radius of the left end of the resulting plume. The resulting angle, ϕ, is calculated as the average of ϕ_1, and ϕ_2 from the merging plumes. The slot length, A, is determined from the equations stated previously.

A merged plume is integrated over step size DS in four stages, whereas, for an individual round plume, a single simple integration step was sufficient. The four stages are made to help determine the new shape of the merged plume as defined by the variables B1, B2 and A. The angle, ϕ, stays constant until further merging occurs with the merged plume.

The first stage involves integration of the governing equations of the individual round plume of radius B1 and fluxes derived from the set of fluxes of the merged plume. The second stage involves integration of the round-plume governing equations for the round plume of radius B2 over the same distance, DS. These two stages result in the computation of two new plume radii, b_{r1} and b_{r2}, along with the centerline velocities of these two half-round plumes V_{r1} and V_{r2}. The third stage involves the integration of the governing equations of the slot jet of length A. The fluxes for the slot are determined by taking one half of the sum of the fluxes for the two end plumes. The fluxes are then divided by the length A resulting in fluxes per unit length of slot. The slot jet is treated as an infinite slot jet with only one variable geometric dimension, b_s, the half-width of the infinite slot. The governing equations for the infinite slot jet were derived (not shown) and were found to be exactly equivalent to the equations involved in round plume integration, but with different meanings applied to some variables. [For example, R is no longer thought of as the round-jet radius, but instead, the half-width of the slot jet, b_s.] The slot jet equations are integrated over the same DS distance whereby a new half width b_s and slot velocity V_s are obtained. The first three stages involve only a determination of the new merged plume shape. The fourth stage provides the time and final determination of plume variables for integration over the step DS. To do this, our plume

shape defined by B1, B2 and A is temporarily modified to represent one "effective" round plume for purposes of integration of our round-plume equations over step DS. Round plume equations are used but the entrainment function is modified to represent separate contributions from the two half-round and single slot portions of the plume. This integration of plume equations in Stage 4 provides us with plume velocity, temperature, etc. which represent model output. Stages 1-3 were required to inform us as to the proper contribution of round and slot components to our entrainment and downwash functions in our effective round-plume integration.

The calculated plume cross-section, defined by b_{r1}, b_{r2} and b_s in Stages 1-3, may not yield a completely smooth shape due to the different entrainment rates between round and slot portions of the merged plume. Figure 2-8 shows potential discontinuities that can occur by the dashed line. To estimate the discontinuity and obtain a modified smooth cross-section described by B1, B2 and A, the following set of equations is used by Wu and Koh:

$$0.5\,\pi\,(b_{r1}^2\,V_{r1} + b_{r2}^2\,V_{r2}) + 2b_s \cdot a \cdot V_s =$$

$$[0.5\,\pi\,(B1^2 + B2^2) + A(B1 + B2)] \cdot V \qquad (2\text{-}5)$$

$$a + b_{r1} + b_{r2} = A + B1 + B2 \qquad (2\text{-}6)$$

$$b_{r1}/b_{r2} = B1/B2 \qquad (2\text{-}7)$$

where a is the value of A at the outset of the integration.

Equation (2-5) describes the redistribution of the volume flux through conservation of mass from the calculated merged plume to the proposed modified plume. Equation (2-6) maintains the same plume size (length of plume cross-section) between the calculated and modified plumes. Equation (2-7) maintains the same ratios of the radii of the two half-round plumes between calculated and modified plumes.

The equations are solved for B1, B2 and A to determine the modified merged plume shape.

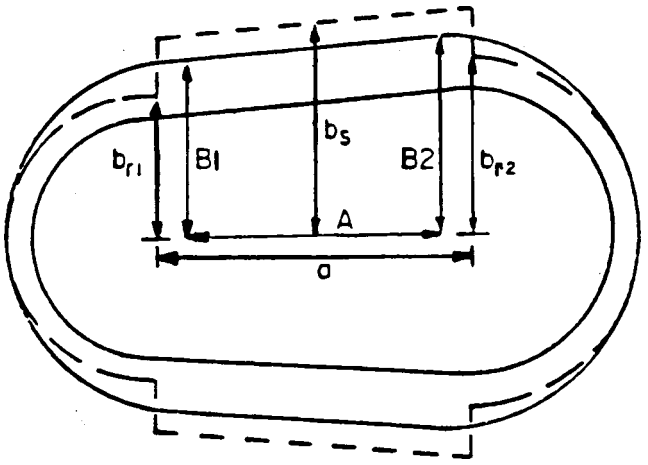

Figure 2-8. Modified merged plume shape.

Inner solid curve: merged plume before integration step DS.

Dashed curve: merged plume configuration after completing Stages 1-3 (see text).

Outer solid curve: result of smoothing of merged plume after step DS has been taken following procedure from Stages 1-4.

[Source: Wu and Koh (1).]

We felt that a fourth condition should be set to insure conservation of all plume fluxes in the application of Eqs. 2-5 to 2-7. The mass flux of the merged plume is $Y(1) = R^2 V\rho$ with R representing the effective radius of the merged plume. The area A1, of a cross-section of the merged plume would then be

$$A1 = \frac{Y(1) \cdot \pi}{V \cdot \rho} \tag{2-8}$$

where V is the plume centerline velocity of the merged plume and ρ the density. The area, A2, of the modified merged plume is simply

$$A2 = \frac{B1^2 \cdot \pi}{2} + \frac{B2^2 \cdot \pi}{2} + A(B1 + B2) \tag{2-9}$$

Let F_A be an area adjustment factor defined by

$$F_A = \sqrt{\frac{A1}{A2}} \tag{2-10}$$

After the modified merged plume shape is determined at each integration step, B1, B2 and A should be adjusted by multiplying each variable by F_A, therefore assuring the conservation of mass flux and consequently, the conservation of momentum, moisture and enthalpy fluxes. We imposed this fourth condition as well, although it was not used by Wu and Koh.

Two other variables are computed from the values B1, B2, A and ϕ at each step; these variables are used for the purpose of checking any new plume merging that may occur at subsequent steps. They are BY, the half width, and BXZ, the half height of the merged plume as seen in Figure 2-1. The following equations are used to determine BY and BXZ:

$$\begin{aligned} BY &= 0.5\,(A \cos\phi + B1 + B2) && \cos\phi \neq 0 \\ &= B1 && B1 \geq B2,\ \cos\phi = 0 \\ &= B2 && B2 > B1,\ \cos\phi = 0 \end{aligned} \tag{2-11}$$

and

$$\begin{aligned} BXZ &= 0.5\,(A \sin\phi + B1 + B2) && \sin\phi \neq 0 \\ &= B1 && B1 \geq B2,\ \sin\phi = 0 \\ &= B2 && B2 > B1,\ \sin\phi = 0 \end{aligned} \tag{2-12}$$

As integration of the merged plume continues, B1, B2 and A will be constantly changing. The Y-coordinate of the plume centroid (which locates the plume centerline) must also be changed due to this uneven change. The following equation is used to calculate the adjustment, Δy, needed as shown in Figure 2-9.

$$\Delta y = \frac{A_j + B1_j - B2_j}{2} \cdot \frac{A_{j+1}}{A_j} + B2_{j+1} - \frac{A_{j+1} + B1_{j+1} + B2_{j+1}}{} \cdot |\cos\phi|$$

$$= 0.5\ |\cos\phi| \cdot (B1_j - B2_j)\ \frac{A_{j+1}}{A_j} + B2_{j+1} - B1_{j+1} \qquad (2\text{-}13)$$

where j and j + 1 refer to consecutive calculational steps. The Y location of the plume is used to test future plume mergings and to estimate the position of the plume in the wake of upwind cooling tower structures (discussed later).

As the merged plume continues downwind, the radii of the two half round plumes increase as A decreases. When A approaches zero, the shape of the merged plume cross-section becomes a circle and the method for integrating a single round plume is reapplied. This behavior of the model matches our physical intuition and experimental data since we expect merged plumes to eventually evolve (in neutral or unstable atmospheres) into a round plume once again.

Entrainment Rate for the Slot Jet and the Merged Plume

The rate of entrainment that occurs for the slot portion of the dispersing merged plume is yet to be specified. The formulation used is as follows.

The mass flux of the slot jet is defined to be

$$\phi_s = A(B1 + B2) \cdot V_s \cdot \rho_s \qquad (2\text{-}14)$$

where V_s is the velocity of the jet and ρ_s the density.

If $\phi_s(s)$ is the mass flux of the slot jet cross-section at s, then in time Δt, the mass balance equation for the slot will be

$$\phi_s(s + \Delta s) \cong \phi_s(s) + (B3 + B4)\ V_e\ \rho_a\ \Delta s \qquad (2\text{-}15)$$

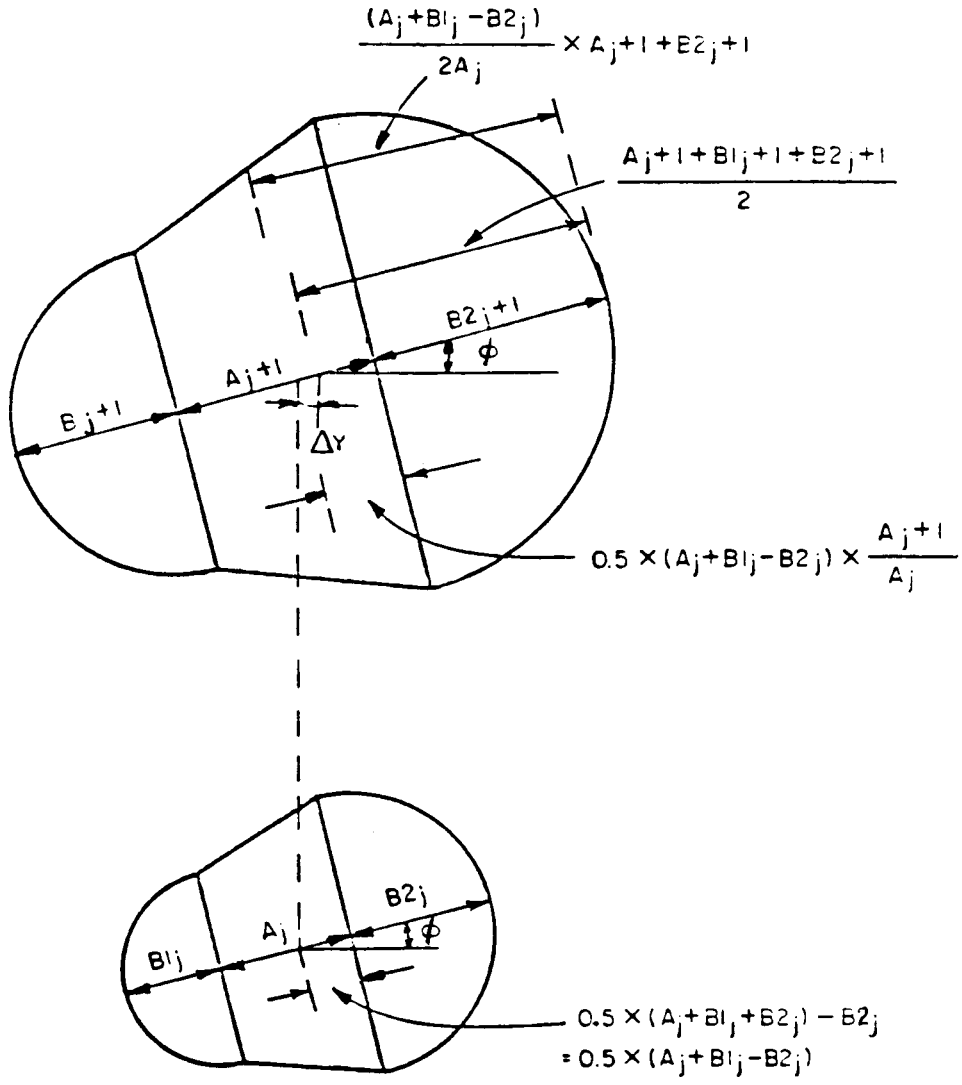

Figure 2-9. Correction Δy for the merged plume to estimate the new location of the centroid of the merged plume. [Source: Wu and Koh (1).]

where B3 and B4 represent the lengths of the top and bottom of the slot as in Figure 2-1. The last term on the right in this equation represents the mass of ambient air added to the slot in time Δt. The slot jet entrains ambient air along the sides labeled B3 and B4. Dividing by Δs and rearranging terms, we obtain

$$\frac{\Delta \phi_s}{\Delta s} \cong (B3 + B4)\ V_e\ \rho_a \tag{2-16}$$

Taking the limit as $\Delta s \to 0$ we get

$$\frac{d\phi_s}{ds} = (B3 + B4)\ V_e\ \rho_a \tag{2-17}$$

The fractional entrainment rate, μ, is defined as

$$\mu = \frac{1}{\phi} \cdot \frac{d\phi}{ds}\ , \tag{2-18}$$

and thus we can obtain the fractional entrainment rate for the slot jet as μ_s,

$$\mu_s = \frac{1}{\phi_s} \cdot \frac{d\phi_s}{ds} = \frac{(B3 + B4)\ V_e\ \rho_a}{A(B1 + B2)\ V_s \cdot \rho_s} \tag{2-19}$$

B3 + B4 is approximated to be 2A and, as a result, Eq. (2-19) can be rewritten as

$$\mu_s = \frac{2 \cdot A \cdot V_e\ \rho_a}{A(B1 + B2)\ V_s\ \rho_s} = \frac{2}{B1 + B2} \cdot \frac{V_e}{V_s} \cdot \frac{\rho_a}{\rho_s} \tag{2-20}$$

With the fractional entrainment rate for a slot jet now known and the fractional entrainment rate for a round jet known earlier from our single source model, we can determine the fractional entrainment rate for a merged plume.

The mass flux, ϕ, of the merged plume is

$$\phi = \phi_1 + \phi_2 + \phi_s \tag{2-21}$$

where ϕ_1 and ϕ_2 are the mass fluxes associated with the two semicircular ends of the merged plume, and ϕ_s the mass flux of the slot jet.

Let μ_1, μ_2 and μ_s correspond to the fractional entrainment rates of the two half round plumes and the slot, respectively. The fractional entrainment rate for the entire merged plume can be easily shown to be

$$\mu = \mu_1 \left(\frac{\phi_1}{\phi}\right) + \mu_2 \left(\frac{\phi_2}{\phi}\right) + \mu_s \left(\frac{\phi_s}{\phi}\right). \qquad (2\text{-}22)$$

The entrainment velocity for circular plumes, V_e, is retained as is from the single source model. The entrainment velocity for the slot jet is assumed to be (taken directly from Wu and Koh)

$$V_e = P\left[0.198 \cdot |v - u\cos\theta| + 0.3536\, u|\sin\theta|\cos\theta\right]$$

where P is the perimeter of the portion of the slot jet which entrains the ambient air, V is the centerline velocity, u is the horizontal component of V, and θ is the angle of inclination between the plume cross-section and the x-axis.

THE TREATMENT OF DOWNWASH IN THE MULTIPLE SOURCE MODEL

Our multiple source model generalizes our single source model in the treatment of downwash in that it accounts for the wake effects from numerous obstructions (mainly the towers themselves) whereas the single source model only accounts for the wake solely from the plume's originating source. Since the multiple source model incorporates the same plume equations as does the single plume model, the generalized model draws heavily from the single source model (See Volume 2).

In modeling a single-source plume, a single effective flat plate was used to simulate the wake effects of the plume source. To generalize this method to multiple sources, we introduce one effective flat plate to simulate each bluff body of significance in the multiple-source configuration. Thus we consider wake contributions from each source structure and possibly also neighboring objects such as large buildings. Once all the equivalent flat plates are determined in terms of size and location for each structure, the same prescription used in the single source model may be used to predict the turbulence level in the wake behind each plate. These turbulence levels are then combined additively leading to the cumulative wake entrainment.

For natural-draft cooling towers, we employ one plate per tower. The size and location of each plate is determined by the theory of Halitsky (2) as described in Volume 2. For a linear mechanical-draft cooling tower, we use a single plate to

represent the entire cooling-tower structure when the wind is directed in crossflow to the line of the tower or $\pm$ 20° from the crossflow direction. For the complementary case when the direction of the wind is outside the $\pm$ 20° range (this range includes the in-line case), we employ a number of plates equal to the number of cells. Each cell is assumed to be a vertical cylinder beginning from the top exit plane and continuing down to the ground. The computer code allows the option of treating the wake effects of buildings on site through the addition of more plates, one per building.

Now that the number of plates are determined for any configuration of cooling towers, we next discuss the treatment of wake turbulence. We take half the sum of the turbulence levels at each point on the plume cross-section due to wake turbulence computed from all the plates to represent the turbulence level on each point on the plume cross-section resulting from cavity wakes. The formulas that relate the turbulence level to wake entrainment are the same as used in the single-source model. We, however, recognize that the turbulence level at a point within the cavities of several towers is less than additive. However, lab data are insufficient to provide an indication on how to correct that sum value. We have chosen to divide the sum turbulence level by 2 in order to provide a more realistic estimate. The factor of 2 was found to be reasonably successful in tests we made of the model to selected laboratory data.

Other aspects of the single-source model remain unchanged in application to multiple sources. One example is the treatment the downward-directed pressure drag force due to the wake of the tower. The same philosophy is kept whereby we average the force around the plume circumference, allowing for variations in the wake characteristics across the plume diameter. Such variations may be slight when the dimensions of the wake effects are much larger than the plume diameter. If so, the user may simplify the procedure, saving computer time, by setting a switch which causes the program to substitute the centerline value in place of the average (determined from integration around the plume parameter). In practice, use of the centerline value leads to nearly the same results as the more complex procedure of integrating the wake force about the plume circumference.

REFERENCES

1. F.H. Wu and R.C. Koh. Mathematical Model for Multiple Cooling Tower Plumes. W.M. Keck Laboratory of Hydraulics and Water Resources. Report KH-R-37. California Institute of Technology. July 1977.

2. J. Halitsky. Wake and Dispersion Models for the EBR-II Building Complex. IN: Atmospheric Environment. Vol. II. No.7. pp 577-596. 1977.

Section 3

CALIBRATION OF THE ANL MULTIPLE-SOURCE PLUME MODEL

INTRODUCTION

The ANL single-source model was calibrated as discussed in Volume 2. However, downwash coefficients (C_{wf} and C_{wv}) do require changing due to special downwash characteristics for different types of multiple source structures. The remaining calibration constants from the ANL-single-source model carry over unaltered to the ANL multiple-source model. Employing the multiple-source model with the constants from the single-tower model would have provided too much dilution in most of the cases. We found that there is less downwash involved in multiple-source plume dispersion than would be expected by applying the single-source downwash formulation individually for each one of our multiple sources. Therefore we felt it was necessary to calibrate the downwash coefficients, C_{wf} and C_{wv}, for the ANL multiple-source model with multiple-source data in order to optimize model performance for both the single- and multiple-source models.

Two sets of laboratory data were used in the calibration of downwash coefficients. The first sets of data were taken in a parametric study on the effects of wind speed on multiple NDCT plume dispersion by Electricité de France (EDF) (1) in Chatou. The lab data were taken in a water flume under isothermal conditions. There were three data cases (Series D) taken with a two-tower configuration with the towers in a line normal to the wind flow. There were eight other data cases (Series E) with four towers in two configurations. Configuration A (four cases) had the four towers located at vertices of a parallelepiped where the wind was in the direction of the parallel faces. Configuration B (four cases) had the towers located at vertices of a diamond with the wind directed along a line converting two towers located opposite to each other. Each individual data case represents a run with a different wind speed where tower and all other ambient parameters remain fixed. The nondimensional parameters for Series D plume study were F_o = 0.65, ALPHA = 0.25 (wind speed power-law exponent), and H/D = 1.85 (tower aspect ratio). These parameters were the same for the Series E plume study except F_o was 0.8.

The second set of laboratory data were taken as a parametric study on the effects of tower orientation with respect to wind direction, Froude number and wind speed on MDCT plume dispersion. These data were acquired by Kannberg and Onishi (2) at Pacific Northwest Laboratories in Richland, Washington. A mechanical-draft tower modeled in the water flume has six cells and is similar to one now in operation at the Centralia Power Plant in southwestern Washington. Of the 28 data cases available, we chose six sets. Three cases represented a mechanical-draft tower in crossflow to the wind direction with Froude number of 3.59, where K takes on values of 0.6, 1.0 and 1.5. The other three data cases represent a mechanical-draft tower inline to the wind flow with K varying exactly as in the crossflow cases. We felt that our choice of these six cases were sufficient enough to give us a good range of cases for model testing. Table 3-1 shows tower configurations for the EDF and Kannberg-Onishi data.

CALIBRATION OF THE DOWNWASH COEFFICIENTS AND DISCUSSION OF RESULTS

Numerical tests revealed that a value of C_{wf} = 0.005 yields nearly no vertical downward pull on the plume trajectory. As a result, we reran our multiple source model with three values of C_{wf}: 0.1, 0.2 and 0.3 and compared predictions with EDF and Kannberg-Onishi lab data. The value of 0.3 for C_{wf} tended to give too much of a downward pull especially for the mechanical-draft tower data. Both of the other values gave good trajectory predictions. However, C_{wf} = 0.2 showed a tendency for overdilution with too much downward pull for K values of two and greater for the lab data with four or more towers. The value of 0.1 was selected as the value for C_{wf} after a few test runs; values smaller than 0.1 showed no difference in trajectory predictions.

Even with C_{wf} = 0.1, the model showed a tendency to too much dilution and so runs were made with the downwash entrainment coefficient, C_{wv}, cut in half, i.e. C_{wv} = 0.4. For multiple towers then, C_{wv} is taken as 0.4.

EDF Data (Figures 3-1 to 3-9.)

Figures 3-1 through 3-3 show trajectory and dilution predictions for the EDF Series D data by the ANL, Slawson-Wigley and Orville Models. The trajectory predictions for the ANL Model in Figure 3-1 are very good although the corresponding dilution curves are underpredicted for K = 2.0 and 3.0. Unfortunately, there is only few data for these cases. From the three points given, it appears that K = 1.0 gives more dilution than K = 2.0, which should have more dilution. More data would show clearly what the situation should be and therefore lead to better interpretation of the model results.

The Slawson-Wigley Model overpredicts bending of the centerline for all three cases (see Figure 3-2). The dilution predictions are all underpredicted because the model does not have any downwash formulation along with the fact that the model is probably not optimally calibrated. The Orville Model (see Figure 3-3) overpredicts plume rise and underpredicts dilutions very severely. This is due, in part, to the simplistic merging method of using an effective source to represent the towers. By combining initial fluxes, the initial buoyancy is increased greatly resulting in a high trajectory prediction. Because of smaller surface area over which entrainment can occur with the effective source method, there is not enough dilution taking place. Also, the Orville Model does not account for any downwash effects.

The EDF Series E data is shown in Figures 3-4 through 3-6 as compared to model predictions. The ANL Model predicts good trajectories (Figure 3-4) and good dilutions except for the dilution curve of K = 2.0 and possibly the trajectory curve of K = 0.5. The jumps in the ANL dilution predictions are due to individual merging of the plumes. Note that the dilution data reveal a minimum dilution for K = 1.0 whereas the model predicts a minimum dilution for K = 2.0. The proper K value for minimum dilution at a given downwind distance and given exit densimetric Froude number depends on the balance of bending, mixing, and downwash effects.

Figure 3-5 shows higher trajectory predictions than indicated by the data for the Slawson-Wigley Model with dilutions that show more underprediction with increasing K. Orville has (Figure 3-6) has very high trajectory predictions without much bending in the curves. Dilutions are all underpredicted with less dilution for higher K.

In all the model predictions for dilutions in Sections 3 and 4, we multiplied predicted values of $(T_p - T_a)/(T_{p_o} - T_{a_o})$, the temperature decay, by a factor of 2. The values of this ratio predicted by the models represent cross-sectionally averaged values due to top-hat assumptions but studies have shown that a plume cross-section is really a Gaussian in two dimensions. Thus we had to change the top-hat-predicted-value by multiplying it by $\sqrt{2} \cdot \sqrt{2} = 2$, which is more likely to be closer to the true value of that ratio at the plume centerline. The Orville Model predicts very slow dilution; as a result, the dilution predictions when multiplied have a value of unity at different downwind locations (not at the source but downwind of it) as seen in Figures 3-3 and 3-6.

The results for Configuration B (Figures 3-7 through 3-9) are almost identical to the results for Configuration A. There appears to be a slight difference in the data between Configurations A and B, but it is not possible to draw final conclusions from slight differences in the data. The Slawson-Wigley and Orville Models predictions are exactly the same between the two configurations. Only the ANL Model showed some difference between plumes from Configurations A and B.

Kannberg-Onishi Data (Figures 3-10 to 3-15)

Figures 3-10 through 3-12 show model comparisons to the Kannberg-Onishi single tower crossflow cases. The ANL Model predictions for trajectory in Figure 3-10 shows too much downwash for K = 1.0 and 1.5 with not enough bendover for K = 0.6. The dilution curves are excellent showing higher dilution for higher K. The Slawson-Wigley and Orville Models predict very high trajectories in Figures 3-11 and 3-12. Neither model has any downwash formulation, so the trajectories will always be high. Dilutions are too low for both models with the reverse trend with respect to K. The Orville Model seems to be very sensitive in the dilution predictions as K changes.

The inline cases (Figures 3-13 through 3-15) show the ANL Model with fair trajectory predictions which are slightly high. The dilution graph shows the correct trend to the data, but unfortunately K = 1.5 is a poor prediction. In an inline situation, there is less dilution with higher K, due in part to lesser downwash effect. This is the opposite of a crossflow situation. The ANL Model is the only model which shows the difference.

Slawson-Wigley shows poor trajectory predictions in Figure 3-14 with a good dilution prediction for K = 0.6. The Orville Model (Figure 3-15) shows poor results overall. Although the Slawson-Wigley and Orville Models show the correct trend in the inline dilution predictions, they still need to be changed to show proper trends in other situations.

The results of the ANL Model are not as excellent as we would want them to be with our calibration. We feel that the model could use a recalibration, preferably with a wider range of data. This work will be carried out in the near future.

REFERENCES

1. Pierre-Louis Viollet. Study of Jets in Transverse Currents and in Stratified Environments. Doctoral Dissertation. Curie University. Paris, France. February 1977. (in French).

2. L. Kannberg and Y. Onishi. Plumes from One and Two Cooling Towers. IN: Environmental Effects of Atmospheric Heat/Moisture Releases. Cooling Towers, Cooling Ponds, and Area Sources. Presented at Second AIAA/ASME Thermophysics and Heat Transfer Conference. Palo Alto, California. May 24-26, 1978. Eds. Kenneth Torrance and Robert Watts. Available from ASME, New York City. 1978.

Table 3-1.

Tower configurations for the
EDF and Kannberg-Onishi data.

EDF Series D: (two towers)

H_o/D_o = 1.85

F_o = 0.65

ALPHA = 0.25

FLOW

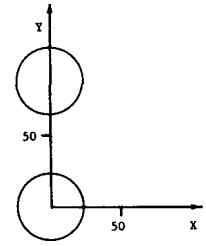

EDF Series E: (four towers)

Configuration A

H_o/D_o = 1.85

F_o = 0.8

ALPHA = 0.25

FLOW

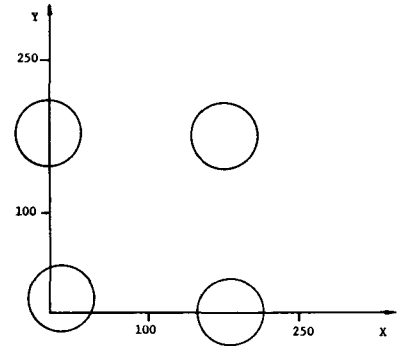

EDF Series E: (four towers)

Configuration B

H_o/D_o = 1.85

F_o = 0.8

ALPHA = 0.25

FLOW

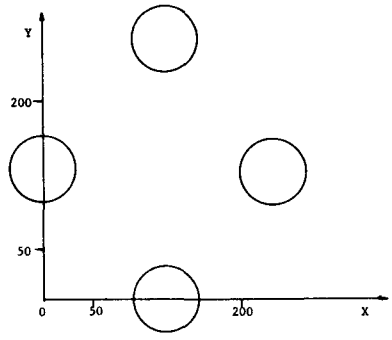

Table 3-1. (continued)

Kannberg-Onishi tower dimensions *

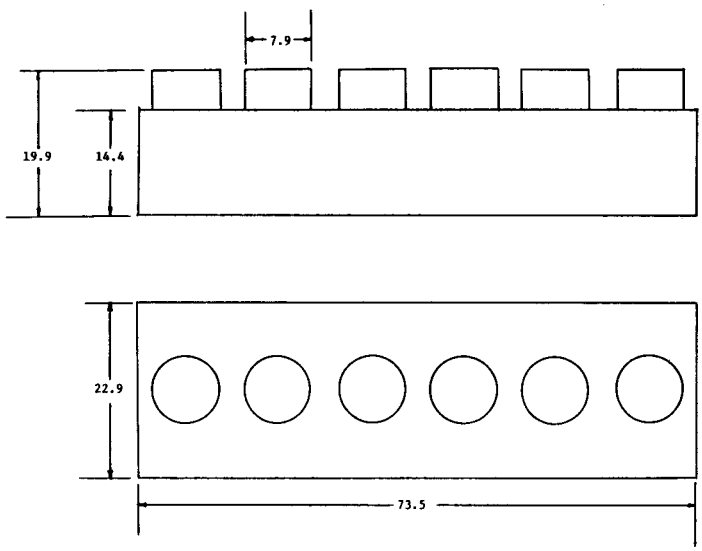

Center-to-center spacing between cells: 12.24 meters

---

*All dimensions are given in meters.

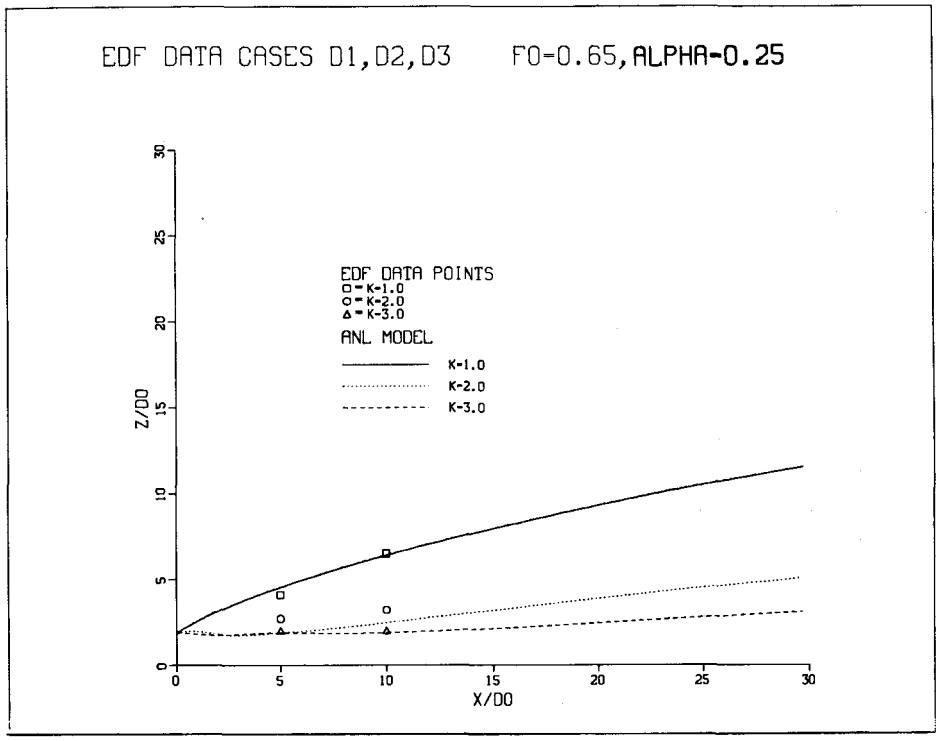

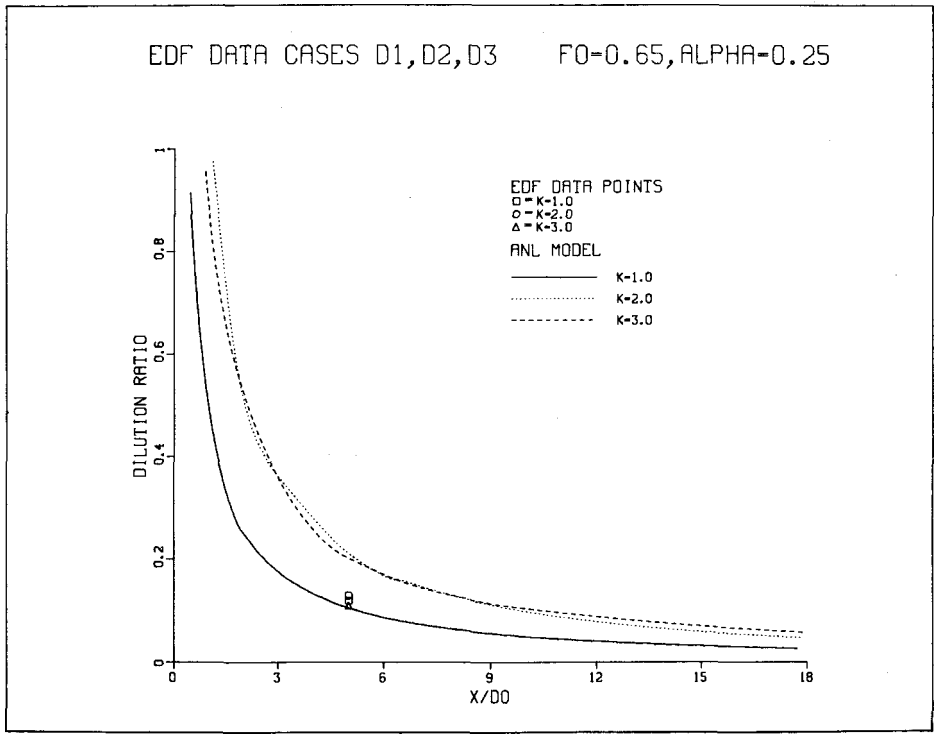

Figure 3-1. Comparison of predictions of ANL model to EDF laboratory data . . . cases D1, D2 and D3 . . . F_0 = 0.65 and ALPHA = 0.25 with variation in K: (top) centerline trajectory, (bottom) centerline dilution.

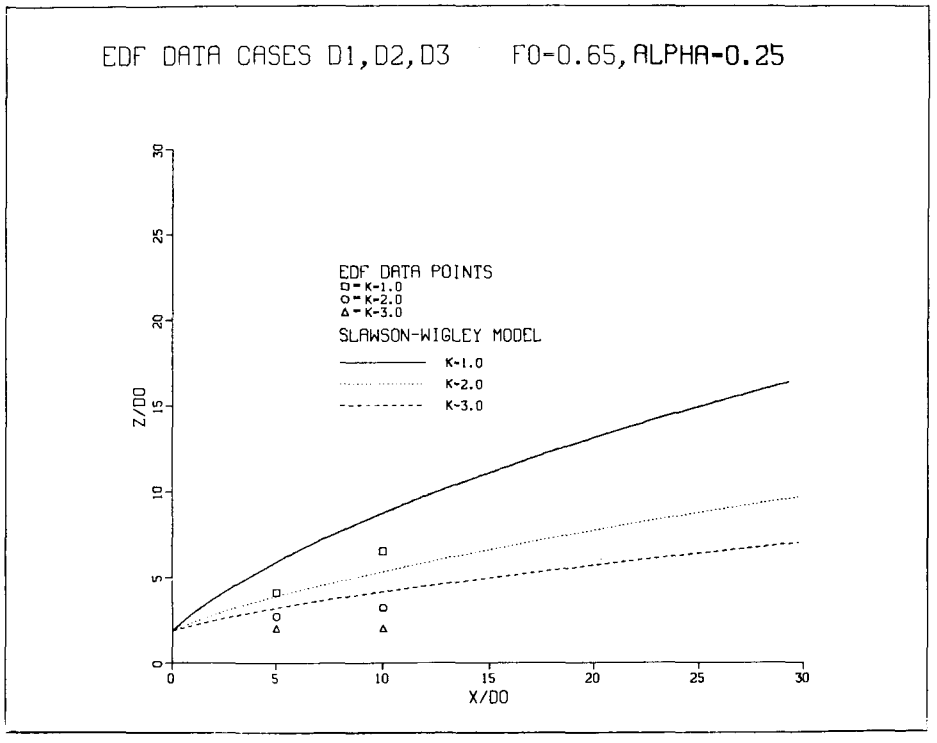

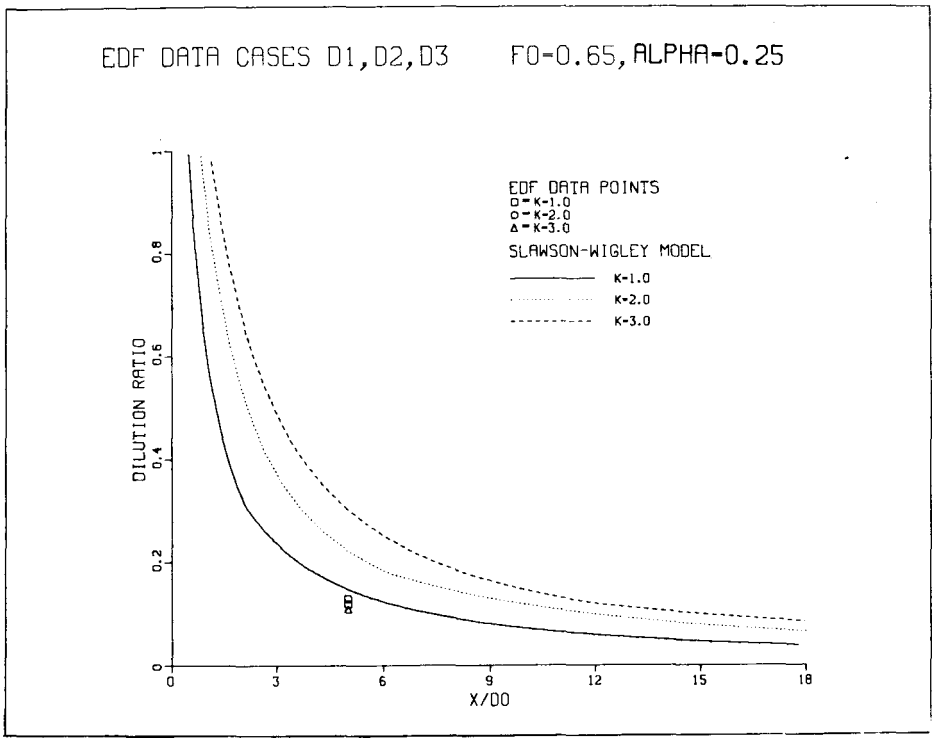

Figure 3-2. Comparison of predictions of Slawson-Wigley model to EDF laboratory data . . . cases D1, D2 and D3 . . . F_o = 0.65 and ALPHA = 0.25 with variation in K: (top) centerline trajectory, (bottom) centerline dilution.

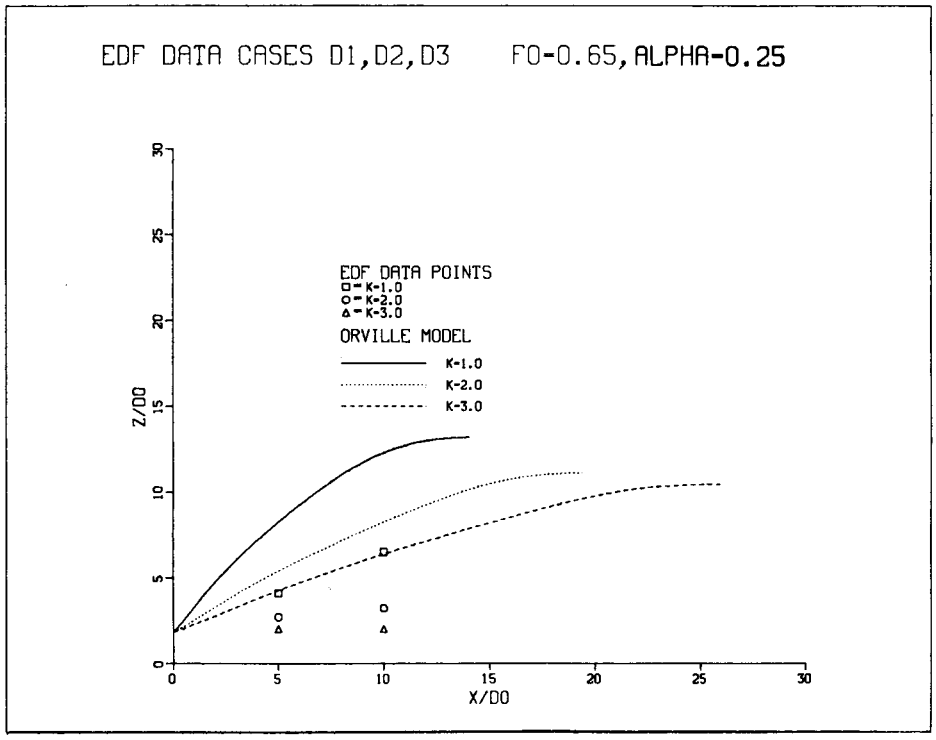

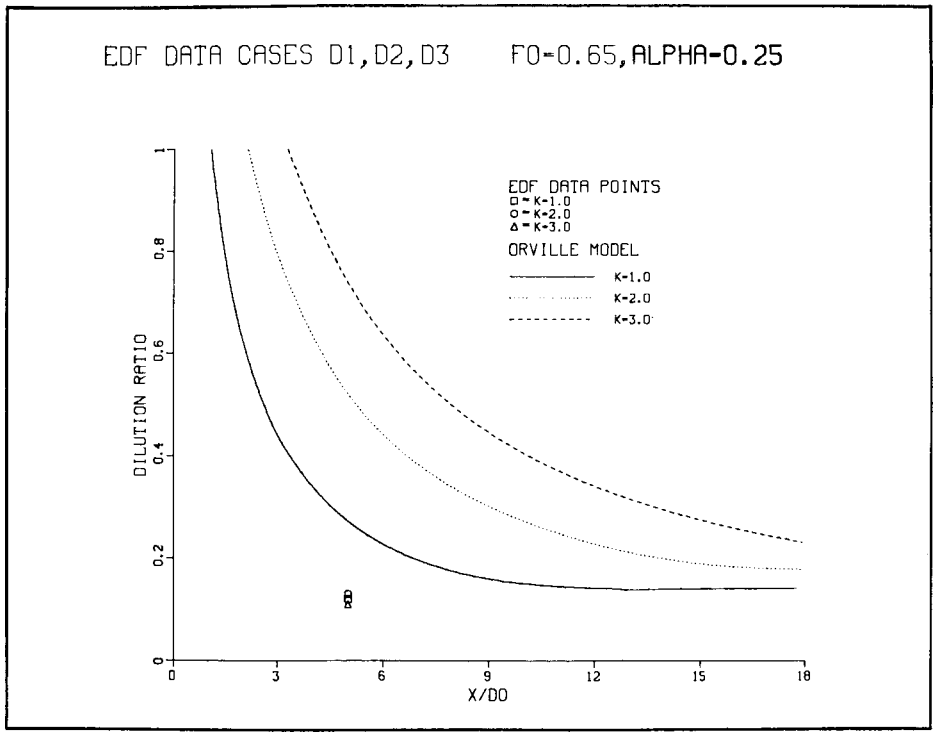

Figure 3-3. Comparison of predictions of Orville model to EDF laboratory data . . . cases D1, D2 and D3 . . . F_o = 0.65 and ALPHA = 0.25 with variation in K: (top) centerline trajectory, (bottom) centerline dilution.

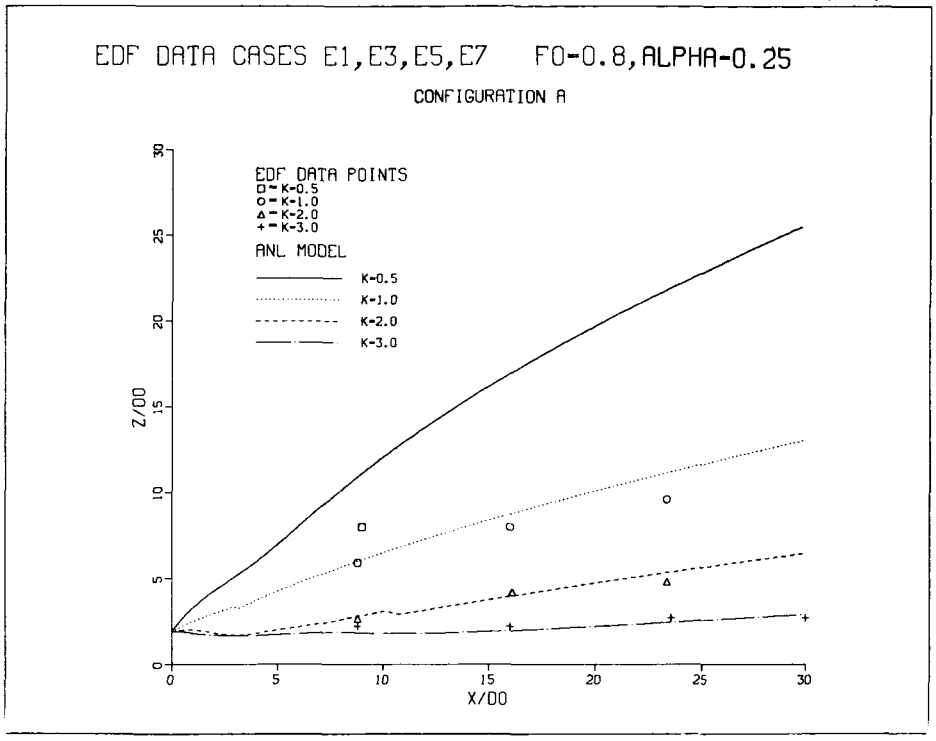

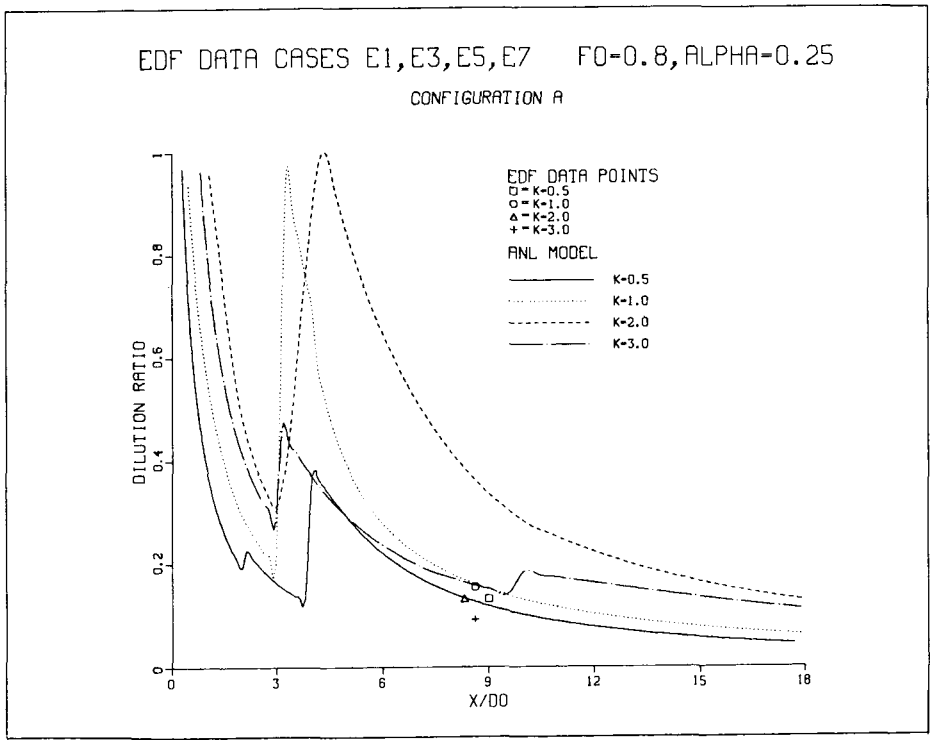

Figure 3-4. Comparison of predictions of ANL model to EDF laboratory data . . . configuration A cases E1, E3, E5 and E7 . . . F_o = 0.8 and ALPHA = 0.25 with variation in K: (top) centerline trajectory, (bottom) centerline dilution.

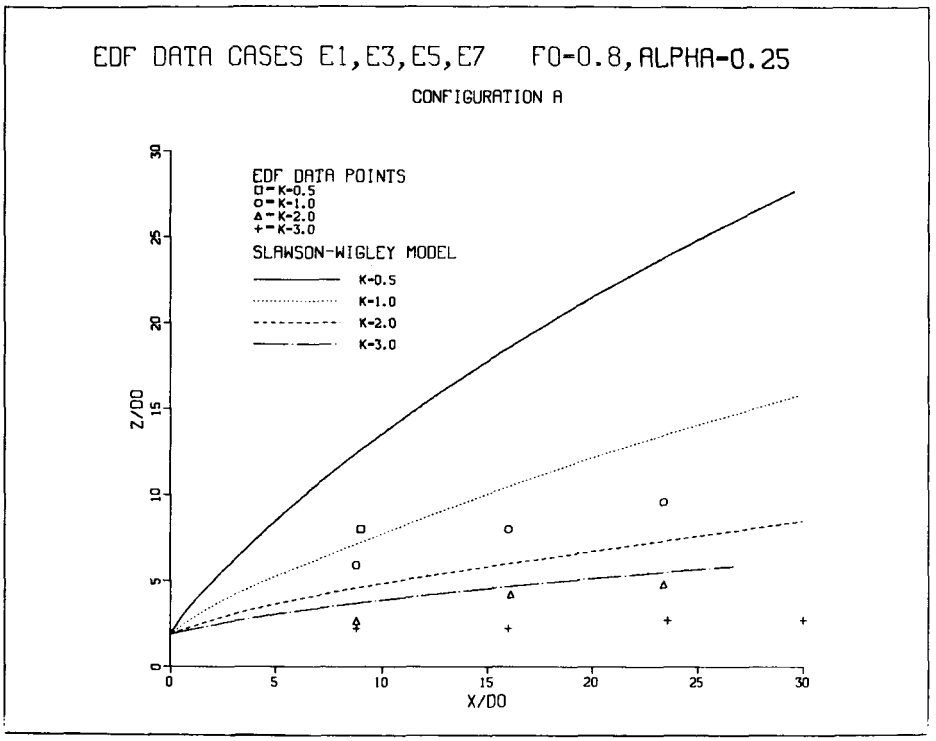

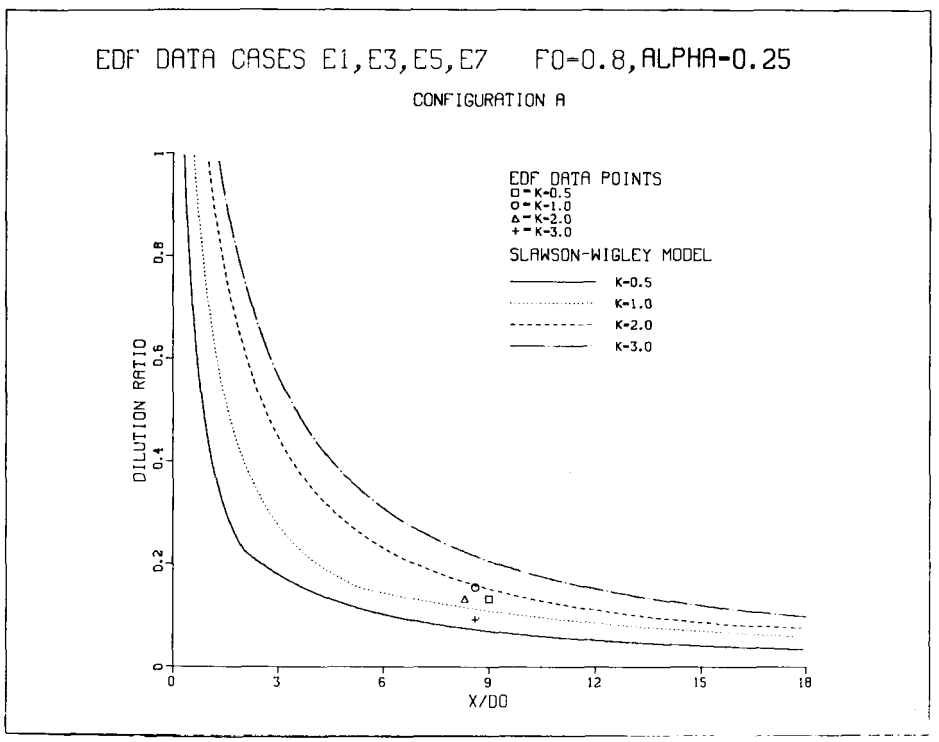

Figure 3-5. Comparison of predictions of Slawson-Wigley model to EDF laboratory data . . . configuration A cases E1, E3, E5 and E7 . . . F_o = 0.8 and ALPHA = 0.25 with variation in K: (top) centerline dilution.

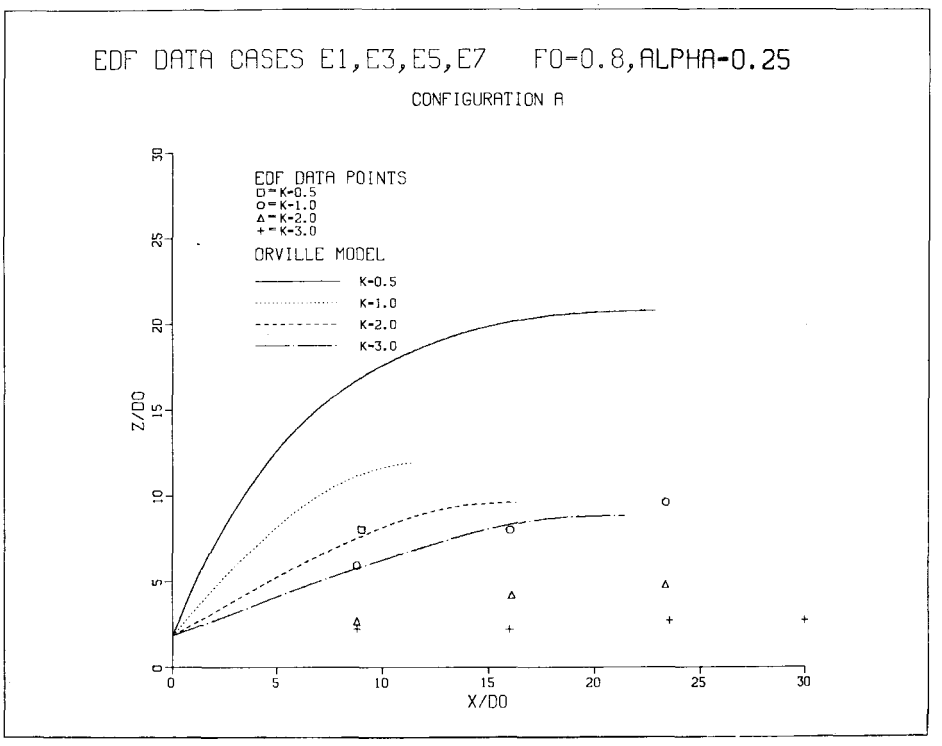

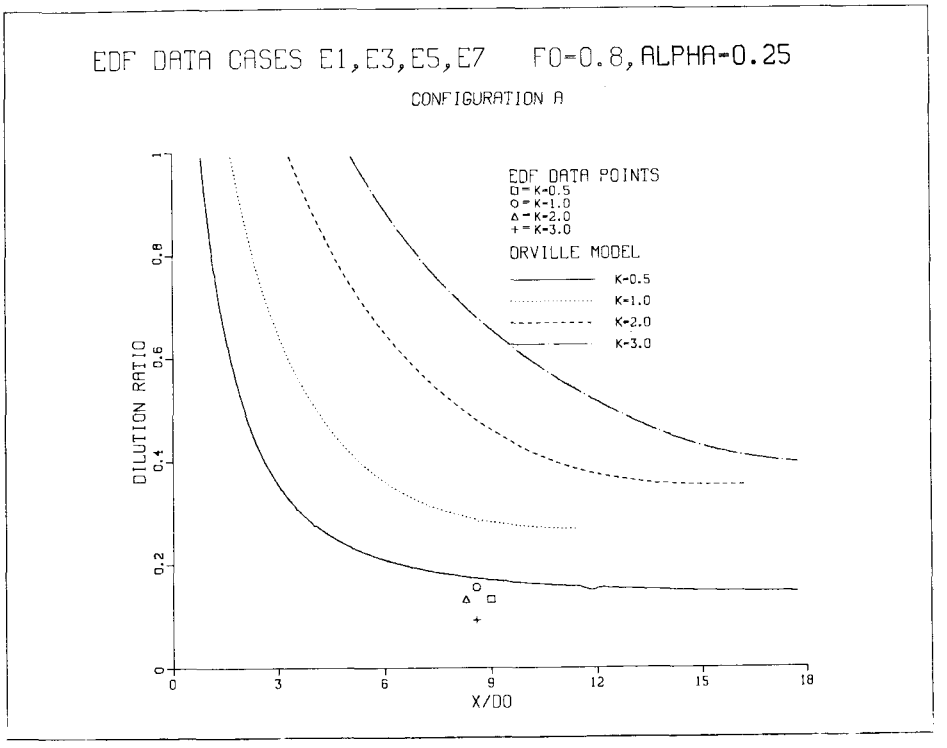

Figure 3-6. Comparison of predictions of Orville model to EDF laboratory data . . . configuration A cases E1, E3, E5 and E7 . . . F_o = 0.8 and ALPHA = 0.25 with variation in K: (top) centerline trajectory, (bottom) centerline dilution.

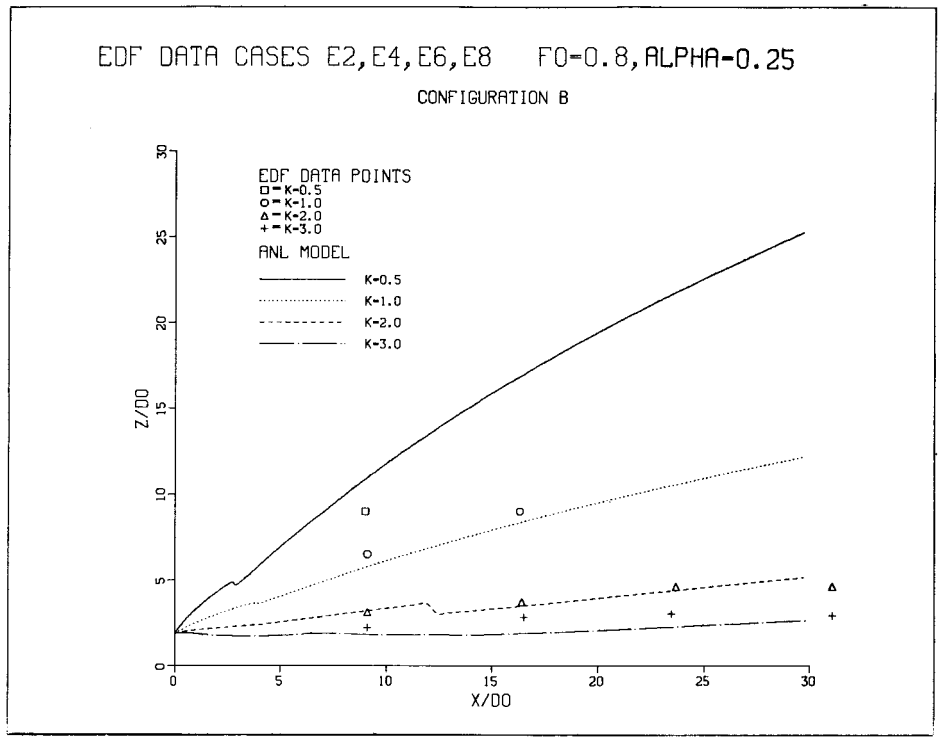

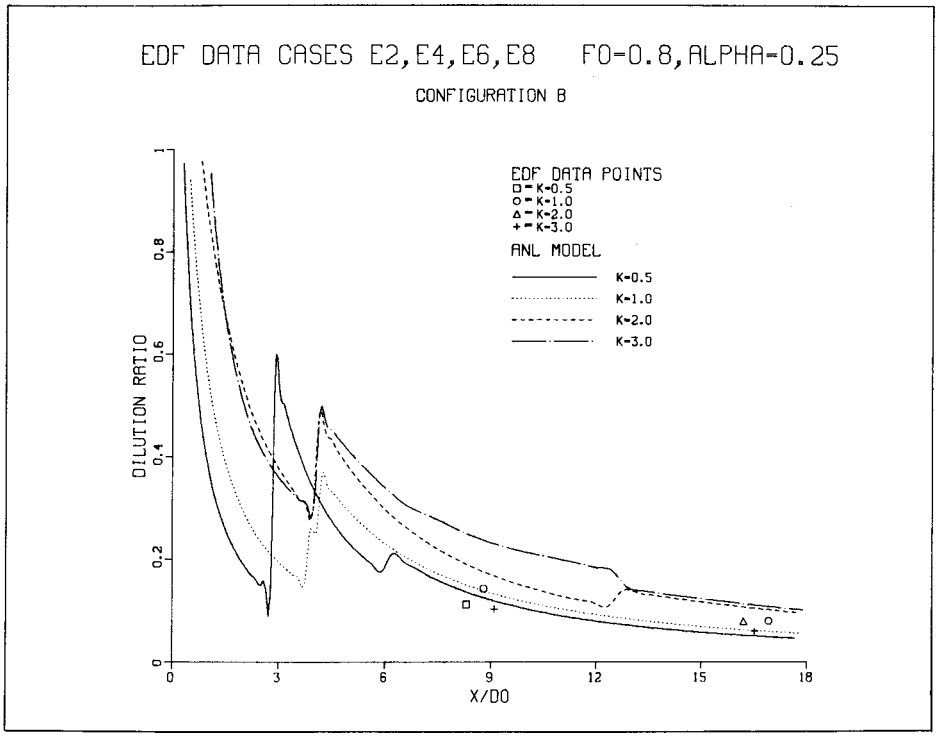

Figure 3-7. Comparison of predictions of ANL model to EDF laboratory data . . . configuration B cases E2, E4, E6 and E8 . . . F_0 = 0.8 and ALPHA = 0.25 with variation in K: (top) centerline trajectory, (bottom) centerline dilution.

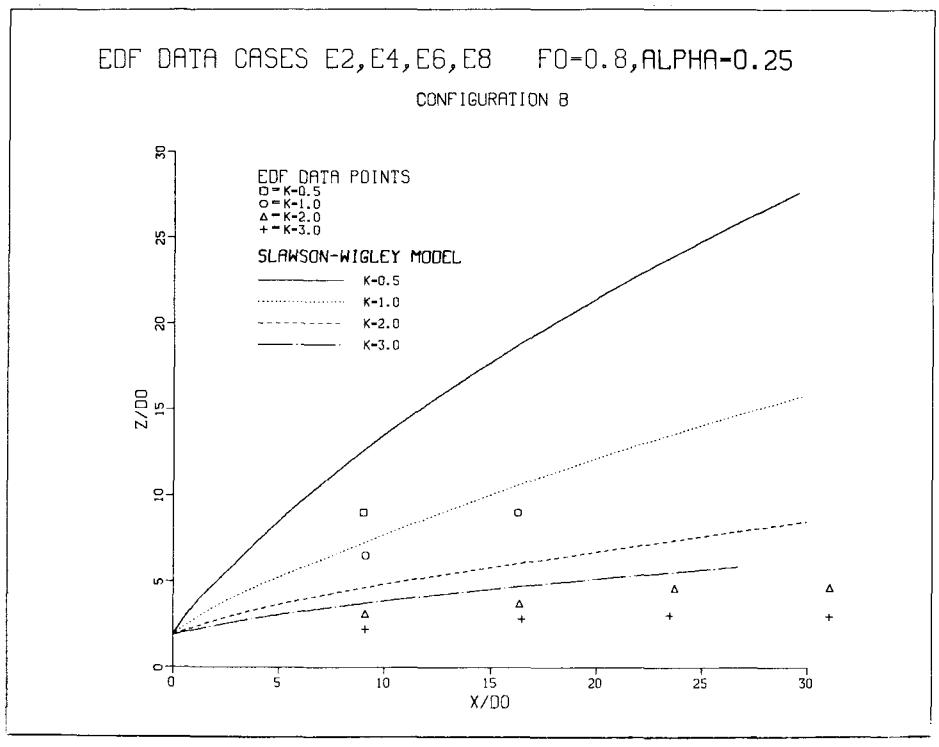

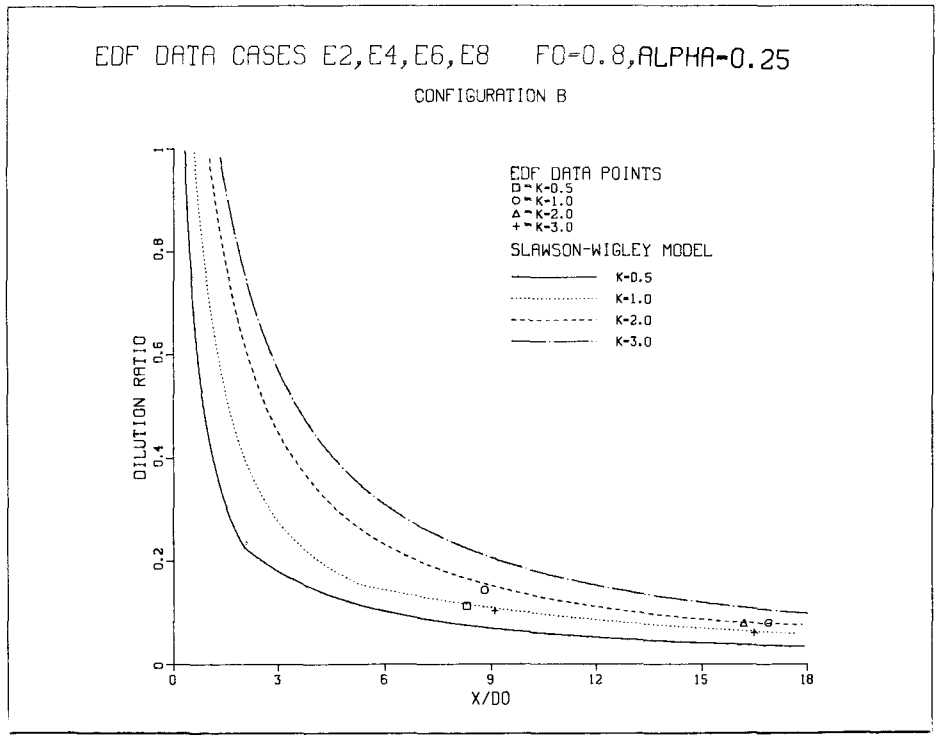

Figure 3-8. Comparison of predictions of Slawson-Wigley model to EDF laboratory data . . . configuration B cases E2, E4, E6 and E8 . . . F_o = 0.8 and ALPHA = 0.25 with variation in K: (top) centerline trajectory, (bottom) centerline dilution.

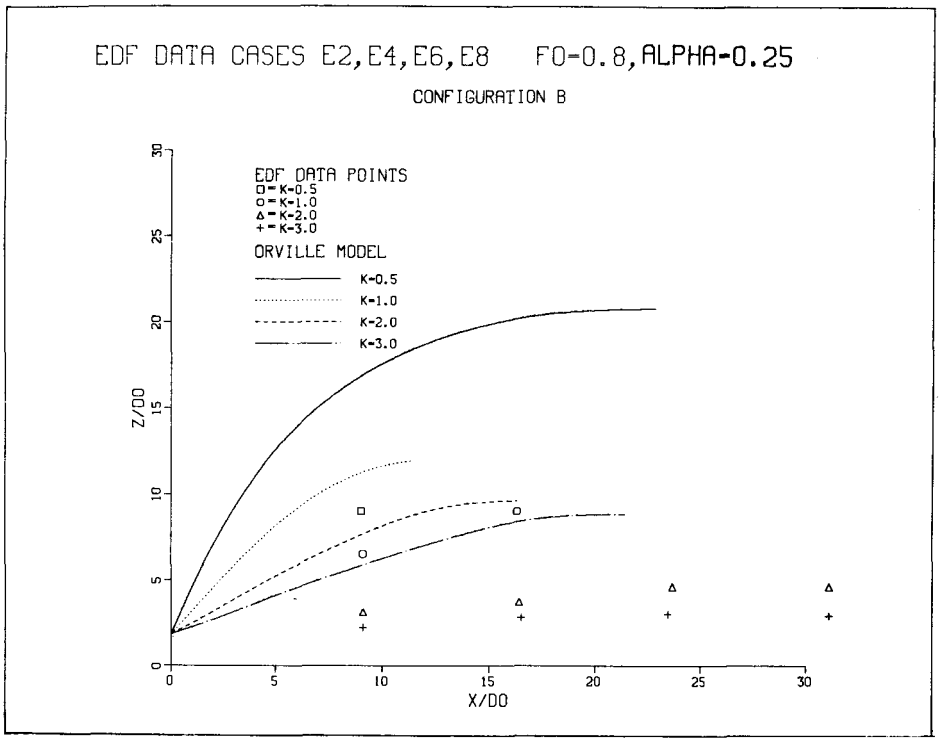

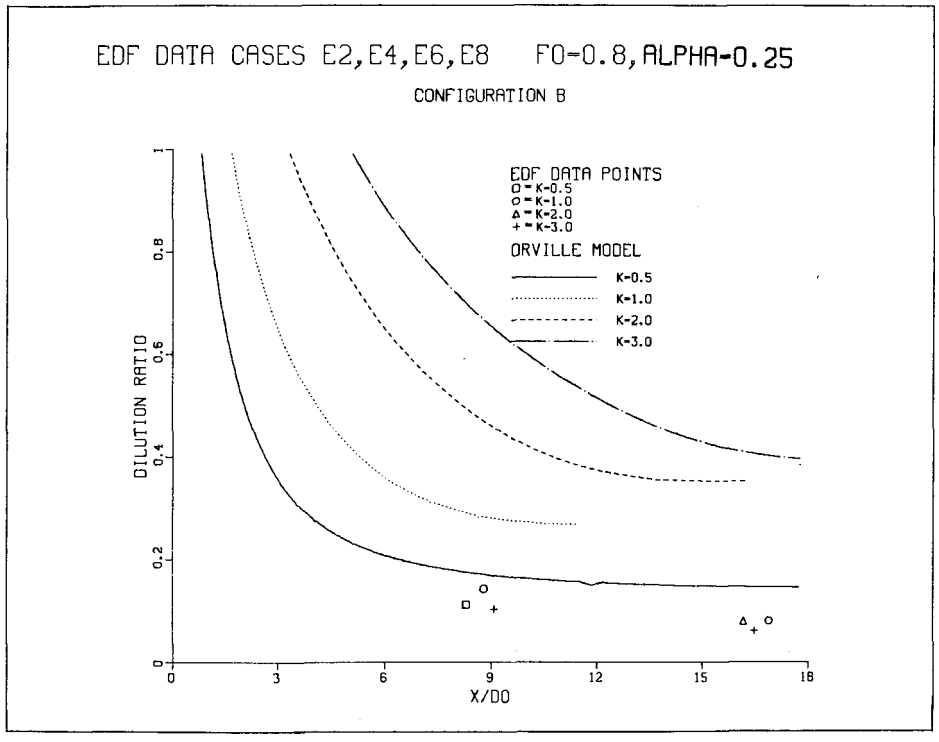

Figure 3-9. Comparison of predictions of Orville model to EDF laboratory data . . . configuration B cases E2, E4, E6 and E8 . . . F_o = 0.8 and ALPHA = 0.25 with variation in K: (top) centerline trajectory, (bottom) centerline dilution.

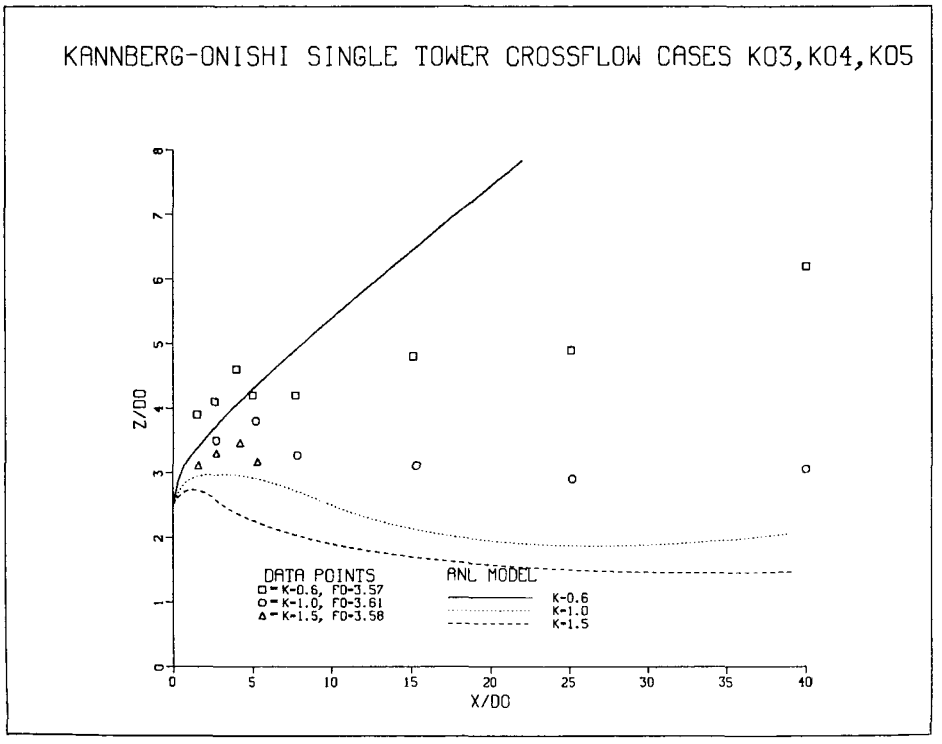

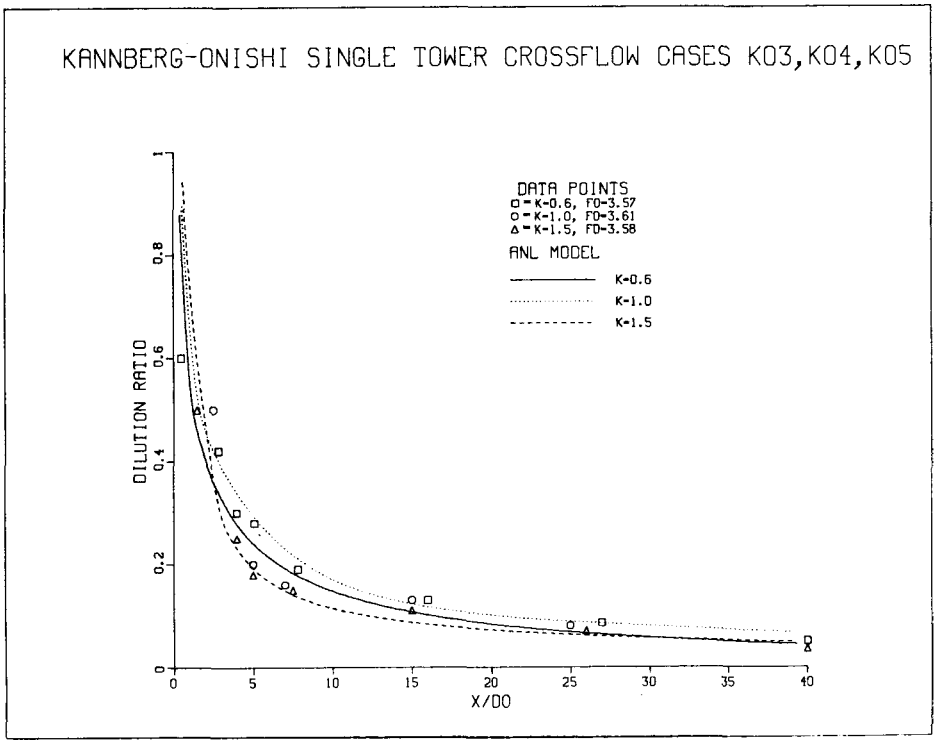

Figure 3-10. Comparison of predictions of ANL model to Kannberg-Onishi laboratory data . . . single tower crossflow to the wind; cases K03, K04 and K05 with variation in K: (top) centerline trajectory, (bottom) centerline dilution.

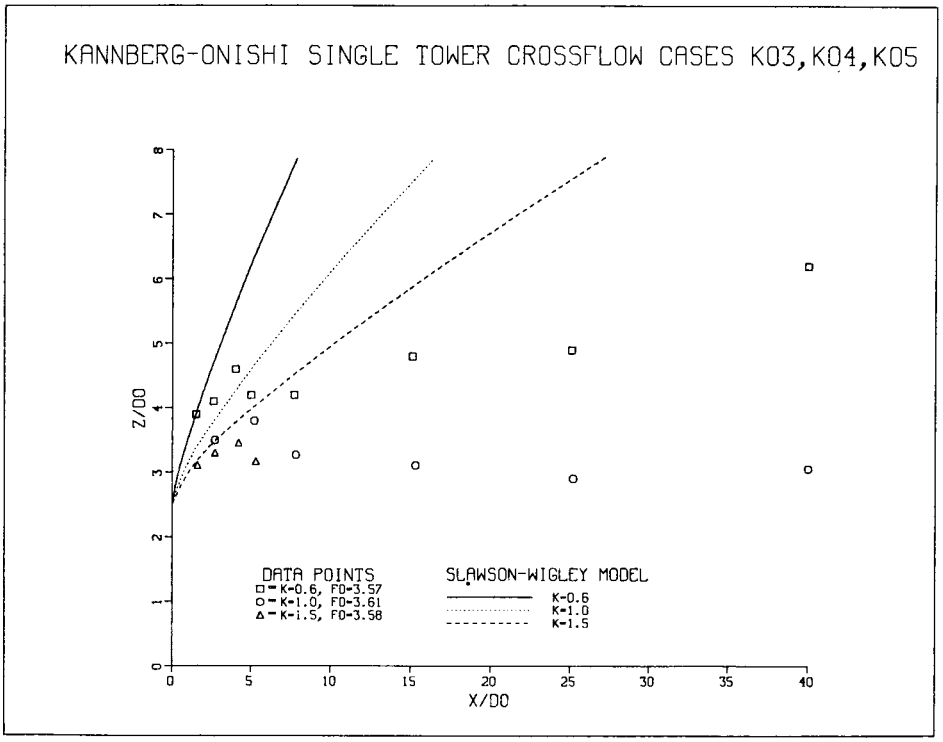

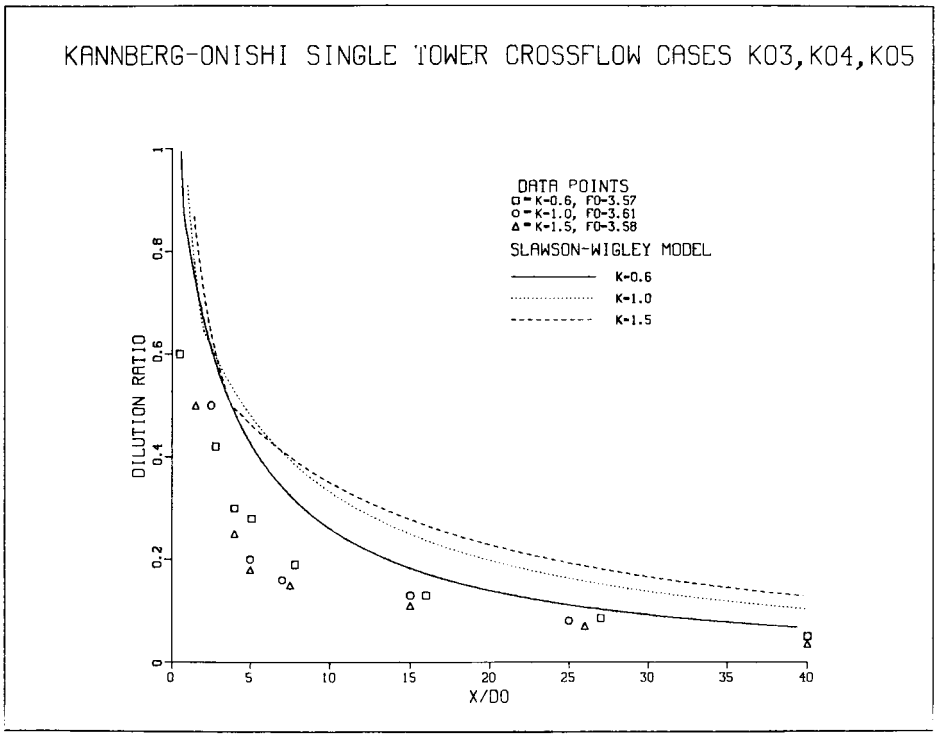

Figure 3-11. Comparison of predictions of Slawson-Wigley model to Kannberg-Onishi laboratory data . . . single tower crossflow to the wind; cases K03, K04 and K05 with variation in K: (top) centerline trajectory, (bottom) centerline dilution.

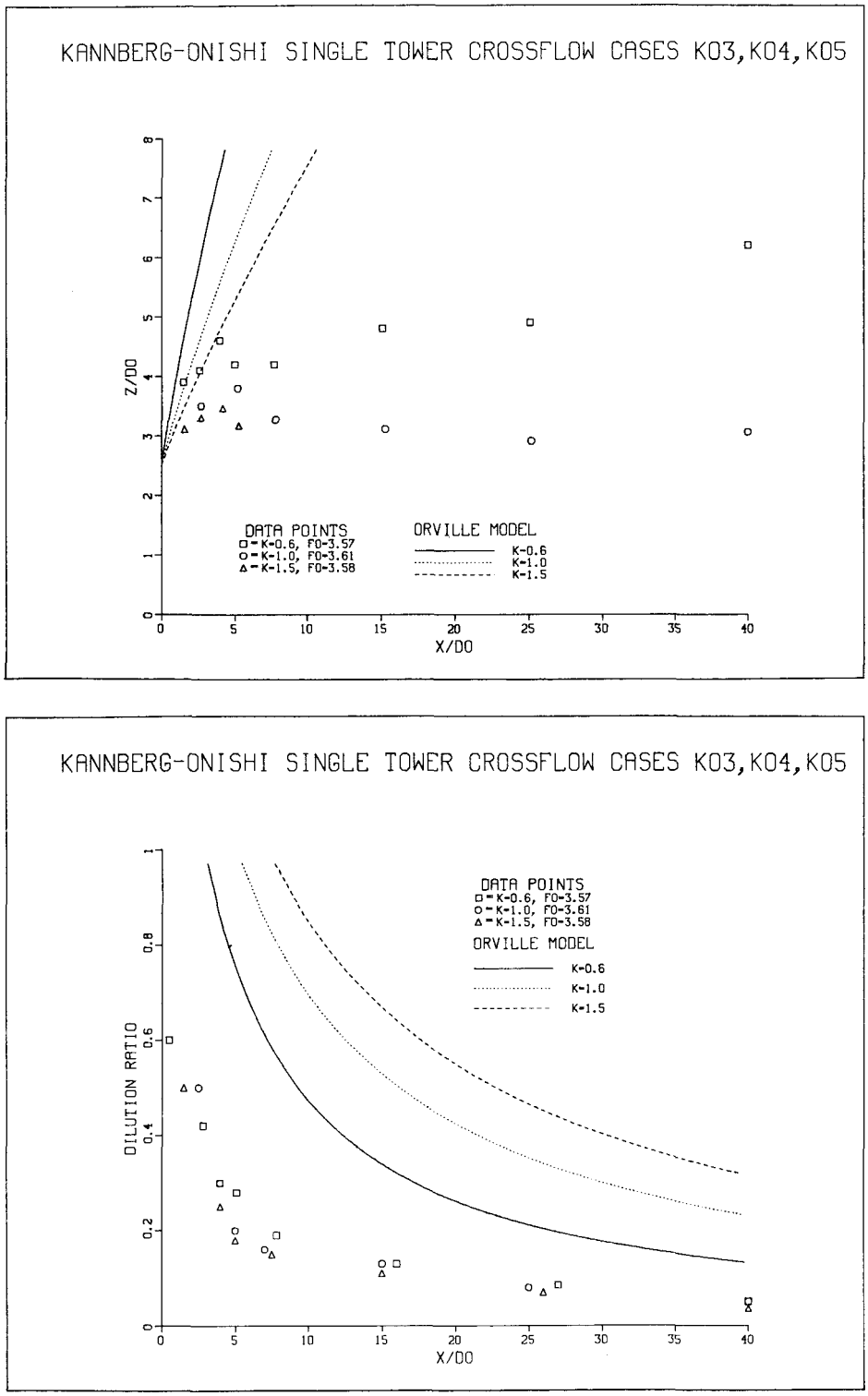

Figure 3-12. Comparison of predictions of Orville model to Kannberg-Onishi laboratory data . . . single tower crossflow to the wind; cases K03, K04 and K05 with variation in K: (top) centerline trajectory, (bottom) centerline dilution.

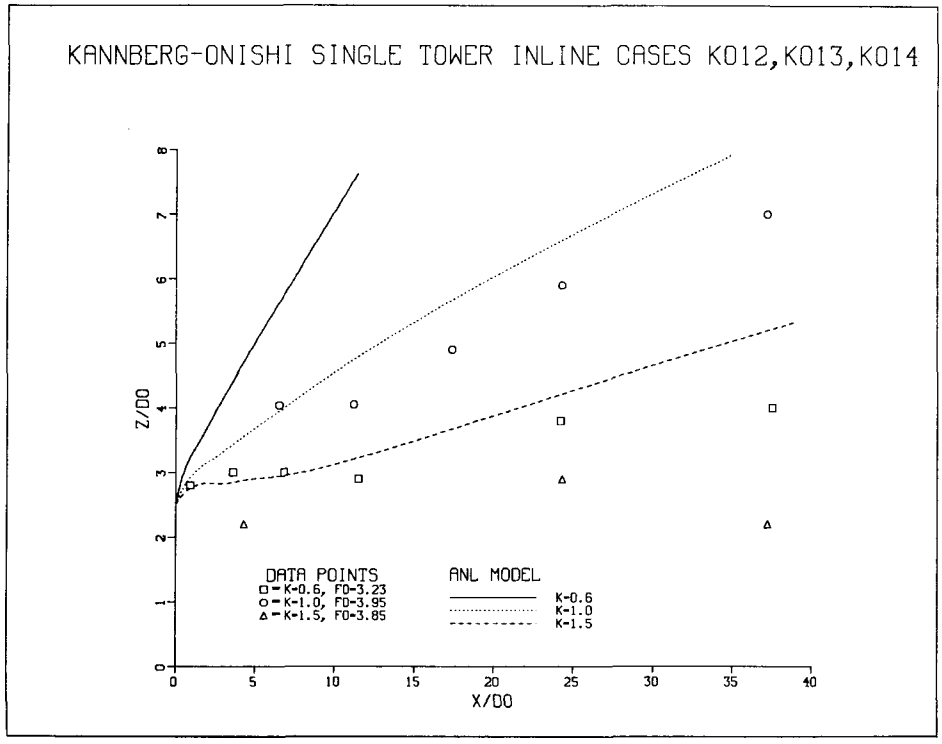

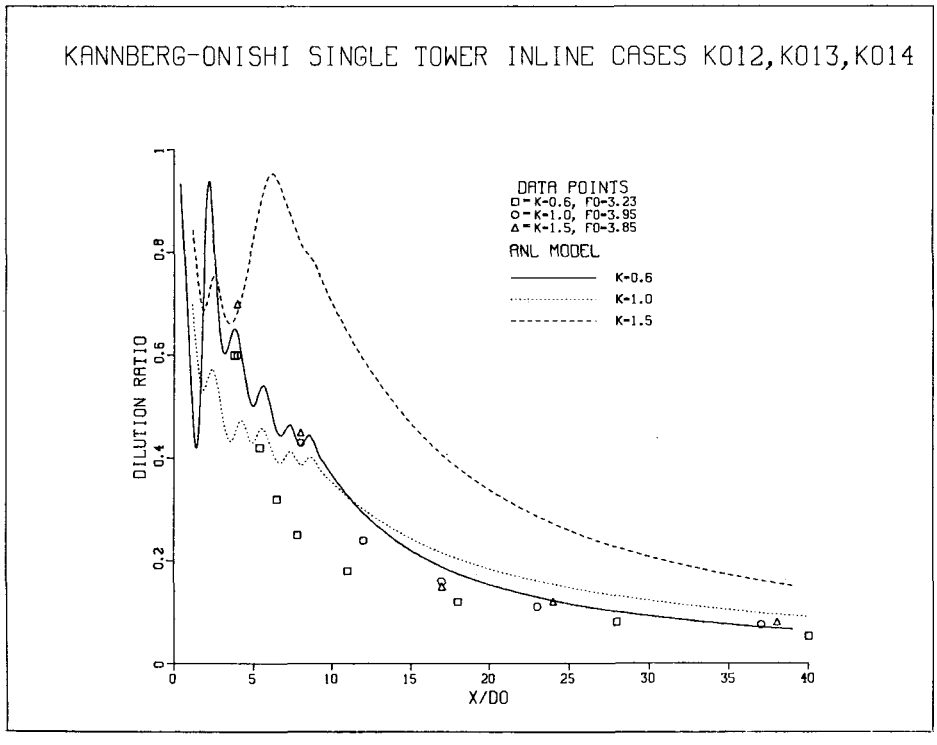

Figure 3-13. Comparison of predictions of ANL model to Kännberg-Onishi laboratory data . . . single tower inline to the wind; cases K012, K013 and K014 with variation in K: (top) centerline trajectory, (bottom) centerline dilution.

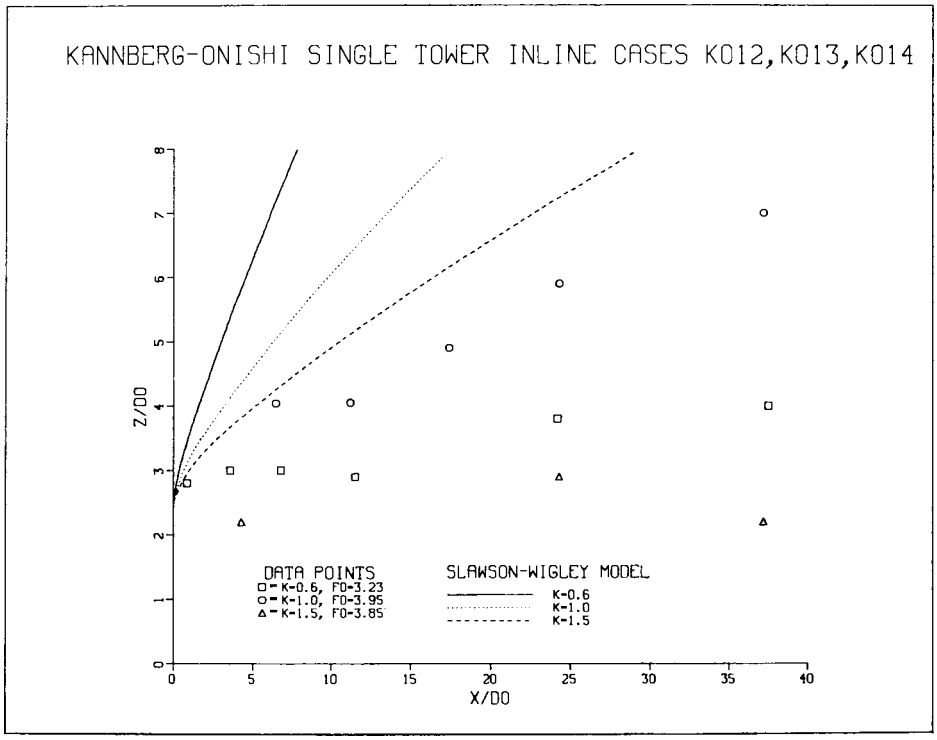

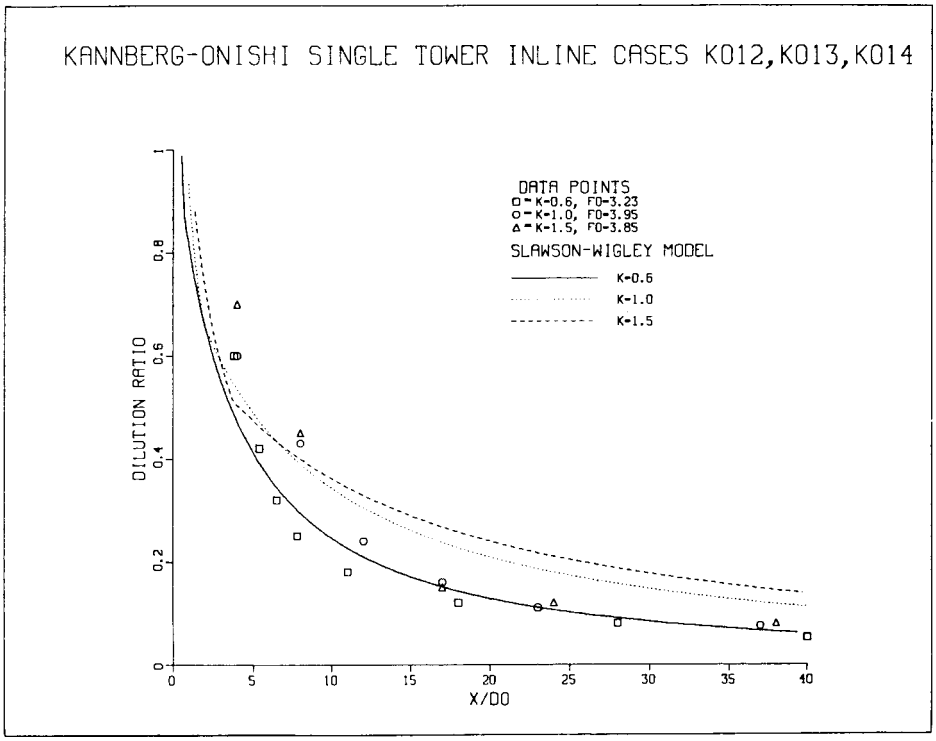

Figure 3-14. Comparison of predictions of Slawson-Wigley model to Kannberg-Onishi laboratory data . . . single tower inline to the wind; cases K012, K013 and K014 with variation in K: (top) centerline trajectory, (bottom) centerline dilution.

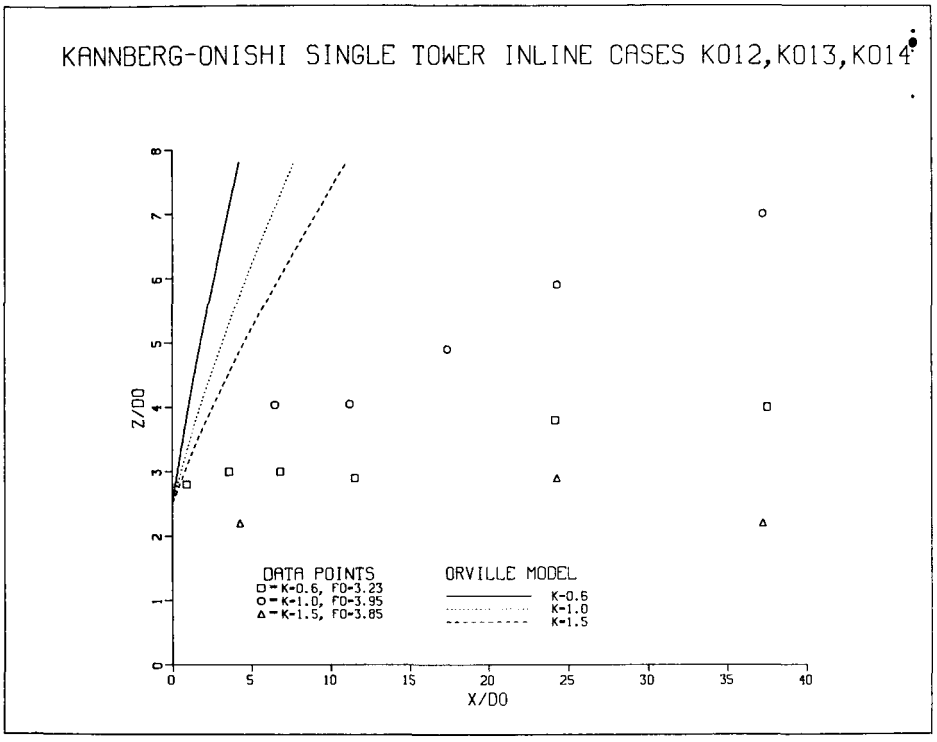

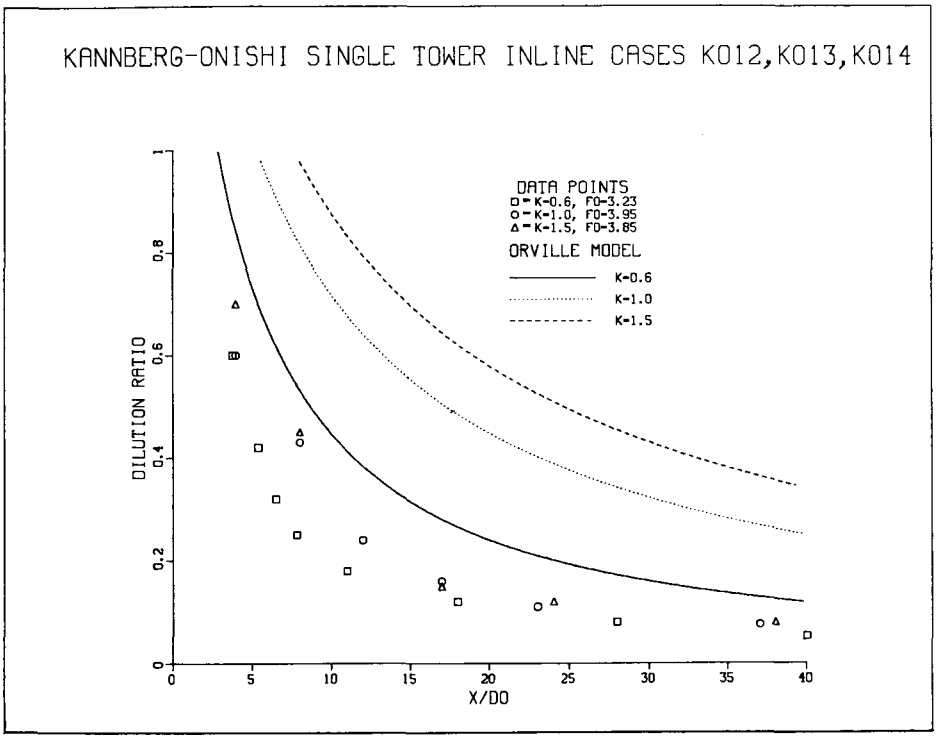

Figure 3-15. Comparison of predictions of Orville model to Kannberg-Onishi laboratory data . . . single tower inline to the wind; cases K012, K013 and K014 with variation in K: (top) centerline trajectory, (bottom) centerline dilution.

Section 4

VERIFICATION OF THE ANL MULTIPLE-SOURCE PLUME MODEL

INTRODUCTION

In order to evaluate the performance of the ANL Model as calibrated, we made comparisons of the ANL Model's predictions to predictions from three other multiple-source models using a wide selection of laboratory and field data (laboratory data from two sources and field data from four sites). The three models chosen for comparison were the KUMULUS, Orville and Slawson-Wigley models. The KUMULUS Model had been calibrated to our single-source field data at Chalk Point, Lünen and Paradise. The Orville Model had been calibrated only to mechanical-draft cooling tower plume data at Benning Road. We only have KUMULUS predictions for the Neurath and Amos field data, so in all other comparisons we used the Slawson-Wigley Model predictions to replace KUMULUS predictions. We decided to use the Slawson-Wigley Model instead of the Hanna multiple-source model since the Hanna model did not employ a diffusion phase whereas the Slawson-Wigley Model did so leading to complete plume predictions. The Hanna Model was not a complete model and therefore its results would not have always been sufficiently illuminating for our model/data comparisons.

Such model/data comparisons are the best way to evaluate the ANL Model and to locate areas that require additional improvement. It also puts us in a position to rate our model among other multiple-source models. Along with visible-plume outline comparisons, there are various summary plots showing each of the model's final visible plume length and rise predictions and, in addition, we present tables comparing various model performance statistics for each of the models and data cases tested. Each of the data sources will now be taken in turn.

KANNBERG DATA (See Figures 4-1 to 4-6)

These set of data were taken from a laboratory study (1) in a water flume on plume dispersion from multiple mechanical-draft cooling towers by Kannberg at Battelle Pacific Northwest Laboratories in Richland, Washington. This parametric study was carried out to determine the effects on plume trajectory and dilution through

variation of various parameters such as initial densimetric Froude number, wind speed and tower configuration. The mechanical-draft cooling tower models employed in the lab study consisted of six cells each and were constructed at a length scale of 250:1. Individual experiments were divided into three groups, each characterized by a particular tower configuration. We chose data from the first two groups in which measurements were made for three towers each. The third group of data were taken from experiments on a four-tower configuration. We felt that data from a three tower configuration was sufficient for our model testing purposes.

The first tower configuration, denoted A, consisted of three towers in line with each other and that line is normal to the flow direction of the wind. Center-to-center spacing of the towers was 1.26 times the length of one tower. The second tower configuration, denoted B, consisted of three towers spaced ten diameters apart along the direction of the wind flow, with each individual tower itself perpendicular to the wind flow (see Table 4-4). Three cases from each configuration were chosen with three values of K; 0.6, 1.0 and 1.6, for each configuration. Figures 4-1 through 4-6 show plume trajectory and dilution predictions from the ANL, Slawson-Wigley and Orville Models. The tower symbol in Figure 4-6 for the Orville Model predictions was placed at ten diameters downwind to represent the center of the tower configuration since the Orville Model is an effective source model. It should also be noted that the tower structures in the graphs are not drawn to scale. They were put there for a clearer understanding of the graphs.

The ANL Model is the only model to show any significant downwash for K = 1.1 and 1.6. This can be attributed to the plate logic incorporated into the downwash formulation. The trajectory predictions for the ANL Model in Figure 4-1 are very good except for the case with K = 0.6 where the predicted plume did not bend over as much as it should have. Figure 4-2 shows good trajectory predictions for K = 0.6 and 1.6, but a trajectory which is too low for K = 1.1. Both dilution graphs for the ANL Model are very close to the data with a slight tendency for overdilution. It should be noted that the ANL Model showed the same trend in predicting trajectories for the single tower Kannberg-Onishi data cases, i.e., more bending with higher K.

The Kannberg data for trajectories looks a bit suspicious due to the leveling off often seen for trajectory data points. We questioned Kannberg about this and he assured us that the points represented mean trajectories and they were recorded correctly. The dilution data for Configuration B in Figure 4-2 shows the grestest

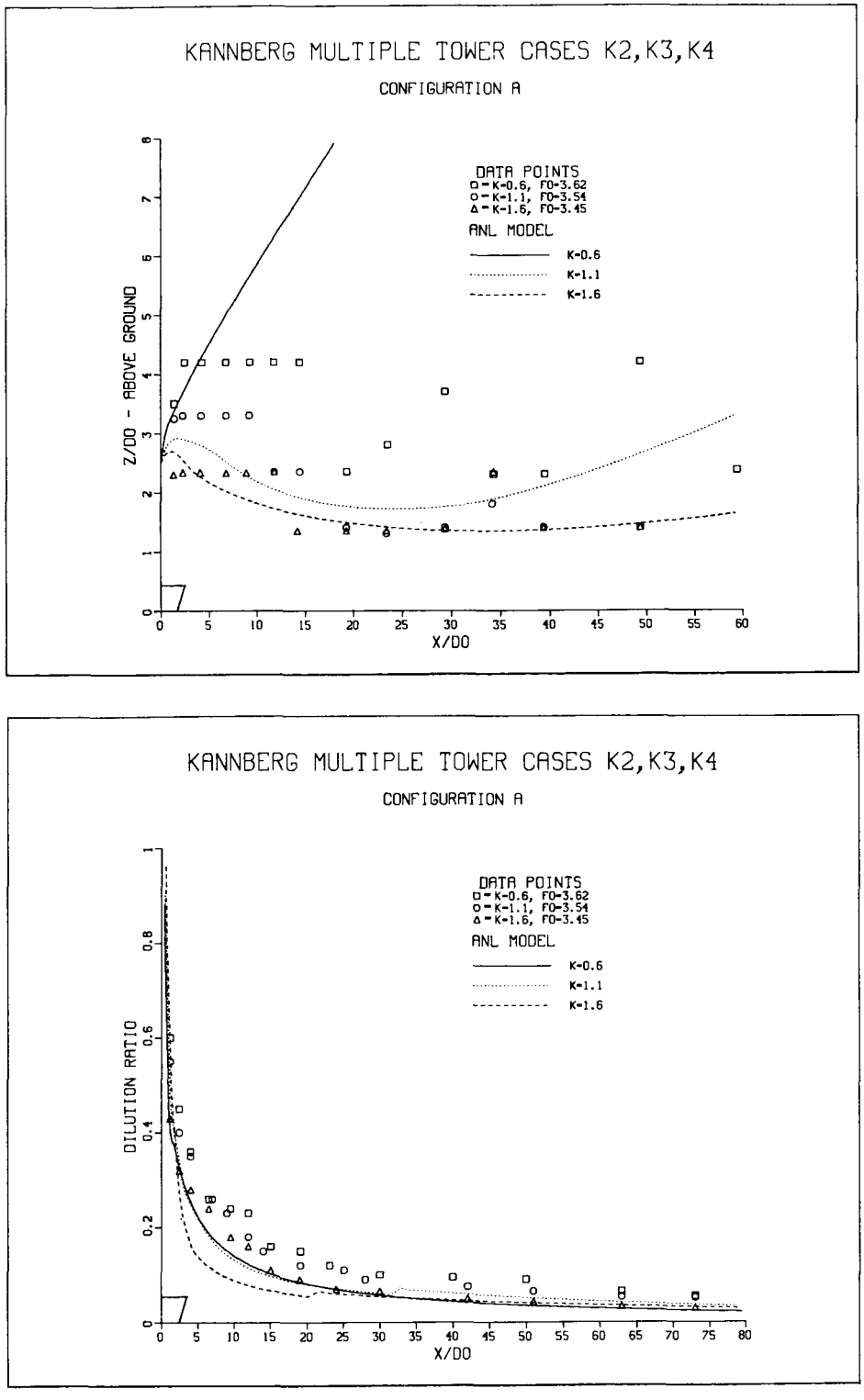

Figure 4-1. Comparison of predictions of ANL model to Kannberg multiple tower laboratory data . . . three towers on a line normal to the wind flow; cases K2, K3 and K4 with variation in K: (top) centerline trajectory, (bottom) centerline temperature decay.

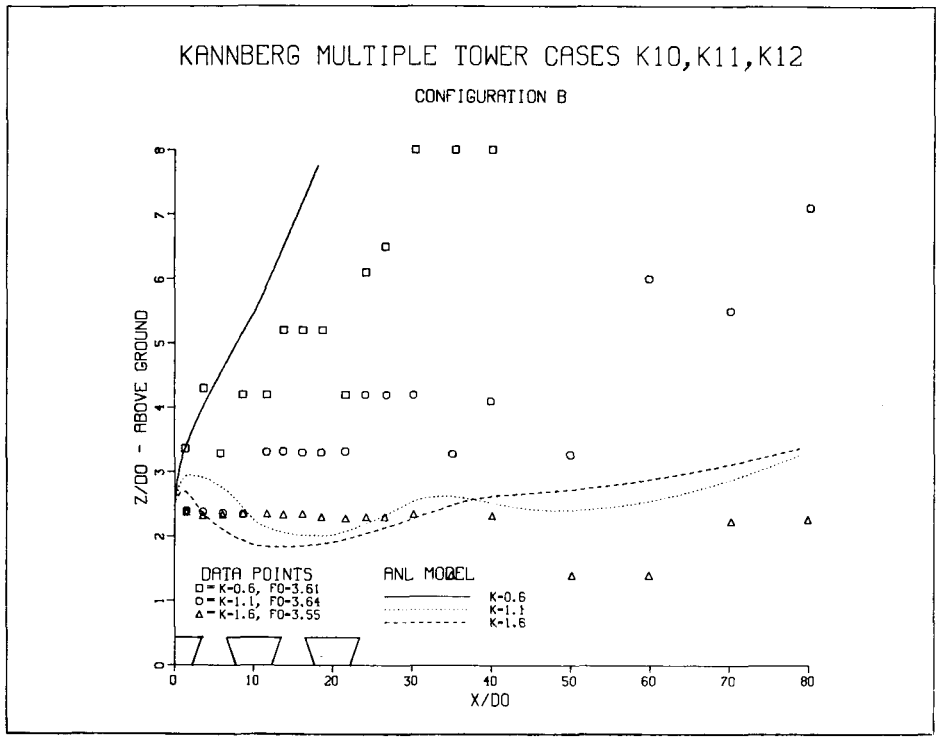

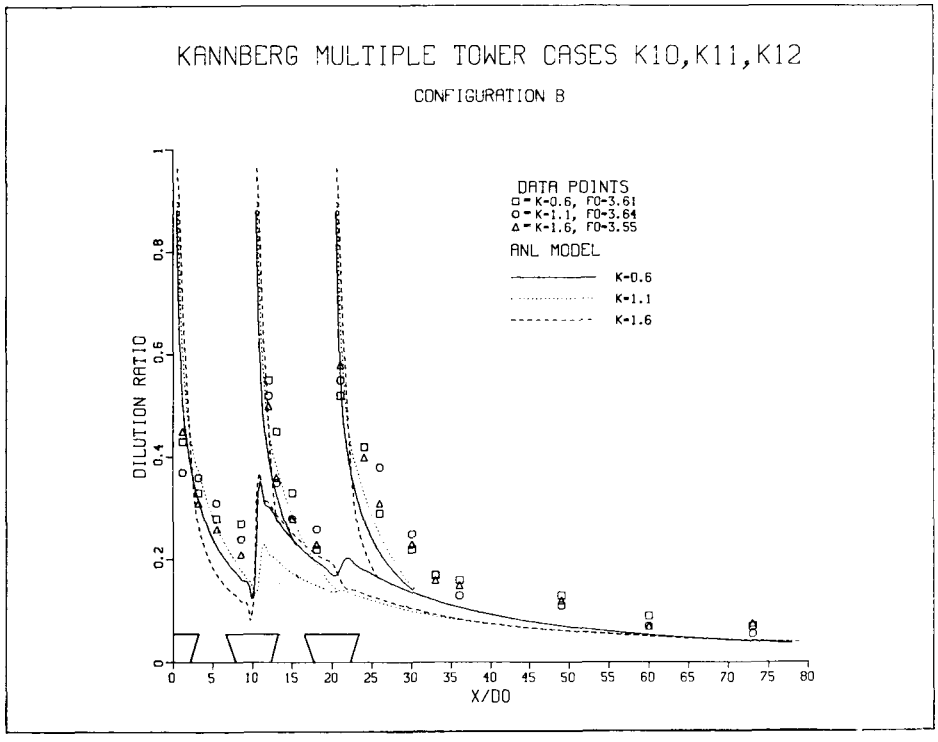

Figure 4-2. Comparison of predictions of ANL model to Kannberg multiple tower laboratory data . . . three towers parallel to each other and crossflow to the wind; cases K10, K11 and K12 with variation in K: (top) centerline trajectory, (bottom) centerline temperature decay.

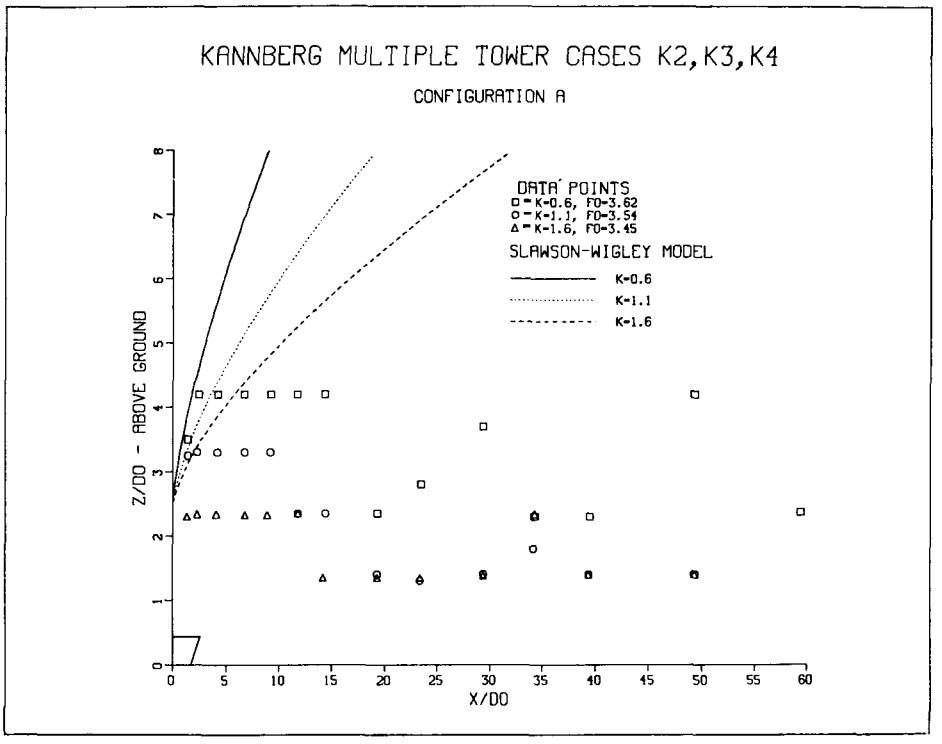

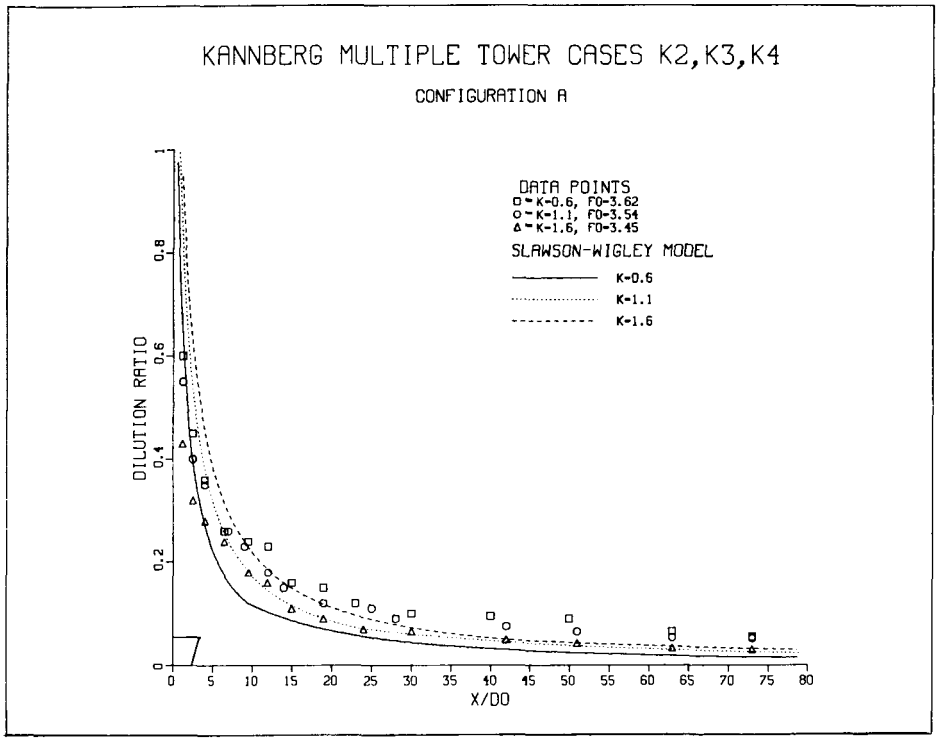

Figure 4-3. Comparison of predictions of Slawson-Wigley model to Kannberg multiple tower laboratory data . . . three towers on a line normal to the wind flow; cases K2, K3 and K4 with variation in K: (top) centerline trajectory, (bottom) centerline temperature decay.

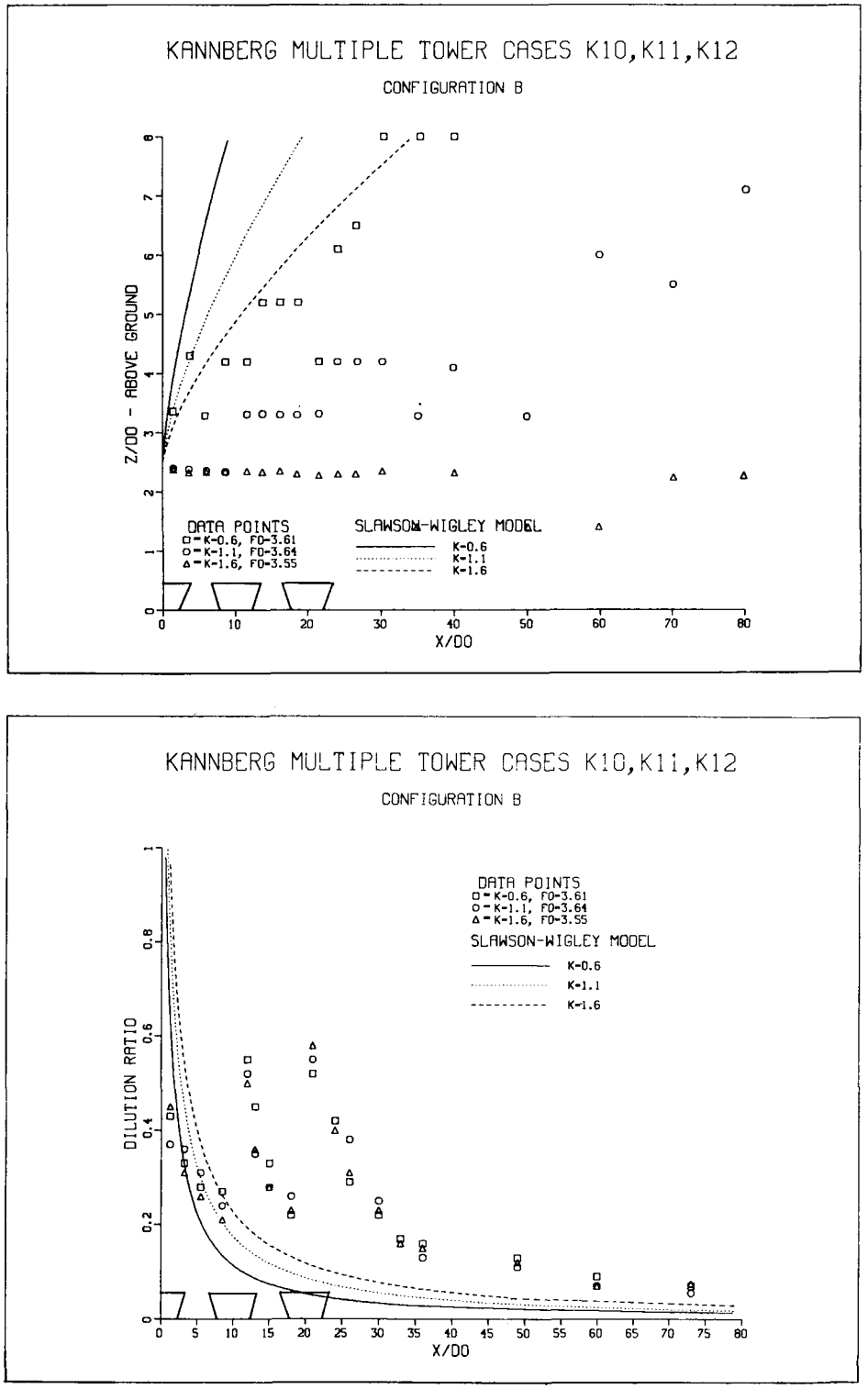

Figure 4-4. Comparison of predictions of Slawson-Wigley model to Kannberg multiple tower laboratory data . . . three towers parallel to each other and crossflow to the wind; cases K10, K11 and K12 with variation in K: (top) centerline trajectory, (bottom) centerline temperature decay.

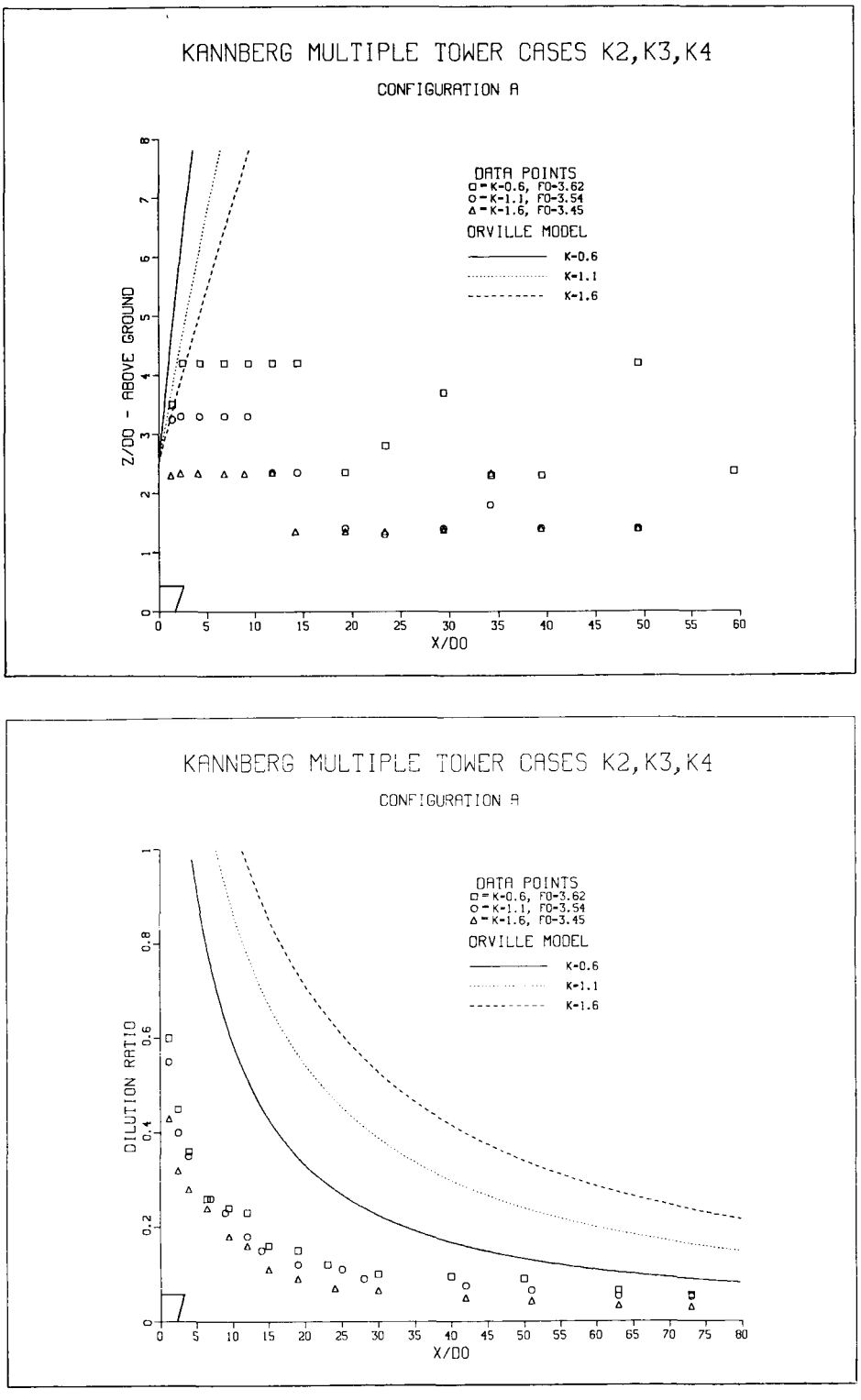

Figure 4-5. Comparison of predictions of Orville model to Kannberg multiple tower laboratory data . . . three towers on a line normal to the wind flow; cases K2, K3 and K4 with variation in K: (top) centerline trajectory, (bottom) centerline temperature decay.

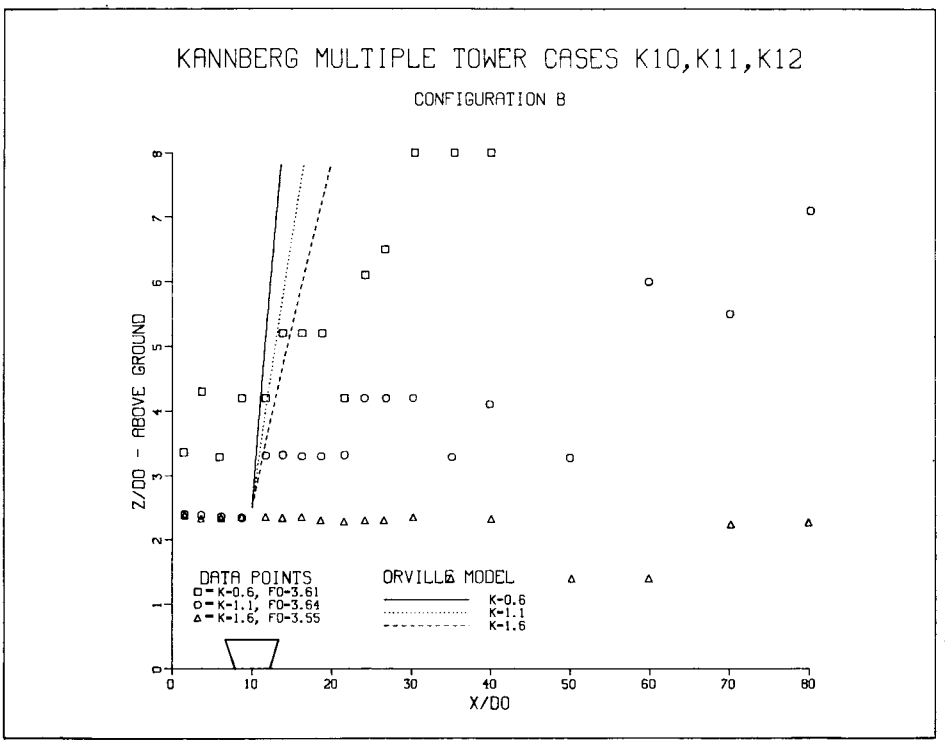

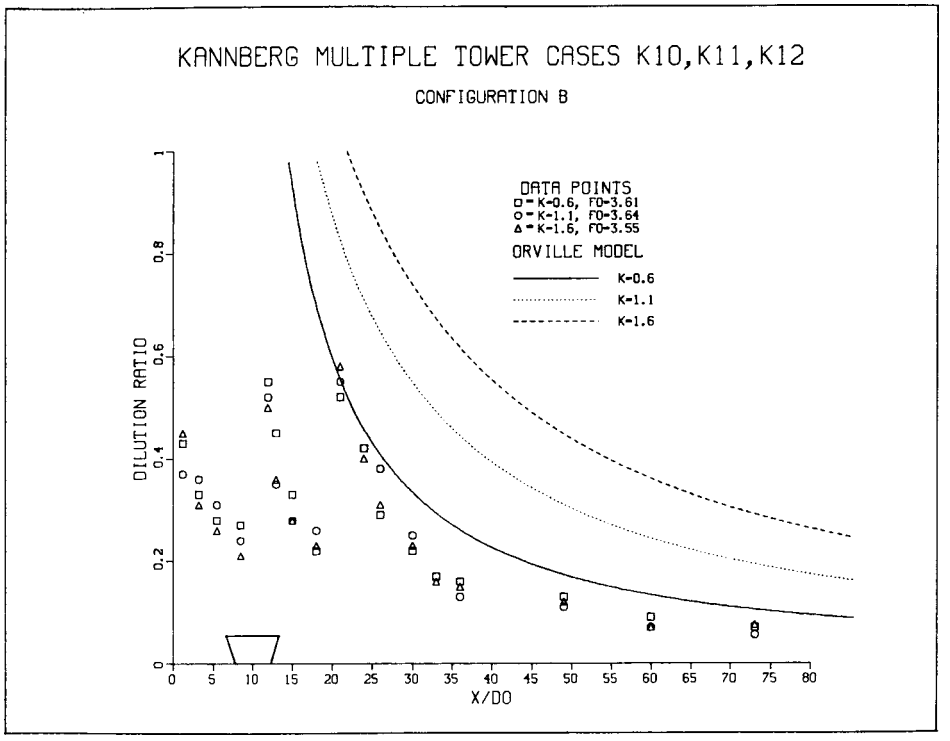

Figure 4-6. Comparison of predictions of Orville model to Kannberg multiple tower laboratory data . . . three towers parallel to each other and crossflow to the wind; cases K10, K11 and K12 with variation in K: (top) centerline trajectory, (bottom) centerline temperature decay.

dilution for the highest K value in the near field, but is is difficult to determine which K provides the greatest dilution in the far field.

The trajectory predictions for the Slawson-Wigley Model in Figures 4-3 and 4-4 are much too steep in rise. The dilution predictions in Figure 4-3 appear to be good, but it should be noticed that the curves are reversed in order. The Slawson-Wigley model predicts that there is less dilution with higher K. Obviously, a higher wind speed would tend to increase dilution in the plume, not decrease it; the data confirm this statement. Interestingly, the predictions in Figure 4-4 would look better if the Slawson-Wigley prediction curves were shifted ten diameters to the right and centered over the second tower due to the fact that the individual plumes merge quickly downstream. In effect then, for these cases, the Slawson-Wigley Model is almost an effective source model. However, Slawson and Wigley have recommended that their predictions be plotted starting from the first tower.

The plume trajectory predictions for the Orville Model in Figure 4-5 and 4-6 are very far from any agreement with the data. The Orville Model is an effective source model and thus by combining all the individual cell fluxes into one, the buoyancy is increased greatly resulting in very steep trajectory predictions. The dilution predictions are far from the data with the reverse behavior in dilutions with respect to K. The model would predict trajectories better if modifications were made to enable the plume to bend over more. The dilution predictions would probably be better due to the increased bending, but a downwash formulation would definitely improve dilution predictions.

GREGORIĆ DATA (See Figures 4-7 to 4-11)

These experiments (2) were conducted at the Hydraulics Laboratory of the U.S. Environmental Protection Agency's Corvallis Environmental Research Laboratory in Oregon by M. Gregorić. The study was aimed at determining the characteristics of merging jets by varying the number of towers, wind speed and the angle between the line connecting the towers and the direction of the wind flow.

The model towers (see Table 4-4) had a center-to-center spacing of 1.33 tower diameters and were mounted on a discharge tank and inserted into the water flume from above. They were then towed at some velocity to simulate a wind flow. A dyed salt water solution was discharged from the towers and photographs were made at selected points downwind of the plume cross-sections.

A total of 32 runs were made, but only seventeen were analyzed in the report by Gregoric. These seventeen cases are grouped into three categories, each with one parameter varying and two fixed. The first category held the number of towers, N, at seven and the angle, θ, between the towers and wind flow at 90°, while the velocity of the wind varied. The second category of tests held wind speed and θ constant with the number of towers varying. The third category varied θ, with the wind speed and the number of towers constant. We chose twelve out of the seventeen cases which provided us with the greatest information. Many of the seventeen runs analyzed in the Gregoric report were duplicate cases.

Figures 4-7 through 4-11 are the comparisons of the ANL, Slawson-Wigley and Orville Model predictions of upper edge trajectory to the Gregoric data. All of the models showed a trend for increasing trajectory height with an increase in the number of towers. The spread of the model predictions among cases plotted is very similar to the spread of the data in almost every case. The Gregoric data represents the upper edge (along with model predictions) of the plume cross-section because it was not very clear as to where the plume centerline was just from the photographs taken by Gregoric. No in-plume measurements were taken in the study. In addition, the densimetric Froude number of 6.0 was used in all data cases. The precise edge of the plume is not clearly determined by these one-dimensional models; this fact beclouds the model/data comparisons somewhat. Values of 6.0 are a little high for mechanical-draft towers. We may be just at the border of the F_o range of our interest.

The vertical coordinates of the predicted trajectories for Slawson-Wigley and Orville were derived by adding the predicted vertical coordinate of the plume centerline to the corresponding radius at each step. Likewise for the ANL Model except that half the plume height (see Section 2) was used instead of the radius.

Figures 4-7 and 4-8 (top) illustrate the predictions and data of the category with θ and K fixed and variation in the number of towers. The ANL Model does show some overprediction, but overall, the predictions are not that far from the data. Downwash effects are very negligible because K is small, but there still is no clear reason why the ANL Model predicts rise above the data. Slawson-Wigley and Orville predict trajectories which are much higher than ANL Model predictions. The Orville Model does not give enough surface entrainment to the plume, thus resulting in high trajectory predictions.

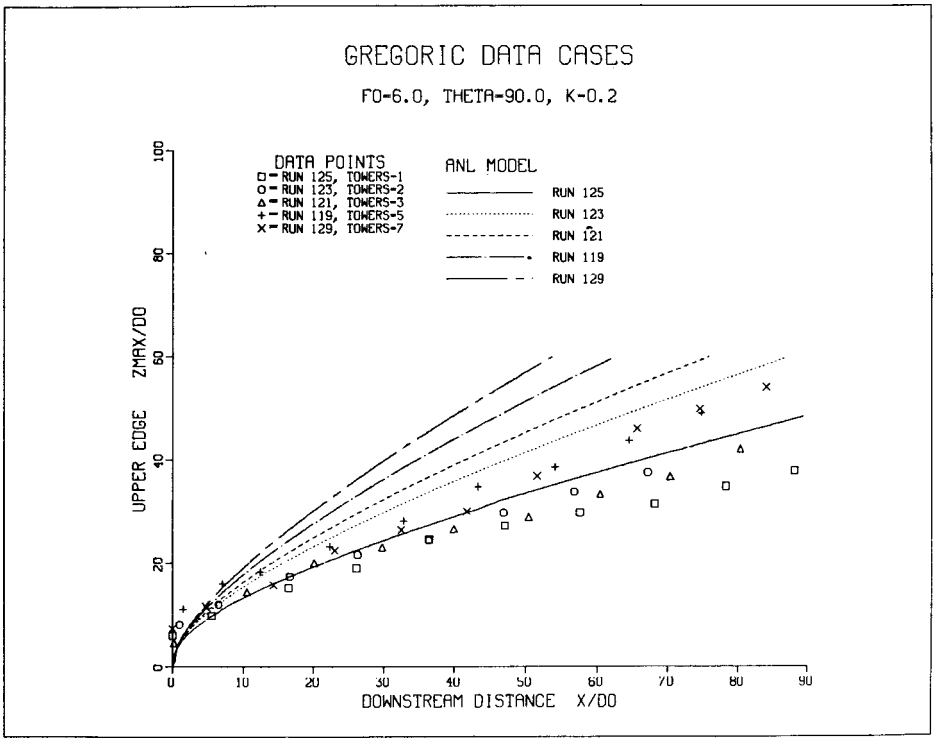

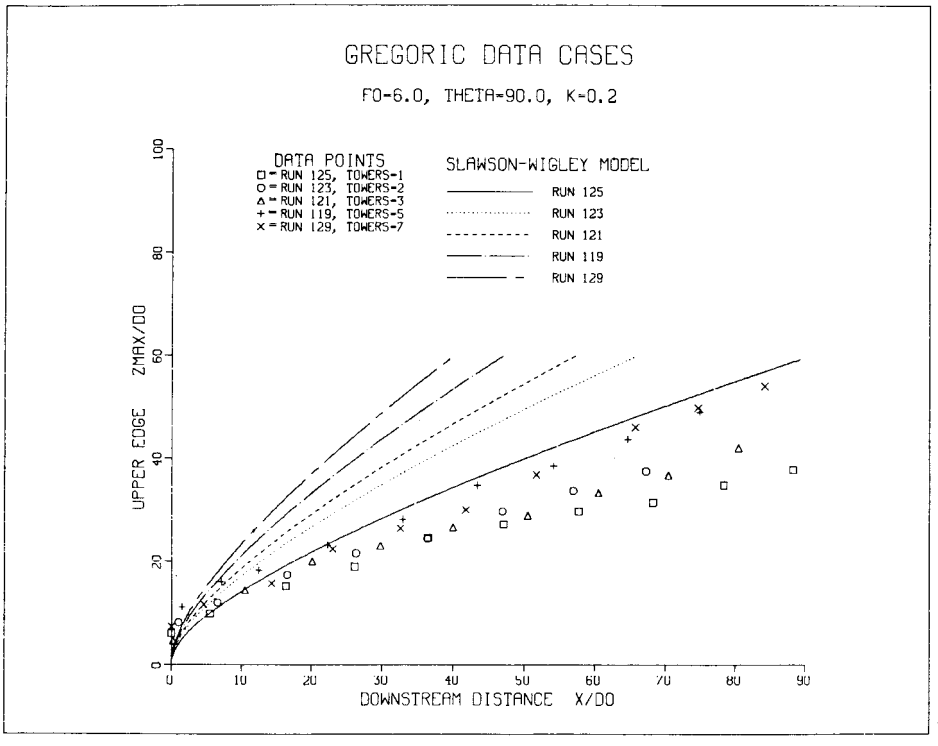

Figure 4-7. Comparison of model predictions to Gregorić laboratory data on upper edge trajectory . . . F_o = 6.0, K = 0.2 and θ = 90.0 with variation in number of towers: (top) ANL model, (bottom) Slawson-Wigley model.

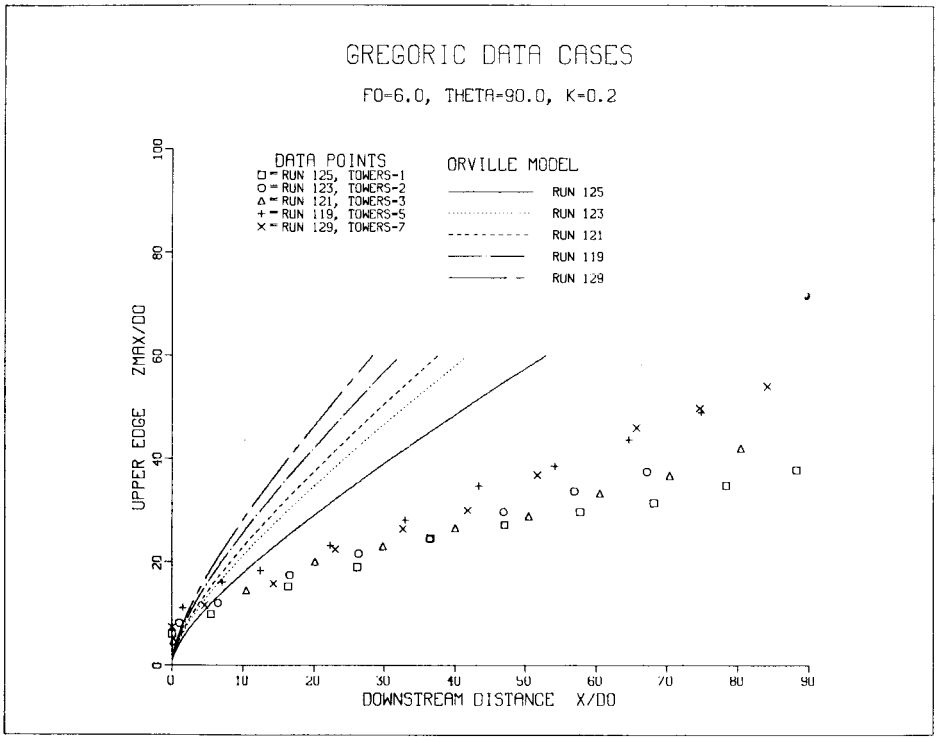

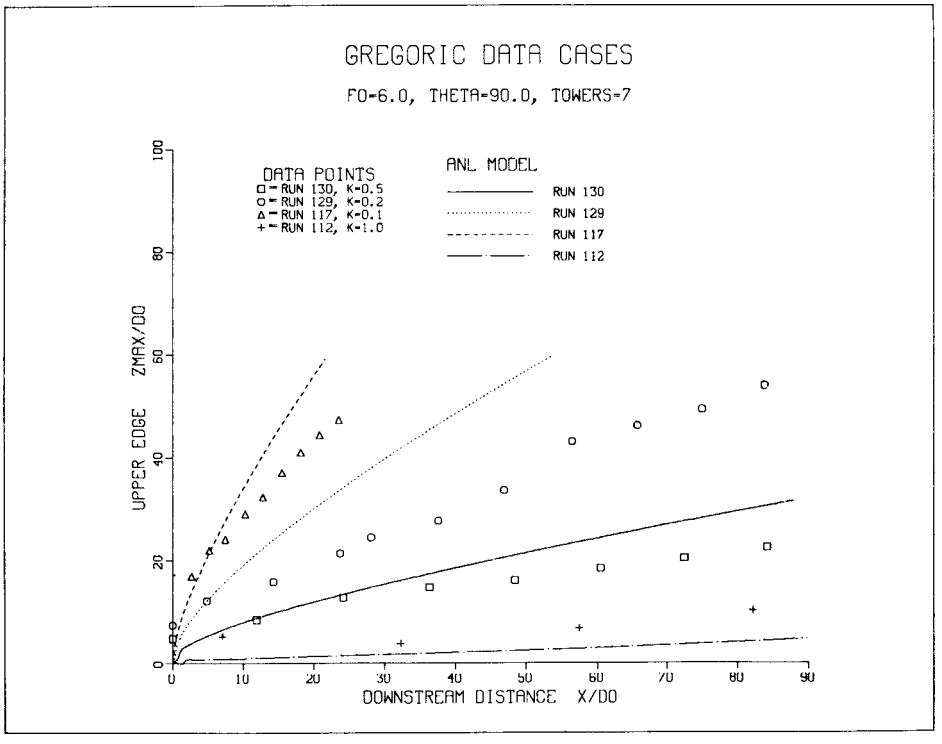

Figure 4-8. (Top) Comparison of predictions of Orville model to Gregorić laboratory data on upper edge trajectory . . . F_o = 6.0, K = 0.2 and θ = 90.0 with variation in number of towers. (Bottom) Comparison of predictions of ANL model to Gregorić laboratory data on upper edge trajectory . . . F_o = 6.0, θ = 90.0 and TOWERS = 7 with variation in K.

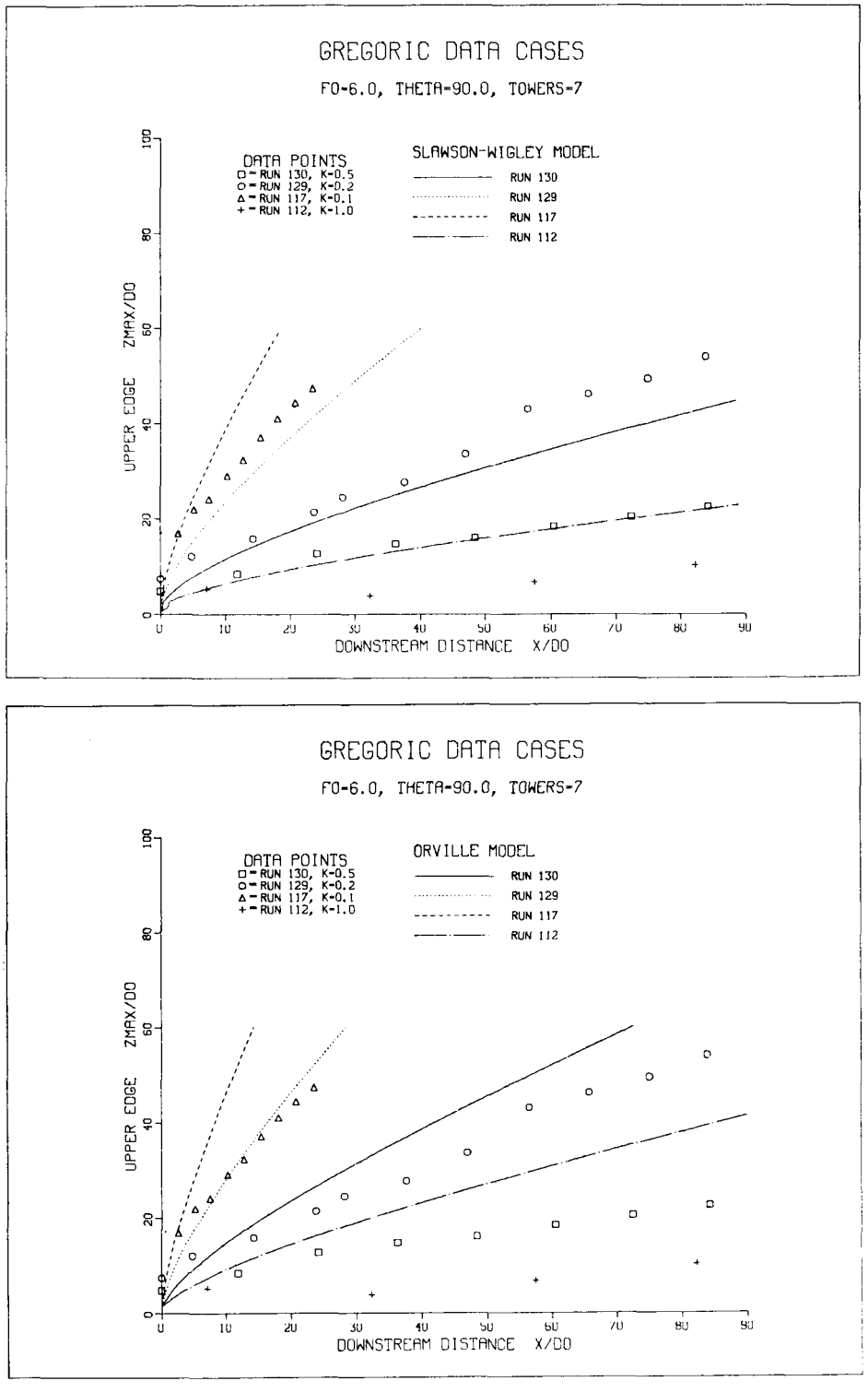

Figure 4-9. Comparison of model predictions to Gregoric laboratory data on upper edge trajectory . . . F_0 = 6.0, θ = 90.0 and TOWERS = 7 with variation in K: (top) Slawson-Wigley model, (bottom) Orville model.

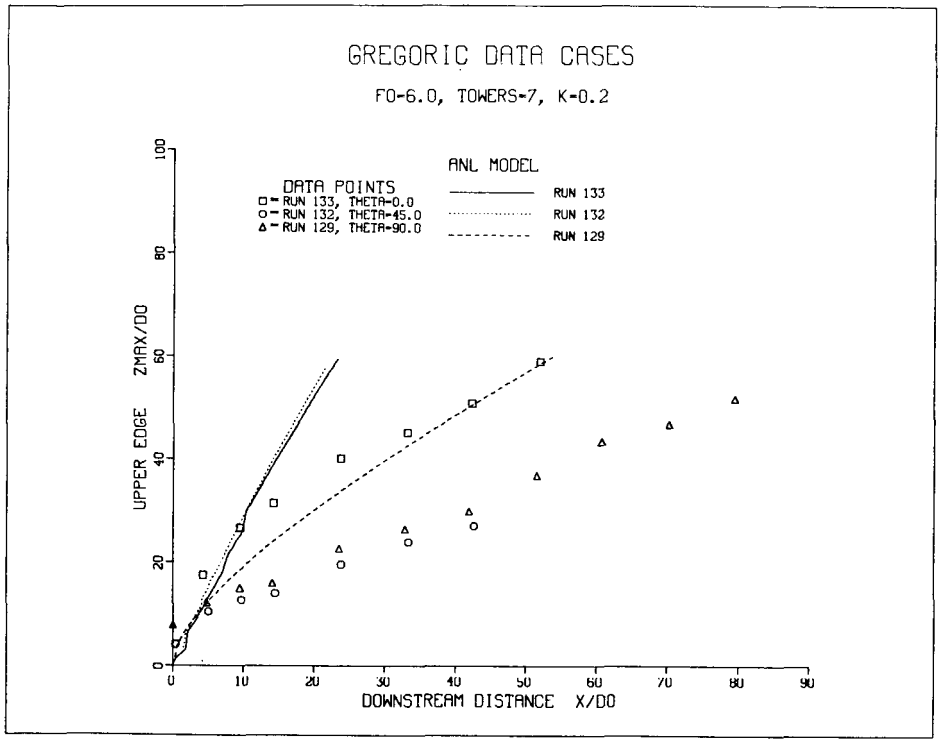

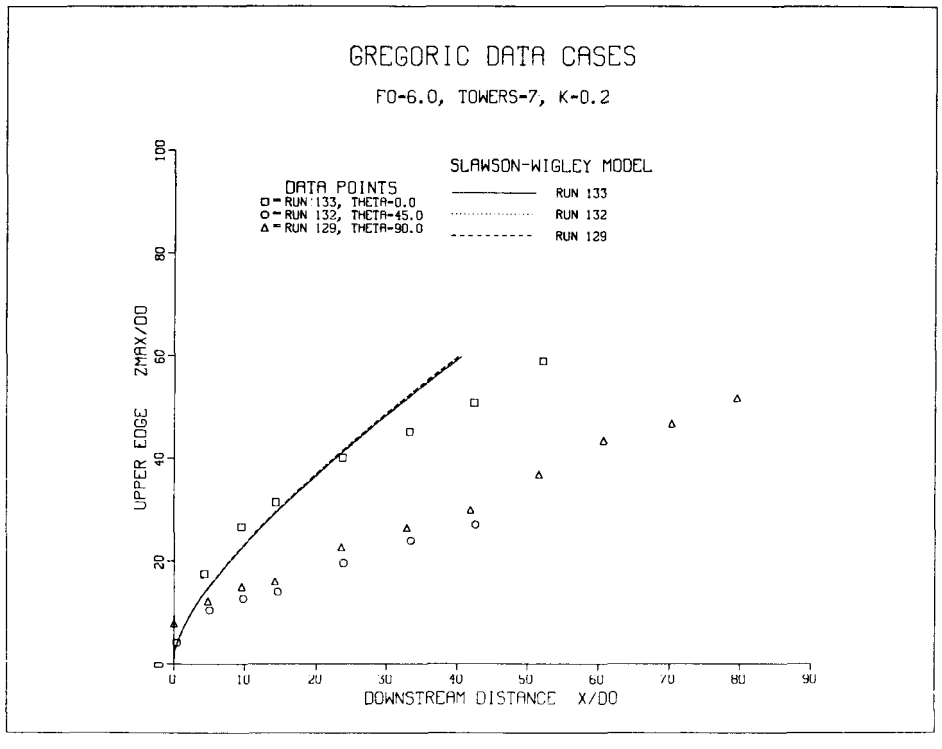

Figure 4-10. Comparison of model predictions to Gregoric laboratory data on upper edge trajectory . . . F_o = 6.0, K = 0.2 and TOWERS = 7 with variation in θ: (top) ANL model, (bottom) Slawson-Wigley model.

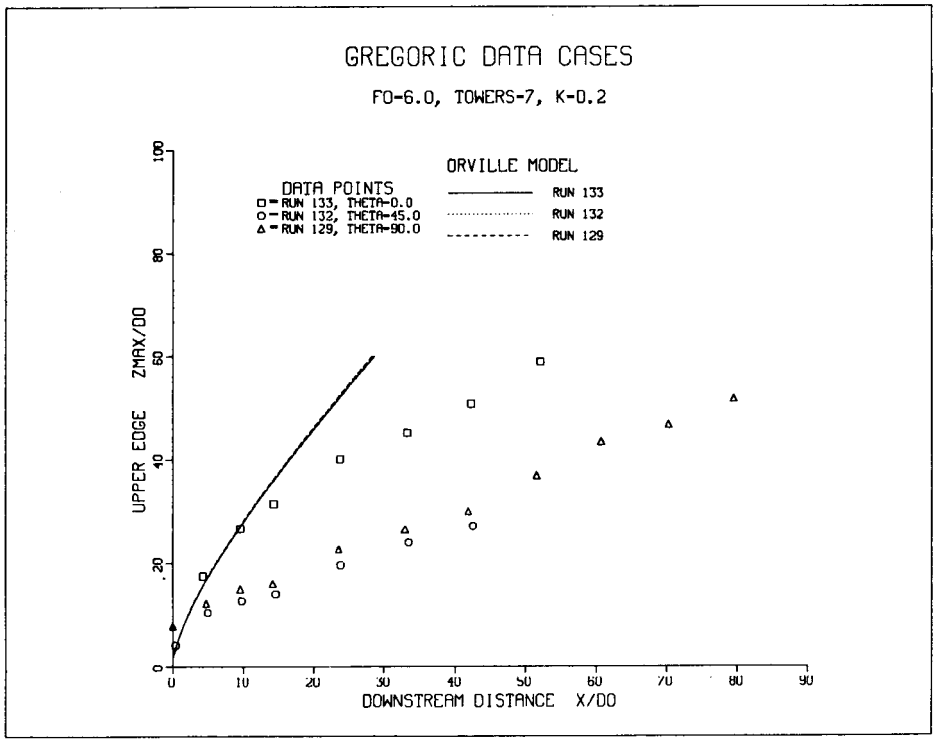

Figure 4-11. Comparison of predictions of Orville model to Gregoric laboratory data on upper edge trajectory . . . F_o = 6.0, K = 0.2 and TOWERS = 7 with variation in θ.

Figures 4-8 (bottom) and 4-9 fix θ and the number of towers while K varies. The ANL Model results are excellent considering there is slight overprediction for all K except K = 1.0 where there is underprediction. The Slawson-Wigley Model overpredicts all cases except when K = 0.1. Downwash is important here for higher K values, but the Slawson-Wigley model does not have any downwash formulation. Buoyancy is high for the Orville Model and again all the results are large overpredictions.

Figures 4-10 and 4-11 fix K and the number of towers while varying θ. Both Slawson-Wigley and Orville models show no difference in predictions with a change in θ, whereas the ANL Model shows fair predictions for $\theta = 0°$ and 90°. Examining the data shows the points for $\theta = 45°$ lower than the points for $\theta = 90°$, which should have the greatest bendover. The ANL Model shows a similar discrepancy in its results with the $\theta = 45°$ prediction being higher than the $\theta = 0°$ prediction. The ANL Model definitely failed for the $\theta = 45°$ case. The Gregorić data make it appear that wake effects at $\theta = 45°$ are likely to be larger than for $\theta = 90°$ for a MDCT; the feature of wake sizes other than for $\theta = 0°$ and $\theta = 90°$ are apparently difficult to represent in our model as presently formulated. However, the validity of the $\theta = 45°$ behavior of the Gregorić data needs to be verified by other experimenters. Otherwise, we believe that $\theta = 90°$ is the angle which leads to the greatest effects of the tower wake on plume trajectory and dilution.

All the models produced curves which were bent over steeply in the near field probably due to each model incorporating the bent-over-plume assumption.

FIELD DATA FROM NEURATH AND AMOS (See Figures 4-12 to 4-31.)

The three natural-draft towers at Neurath (3), each cooling a 300 MW_e unit, are positioned in a fairly compact equilateral triangle as can be seen in Figure 4-72. Except for possible additional downwash effects from two inoperative large NDCTs nearby, the three separate tower plumes will normally merge quickly with the merging process depending only weakly on wind direction. Differences in merging logic between different models will probably not be apparent in predictions for this site; model predictive behaviors should be similar to those for single tower cases.

The Amos towers (4), cooling a total of 2900 MW_e, lie in nearly a straight line (Figure 4-73), offering more opportunity for wind-direction-dependence of the merging process. However, there are only three towers, and they lie fairly close together. We expect only minor differences among models predictions as a result of the various merging logics selected as applied to Amos data. It is only for the mechanical draft tower data that we expect and can attribute significant model predictive differences to differences in merging logic as the wind direction varies from case to case.

The first Neurath data case, N15 (see Figure 4-12), exhibits an unstable ambient stratification over the observed plume rise region in conjunction with a moderate saturation deficit and high winds. The KUMULUS Model visible plume length prediction is too short, reflecting the tendency of that model to experience too much entrainment in high winds as we noted for our single-tower model/data comparisons. As detailed in Volume 2, the Orville Model formulation does not yield an increase entrainment in high winds; the plume is lengthened due only to more rapid passive downwind transport. Thus, as noted previously, the Orville predicted visible plume is too long, and has a trajectory which bends over too slowly. The presence of low saturation deficits aloft increases the overprediction here. In this case, the ANL Model demonstrates again that the downwash formulation generally has somewhat too little entrainment at very high winds, yielding long visible plume length predictions in such cases.

The case N34 (see Figure 4-13) is interesting because it was taken at night and shows a typical nocturnal inversion near the ground. The visible plume is quite short and low. The ground inversion extending to 300 m above the ground helps limit the rise of the plume; the main effects are the high saturation deficit coupled with moderate wind speeds, which combine to evaporate the plume quickly. All three models predict this general behavior, but the predicted trajectory of the Orville Model is too high.

A very similar case is shown next in Figure 4-13, representing Neurath case N37. Comments on model predictions for this case are the same as the previous case, except that it is somewhat puzzling that a ground inversion still exists at 100 meters above ground. Perhaps significant cloud cover was present; no weather map for this data was presented.

The following two cases, Neurath cases N49 and N51, can profitably be considered together. See Figures 4-14 and 4-15 for model/data comparisons. They illustrate the interesting changes that can occur on a single day as ambient conditions change. The average stability for these two cases over the visible plume rise region is about the same, with weakly stable average stratifications in both cases. Also, the average wind speeds are apparently similar and both moderate. (However, only <u>one</u> measured windspeed point near the ground is available for N49; the highly bentover character of the observed plume suggests much higher winds at plume height). However, the average saturation deficit is 0.5 gm/kg for N49 at 0900 hours and 1.0 gm/kg at 1130 hours. This difference helps to explain the reduction in size of the visible plume from a length of 2100 m at 0900 hours to 1000 m at 1130 hours.

The KUMULUS Model overpredicts visible length for N49, as it usually does for small saturation deficits. The ANL and Orville Models for this case underpredict length moderately. All three models yield high trajectories, probably due to inaccurate ambient windspeed values, with the Orville Model exhibiting the greatest rise overprediction.

For N51, both the ANL and KUMULUS Models give good predictions, except for the thin but long reappearance of the visible plume predicted by KUMULUS from 1500 m to 3000 m downwind. This case may be seen in Figure 4-15. The Orville Model's consistent tendency to rather strong rise overprediction is evident here.

The next data case, Neurath case N54 (see Figure 4-14) was taken later the same day at 1500 hours. It further emphasizes the natural variations of plume behavior during a single day. Temperature stratification has become neutral, the average windspeed has increased, but the saturation deficit still averages about 1.0 gm/kg. The reduction in plume length to 800 m is apparently due to stronger entrainment due to the presence of elevated windspeeds. All three models give similar length and rise predictions, moderately overestimating both. The predicted trajectories of the ANL and KUMULUS Models are good.

The final Neurath data case, N67 (see Figure 4-16), presents a difficult test for models. Windspeeds are high with marked downwash evident in the observed plume, which even touches the ground from 500-650 m downwind of the towers. The ambient stratification is unstable and the saturation deficits are low. As expected from past experience the Orville and ANL Models both overpredict plume length for different reasons. KUMULUS predicts a very thin plume of about the right length. Its trajectory, however, does not exhibit as much downwash as the observed plume does. The ANL Model's predicted trajectory and visible plume width fit the observed plume very well. Thus, the downwash <u>force</u> formulation in the ANL Model, severely tested here, seems accurate; however, the modeling of downwash-enhanced entrainment appears too weak at these high wind speeds.

The Amos data cases involve a heat release which is larger than three times the cumulative heat release of the Neurath towers. A study by Kramer et al. (<u>5</u>) demonstrated that the visible plume from this plant usually rose until it encountered a strong elevated inversion, responsible for the so-called "haze layer." Of course, this result presupposes that most Amos plumes do not evaporate before reaching final rise, defined as the location where buoyancy and momentum fall nearly zero. Since the Amos data were taken largely under cold winter conditions, the assumption holds

generally for these data sets but probably not nearly so well for a year-round characterization of the visible plume, especially in the summer season. Thus, to predict the available Amos data accurately, a model must have an accurate atmospheric diffusion phase submodel. Since snowfall from the plume and glaciation of the plume were documented on several occasions, it would also be desirable for a model to allow for plume freezing at appropriate temperatures below 0°C. The ANL and Orville Models allow for plume freezing; the KUMULUS Model does not. We have selected a subset of 19 cases from the full collection of available datasets taken during the study. We have selected cases which are more interesting and often more difficult for models to predict. A model's performance for the full collection of Amos data would probably be better than for this subset.

The first Amos data case shown, A1 (see Figure 4-17), has isothermal stratification with a thin inversion midway in plume rise. The windspeeds are high and saturation deficits low, increasing to moderate. The observed visible plume evaporates 500 m above ground; the haze layer in at 700 m. The ANL and Orville Models predict fairly accurate plume lengths, while KUMULUS overpredicts length considerably, as it often does for small saturation deficit. The fact that all three predicted trajectories are lower in relation to the observed trajectory than is normally the case suggests that the sparsely measured wind profile may be somewhat inaccurate, with 12 m/s velocities extending higher than linear interpolation would suggest. (A clear break in ambient properties at 675 m, near the final plume rise height, may be associated with a sudden windspeed increase).

For Amos data case A3 (see Figure 4-17), we find near-neutral stratification, moderate winds increasing with height to high winds and moderate saturation deficits. The ANL Model predicts the plume well, and the Orville Model predicts an overly long and high plume as it usually does in high winds. (In this case, the observed plume evaporates well below the inversion associated with a cloud layer at 1050 m).

Case A6, shown next in Figure 4-18, poses a very difficult challenge for plume models. Temperature stratification is near-neutral; windspeeds are high and saturation deficits are very low, reaching zero from 500 m to 800 m above ground. The observed plume merges with a layer of broken clouds at 950 m. None of the three models is formulated to describe the merging of a plume with an existing cloud layer. It is not surprising, then, that two of the models strongly over-predict the length (Orville and KUMULUS). Perhaps it is more surprising that the models yield terminating predicted plumes at all. However, the nature of the diffusion phases in the models allows termination to occur. The Orville Model-predicted-plume levels

off above the 100% relative humidity region. The ANL Model assumes air is entrained around the plume perimeter with temperature and mixing ratio averaged around the circumference. It's length prediction is very good; but it predicts artificial ground fogging from 9.3 km to 12.0 km downwind. (The excessive radial growth must occur before the perimeter can sample sufficiently dry air to evaporate the plume). It is not clear how the KUMULUS Model achieves a finite length prediction, because it levels off at a height where the relative humidity is 100%.

In the next example, Amos case A8A seen in Figure 4-19, there is a layer of ground fog up to 400 m, as evidenced by 100% relative humidities. Windspeeds are high from 250 m upward (the lowest measured point) and saturation deficits rapidly become large above 700 m, but are small from 400 m to 600 m above ground. The temperature stratification is stable with an inversion from 250 m to 350 m above ground and isothermal conditions above 350 m and below 1250 m.

The KUMULUS Model predicted plume becomes involved with the ground-fog ambient conditions; but the model does not include logic to handle ambient fog. Instead it predicts additional extensive ground fog to 18 km. The Orville plume prediction is short because the high trajectory reaches dry air aloft too quickly. The ANL Model yields a fairly good prediction, which is slightly short. It does not become involved in the low-lying ambient conditions characterizing the fog.

Another challenging case appears in Amos A10A seen in Figure 4-20. Neutral stratification persists up to an elevated inversion at 850 m, which halts the rise of the observed plume. Windspeeds are moderate-to-high; and saturation deficits are low. Plume conditional and ambient latent instability insure that the plume will continue to rise and remain visible up to a capping inversion, as is observed. The Orville Model's predicted plume is short because excessive rise places the diffusion phase at a height where the saturation deficit is larger. The KUMULUS Model makes a very good prediction for this case, strengthening one's confidence in the accuracy of its atmospheric diffusion phase formulation. That ANL Model prediction for this case is extreme, with ground fog beyond 2600 m from the towers and unlimited plume radial growth. This result stems from an accidental relationship between choice of ice nucleation temperature, ambient averaging procedure and actual ambient conditions. At, and near the observed plume levelling-off height, the ambient mixing ratio and temperature are nearly saturated over water. But over ice they represent slightly supersaturated conditions. Since we selected -10°C as a reasonable ice nucleation temperature based on reported cases of plume glaciation and other cloud

physics studies, the predicted plume freezes when the ambient temperature drops to -11°C before the plume levels off. From then on, all saturation comparisons refer to saturation over ice. From the viewpoint of a glaciated plume, the air at plume height is supersaturated, and mixing can never evaporate the remaining ice. A -2°C adjustment in T_i (ice nucleation temperature) would rescue the ANL Model prediction for this case, but would also worsen two other predictions somewhat. In actuality, T_i varies from day to day depending on ambient particulate concentrations; on this data it was evidently below -11°C, or else the observed plume would have glaciated and shown more extreme behavior.

Amos case A12 seen in Figure 4-21, involves another situation where the observed plume merges with an existing cloud layer with 100% ambient relative humidity reported. Moderate wind, low saturation deficit and neutral stratification accompany this behavior. The Orville Model predicted plume again rises too high, above the saturated region; the length prediction is finite and near that of the section of plume visible prior to merging with the cloud layer. KUMULUS predicts visible rise very well if one discounts the predicted gap which was not observed; its extreme length overprediction is reasonable given the presence of the cloud layer (again, termination at all is a puzzle). The ANL Model predicted trajectory is low and the predicted visible length is about half of observed, consistent with higher saturation deficits below the cloud layer. Only two wind profile points are available over 800 m of vertical rise, which makes accurate prediction of plume trajectory unlikely.

The importance of accurate windspeed profiles in obtaining accurate plume predictions is underscored by the next case, Amos A15 (see Figure 4-22). None of the three models tested adequately exhibits the observed trajectory behavior in its prediction. With zero winds reported 150 m above the tower exit and no further point measured until 760 m above the exit, where a moderate wind of 5 m/s is reported, it is very difficult to know what the cross-flow velocity should be over 600 m of plume rise. The universal assumption of linear interpolation is undoubtedly in error here. It does seem that the observed plume should bend over more than its outline shows above the 5 m/s wind profile point.

Isothermal ambient temperature exists up to 900 m, followed by 450 m of near-neutral air capped by an inversion. The observed plume evaporates at the height of the inversion. The Orville and ANL Models predict leveling-off of the plume at the same height, well below the actual final rise height. Actual windspeeds are probably lower than linear interpolation suggests, and entrainment considerably less as a result. Thus, in the observed case moisture-related plume instabilities are able to influence rise and sustain buoyancy from 900 to 1350 m above ground (near-neutral

layer) without the plume evaporating below 900 m. We suspect an error in the input data used for the KUMULUS Model, because its predicted plume slope bears no relationship to the calm conditions reported near tower exit.

Strong expression of moisture-related instabilities are clearly present for Amos case A16 (see Figure 4-23). Despite moderate saturation deficits above 500 m the plume rise only stops due to an elevated inversion starting at 1150 m. Winds are moderate and the stratification is near-neutral below 1150 m. Again, however, error in the interpolated windspeeds seem to pose a problem. The Orville predicted trajectory is correct, although it normally lies well above the observed one. And both KUMULUS and ANL Model trajectories are quite low. It seems likely that 5 m/s winds present at 300 m do not increase much until nearly the height of the next measured profile point, about 8 m/s at 1350 m. A gap of 1000 m in a wind profile makes accurate plume prediction very unlikely. The excessive length predicted by the KUMULUS Model is related to its rise underprediction, because saturation deficit increases with height in this case.

An 8.3 km long observed plume occurs when the plume is trapped at low elevations by a strong ground inversion extending upward to 1500 m in the next case, Amos A28A (see Figure 4-24). Since the plume ceases to rise in ambient air of low saturation deficit; and because turbulent mixing is strongly inhibited in very stable air, the visible plume extends far downwind. From the accompanying photograph in the Amos databook, the plume apparently also glaciates at a point where the temperature is -6°C; but no snowfall was reported.

All three models predict approximately the right amount of rise; but all three predict very short plumes compared to the observed. Evidently none of the formulations of atmospheric diffusion reduces turbulent mixing sufficiently under the very stable conditions characteristic of an extensive ground inversion.

For Amos case A34 (see Figure 4-22) we were not given a KUMULUS Model prediction. The ANL predicted plume fits the observed plume well, but the Orville Model prediction has a trajectory which is too high and an atmospheric diffusion phase of inadequate length. The ambient conditions for this case exhibit a ground inversion, quite high temperatures for February, moderate winds and large saturation deficits. As Amos plumes go, this one is quite short.

For Amos case A35A (see Figure 4-25) one can understand the 24 km extent of the observed plume easily. Uninfluenced by ground fog in a shallow ground inversion, the plume rises under near-neutral conditions, low winds and small saturation deficit; until it encounters an elevated inversion. Where it levels off, further atmospheric turbulent mixing is weak and the saturation deficit is only 0.5 gm/kg. The KUMULUS and ANL Models predict good trajectories. The Orville Model does not; and yields a very short prediction because much drier air lies just above the plume leveling-off height. The ANL Model predicted length is short, while the KUMULUS Model predicted length is good, again suggesting reliability in its atmospheric diffusion phase formulation for stable conditions. (Moisture-related instabilities strongly affect the rising plume in this case.)

However, the following case, Amos A36 (see Figure 4-26), shows how delicate accurate length predictions are for these long plumes; (here 7.8 km long). A segment of the observed plume is seen to break off at 700 m, about half of the 1300 m final height of the main plume. Nothing unusual occurs in the temperature profile to help explain this behavior, such as a thin-but-sharp inversion in which some plume parcels could become trapped. An excursion in relative humidity near this height could indicate a thin layer of fast-moving air but this is unlikely. The model predictions all seem to follow the upper portion more closely; and the reasons for the lower segment are not apparent to us. Moderate winds, low saturation deficit and neutral stratification insure a long, high plume, as we have often seen, where rise is terminated only when it encounters a strong elevated inversion. Plume conditional and ambient latent instability both occur strongly for this case. The ANL Model prediction is somewhat low and much too short, which are related; because the saturation deficit at 900 m is large by a factor of two than at the observed height of final rise. The Orville Model prediction again overshoots into dry air, yielding a very short prediction.

Again for A45 (see Figure 4-27) we received no KUMULUS Model prediction for reasons not clear to us. This interesting case shows a ground inversion up to 300 m with neutral conditions above this up to isothermal stratification beginning at 1100 m. Moderate saturation deficits prevent strong effects of moisture-related instabilities. Winds are also moderate. The Orville Model and the ANL Model predictions are both apparently blocked in rise by the ground inversion. Because the ANL Model usually follows plume trajectory well with only a slight tendency to be low, one can assume that the observed plume barely penetrates the ground inversion. Once above it, however, plume conditional instability allows the plume to gain buoyancy and rise another 750 m, where isothermal air intervenes. This inference would explain the predicted/ observed plume discrepancies here seen.

A capping inversion also limits rise of the observed plume for case A47 (see Figure 4-27). Moisture-related instabilities clearly help cause the extensive visible plume here. But the saturation deficit of nearly 2 gm/kg at the height of the inversion allows rapid evaporation of the plume - a short atmospheric diffusion phase for the visible portion. Wind speeds are low. The ANL Model prediction fits the observed plume very well; but the KUMULUS Model prediction shows a reappearance at 1300 m which is 1.7 km long. It is difficult to reconsile this behavior with the ambient profiles at this height. The Orville Model's early evaporation in this case is also very hard to explain; as usually in low winds the model predicts rise well.

For completeness we included a fully calm case, Amos A102 (see Figure 4-28), to test the validity of the zero-wind entrainment rate of the ANL Model. No integral model is equipped to predict the spreading concentric rings of visible plume observed to emanate from the vertical portion of the leveling-off height. Clearly no "length" prediction comparisons can be made in this case. The KUMULUS Model cannot handle zero wind, and we were furnished with no prediction for this case. Low saturation deficits (about 0.5 gm/kg), zero wind and weakly stable stratification insure strong effects of the two moisture-related instabilities. Only a capping inversion can limit the rise; and the plume stays visible for nearly 5 km of lateral spread in all directions. The plume also glaciates, with average temperatures around -15°C. (The momentum overshoot actually carries about 650 m above the height of leveling-off.) The ANL Model is internally limited to avoid predicting any momentum overshoot; but rather to cease rising at the zero buoyancy point. Its rise prediction here is very accurate. The Orville Model prediction follows the overshoot, also with good accuracy. (Zero wind is the case where the Orville Model's assumptions are closest to reality.

A very long observed plume which gave rise to snowfall reaching the ground 8 km from the tower at the end of visible plume travel and extended to 22 km is encountered for Amos case A105 (See Figure 4-28). Temperature stratification was near-neutral up to an elevated inversion at 780 m, which blocks the rise of the observed plume. Saturation deficits were low and winds moderate-to-high. Ambient latent instability may operate here to enhance visible plume extent, but the low temperatures (below -15°C) and high winds effectively prevent plume conditional instability from occurring.

The Orville Model's predicted plume rise is correct, the KUMULUS Model's predicted rise a little low and the ANL Model's predicted rise significantly low. Judging from the normal relationship between predicted and observed rise for each of the

models, we again question the validity of the interpolated windspeed values. We suspect the interpolated values may exceed the actual values over much of the plume rise region. The Orville and ANL Models both predict shorter-than-observed plumes, while the KUMULUS Model's predicted length is very accurate, again commending its atmospheric diffusion phase logic (whose calibrated parameters are not available in the open literature, unfortunately). The ANL and Orville Model plumes do, indeed, glaciate; the KUMULUS Model does not include glaciation logic. None of the three are equipped to predict the observed snowfall.

Another case, Amos A107 (See Figure 4-31), again illustrates the fact that NDCT plumes normally do not become involved with a layer of ground fog, when present, even in high winds. A ground inversion is present up to 300 m, containing fog and mist up to 170 m above ground. Winds are high and saturation deficits moderate. The available visible plume outline is not very reliable, as it is short, but is presented at a very small scale. In the printed data a length downwind of 320 m is given. The ANL Model predicted plume agrees with this length extremely well, while the Orville Model's predicted length is only slightly long. Rise comparisons for this case cannot be trusted due to the inaccurate observed outline. Again, for reasons we do not have, the KUMULUS Model predictions were not given to us for this case.

Amos case A109 (See Figure 4-29) shows very extensive snowfall, emphasizing the desirability of augmenting present models to include snowfall. Light snow begins to reach the ground about 8 km downwind of the towers, and continues to 70 km downwind! On this occasion saturation deficits were low, wind speeds moderate and temperature stratification neutral up to 800 m, isothermal from 800 to 1100 m, and near-neutral above. The observed visible plume levels off just above the top of the stable isothermal layer. (With a little more momentum it would apparently have reached the inversion at 1800 m!) Temperatures over the plume rise region decreased from -7°C to -14°C. Ambient latent instability over much of the plume rise region apparently helps to sustain the extensive visible plume, but plume conditional instability is not a factor at these temperatures. All three models give reasonable plume rise predictions, but the ANL and Orville Models significantly underpredict length of the reported "visible" portion of the plume; and both models predict glaciation. The KUMULUS Model overpredicts visible plume length somewhat. As for case A107 no model is equipped to predict the extensive light snowfall, which represents a significant environmental impact.

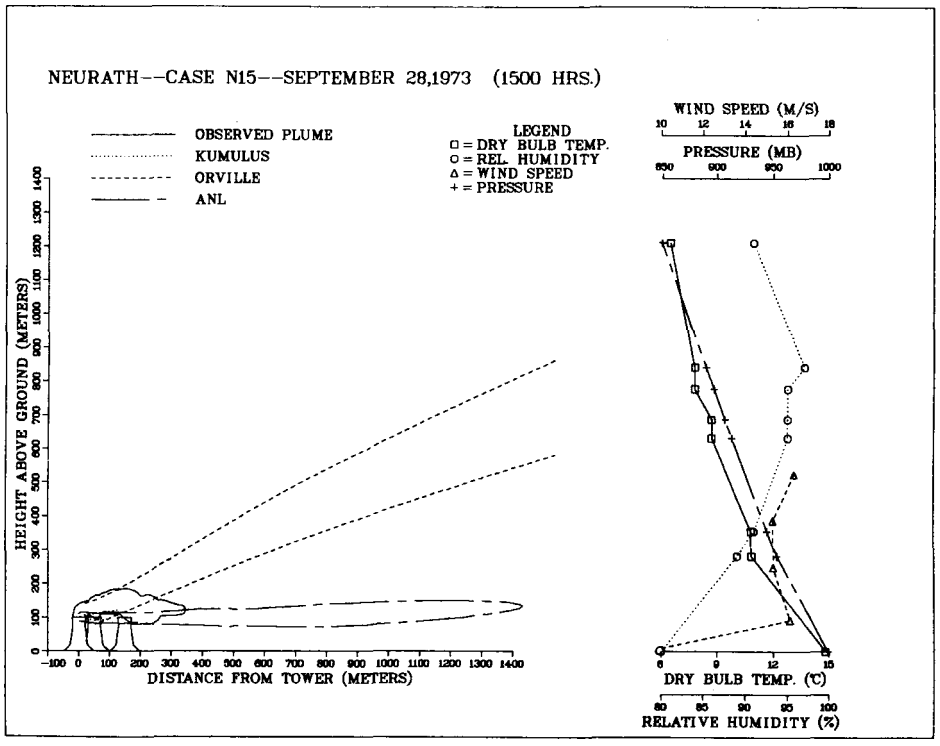

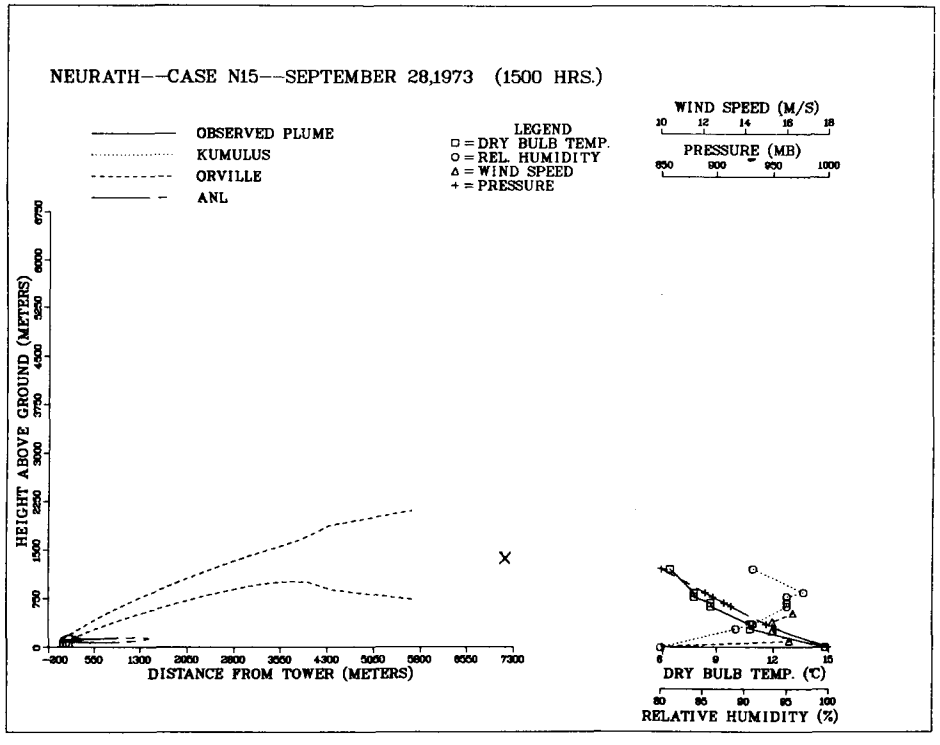

Figure 4-12. Comparison of predictions of KUMULUS, Orville and ANL models to observed visible-plume outlines at Neurath: September 28, 1973 (1500 Hrs.).

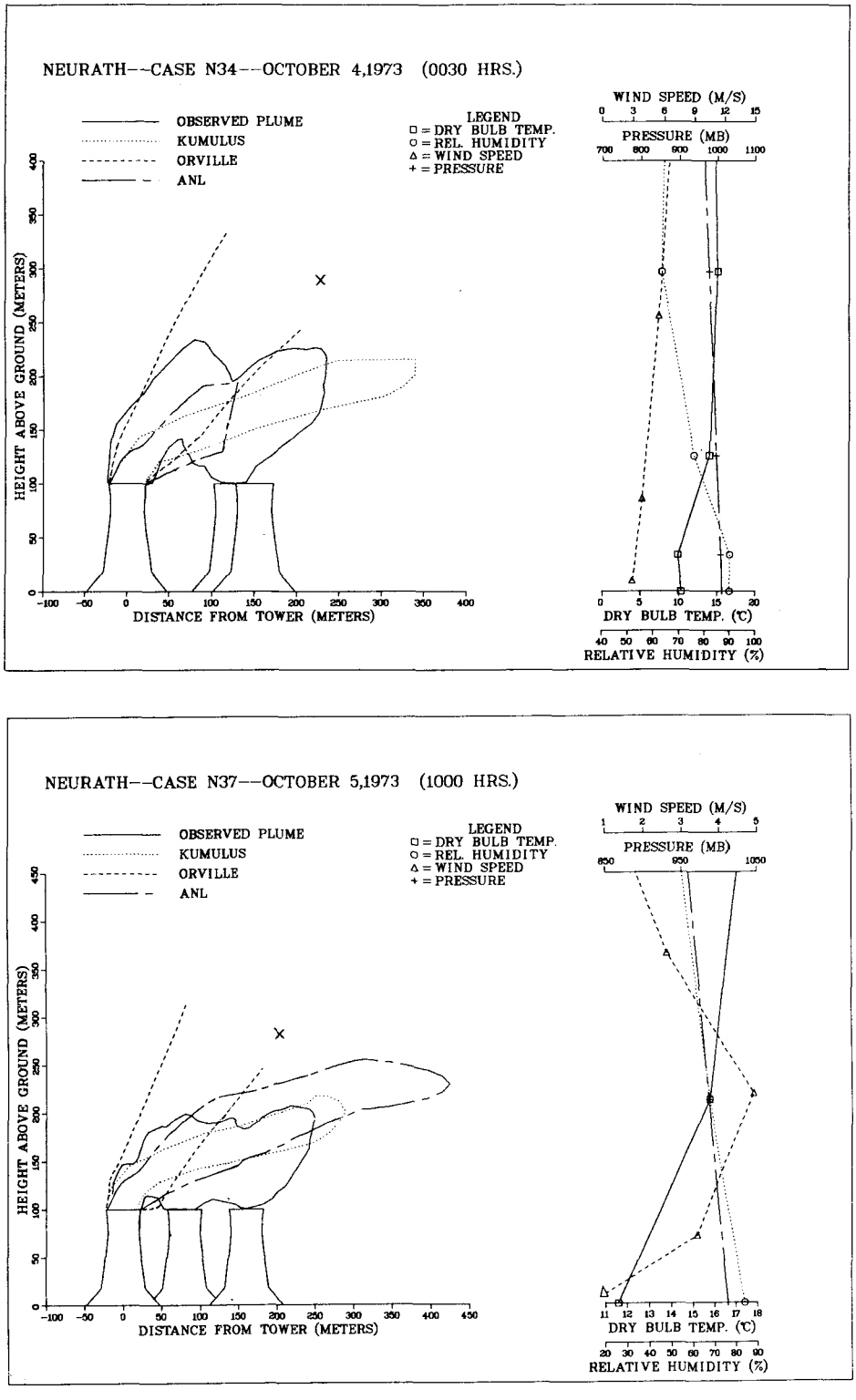

Figure 4-13. Comparison of predictions of KUMULUS, Orville and ANL models to observed visible-plume outlines at Neurath: (top) October 4, 1974 (0030 Hrs.), (bottom) October 5, 1973 (1000 Hrs.).

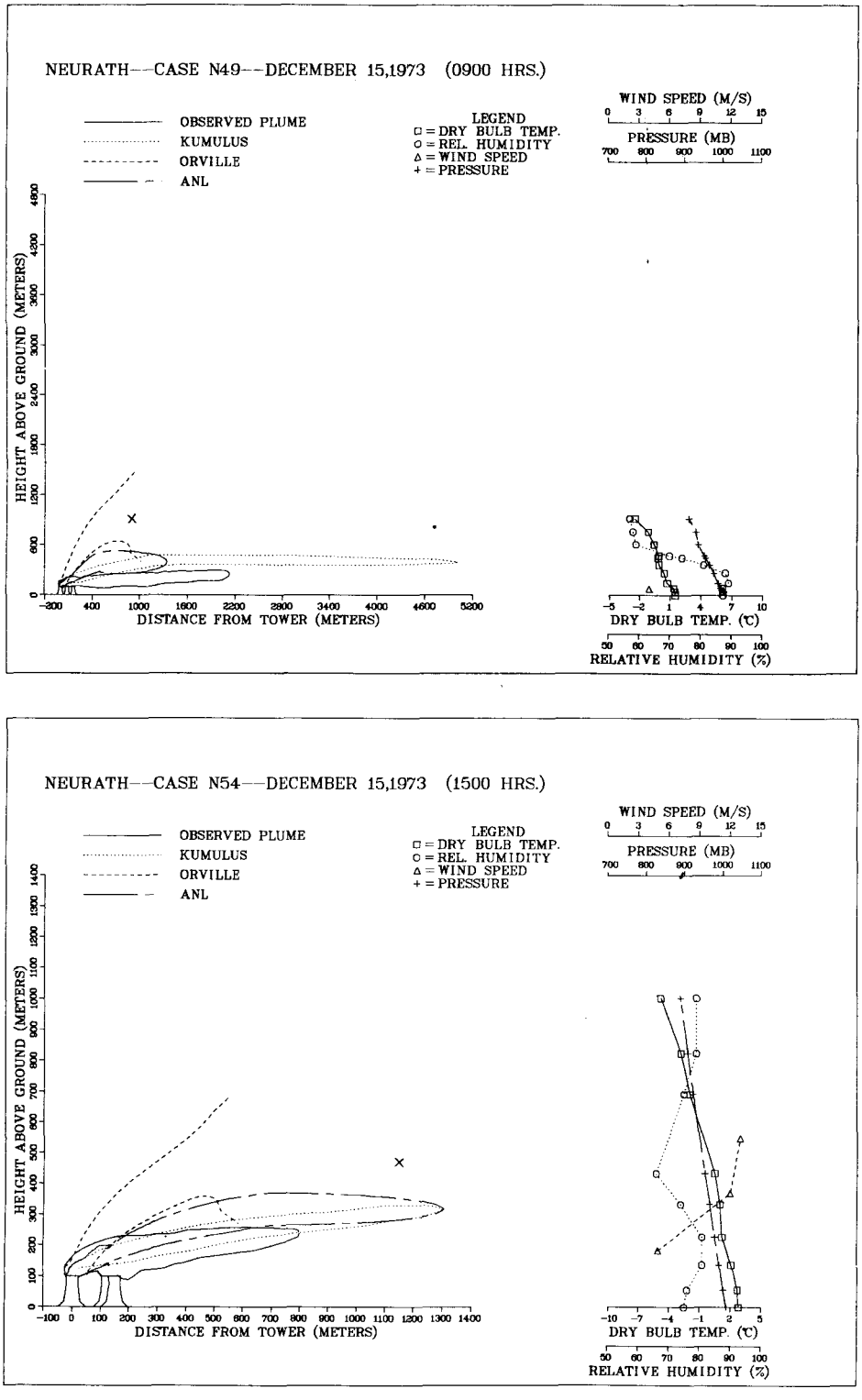

Figure 4-14. Comparison of predictions of KUMULUS, Orville and ANL models to observed visibleplume outlines at Neurath: (top) December 15, 1973 (0900 Hrs.), (bottom) December 15, 1973 (1500 Hrs.).

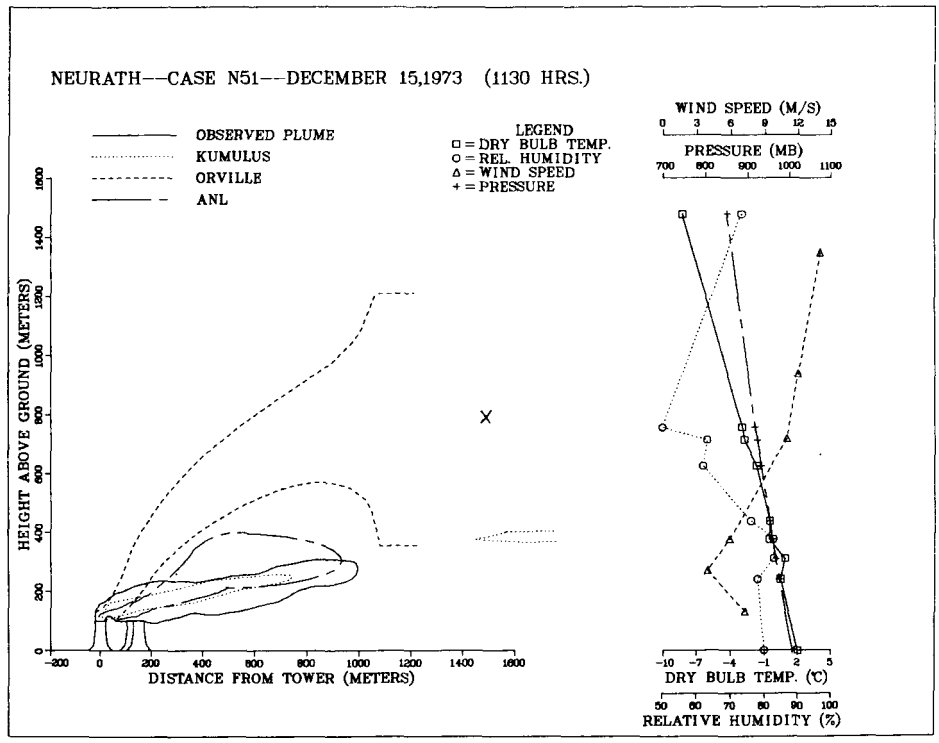

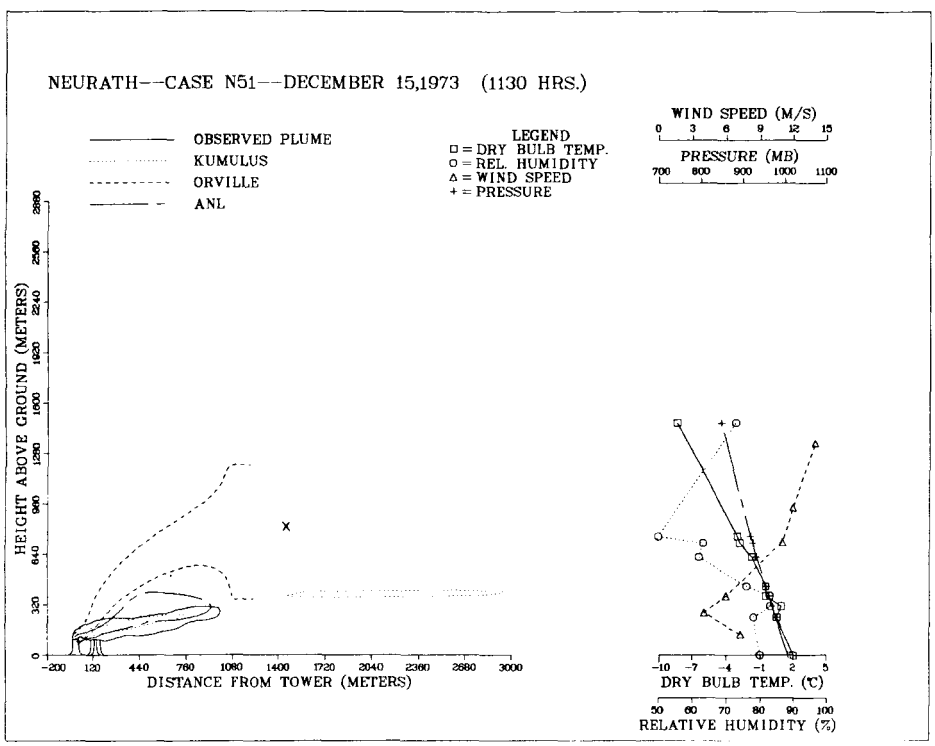

Figure 4-15. Comparison of predictions of KUMULUS, Orville and ANL models to observed visibleplume outlines at Neurath: December 15, 1973 (1130 Hrs.).

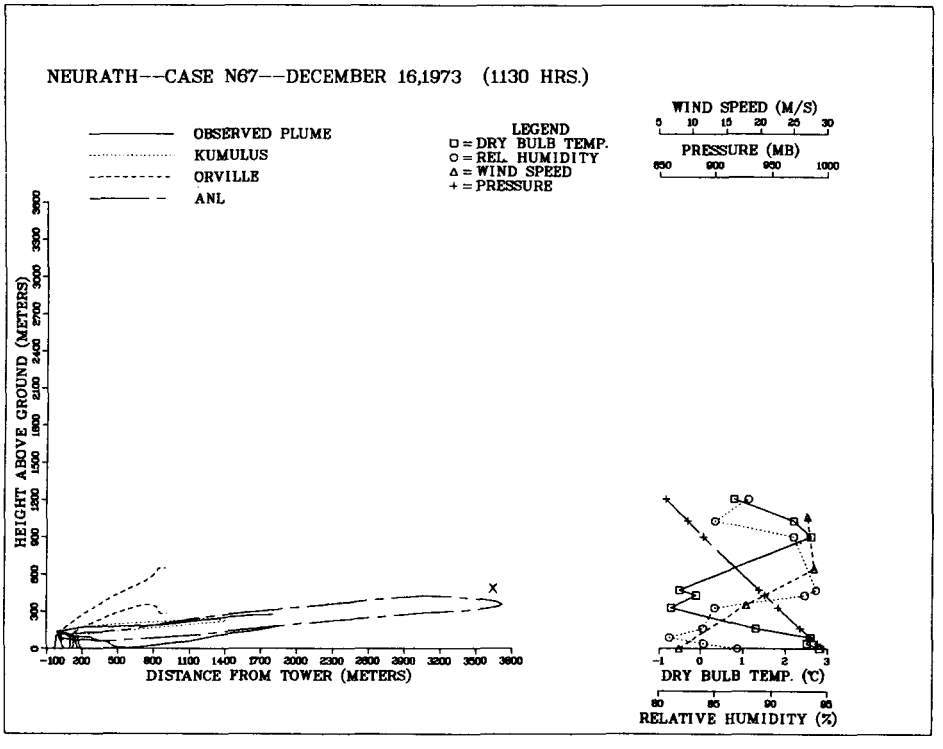

Figure 4-16. Comparison of predictions of KUMULUS, Orville and ANL models to observed visible-plume outlines at Neurath: December 16, 1973 (1130 Hrs.).

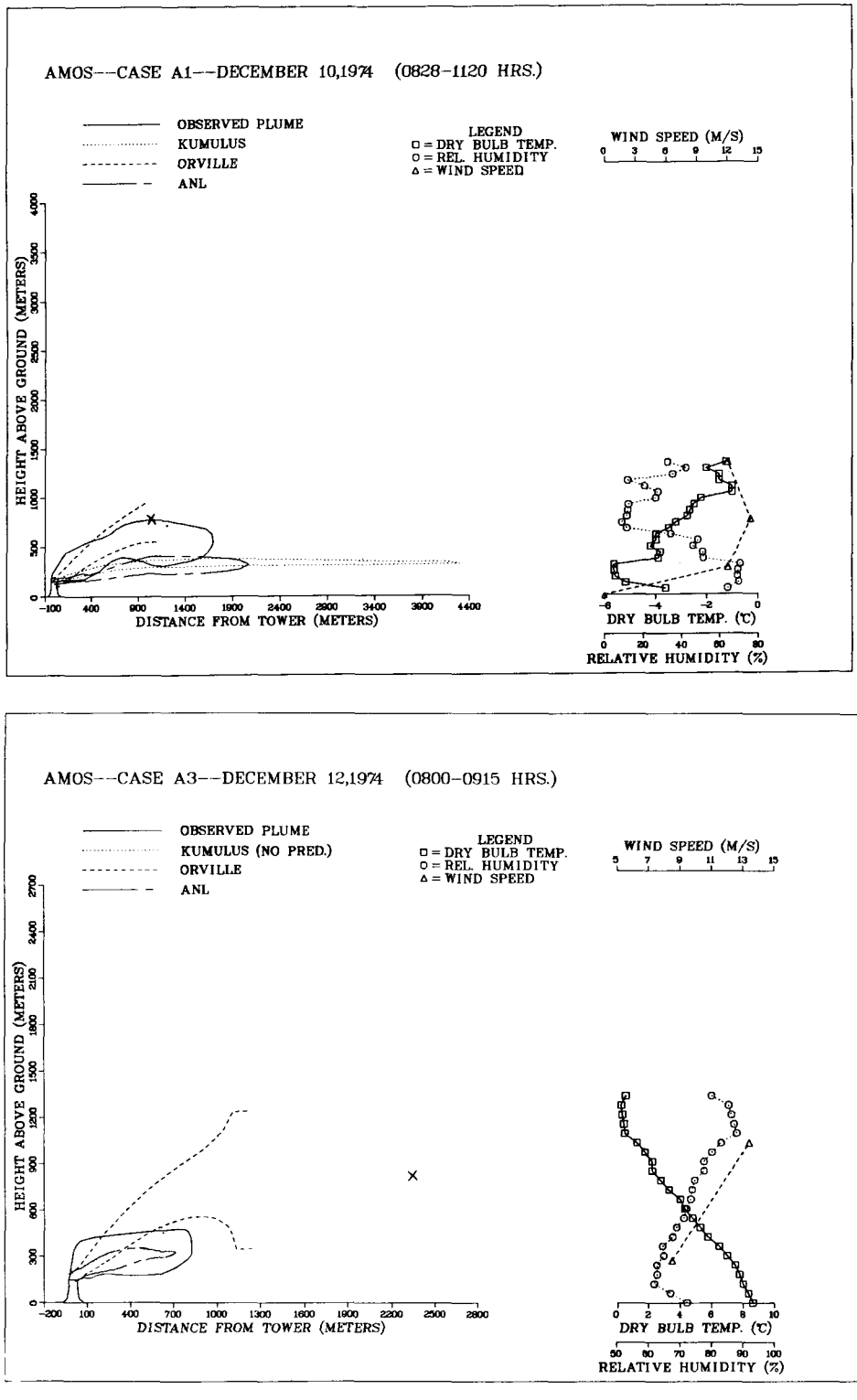

Figure 4-17. Comparison of predictions of KUMULUS, Orville and ANL models to observed visible-plume outlines at Amos: (top) December 10, 1974 (0828-1120 Hrs.), (bottom) December 12, 1974 (0800-0915 Hrs.).

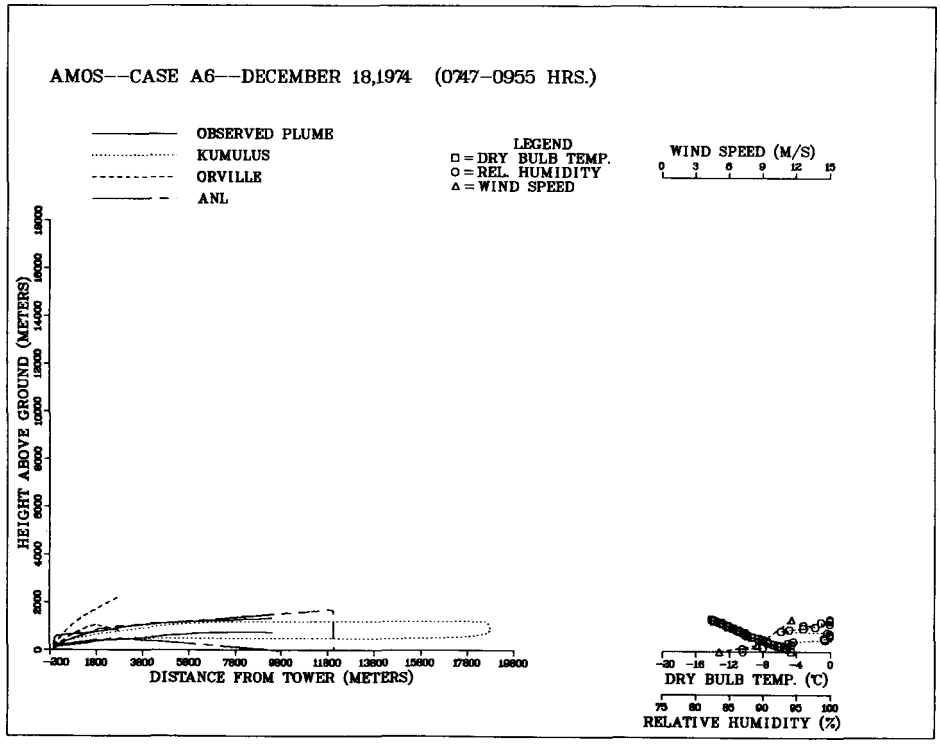

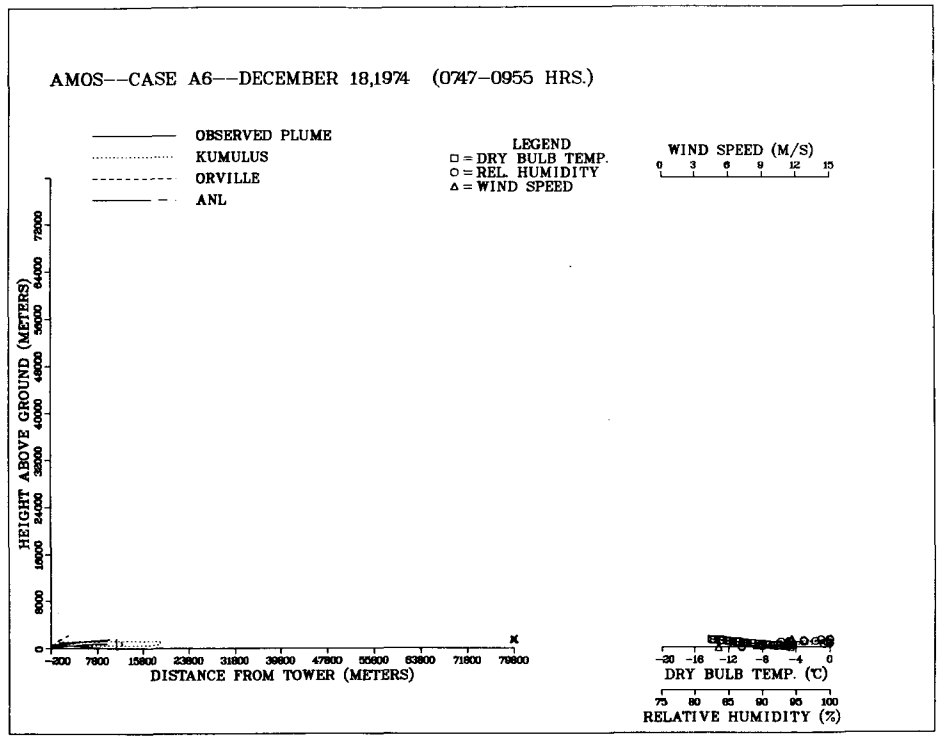

Figure 4-18. Comparison of predictions of KUMULUS, Orville and ANL models to observed visible-plume outlines at Amos: December 18, 1974 (0747-0955 Hrs.).

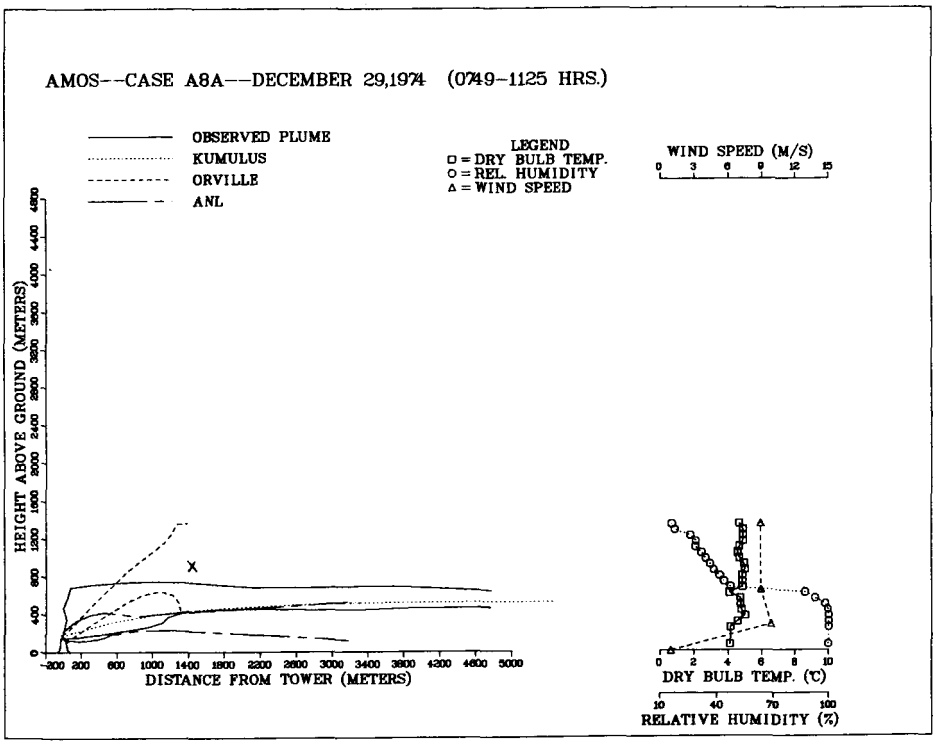

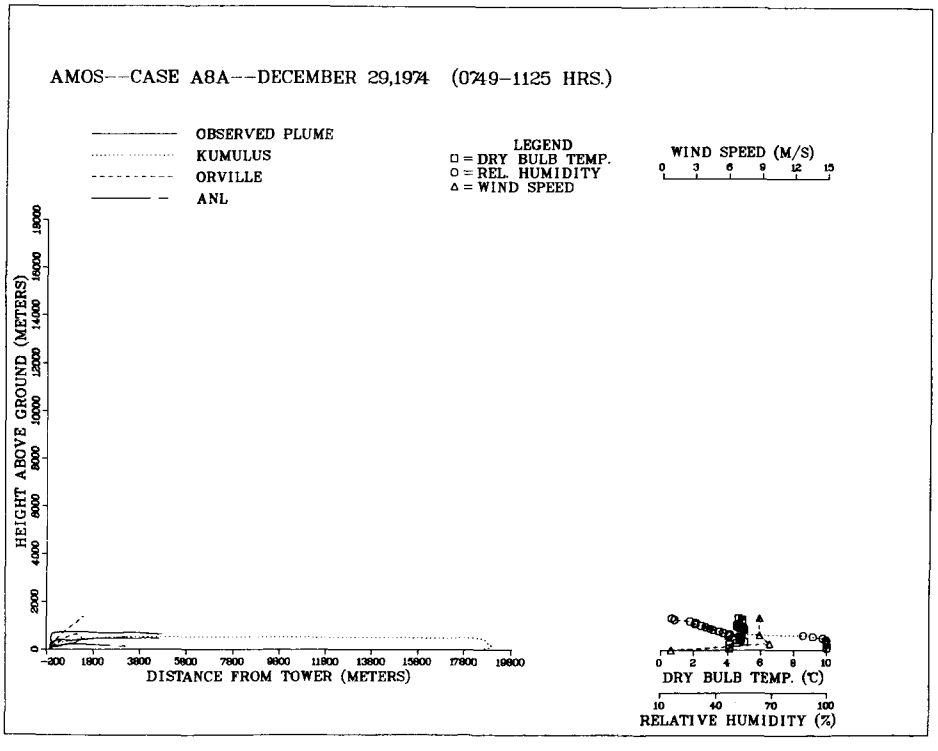

Figure 4-19. Comparison of predictions of KUMULUS, Orville and ANL models to observed visible-plume outlines at Amos: December 29, 1974 (0749-1125 Hrs.).

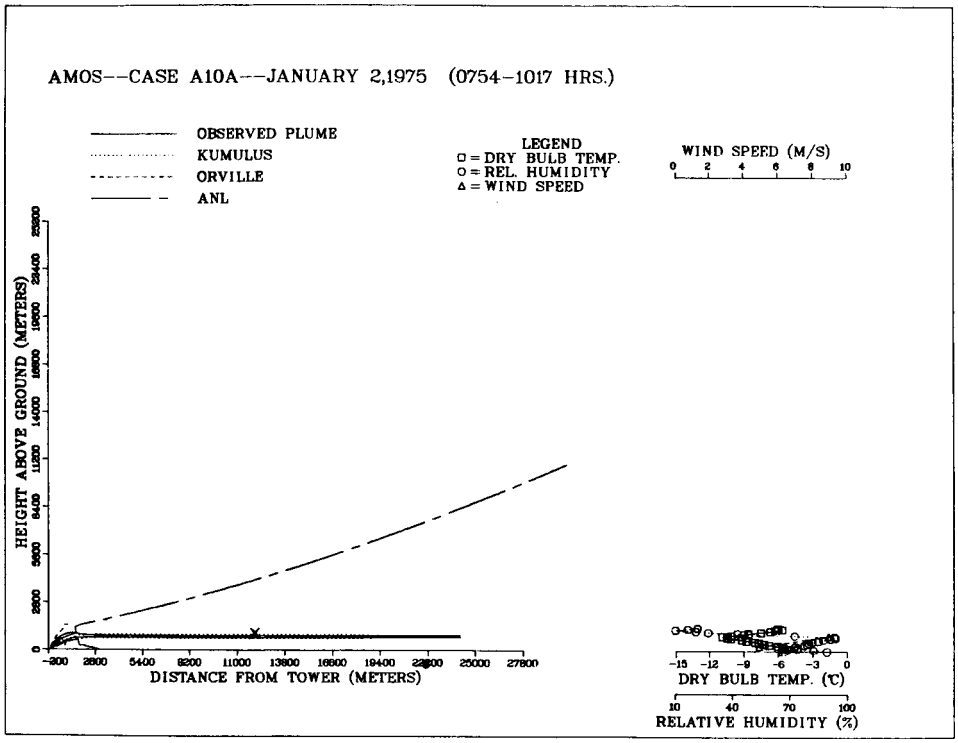

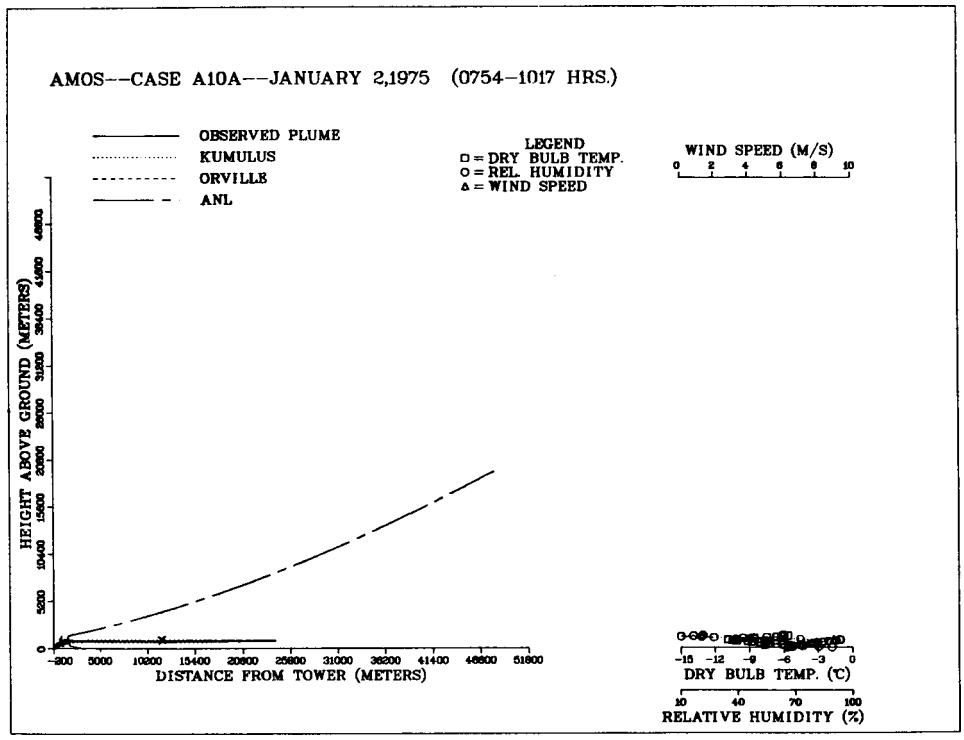

Figure 4-20. Comparison of predictions of KUMULUS, Orville and ANL models to observed visible-plume outlines at Amos: January 2, 1975 (0754-1017 Hrs.).

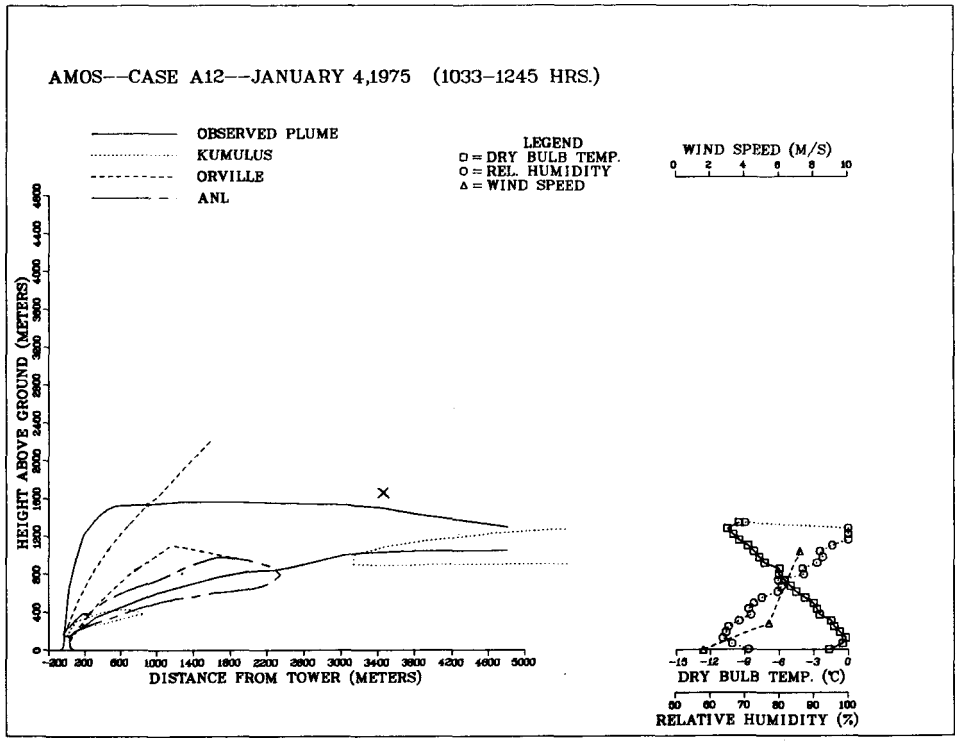

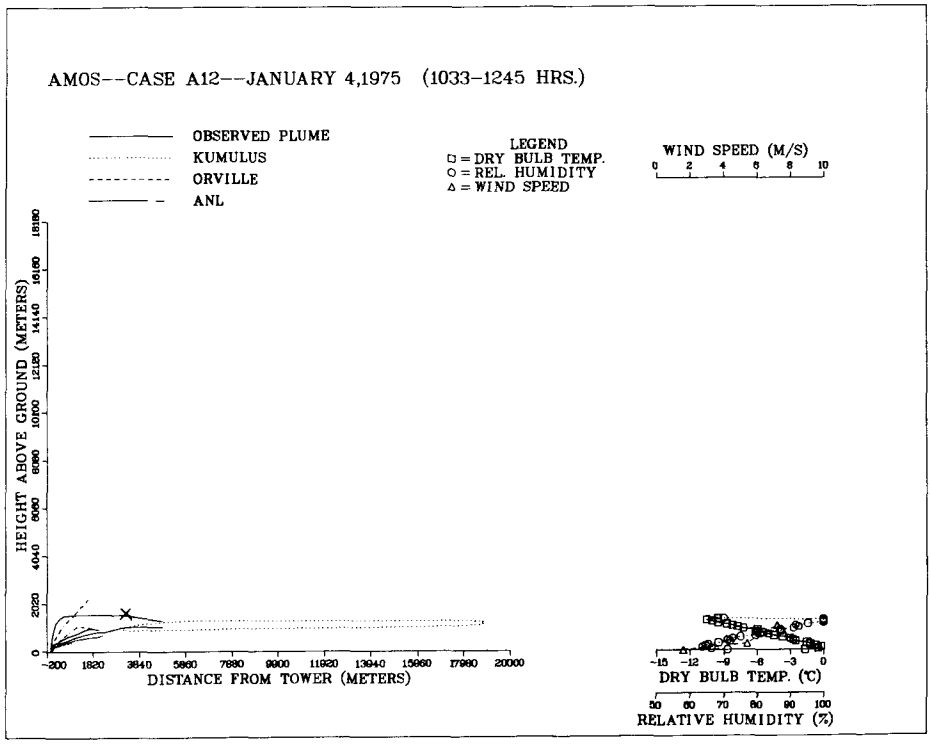

Figure 4-21. Comparison of predictions of KUMULUS, Orville and ANL models to observed visible-plume outlines at Amos: January 4, 1975 (1033-1245 Hrs.).

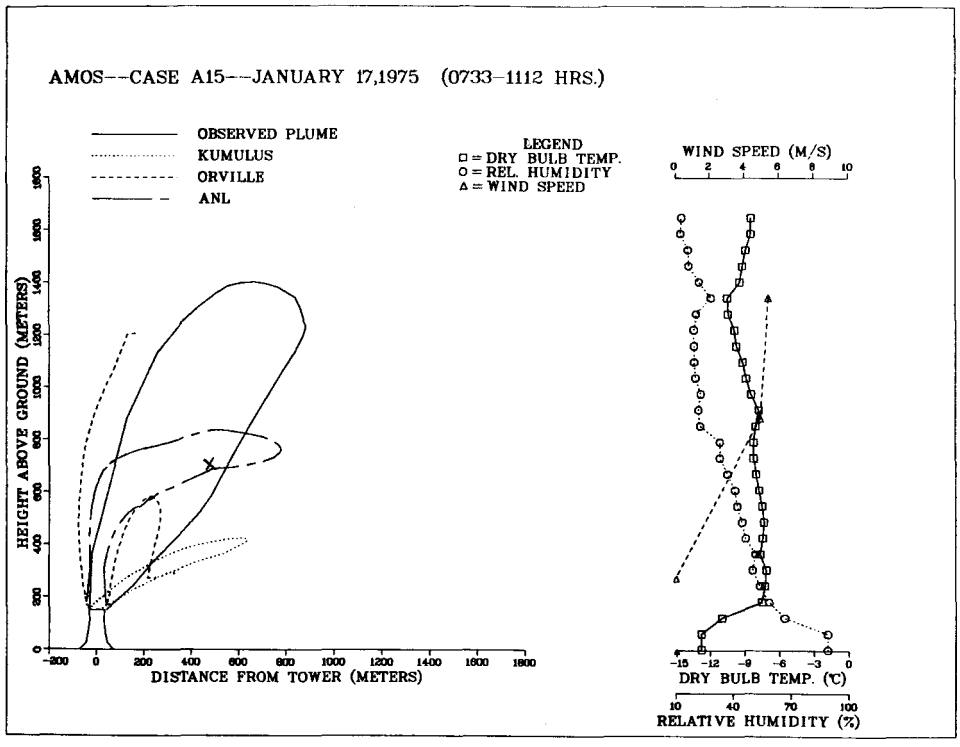

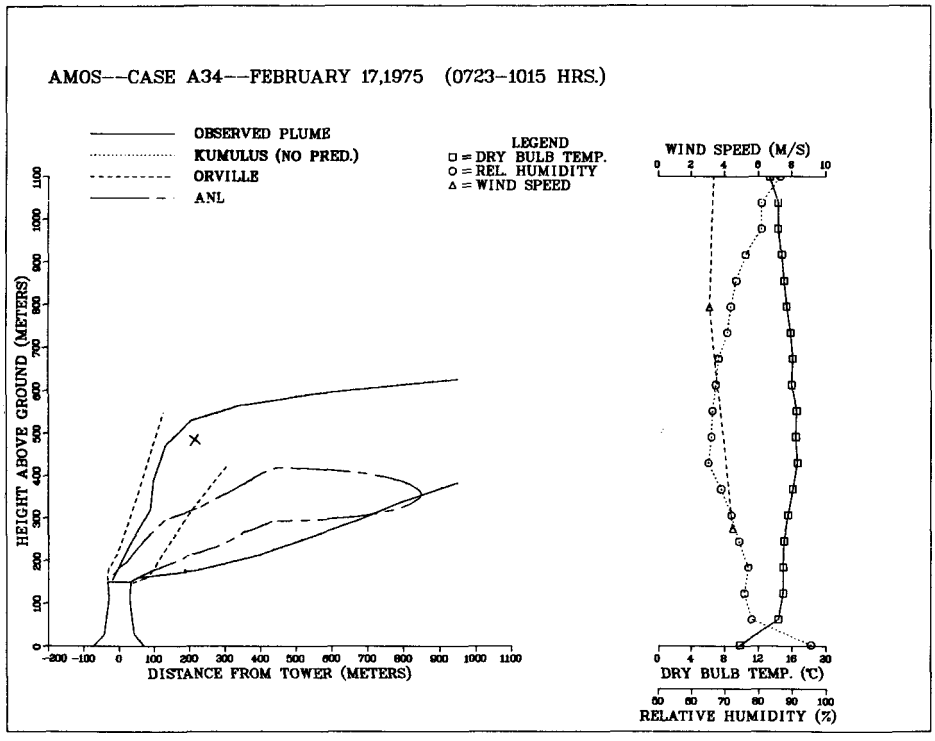

Figure 4-22. Comparison of predictions of KUMULUS, Orville and ANL models to observed visible-plume outlines at Amos: (top) January 17, 1975 (0733-1112 Hrs.), (bottom) February 17, 1975 (0723-1015 Hrs.).

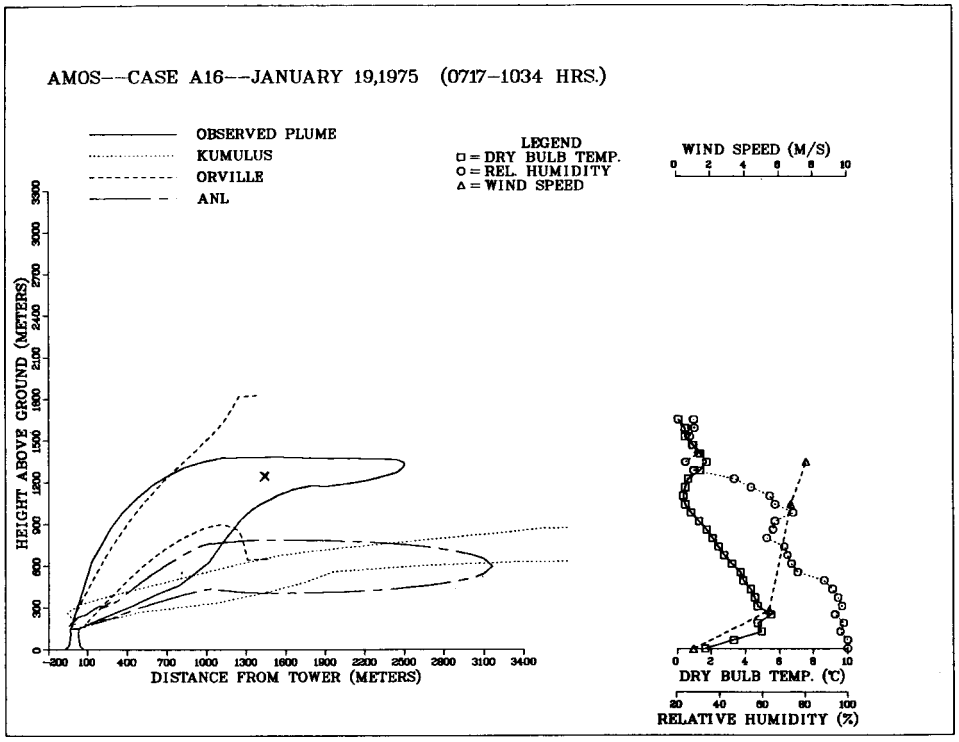

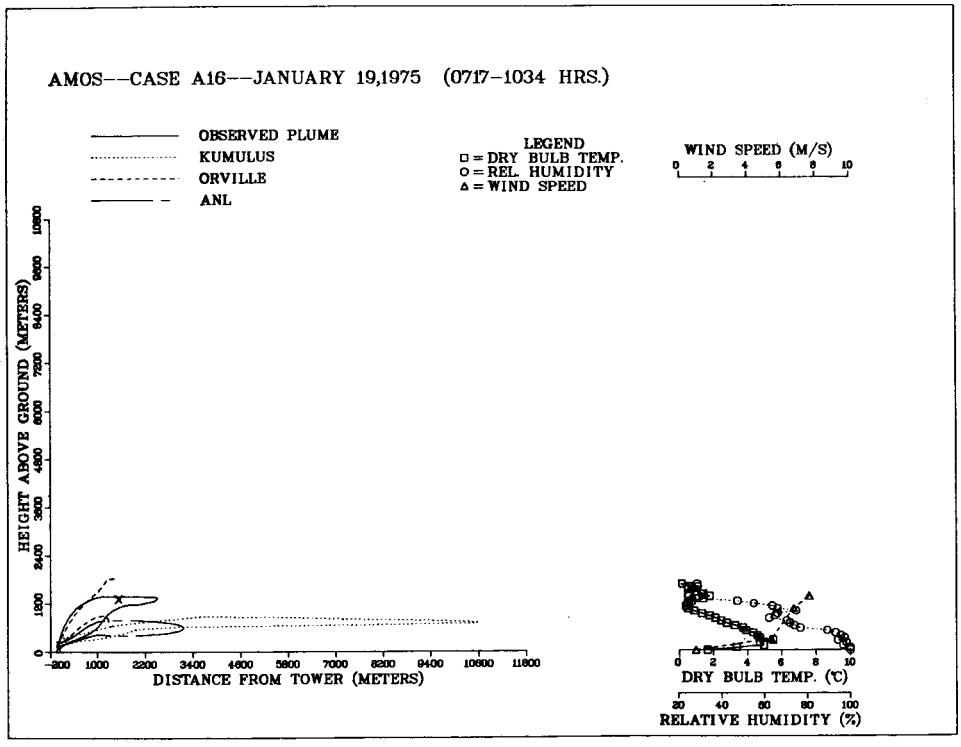

Figure 4-23. Comparison of predictions of KUMULUS, Orville and ANL models to observed visible-plume outlines at Amos: January 19, 1975 (0717-1034 Hrs.).

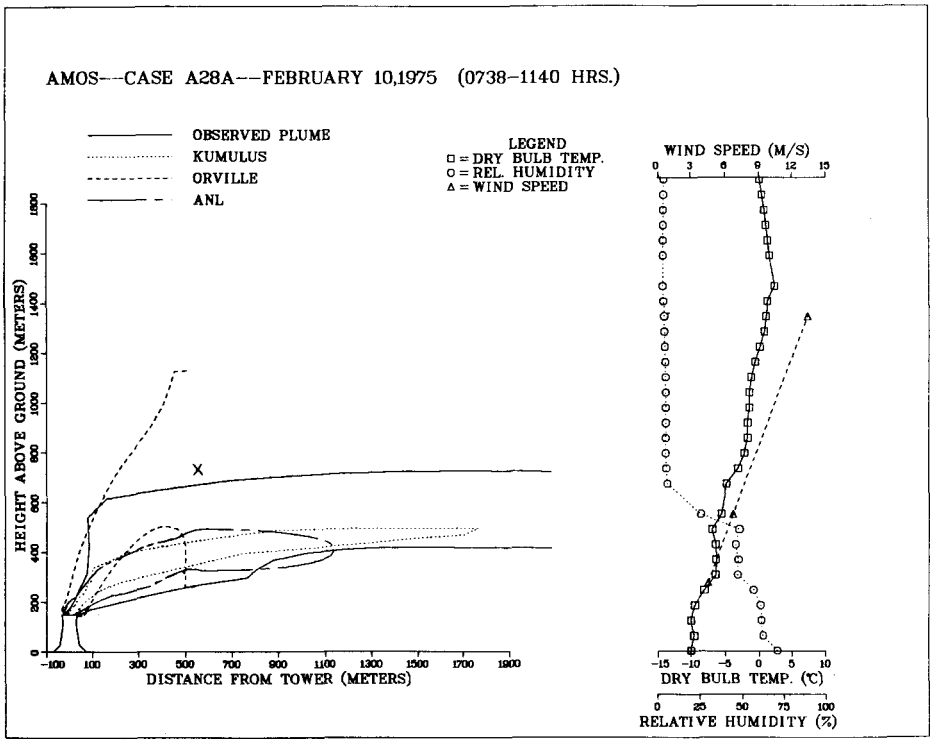

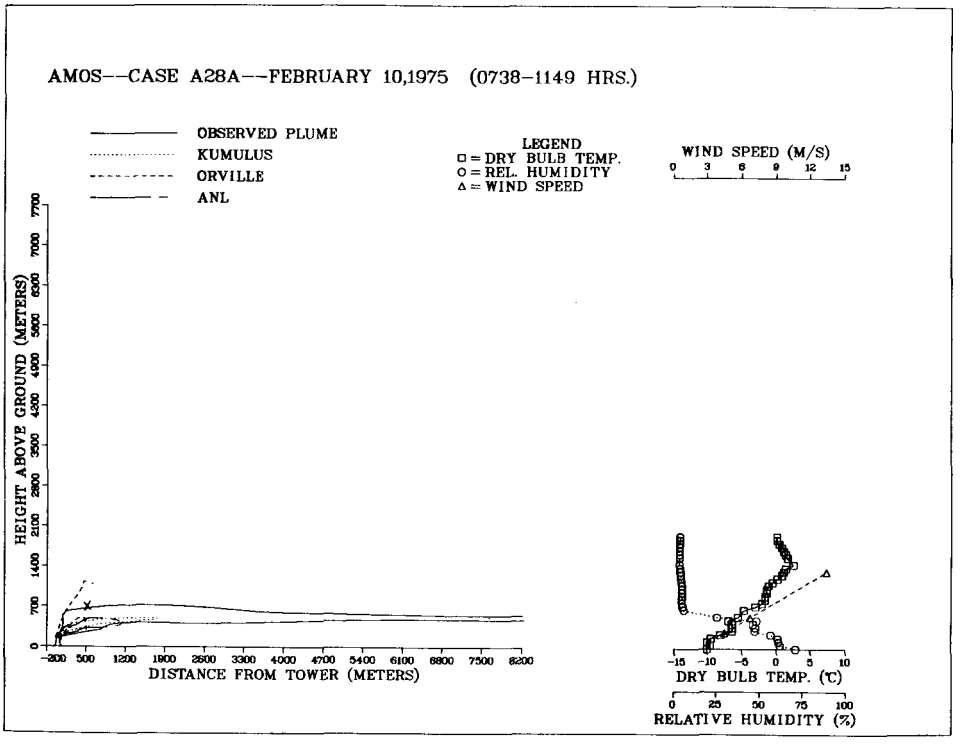

Figure 4-24. Comparison of predictions of KUMULUS, Orville and ANL models to observed visible-plume outlines at Amos: February 10, 1975 (0738-1140 Hrs.).

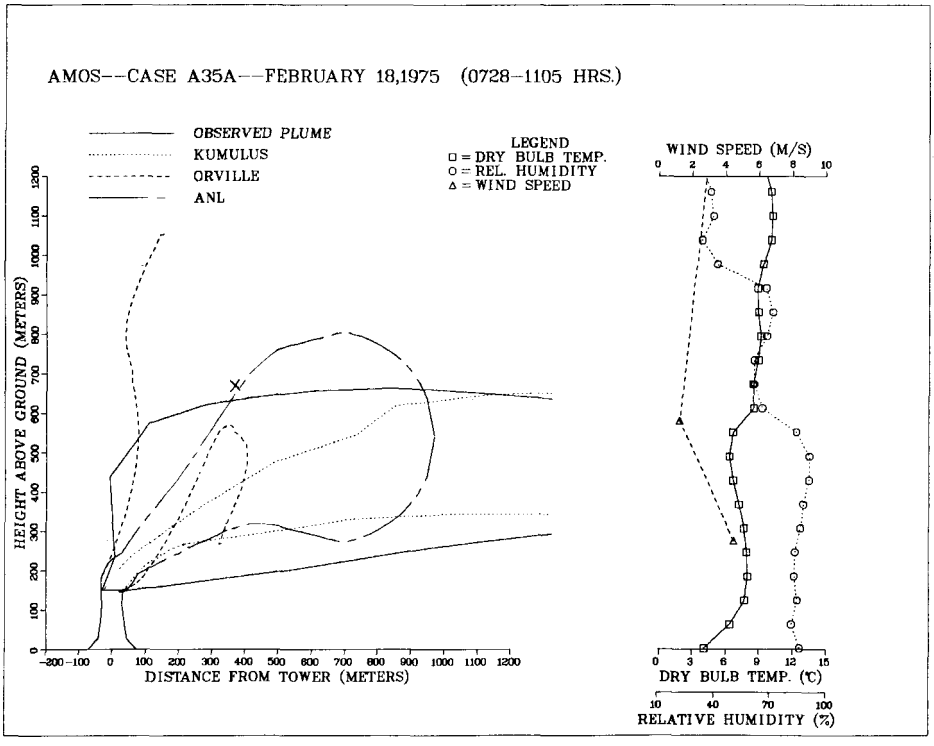

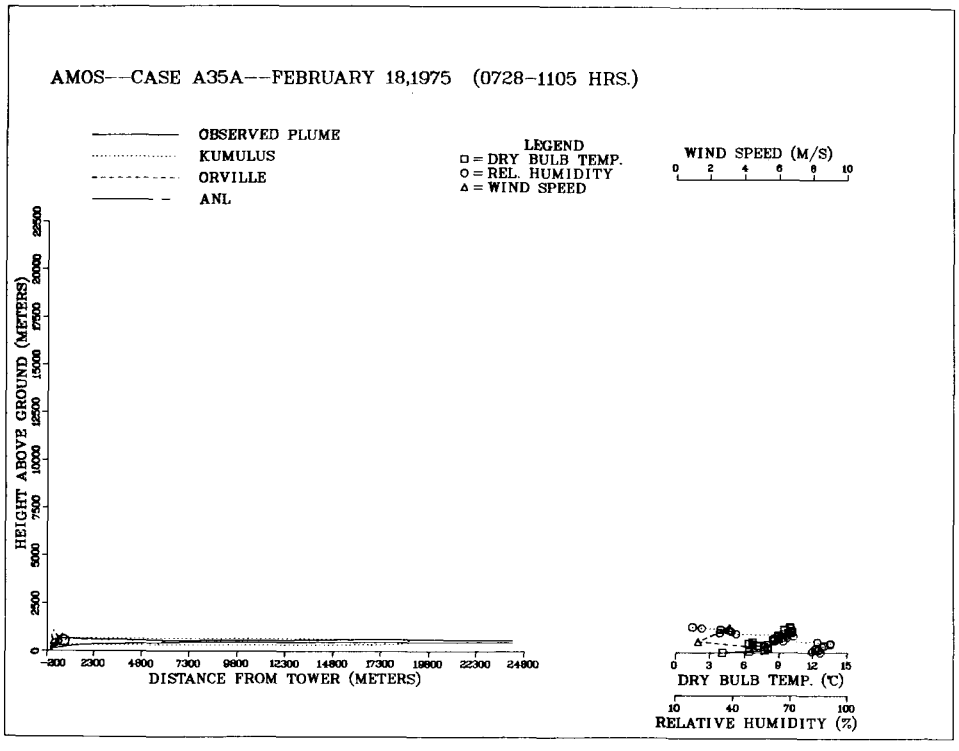

Figure 4-25. Comparison of predictions of KUMULUS, Orville and ANL models to observed visible-plume outlines at Amos: February 18, 1975 (0728-1105 Hrs.).

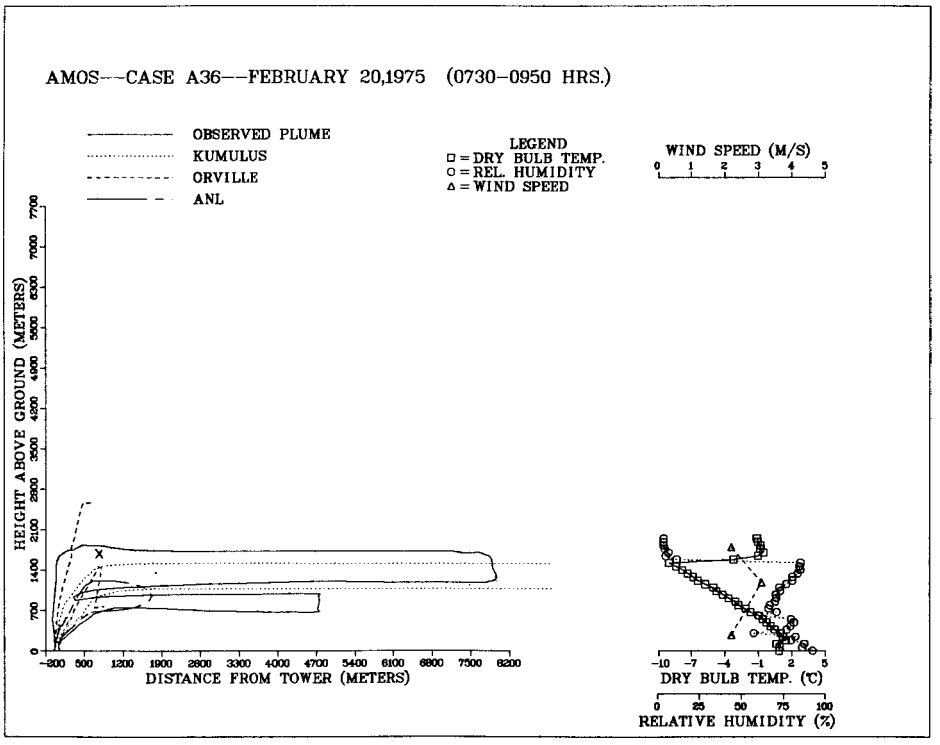

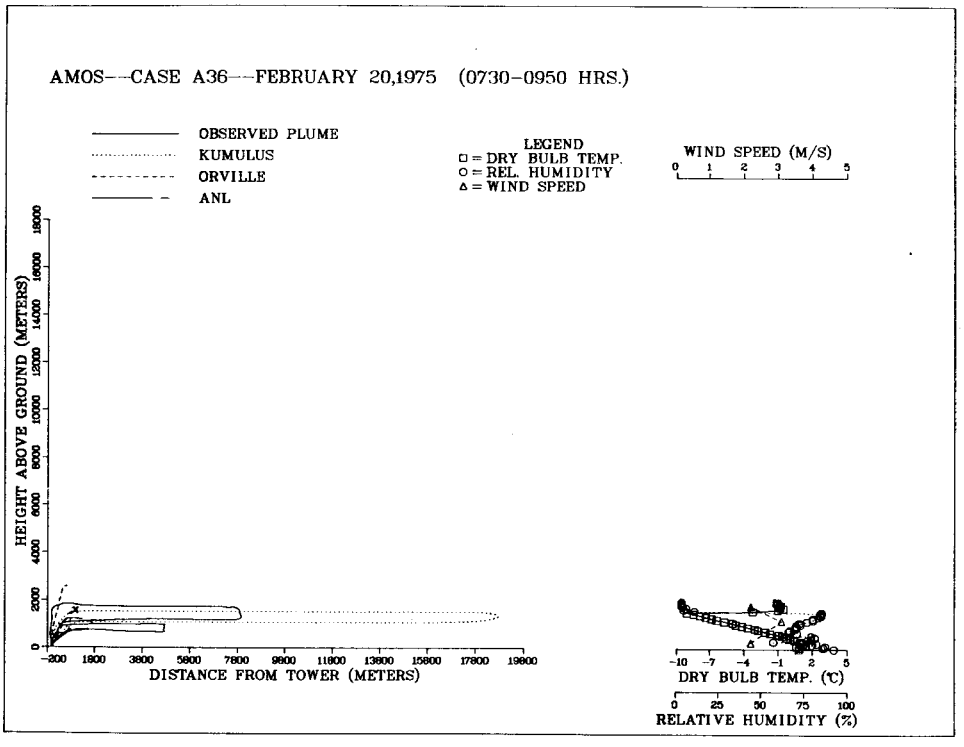

Figure 4-26. Comparison of predictions of KUMULUS, Orville and ANL models to observed visible-plume outlines at Amos: February 20, 1975 (0730-0950 Hrs.).

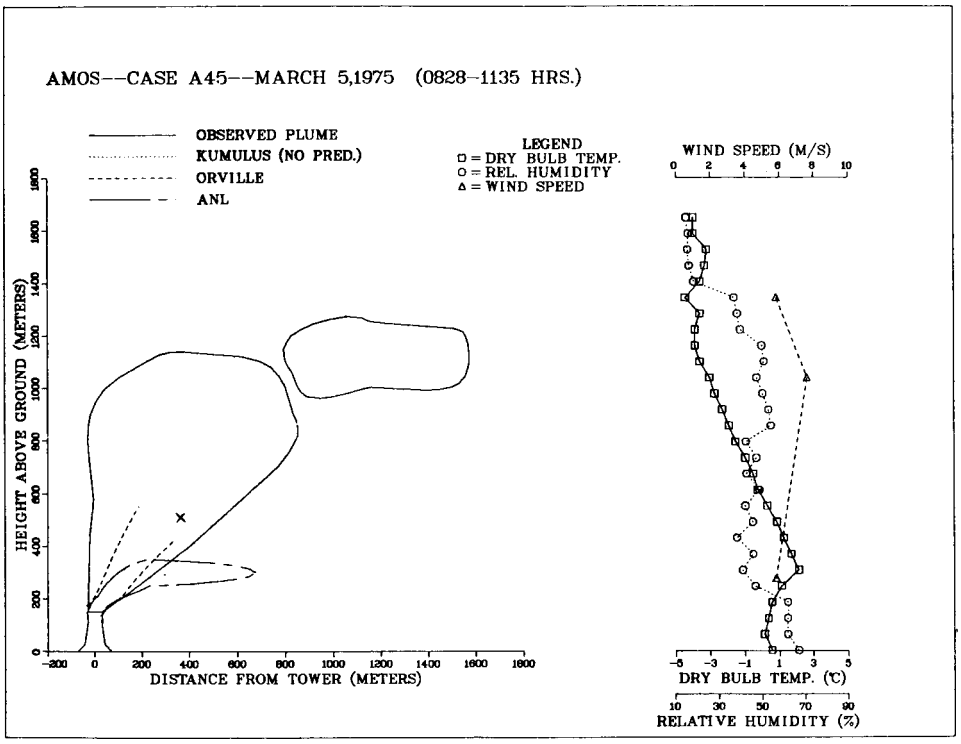

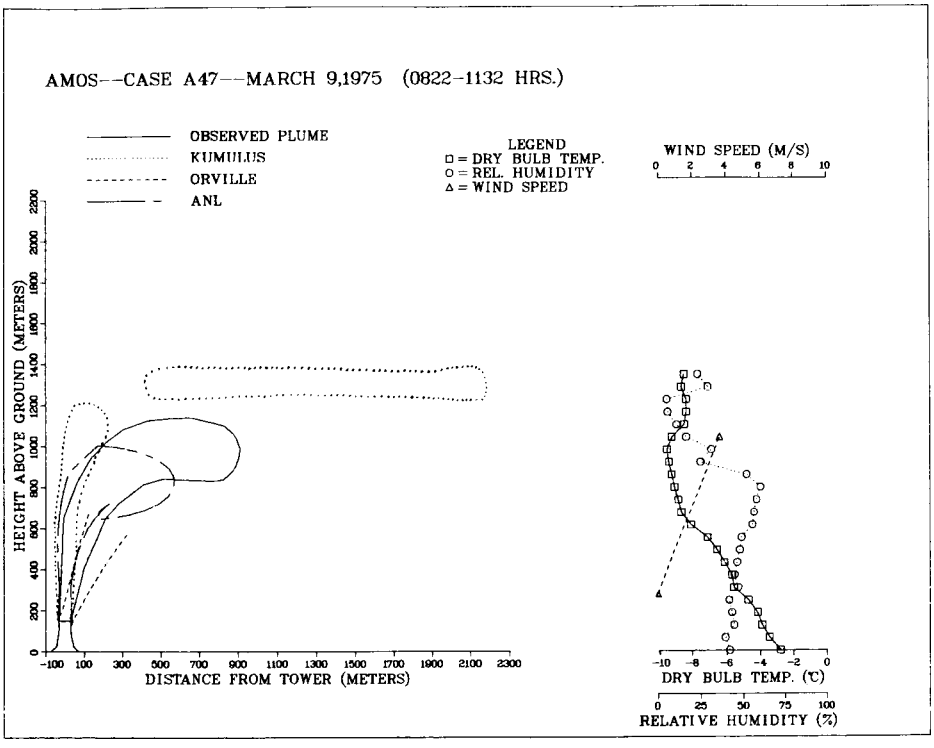

Figure 4-27. Comparison of predictions of KUMULUS, Orville and ANL models to observed visible-plume outlines at Amos: (top) March 5, 1975 (0828-1135 Hrs.), (bottom) March 9, 1975 (0822-1132 Hrs.).

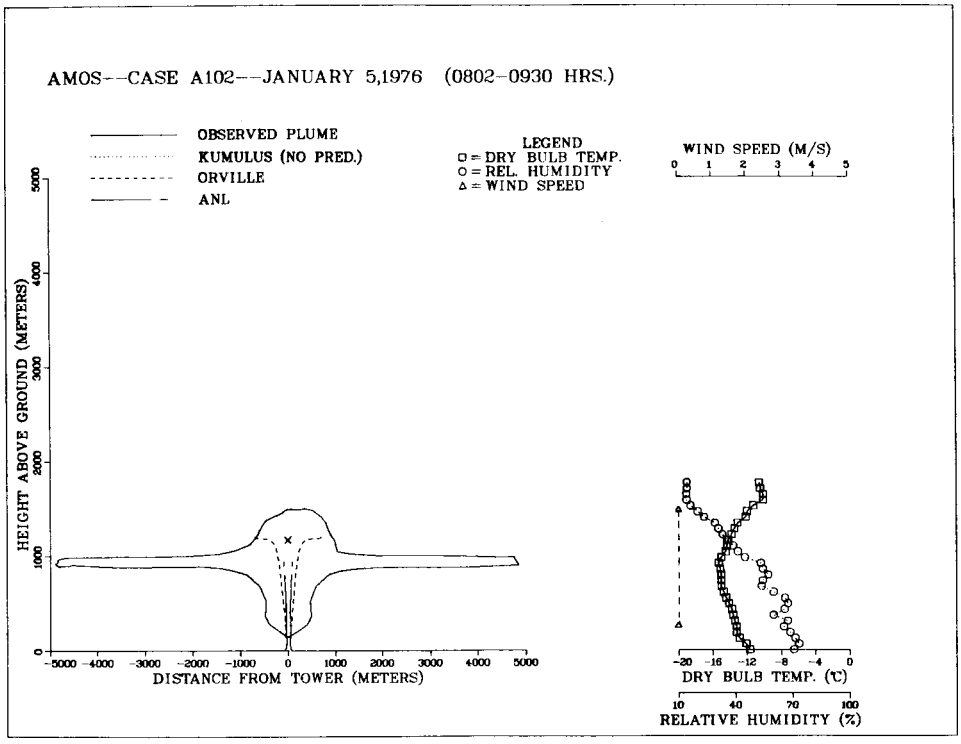

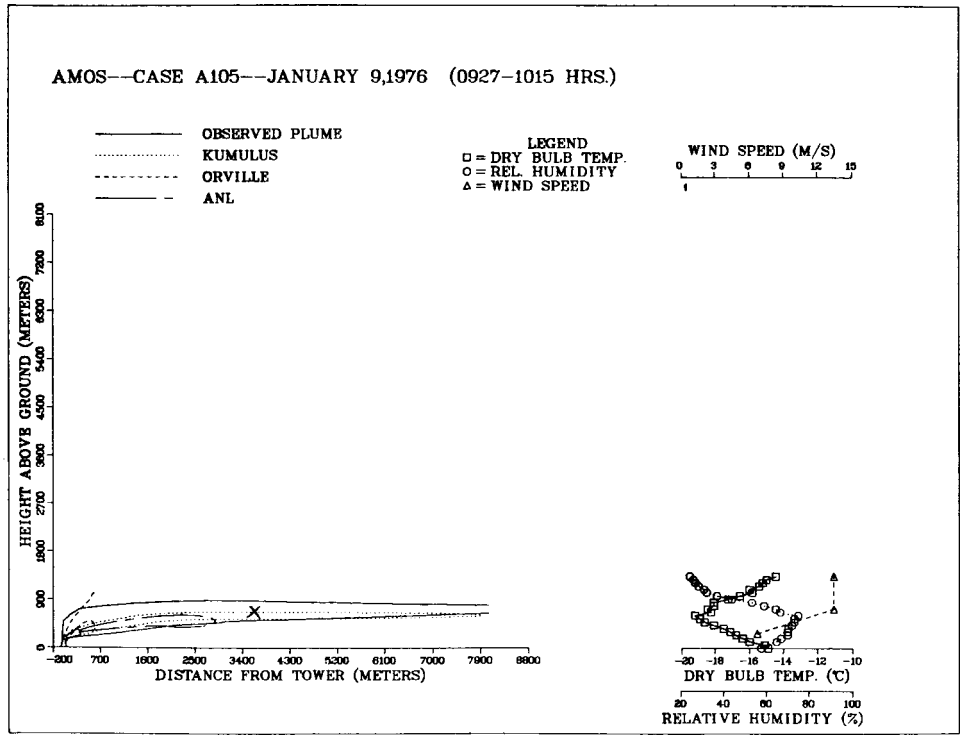

Figure 4-28. Comparison of predictions of KUMULUS, Orville and ANL models to observed visible-plume outlines at Amos: (top) January 5, 1976 (0802-0930 Hrs.), (bottom) January 9, 1976 (0927-1015 Hrs.).

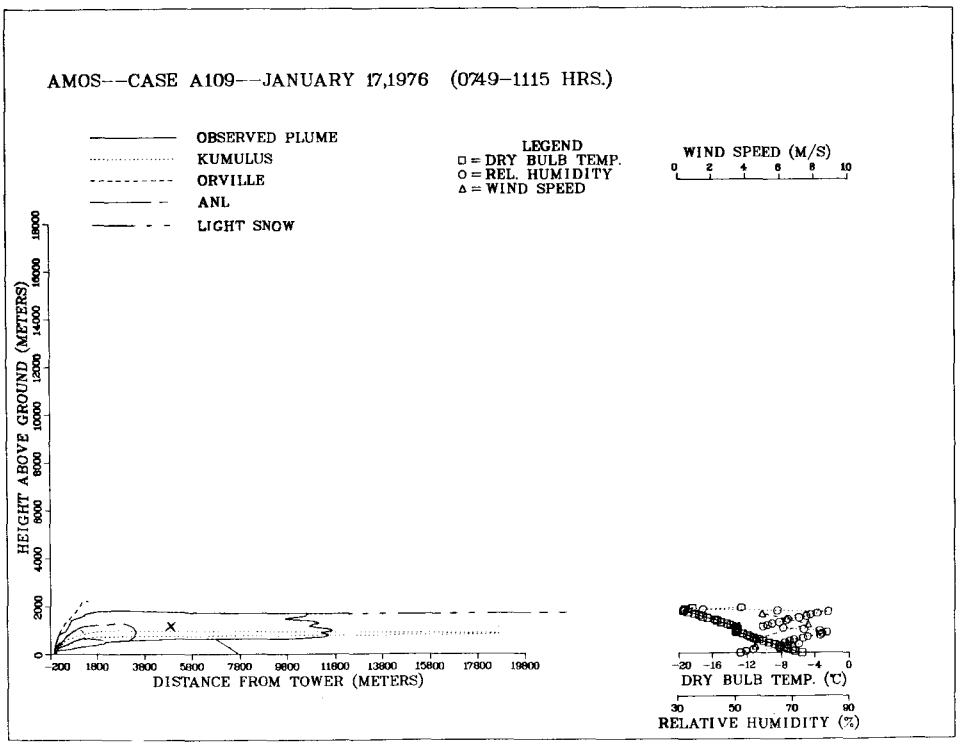

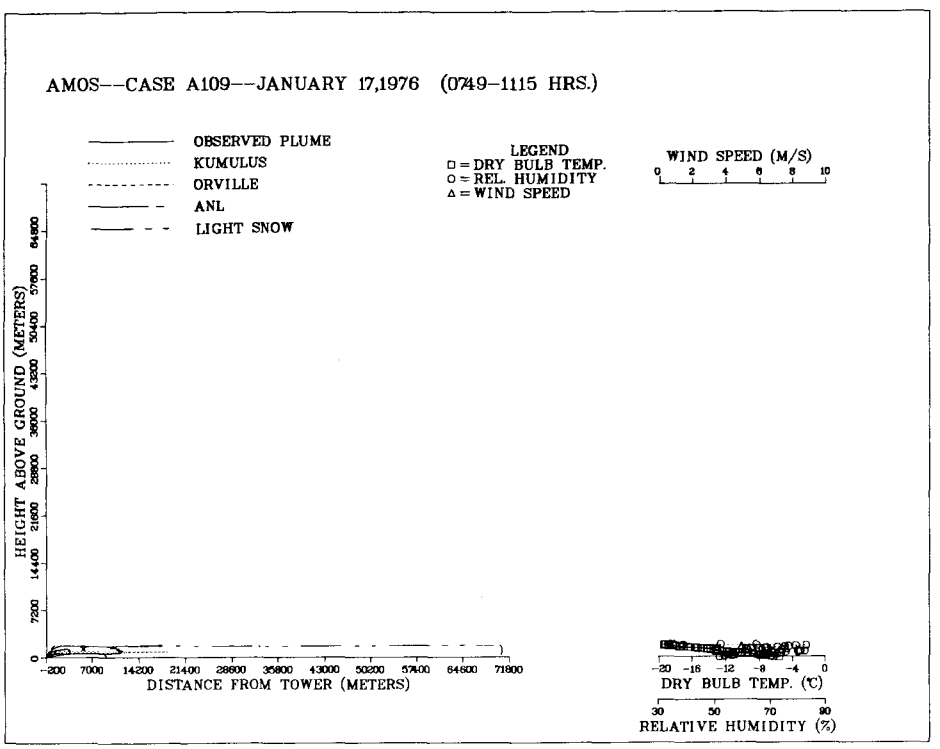

Figure 4-29. Comparison of predictions of KUMULUS, Orville and ANL models to observed visible-plume outlines at Amos: January 17, 1976 (0749-1115 Hrs.).

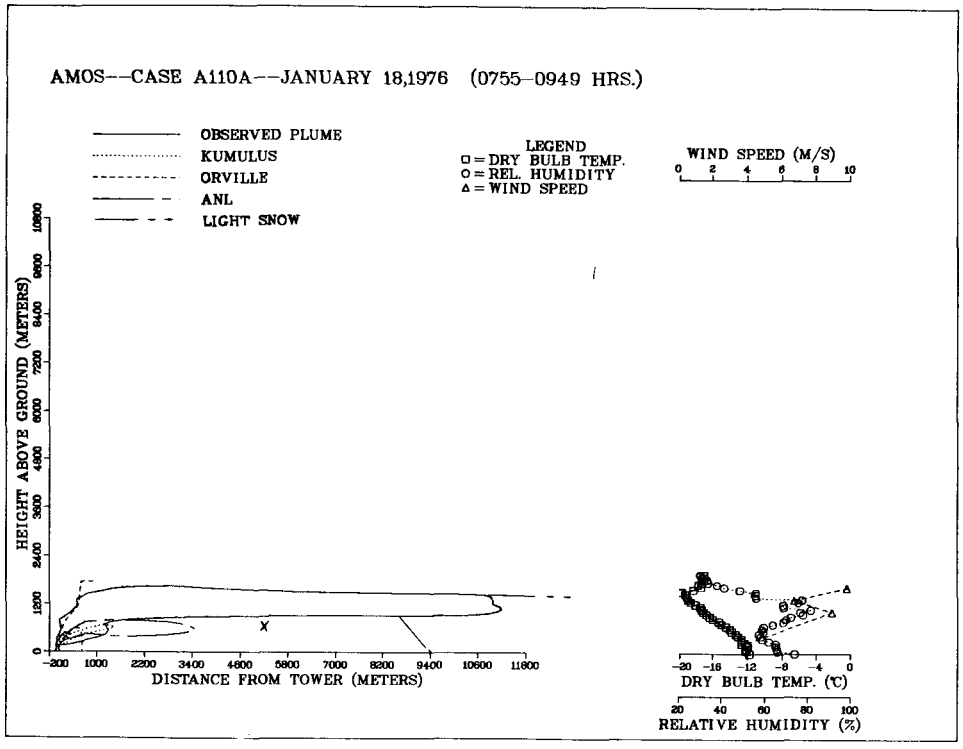

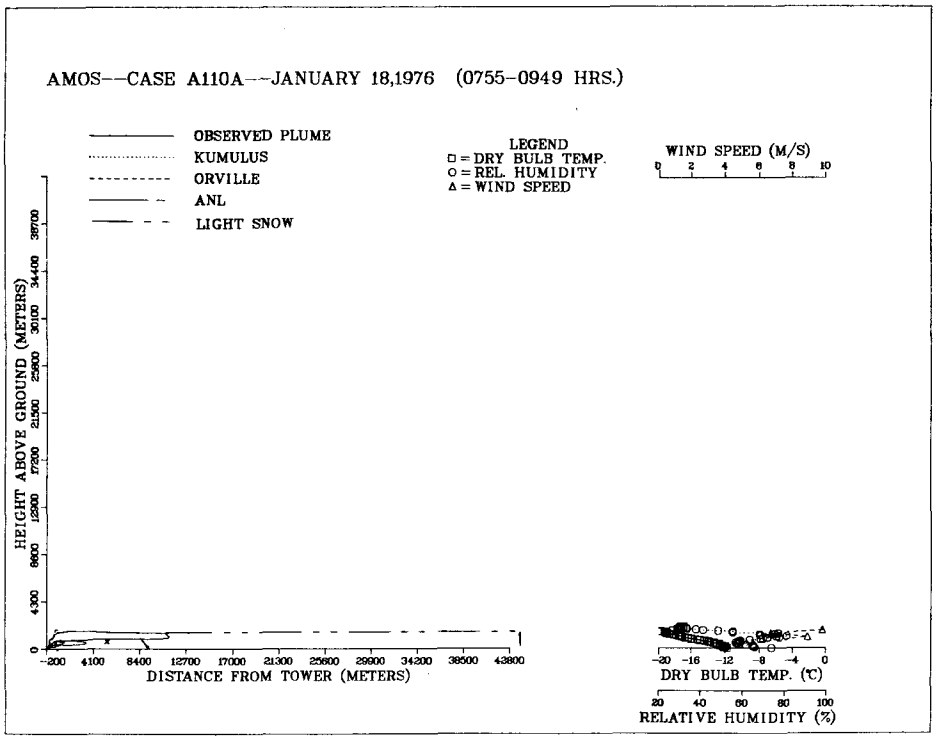

Figure 4-30. Comparison of predictions of KUMULUS, Orville and ANL models to observed visible-plume outlines at Amos: January 18, 1976 (0755-0949 Hrs.).

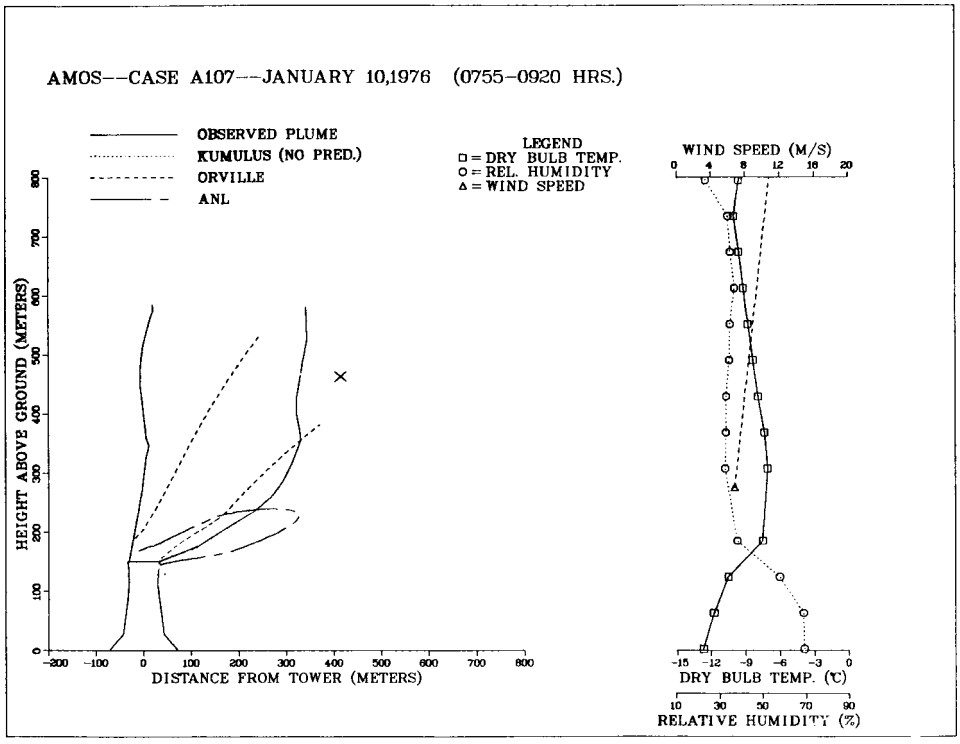

Figure 4-31. Comparison of predictions of KUMULUS, Orville and ANL models to observed visible-plume outlines at Amos: January 10, 1976 (0755-0920 Hrs.).

The final Amos case, A110A (See Figure 4-30), also presents significant snowfall, beginning 9.4 km and ending about 43 km downwind. Again we encounter very low temperatures, below -12°C, moderate winds and low saturation deficits. The stratification is weakly stable, about 0.5°C/100m, and by itself eventually causes the plume to level off. At warmer temperatures, where plume conditional instability would be a factor, the plume would probably continue to rise up to the elevated inversion at 1500 m rather than leveling off at 1200 m. Again adequacy of the wind profile is an issue, because all three models predict trajectories which are too low. All three predicted plumes level off in regions where the saturation deficit is 0.5 gm/ kg, while the saturation deficit at the actual height of final rise is 0.25 gm/kg. In this case the low trajectories, then, lead to short predictions with the KUMULUS Model prediction the shortest, against prior trends. Again Orville and ANL predict glaciation, but no model handles potential snowfall. The need for adequate boundary-layer wind field characterization is emphasized by the sensitivity of model predictions to winds in these high-environmental-impact cases. And clearly, in northern climates the need is great for improved models which handle snowfall prediction well.

FIELD DATA FROM BENNING ROAD (6) (See Figures 4-32 to 4-46)

At the Benning Road plant outside of Washington, D.C., two mechanical draft towers of 8 cells each are arranged side-by-side so that they nearly amount to a single very long and narrow mechanical draft tower of 16 cells along an east-west line (see Table 4-4). Total electric generating capacity cooled is 560 MWe. For most of the measured data cases, only part (or all) of one 8-cell tower was operating. A fairly even balance of wind directions between cross-flow and in-line occur for the ten cases selected out of 22 available to us. Ambient temperatures range from 0°C to 15°C, and most cases exhibit neutral or near-neutral stratification over the observed visible plume-rise region. Wind speeds range generally from 2 to 8 m/s, and saturation deficits from 1 to 5 gm/kg with most cases in the range of 1.5 to 3.0 gm/kg. Ambient profiles of measured variables and associated profiles of mixing ratio and saturation deficit for each case are given between figures of predicted outlines. The plumes are generally fairly short ranging from 100 to 400 meters downwind. Another important possible explanation, which we are investigating further is that our use of the cumulative effect of 12 small plates, one for each cell, to represent the wake effects for the in-line wind orientation strongly overestimates the enhancement of turbulent mixing of the plume near the tower. This would also help explain the underprediction for case 7, as the wind direction is only 10° from the line of the cells in that case.

The first three Benning Road data cases can profitably be considered together, cases 1, 2 and 3 (see Figures 4-32 to 4-35). Over the observed visible plume rise region, all three sets of ambient conditions possess neutral or near-neutral temperature stratification and large saturation deficits. Temperatures are warm for cases 1 and 2 (above 10°C) and colder for case 3 (in the range 0°-5°C). Cases 1 and 2 have wind directions within 5° of pure "cross-flow" with the tower and low windspeeds, while case 3 has a wind direction 37° away from pure "in-line flow" with the tower with moderate wind speed. Considerably more downwash is observed for the plume in case 3 than is seen for cases 1 and 2.

The usual trajectory relationships between the three model-predicted plumes occur. The Orville Model predicts the highest trajectory; the Slawson-Wigley Model predicts the next highest; and the ANL Model predicts the lowest and most accurate trajectory. The inclusion of the downwash effects in the ANL Model helps to explain its trend, particularly for mechanical-draft towers, although the downwash-related vertical force is evidently not strong enough for case 3. The Slawson-Wigley Model predicted plume is extremely short, mainly because the model does not assume the presence of initial liquid water; also, temperatures are relatively warm. The Orville Model visible plume length and rise predictions are good as expected, because the model was calibrated to the Benning Road data. However, the ANL Model achieves factor-of-two accuracy for visible length and rise, despite its being calibrated to other data. None of the three models correctly predicts the full lateral extent of the observed visible plume, especially farther from the tower. Another pair of cases which yield an interesting contrast are cases 5 and 6 (see Figures 4-35 to 4-38). Both show large saturation deficits and neutral temperature stratification, but case 5 is a low wind case in a cross-flow orientation, while case 6 is a high wind case nearly with the wind directed 45° from both cross-flow and in-line wind directions. Some evidence from bluff-body wake studies suggest that the wake behind an obstacle is actually greater in extent and "strength" for directions other than pure cross-flow, until the wind direction approaches in-line. However, the tower structure is long and narrow, and the wind 50° from cross-flow (40° from in-line); we expect wake effects comparable to or somewhat less than those for pure cross-flow. The Orville Model predictions are good for both cases; the Slawson-Wigley Model predicts plumes which are very short; the ANL Model yields an excellent prediction for case 6. However, for case 5, the ANL Model predicts a very limited plume, while the actual plume is much longer and higher. The very large saturation deficit seems to be responsible, and its effect is enhanced by the effects of plume merging. In the model run, only

4 of the 8 cells merged before disappearance, while from the observed outline, clearly all merge. Thus, the reduced surface area and lessened relative entrainment of a fully merged plume is not attained by the model prediction.

In Benning Road case 7 (see Figure 4-38), conditions occur which favor a large visible plume. Ambient windspeed is low, temperature stratification is neutral (enhancing effects of moisture-related instabilities), and saturation deficit is moderate (about 1.75 gm/kg). The wind direction is nearly in-line, leading to relatively less wake effect. Both the Orville and ANL Models give reasonable predictions for this case, both being somewhat short.

As a departure from the first 5 cases with largely neutral stratifications over the plume rise region, we turn to case 14 (see Figure 4-41), which shows a strong ground inversion. The isolated puff at the end of the plume, however, occurs in a region with neutral stratification, above the inversion. Ambient deficits are moderate, as are winds; and the wind direction is in-line. All three models underpredict the plume; the Slawson-Wigley and ANL Models do so strongly, and the Orville Model does so moderately. In the ANL Model prediction, only 5 of 8 plumes have merged before evaporation occurs, which partly explains the marked underprediction given.

The following case, case 16 (see Figure 4-41), also has a nearly in-line wind direction. It is similar except for ambient stratification level to the previous case, but here all three models predict longer plumes. Significant amounts of plume conditional and ambient latent instability probably accounts for the much longer predictions for models in this case or compared with case 14. The ANL and Orville model predictions are quite accurate, while the Slawson-Wigley model prediction is short and low by more than a factor of two.

For the Benning Road model/data comparisons shown in this section, the first significant overprediction by the ANL model occurs for case 18 in Figure 4-44. The wind direction for this case is 20° from cross-flow, stratification is near-neutral with temperatures around 8°C, wind speeds are high and saturation deficits are large. The tendency of the ANL model to underdilute in high winds is undoubtedly a major factor in its overprediction, as is the decrease to 2 gm/kg of the saturation deficit at the level of the inversion. This inversion level blocks further rise of the predicted plume (160 m). The Orville model yields a good prediction, while the Slawson-Wigley model gives, again, a very short predicted plume.

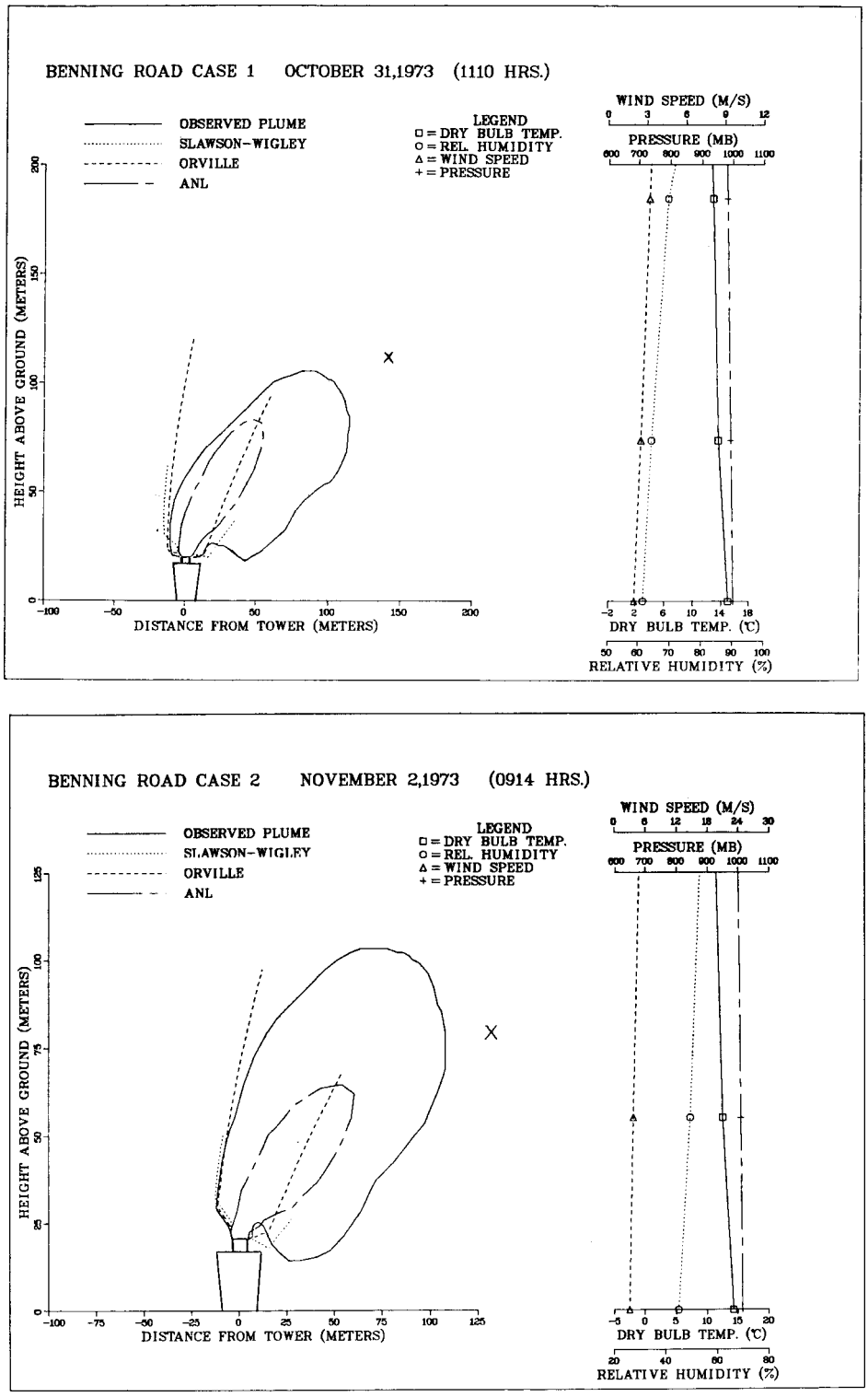

Figure 4-32. Comparison of predictions of Slawson-Wigley, Orville and ANL models to observed visible-plume outlines at Benning Road: (top) October 31, 1973 (1110 Hrs.), (bottom) November 2, 1973 (0914 Hrs.).

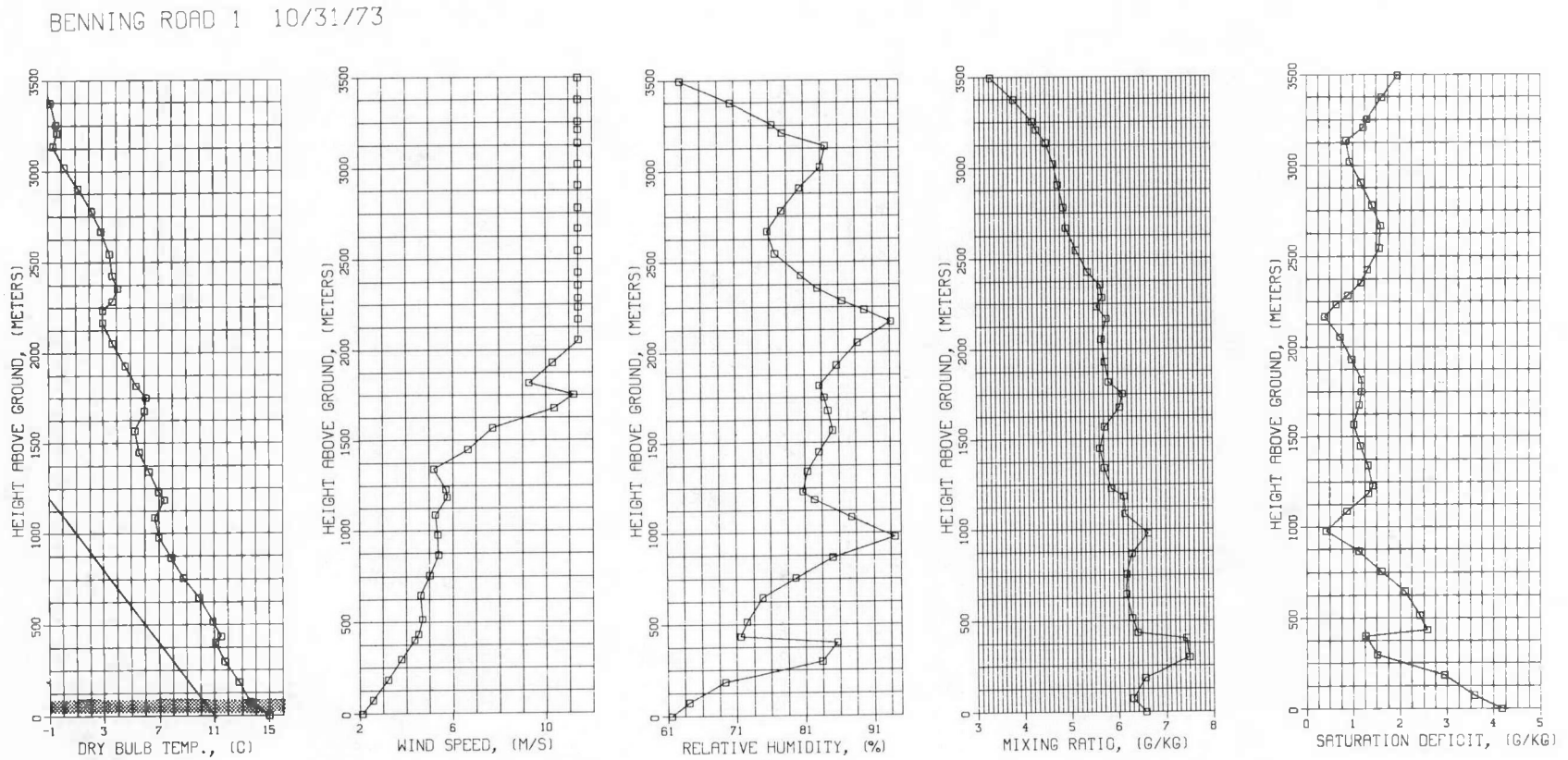

Figure 4-33. Ambient profiles of measured dry-bulb temperature, wind speed and relative humidity along with associated profiles of mixing ratio and saturation deficit . . . Benning Road Case 1. 10/31/73 (1110 Hrs.).

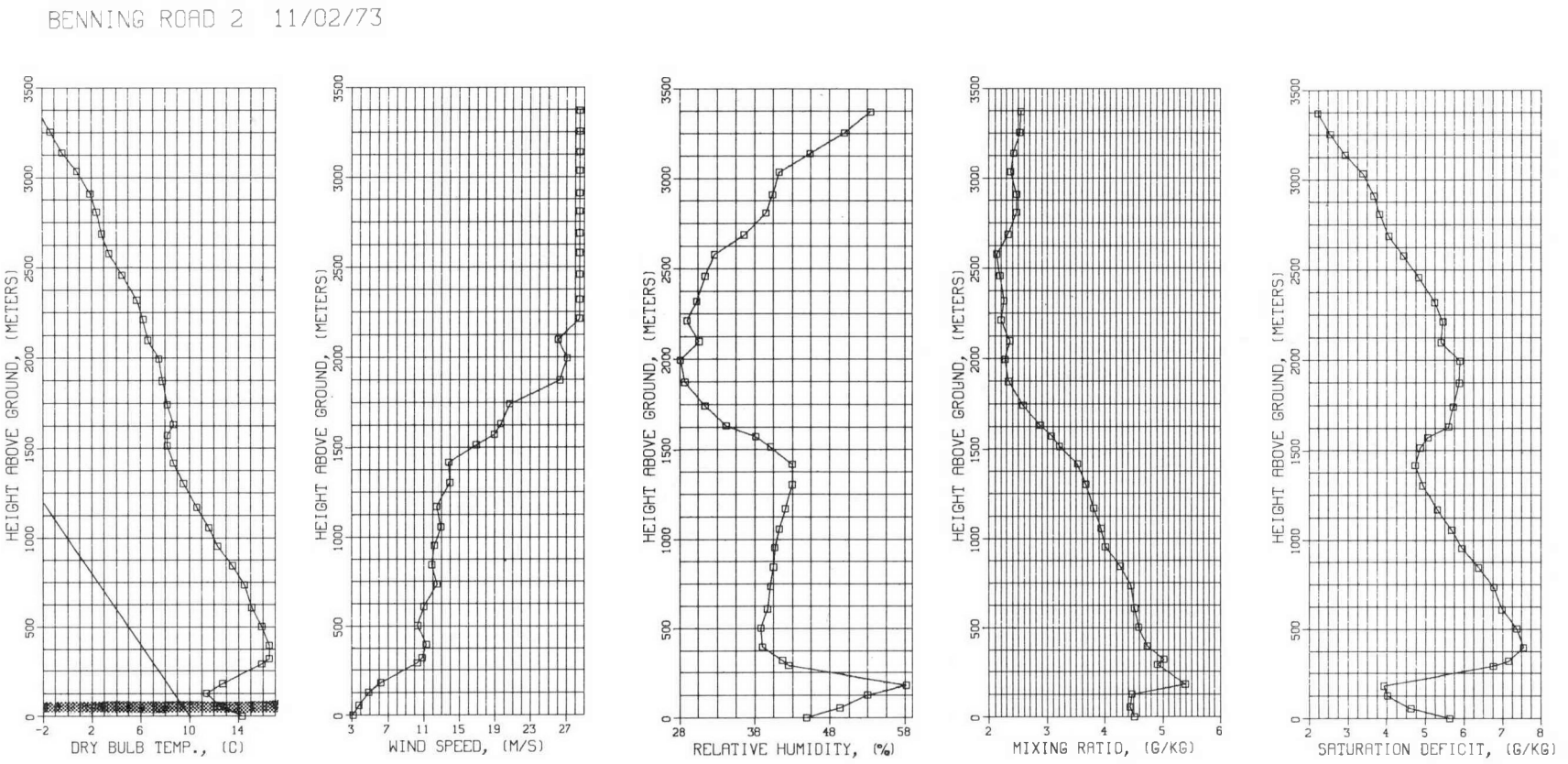

Figure 4-34. Ambient profiles of measured dry-bulb temperature, wind speed and relative humidity along with associated profiles of mixing ratio and saturation deficit . . . Benning Road Case 2. 11/2/73 (0914 Hrs.).

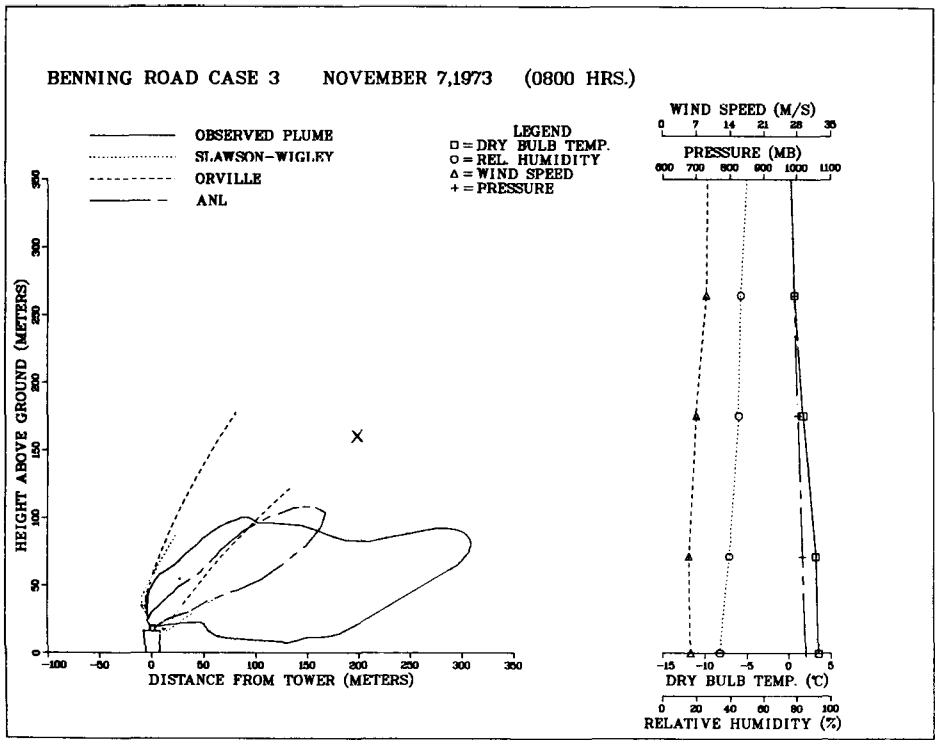

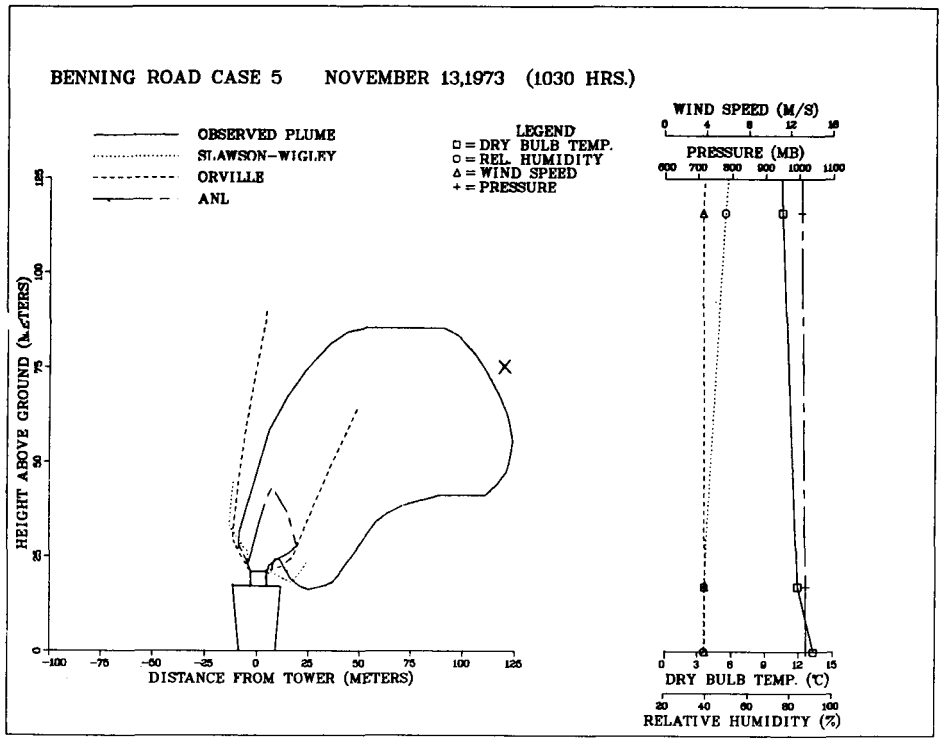

Figure 4-35. Comparison of predictions of Slawson-Wigley, Orville and ANL models to observed visible-plume outlines at Benning Road: (top) November 7, 1973 (0800 Hrs.), (bottom) November 13, 1973 (1030 Hrs.).

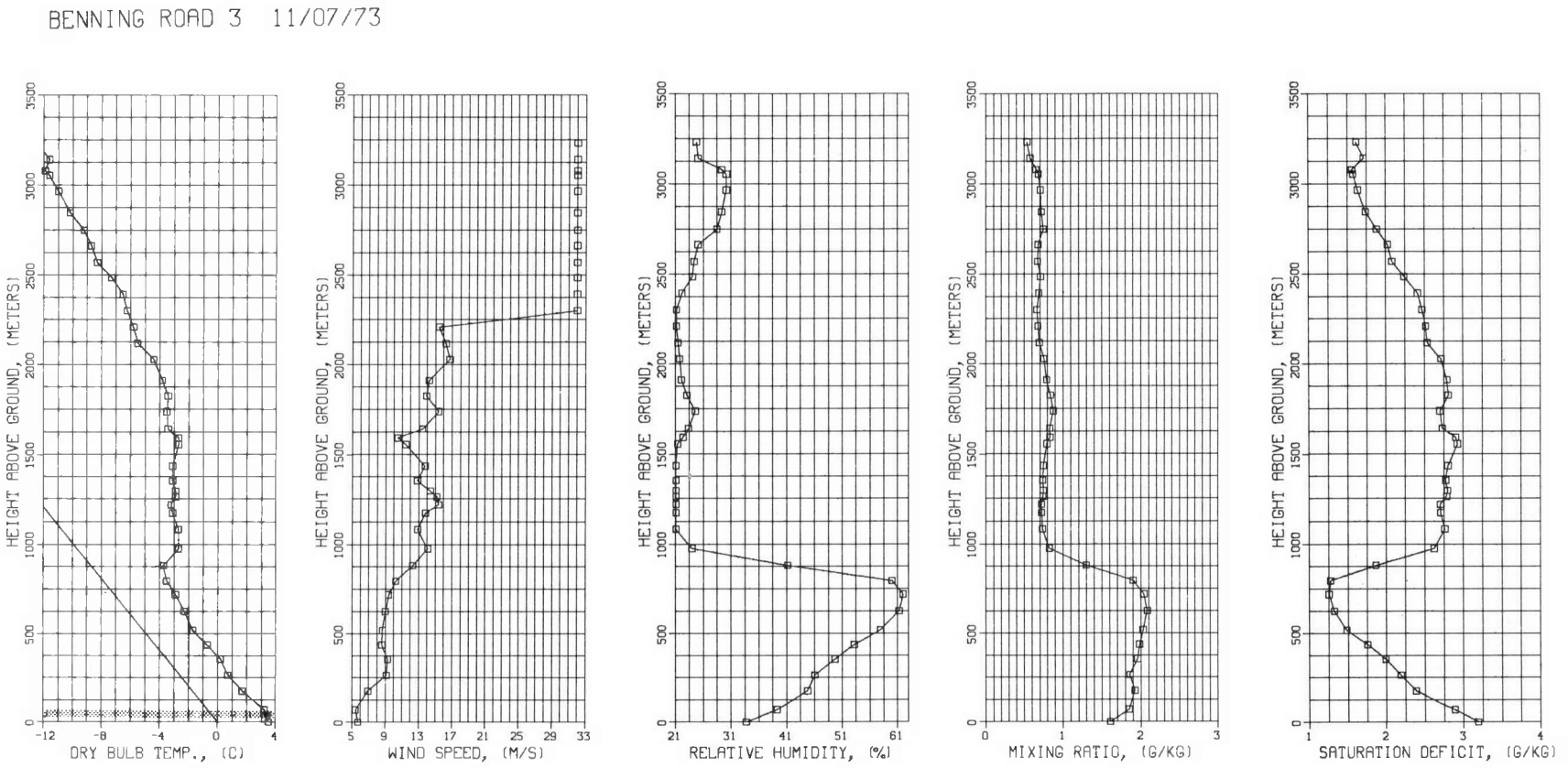

Figure 4-36. Ambient profiles of measured dry-bulb temperature, wind speed and relative humidity along with associated profiles of mixing ratio and saturation deficit . . . Benning Road Case 3. 11/7/73 (0800 Hrs.).

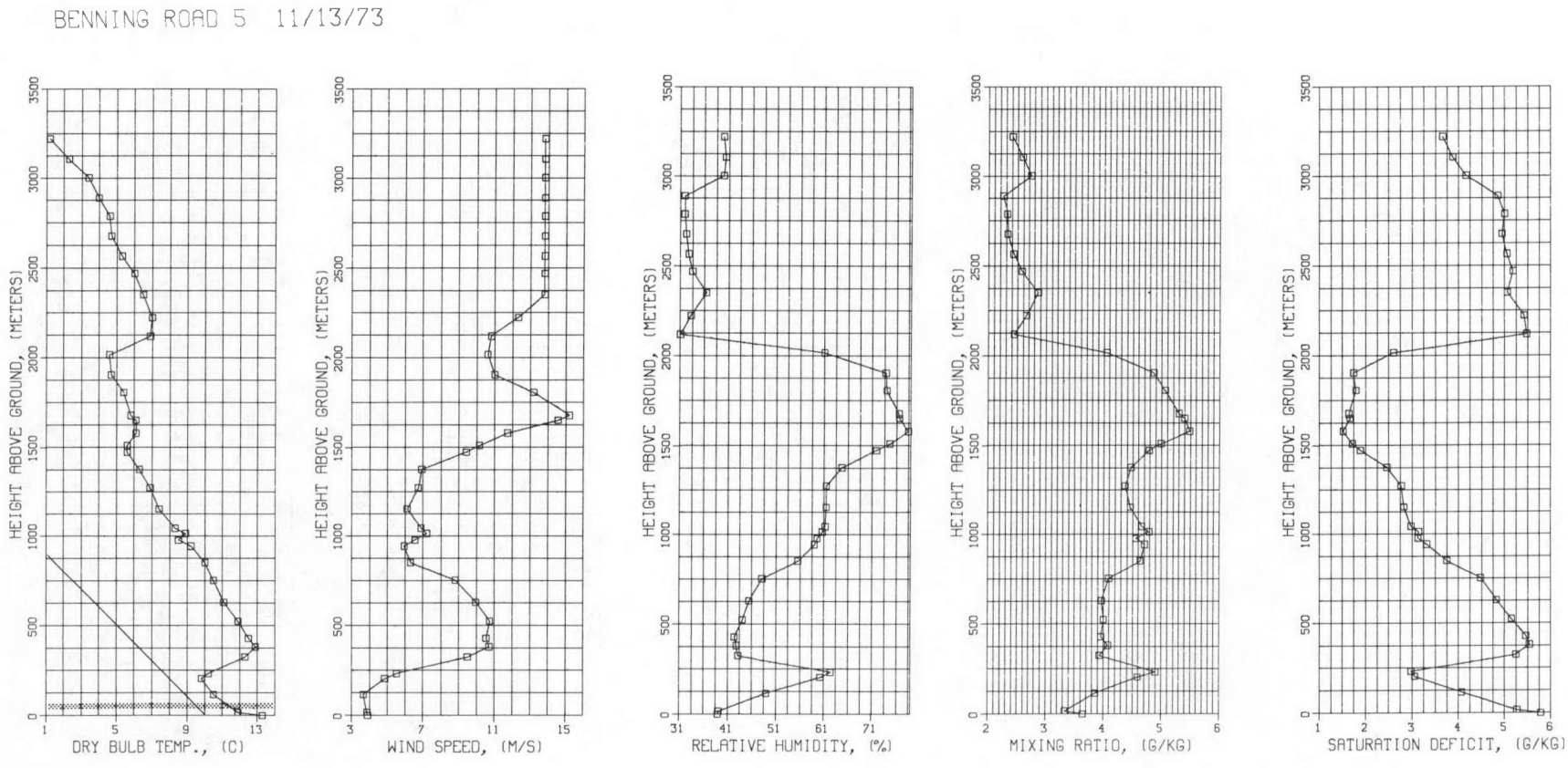

Figure 4-37. Ambient profiles of measured dry-bulb temperature, wind speed and relative humidity along with associated profiles of mixing ratio and saturation deficit . . . Benning Road Case 5. 11/13/73 (1030 Hrs.).

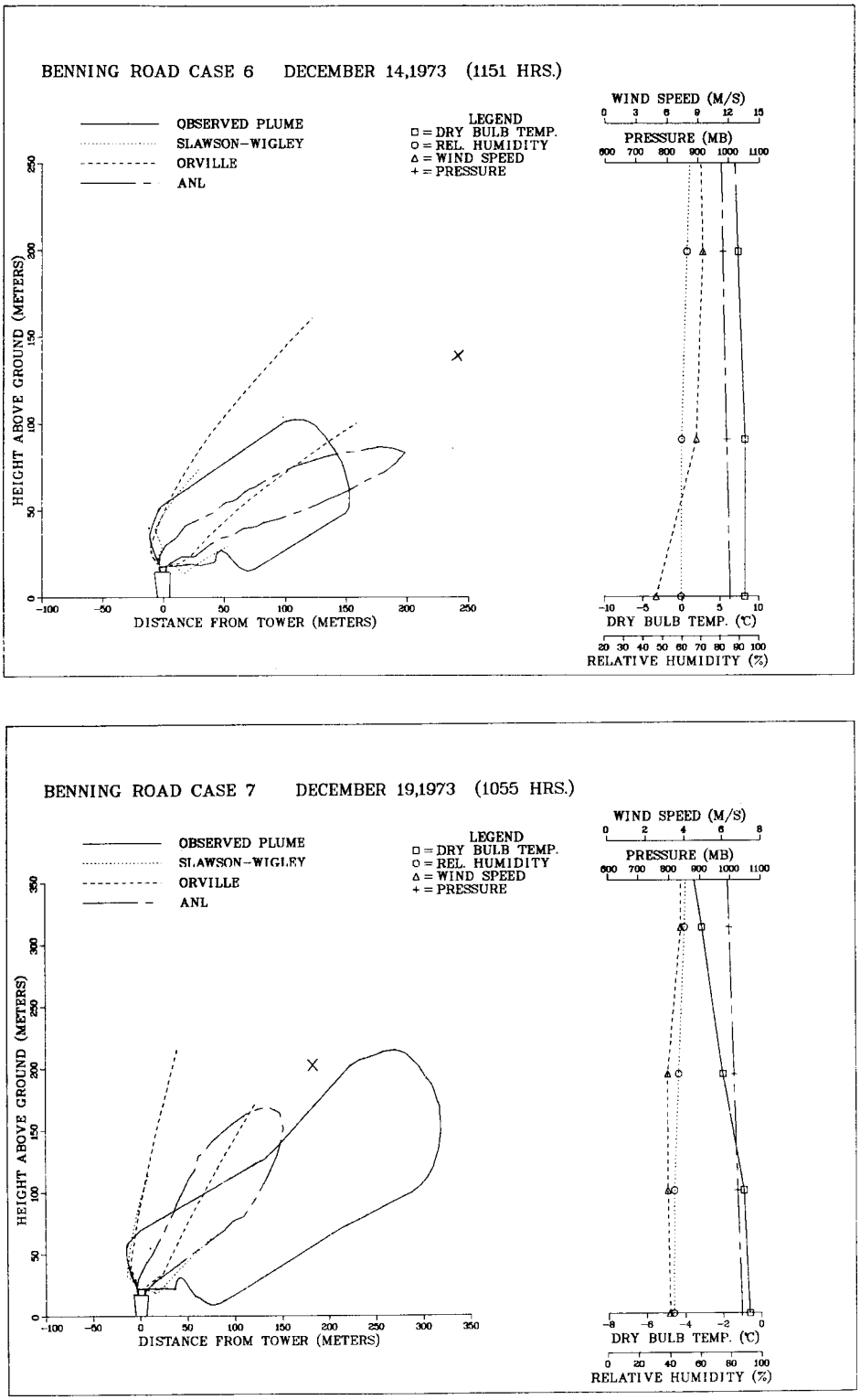

Figure 4-38. Comparison of predictions of Slawson-Wigley, Orville and ANL models to observed visible-plume outlines at Benning Road: (top) December 14, 1973 (1151 Hrs.), (bottom) December 19, 1973 (1055 Hrs.).

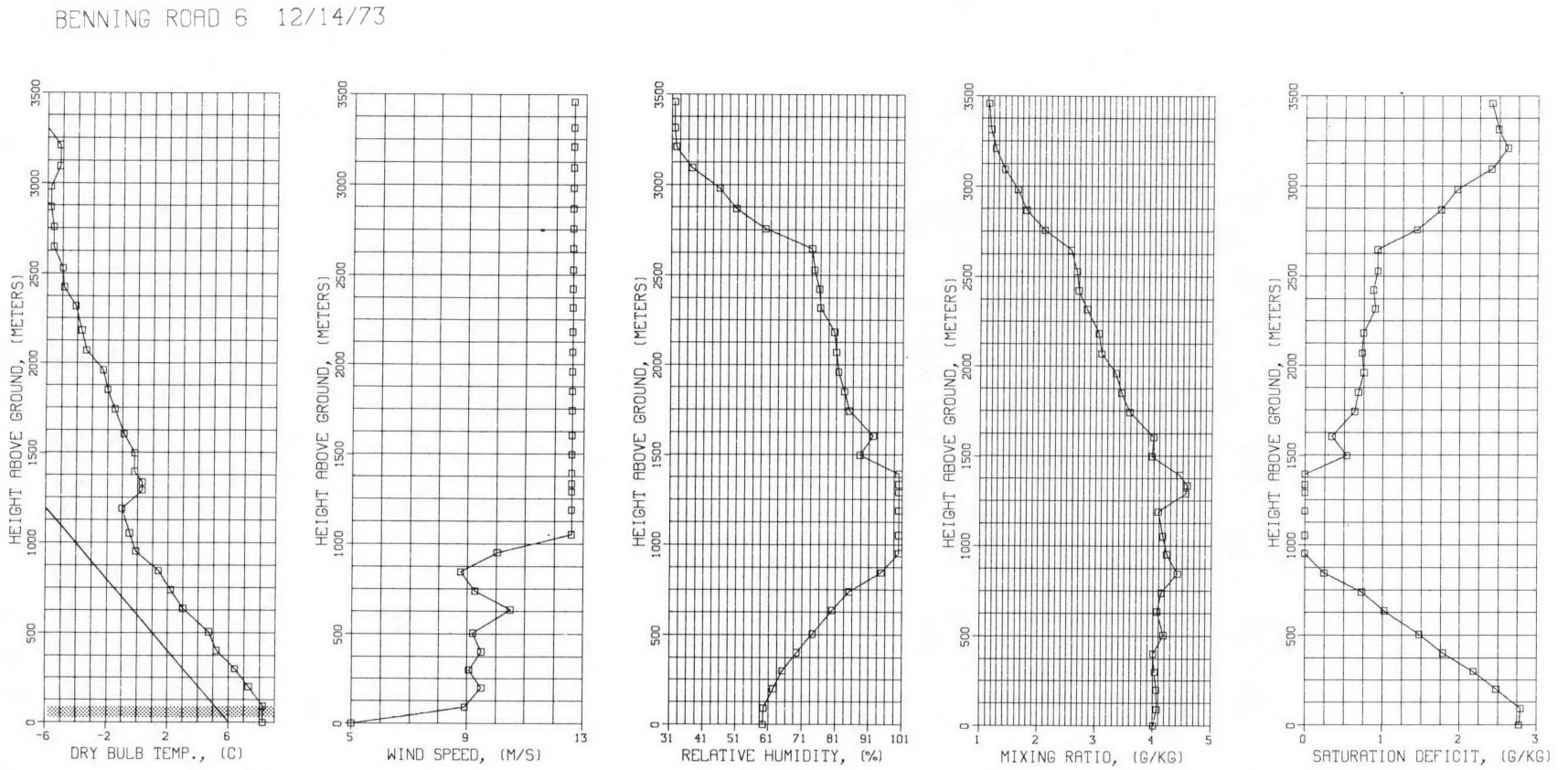

Figure 4-39. Ambient profiles of measured dry-bulb temperature, wind speed and relative humidity along with associated profiles of mixing ratio and saturation deficit . . . Benning Road Case 6. 12/14/73 (1151 Hrs.).

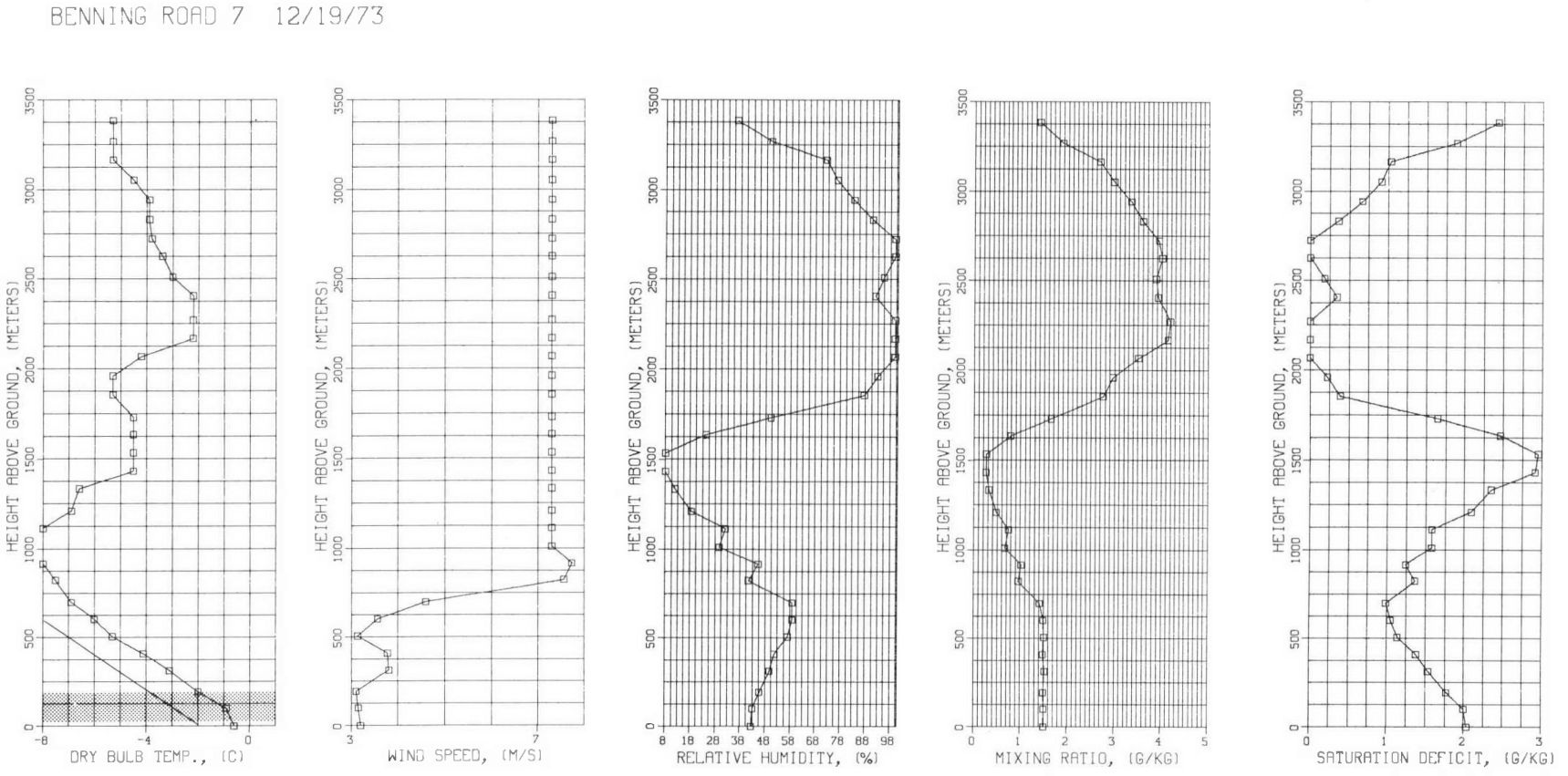

Figure 4-40. Ambient profiles of measured dry-bulb temperature, wind speed and relative humidity along with associated profiles of mixing ratio and saturation deficit . . . Benning Road Case 7. 12/19/73 (1055 Hrs.).

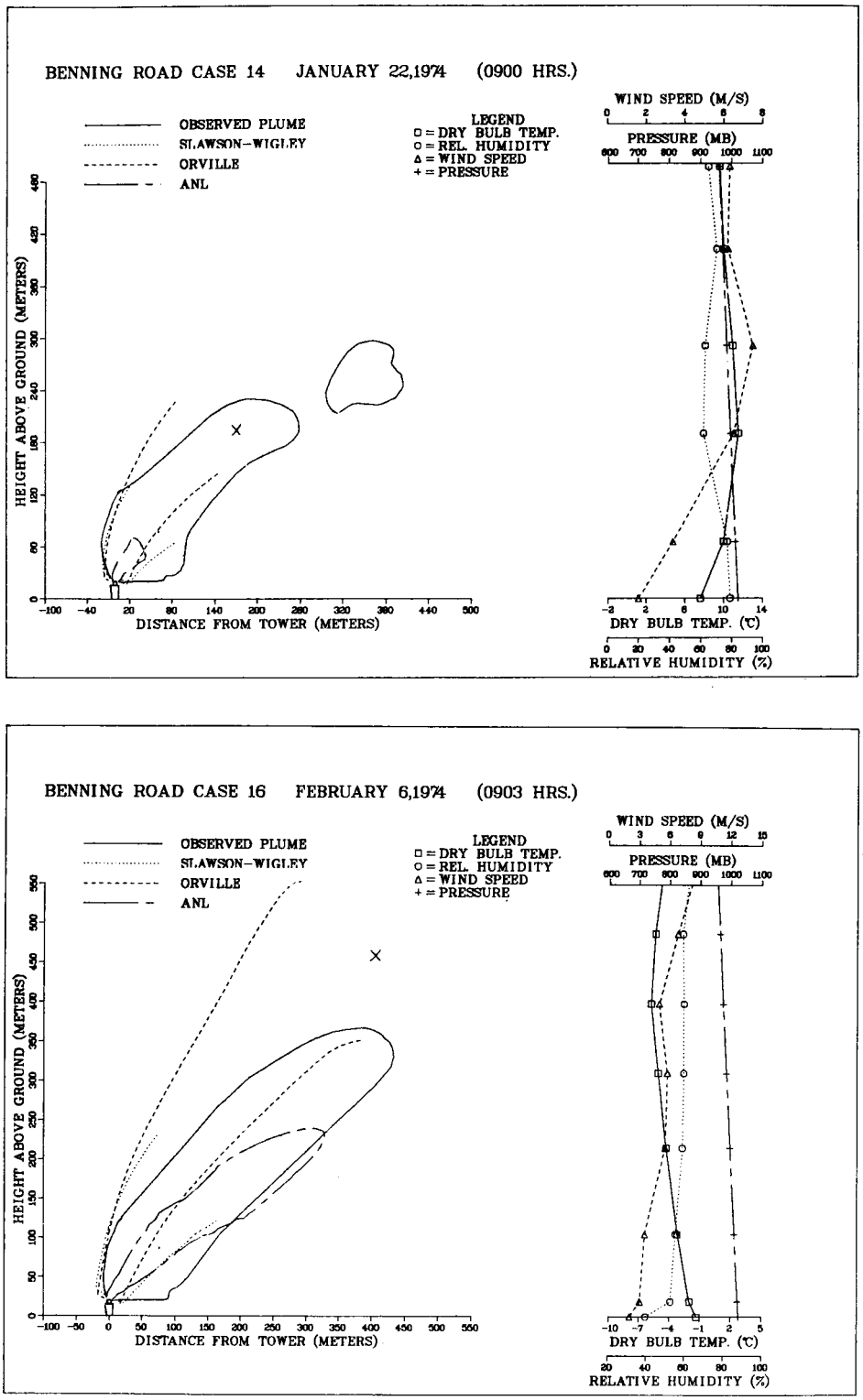

Figure 4-41. Comparison of predictions of Slawson-Wigley, Orville and ANL models to observed visible-plume outlines at Benning Road: (top) January 22, 1974 (0900 Hrs.), (bottom) February 6, 1974 (0903 Hrs.).

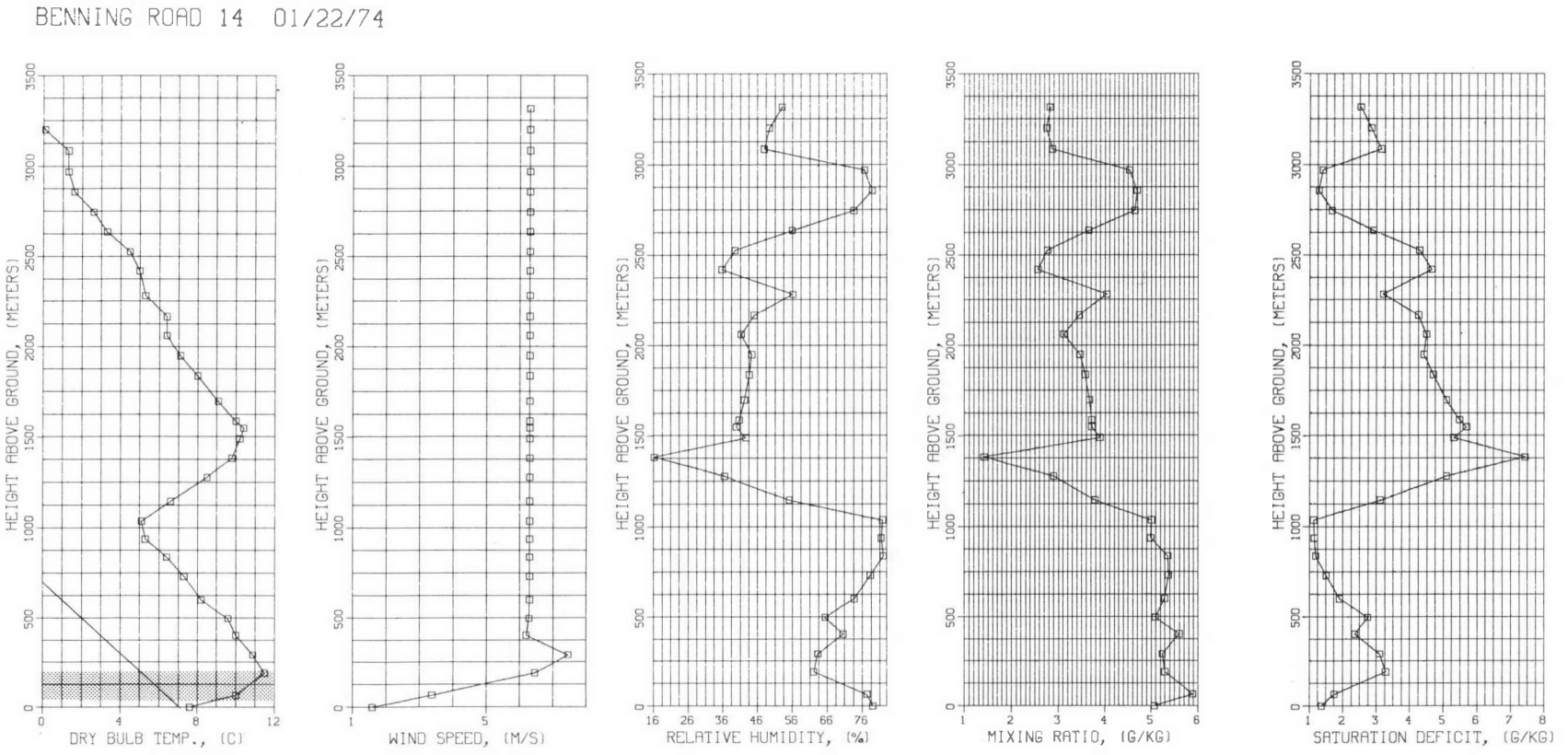

Figure 4-42. Ambient profiles of measured dry-bulb temperature, wind speed and relative humidity along with associated profiles of mixing ratio and saturation deficit . . . Benning Road Case 14. 1/22/74 (0900 Hrs.).

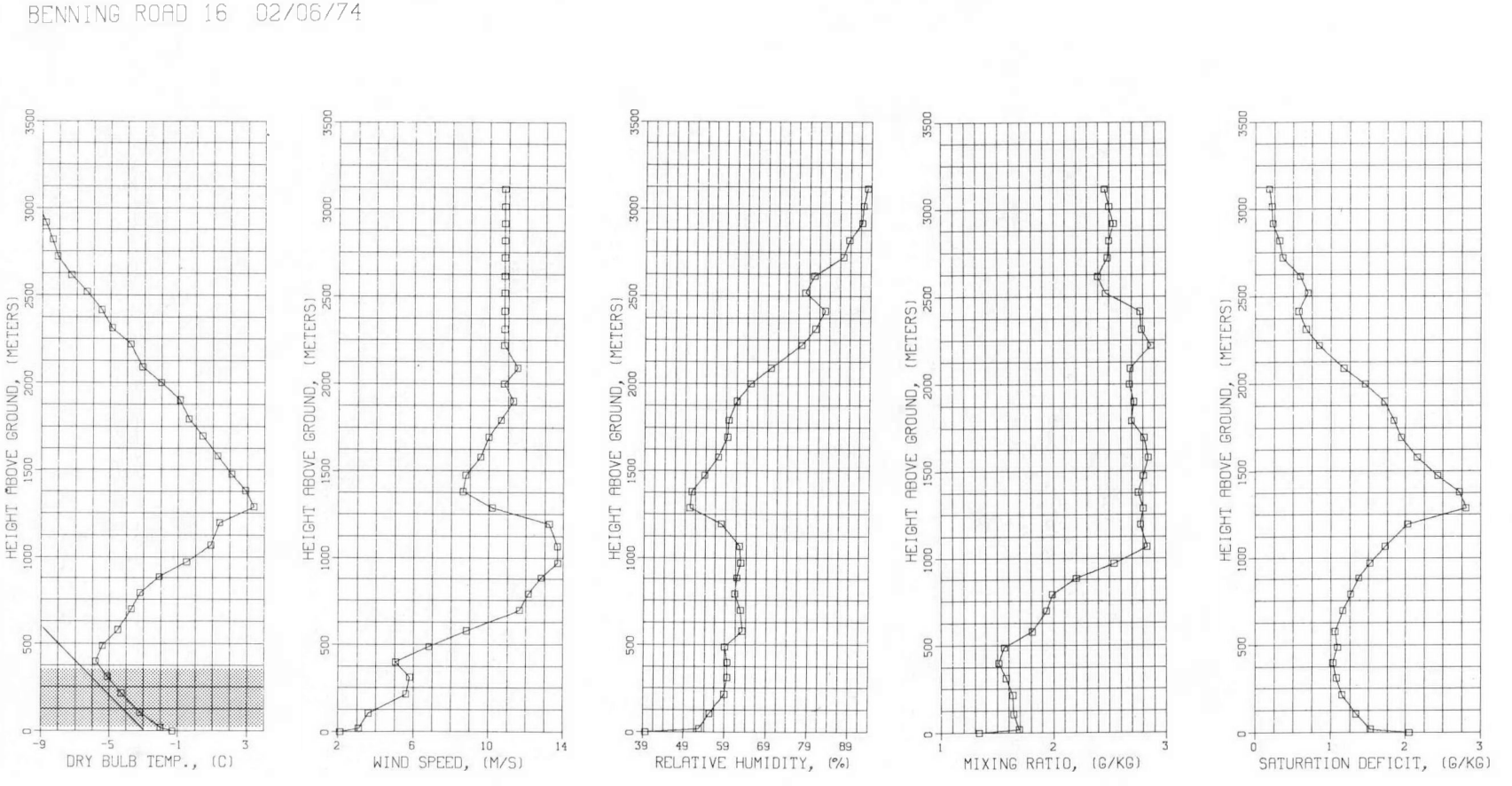

Figure 4-43. Ambient profiles of measured dry-bulb temperature, wind speed and relative humidity along with associated profiles of mixing ratio and saturation deficit . . . Benning Road Case 16. 2/6/74 (0903 Hrs.).

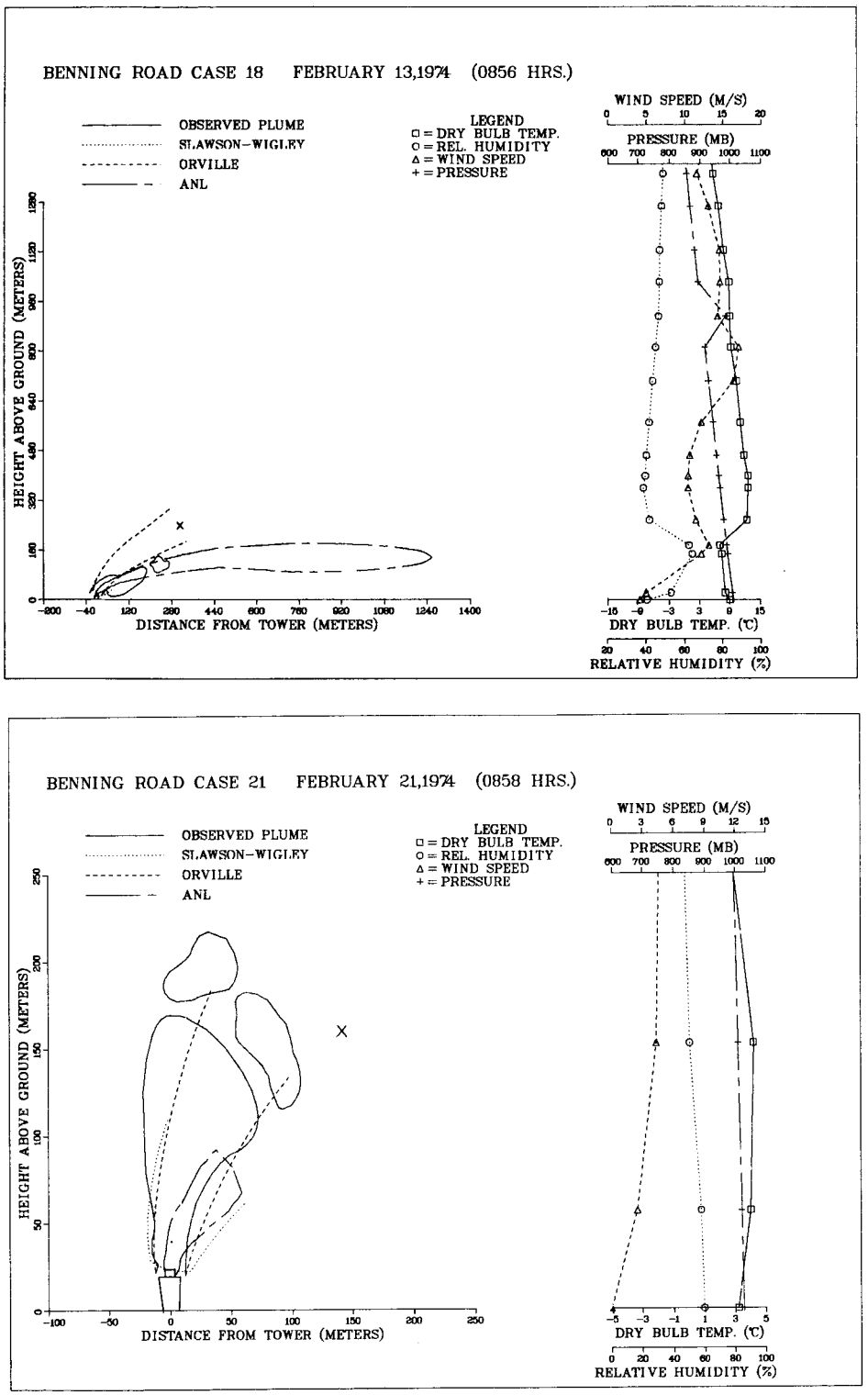

Figure 4-44. Comparison of predictions of Slawson-Wigley, Orville and ANL models to observed visible-plume outlines at Benning Road: (top) February 13, 1974 (0856 Hrs.), (bottom) February 21, 1974 (0858 Hrs.).

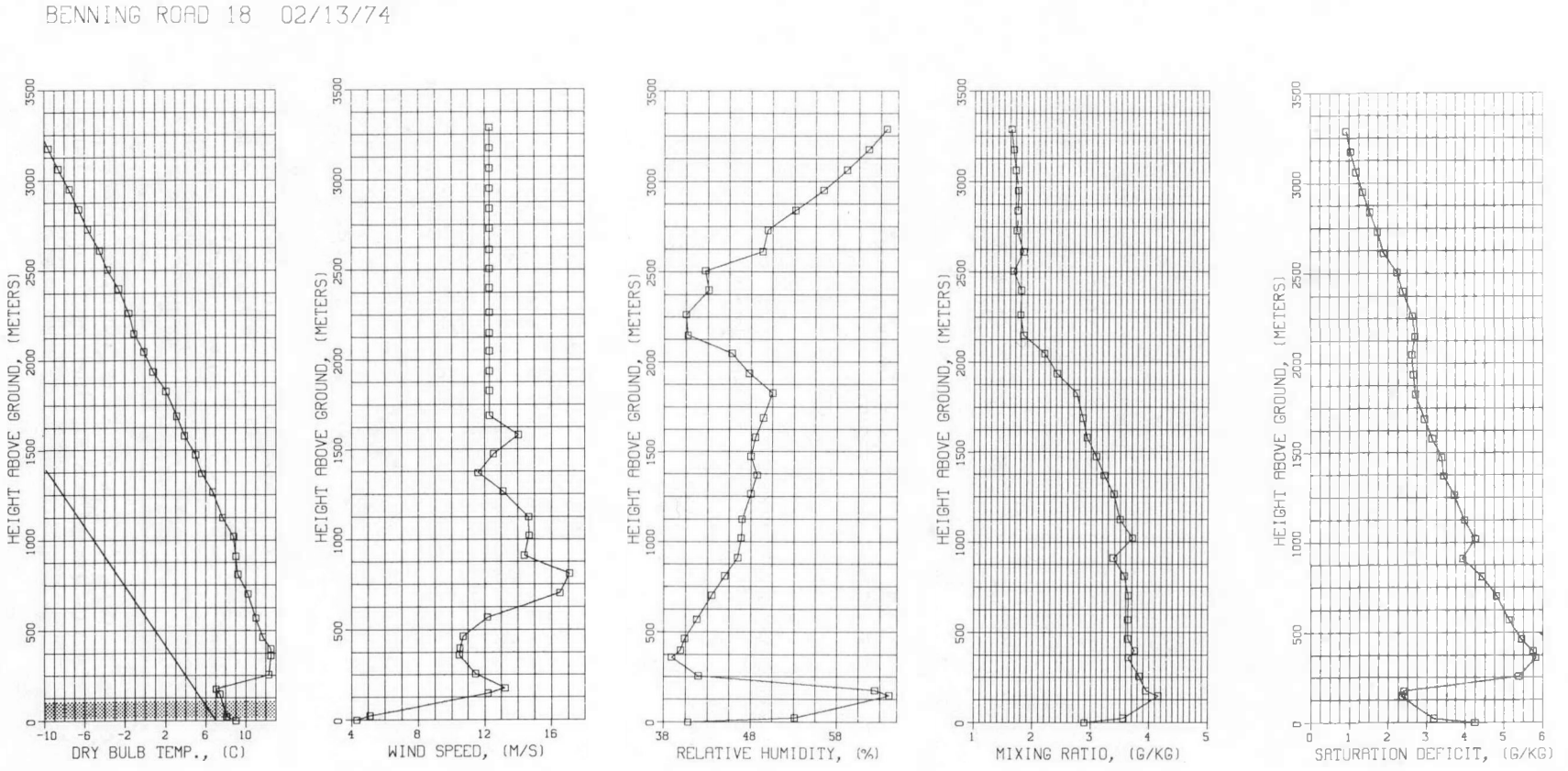

Figure 4-45. Ambient profiles of measured dry-bulb temperature, wind speed and relative humidity along with associated profiles of mixing ratio and saturation deficit . . . Benning Road Case 18. 2/13/74 (0856 Hrs.).

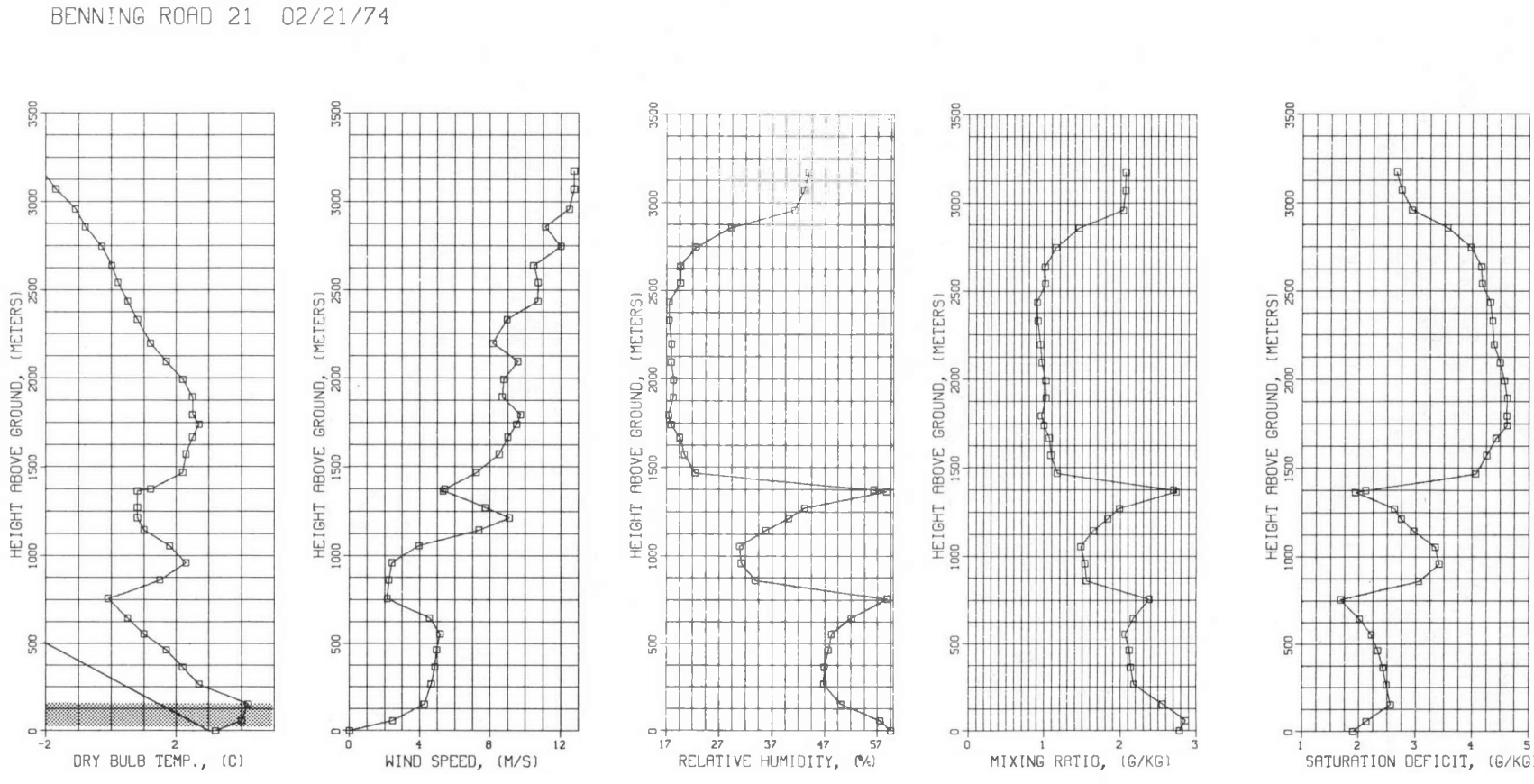

Figure 4-46. Ambient profiles of measured dry-bulb temperature, wind speed and relative humidity along with associated profiles of mixing ratio and saturation deficit . . . Benning Road Case 21. 2/21/74 (0858 Hrs.).

For the final Benning Road case, case 21 in Figure 4-44, the Orville model gives an excellent prediction as it usually does for low winds. The Slawson-Wigley and ANL model predicted plumes are reasonable, but both short; and both yield trajectories lying below the actual one, causing us to question the accuracy of the wind speed data. Downwash is not important for such low winds. The ground inversion barely blocks plume rise, because neutral conditions begin at the top of the observed visible plume. Saturation deficits are moderate.

FIELD DATA FROM GASTON (7) (See Figures 4-47 to 4-61)

The final set of mechanical-draft field data cases come from the Gaston Plant in Alabama. The two towers with 9 cells apiece are each 100 m long and lie with their long axes parallel. They are separated by 140 m perpendicular to their centerlines. Maximum generating capacity cooled by the two towers at this coal-fired plant is 800 MWe, about 43% greater than at Benning Road. Surrounding terrain is relatively flat as at Benning Road. Ambient profiles of measured dry-bulb temperature wind speed and relative humidity along with associated profiles of mixing ratio and saturation deficit are given for each Gaston case between the figures of predicted outlines.

The first case out of 10 selected for study (from a total of 20 available) was case 7 as seen in Figure 4-47. Saturation deficits were very low, about 0.25 gm/kg; stratification is isothermal (quite stable) and winds are moderate. Ambient temperatures in the 0°C range were present. These conditions eliminate moisture-related instabilities as a cause of the large observed plume. Near-saturated conditions are the cause. The Orville model predicted plume is short and rises too high. Entrainment in the model's atmospheric diffusion phase seems to be too large. The Slawson-Wigley model regularly overpredicts plume length under very himid conditions. Also, as noted earlier, the ANL model's atmospheric diffusion phase may contain too little entrainment for some stratifications. However, the trajectory of the ANL predicted plume is quite accurate for this case and is better than the predictions of the other two models.

Very similar conditions occur for case 8, seen in Figure 4-47 and the discussion follows the same lines. No model represents fully the actual pulling down of the near-tower portions of the plume into the tower wake region, although the ANL model represents the average trajectory very well.

Moisture-related plume and ambient instabilities are likely to play a role in case 9 (see Figure 4-50) causing a production of large visible plume volume and rise. The stratification is near neutral, the wind moderate and the saturation deficit small for this case. The visible plume pentrates a full 160 meters into the elevated inversion, indicating moisture-instability-augmented buoyancy. The Slawson-Wigley and ANL model predictions are very good, and that of the Orville model is reasonable, even though the latter prediction rises somewhat too high.

The additional downwash which can be produced by a second tower, and the filling of the cavity between them with visible plume is evident in case 10, seen in Figure 4-50 where the wind direction is nearly pure cross-flow. The observed plume penetrates 250 meters into an elevated inversion after 75 m of rise in unstable air. Ambient data reveal low saturation deficits about 1 gm/kg and low wind. Such conditions produce strong additional buoyancy because of plume conditional instability, explaining the vigorous penetration of the inversion and the relatively large plume volume. The ANL model clearly gives the best prediction of plume trajectory and length; however, no model is equipped to predict this type of visible plume lateral shape. In fact, it is unlikely that the individual plumes have fully merged at the point of visible plume disappearance. In assessing this type of ANL model predictive success, it should be remembered that the Gaston data were not used in our calibration process. One could consider Benning Road and Gaston data as verification cases for the model.

Case 11 seen in Figure 4-53 is also a cross-flow case, but lower winds reduce the downwash effects. Saturation deficits are moderate (1.5 to 2 gm/kg) and the stratification is inverted from the ground up to 250 m. Plume conditional and ambient latent instability do not occur under inverted conditions. The ANL model predicted a plume which levels off at too low an elevation, but the length prediction is good. Ambient properties do not vary rapidly with height in this case. The Orville model's length prediction is also good, but its rise is too large. As expected from behavior for Benning Road data, the Slawson-Wigley model predicts a very short plume, since the ambient humidity is not high and no initial liquid water is assumed.

In case 12 seen in Figure 4-53, the first 75 m of isothermal ambient air gives way to neutral stratification above that. Saturation deficits and winds are large, coming at a 30° angle to the cross-flow direction. The Orville model prediction is very long and high here, because neutral air aloft with decreasing

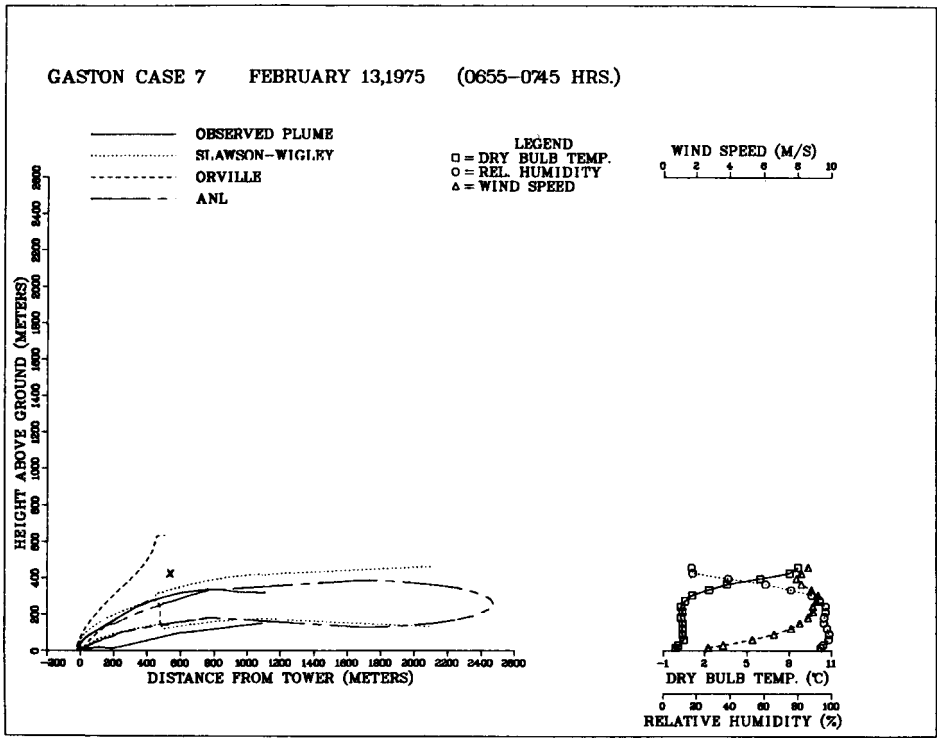

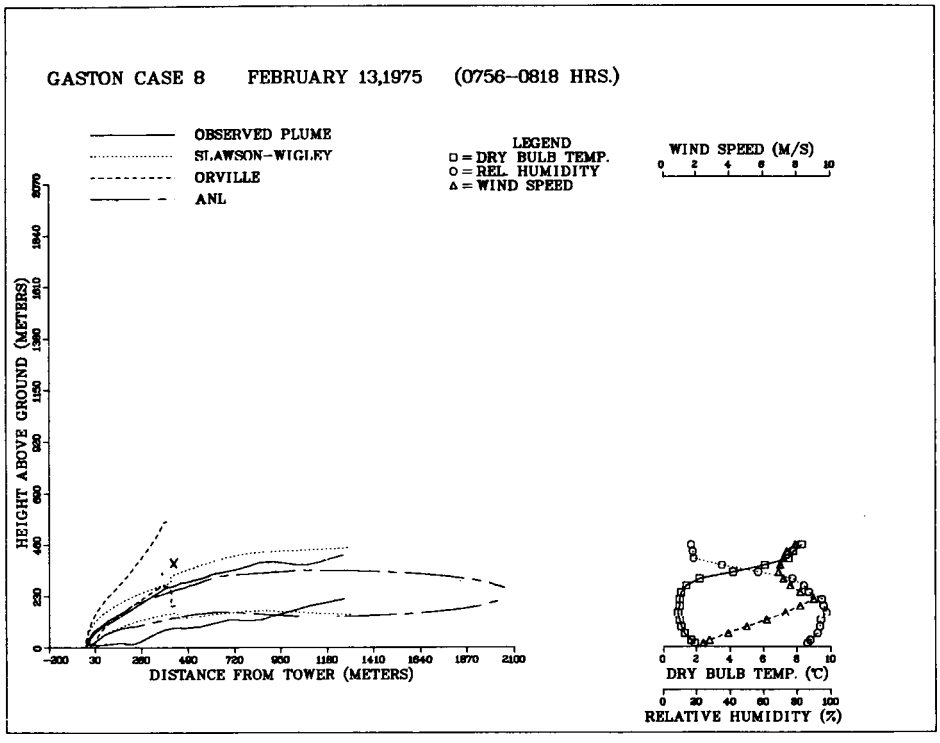

Figure 4-47. Comparison of predictions of Slawson-Wigley, Orville and ANL models to observed visible-plume outlines at Gaston: (top) February 13, 1975 (0655-0745 Hrs.), (bottom) February 13, 1975 (0756-0818 Hrs.).

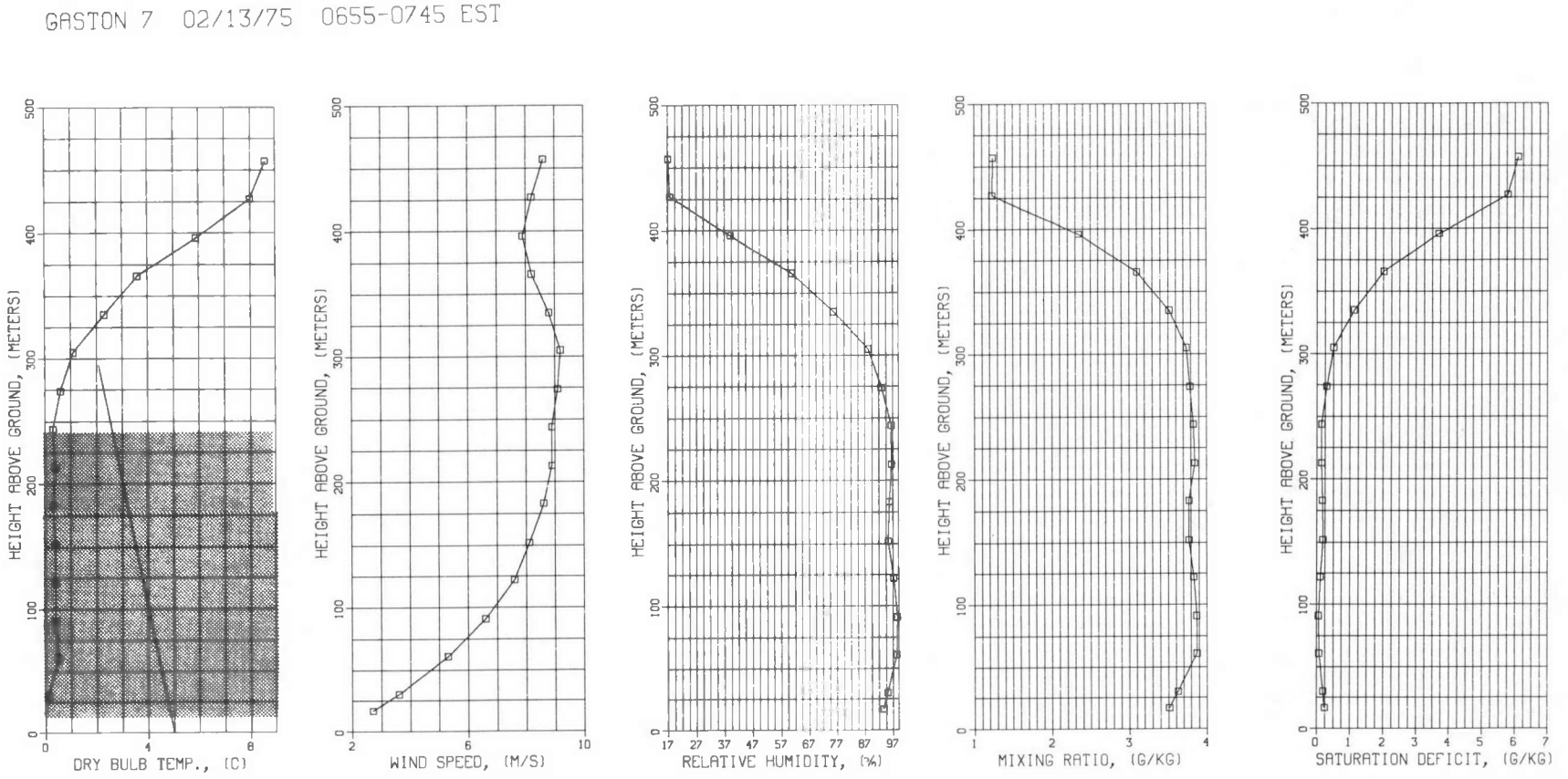

Figure 4-48. Ambient profiles of measured dry-bulb temperature, wind speed and relative humidity along with associated profiles of mixing ratio and saturation deficit . . . Gaston Case 7. 2/13/75 (0655-0745 Hrs.).

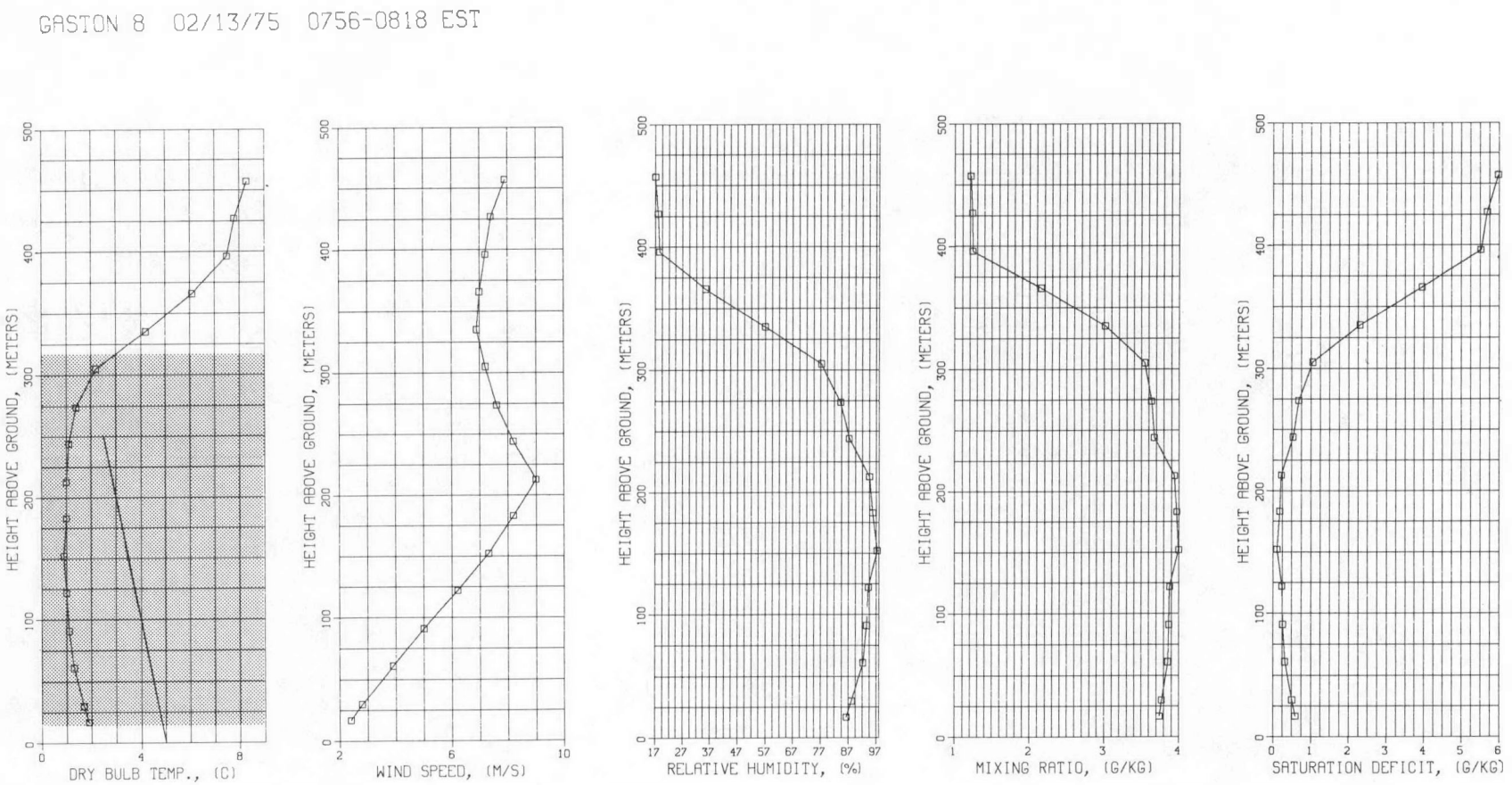

Figure 4-49. Ambient profiles of measured dry-bulb temperature, wind speed and relative humidity along with associated profiles of mixing ratio and saturation deficit . . . Gaston Case 8. 2/13/75 (0756-0818 Hrs.).

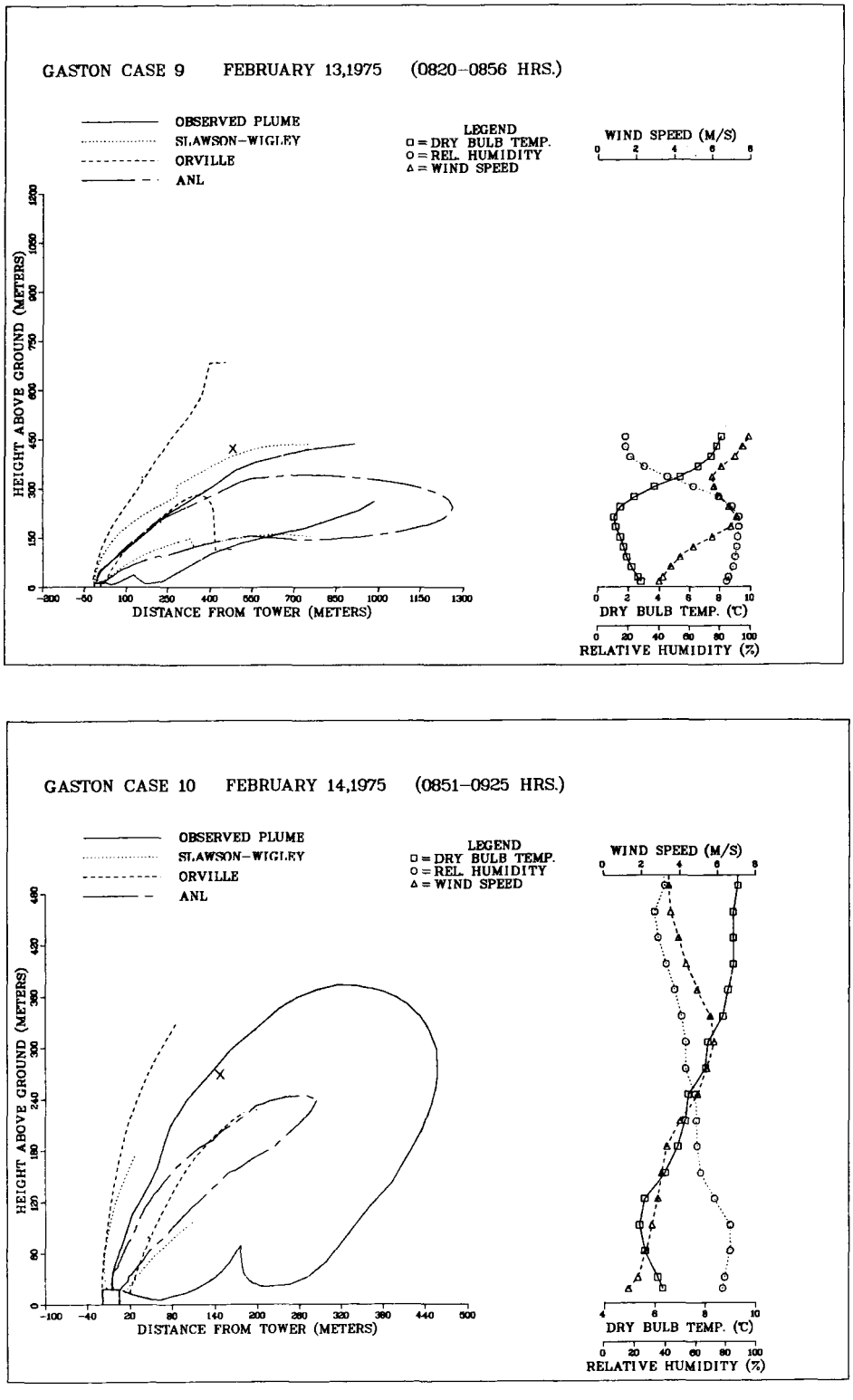

Figure 4-50. Comparison of predictions of Slawson-Wigley, Orville and ANL models to observed visible-plume outlines at Gaston: (top) February 13, 1975 (0820-0856 Hrs.), (bottom) February 14, 1975 (0851-0925 Hrs.).

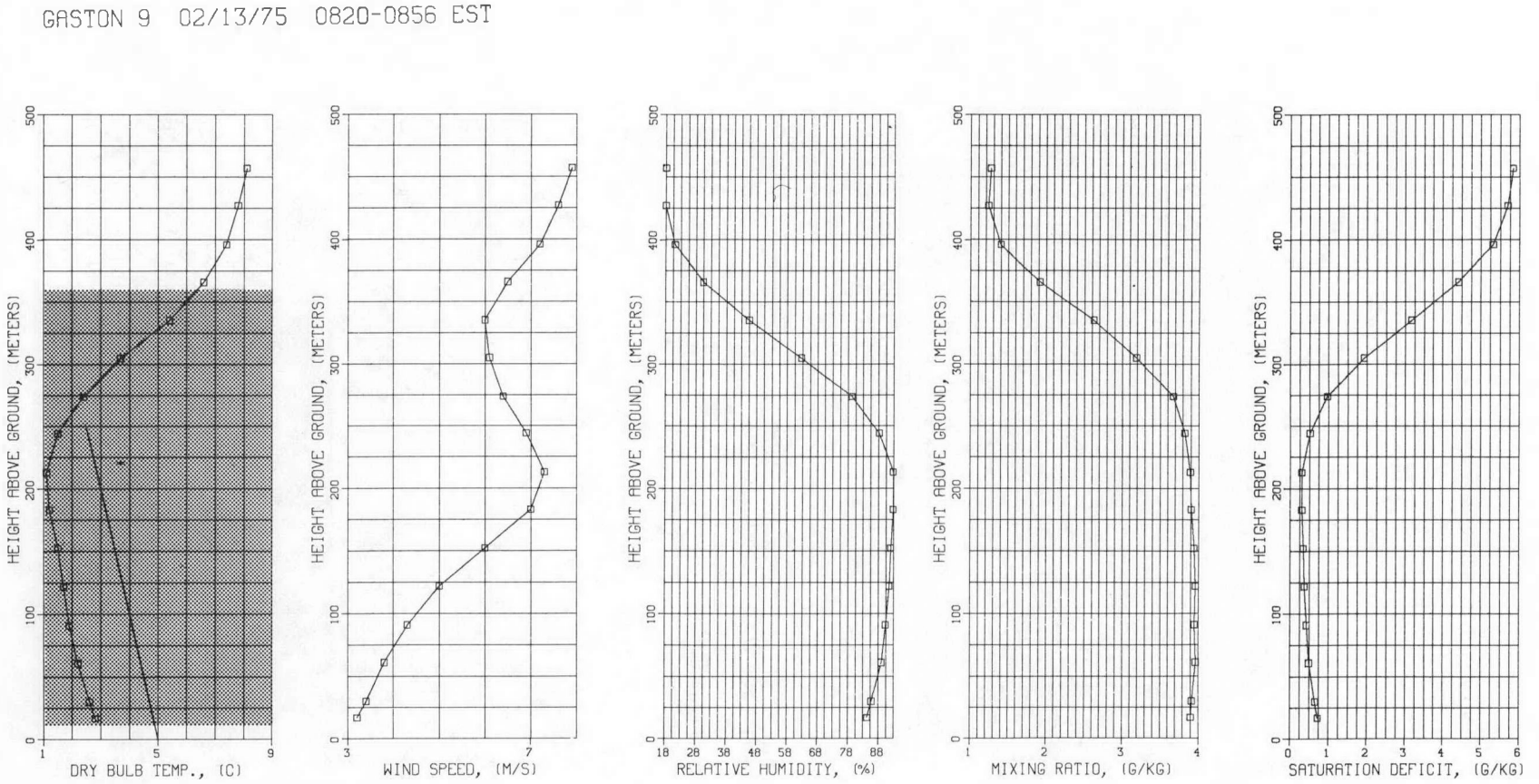

Figure 4-51. Ambient profiles of measured dry-bulb temperature, wind speed and relative humidity along with associated profiles of mixing ratio and saturation deficit . . . Gaston Case 9. 2/13/75 (0820-0856 Hrs.).

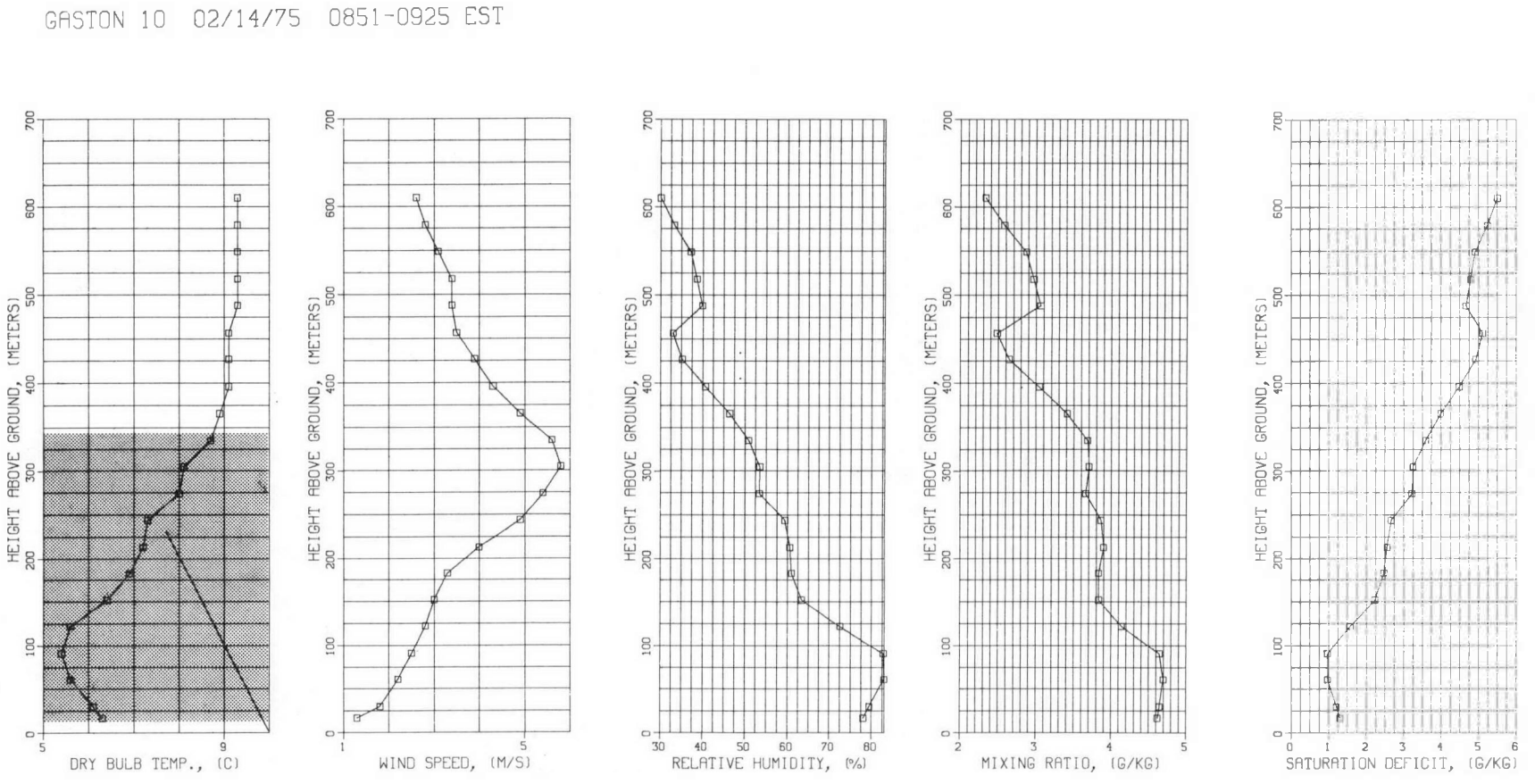

Figure 4-52. Ambient profiles of measured dry-bulb temperature, wind speed and relative humidity along with associated profiles of mixing ratio and saturation deficit . . . Gaston Case 10. 2/14/75 (0851-0925 Hrs.).

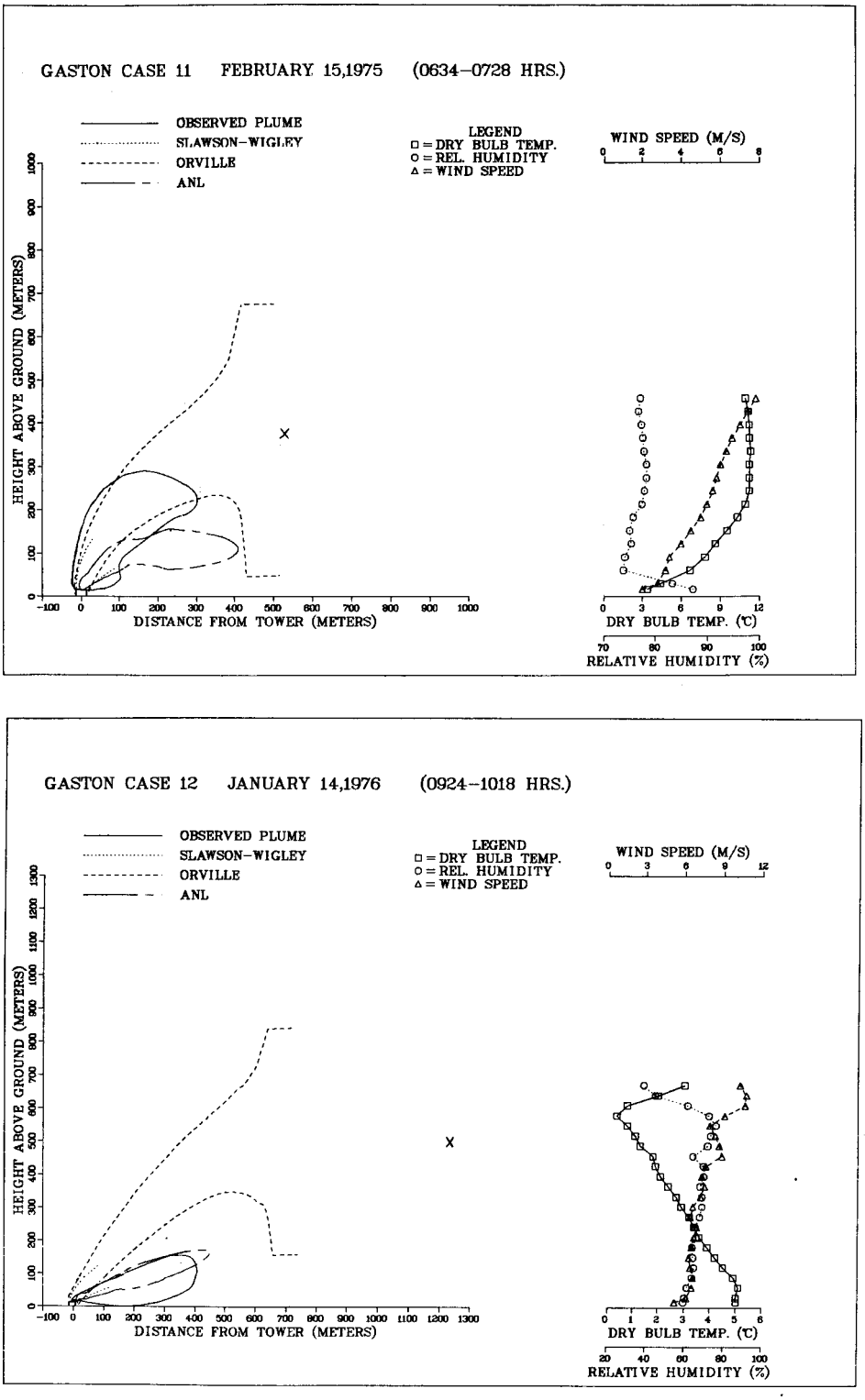

Figure 4-53. Comparison of predictions of Slawson-Wigley, Orville and ANL models to observed visible-plume outlines at Gaston: (top) February 15, 1975 (0634-0728 Hrs.), (bottom) January 14, 1976 (0924-1018 Hrs.).

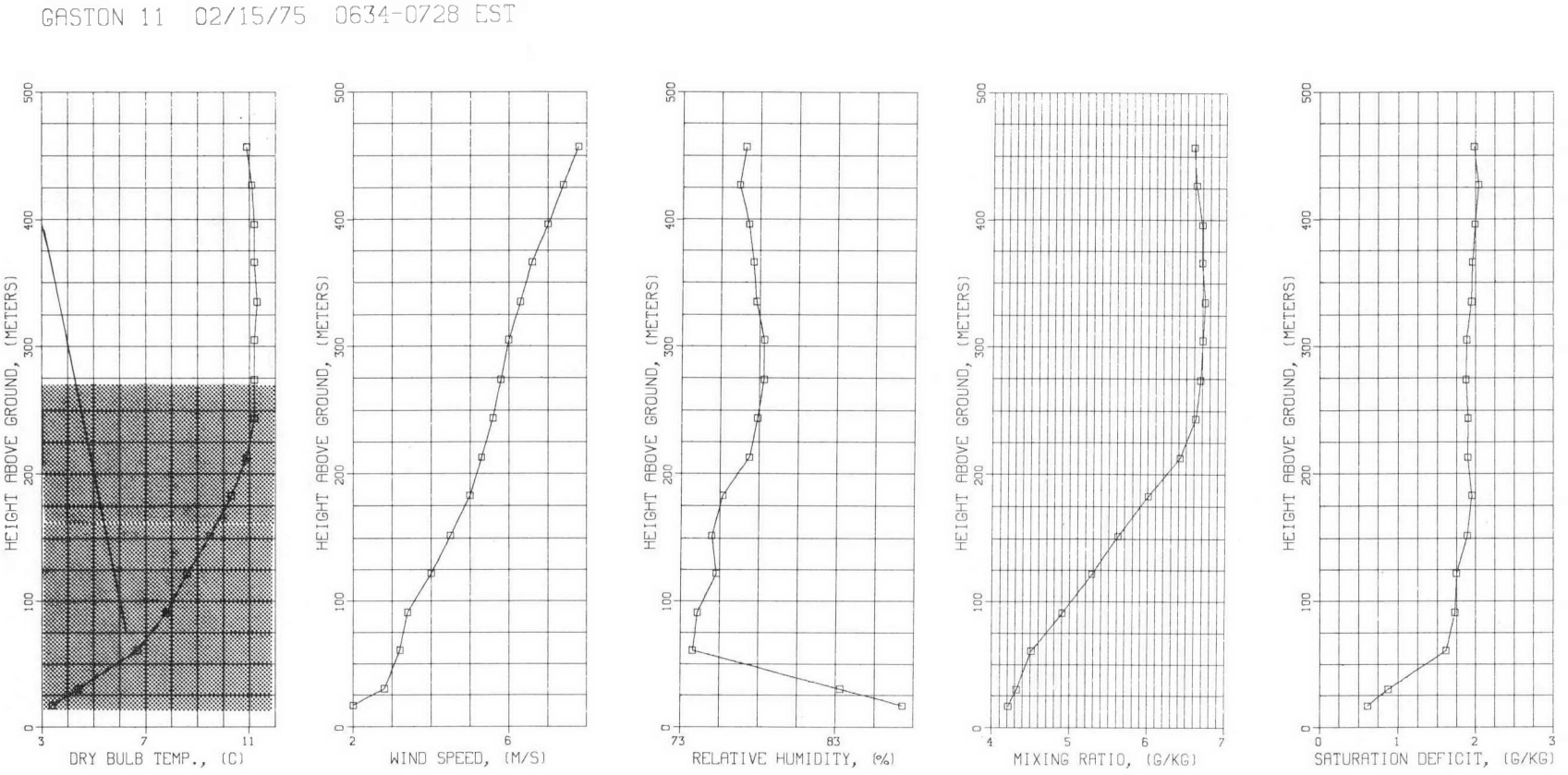

Figure 4-54. Ambient profiles of measured dry-bulb temperature, wind speed and relative humidity along with associated profiles of mixing ratio and saturation deficit . . . Gaston Case 11. 2/15/75 (0634-0728 Hrs.).

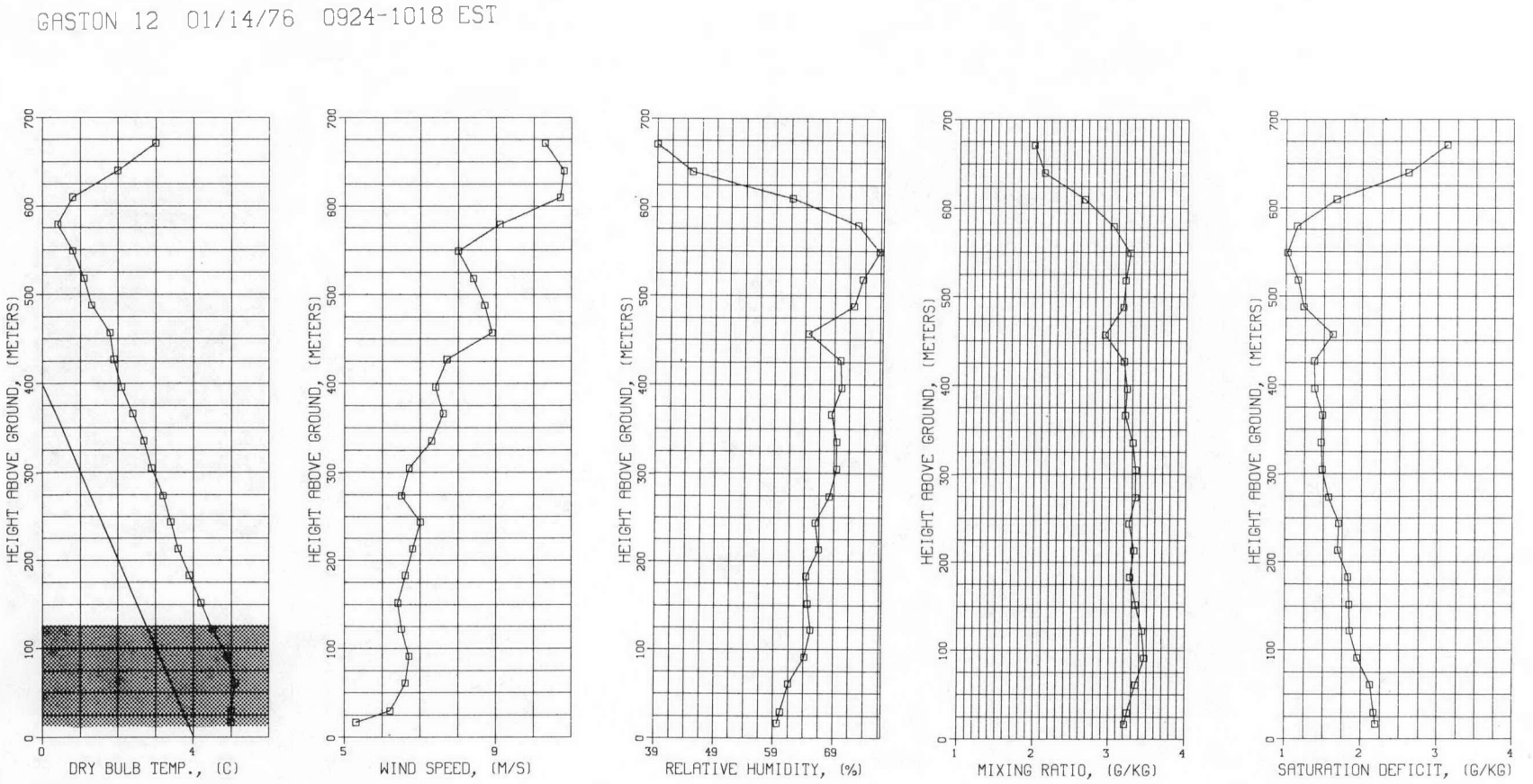

Figure 4-55. Ambient profiles of measured dry-bulb temperature, wind speed and relative humidity along with associated profiles of mixing ratio and saturation deficit . . . Gaston Case 12. 1/14/76 (0924-1018 Hrs.).

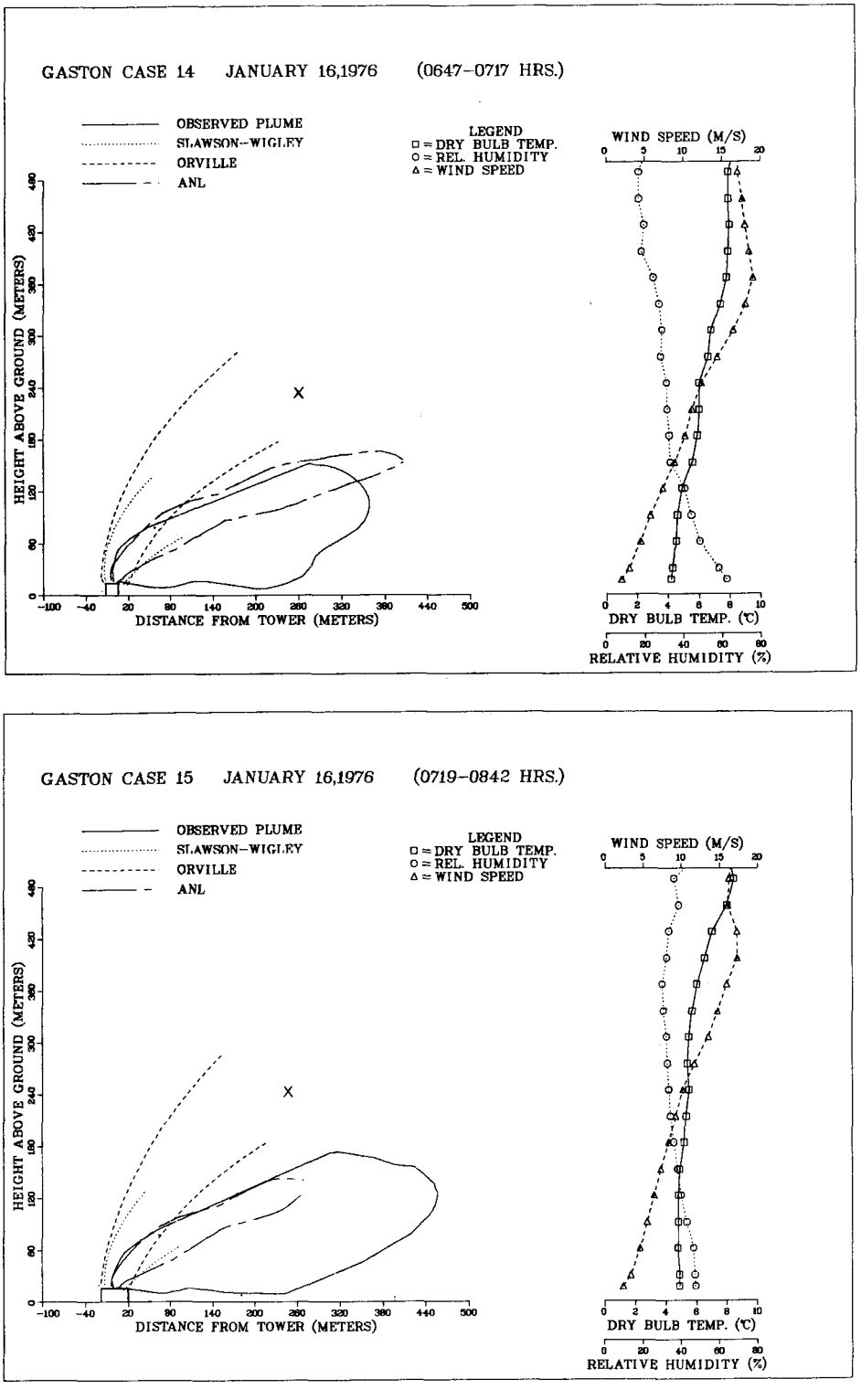

Figure 4-56. Comparison of predictions of Slawson-Wigley, Orville and ANL models to observed visible-plume outlines at Gaston: (top) January 16, 1976 (0647-0717 Hrs.), (bottom) January 16, 1976 (0719-0842 Hrs.).

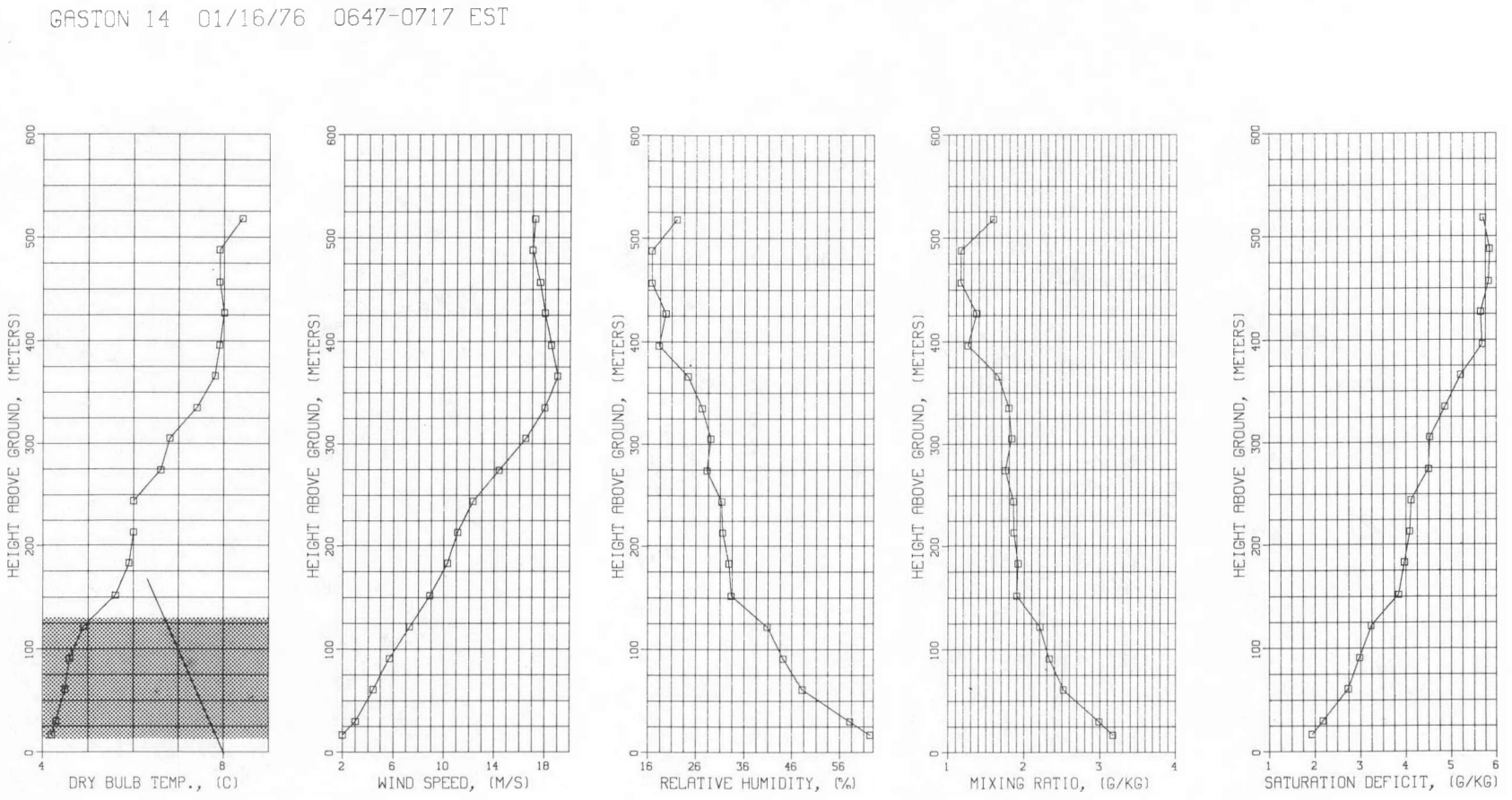

Figure 4-57. Ambient profiles of measured dry-bulb temperature, wind speed and relative humidity along with associated profiles of mixing ratio and saturation deficit . . . Gaston Case 14. 1/16/76 (0647-0717 Hrs.).

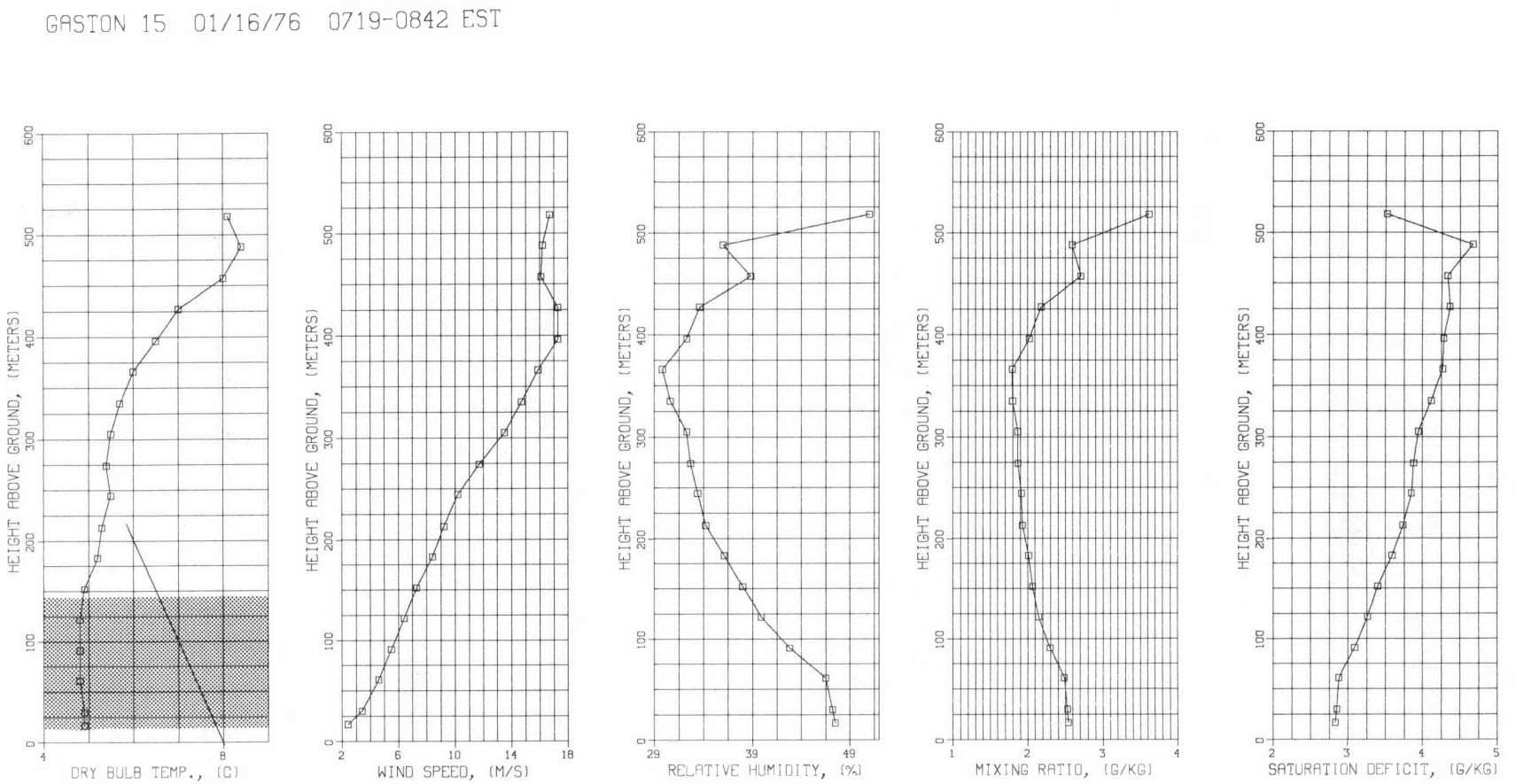

Figure 4-58. Ambient profiles of measured dry-bulb temperature, wind speed and relative humidity along with associated profiles of mixing ratio and saturation deficit . . . Gaston Case 15. 1/16/76 (0719-0842 Hrs.).

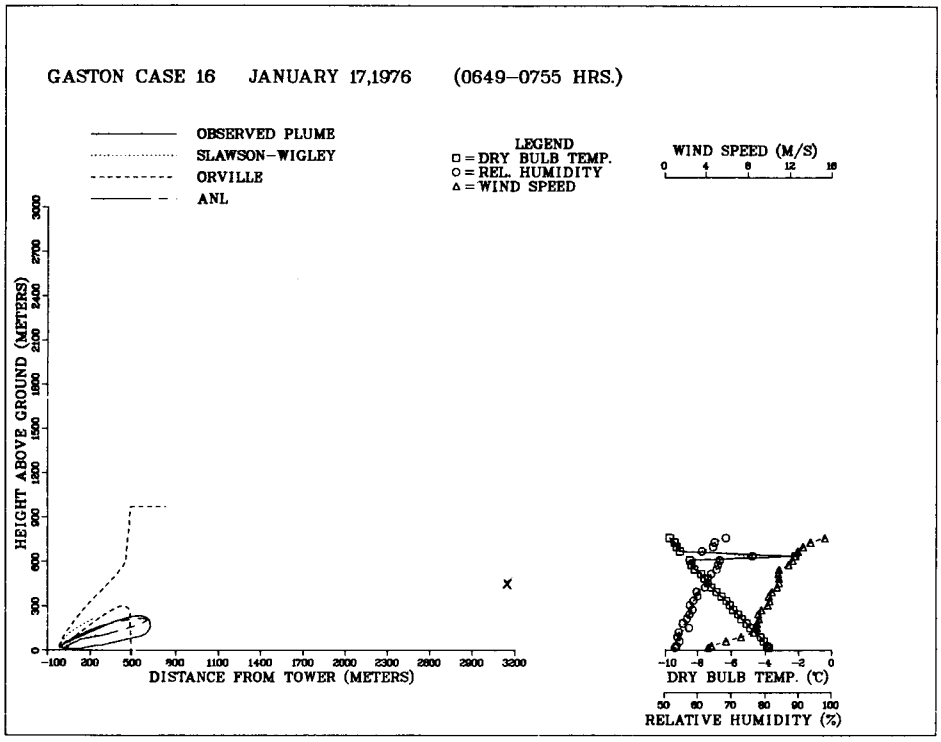

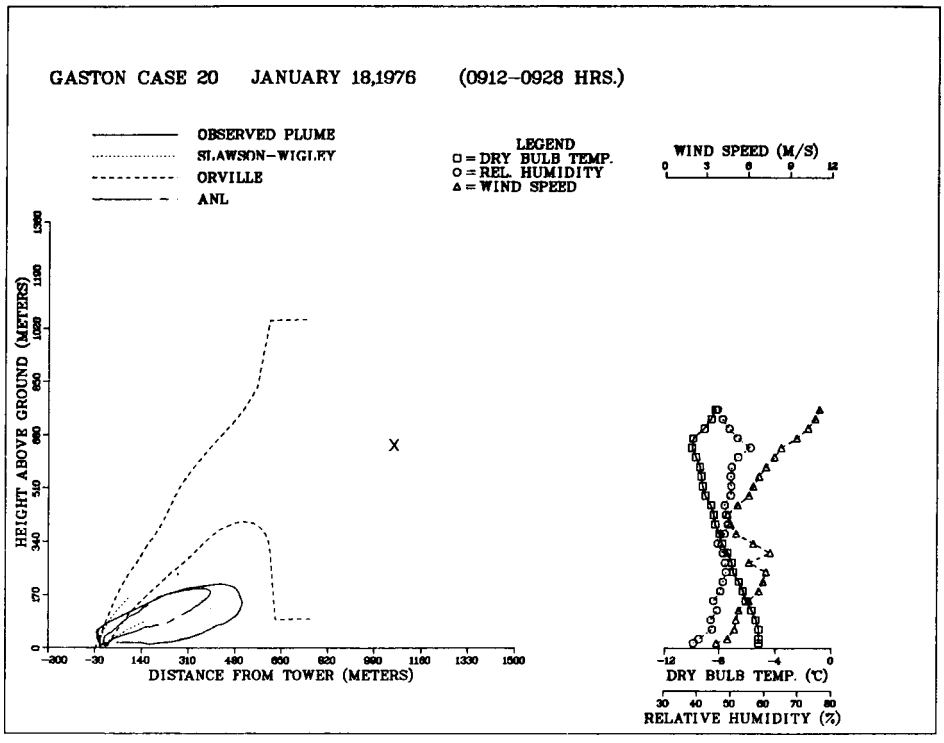

Figure 4-59. Comparison of predictions of Slawson-Wigley, Orville and ANL models to observed visible-plume outlines at Gaston: (top) January 17, 1976 (0649-0755 Hrs.), (bottom) January 18, 1976 (0912-0928 Hrs.).

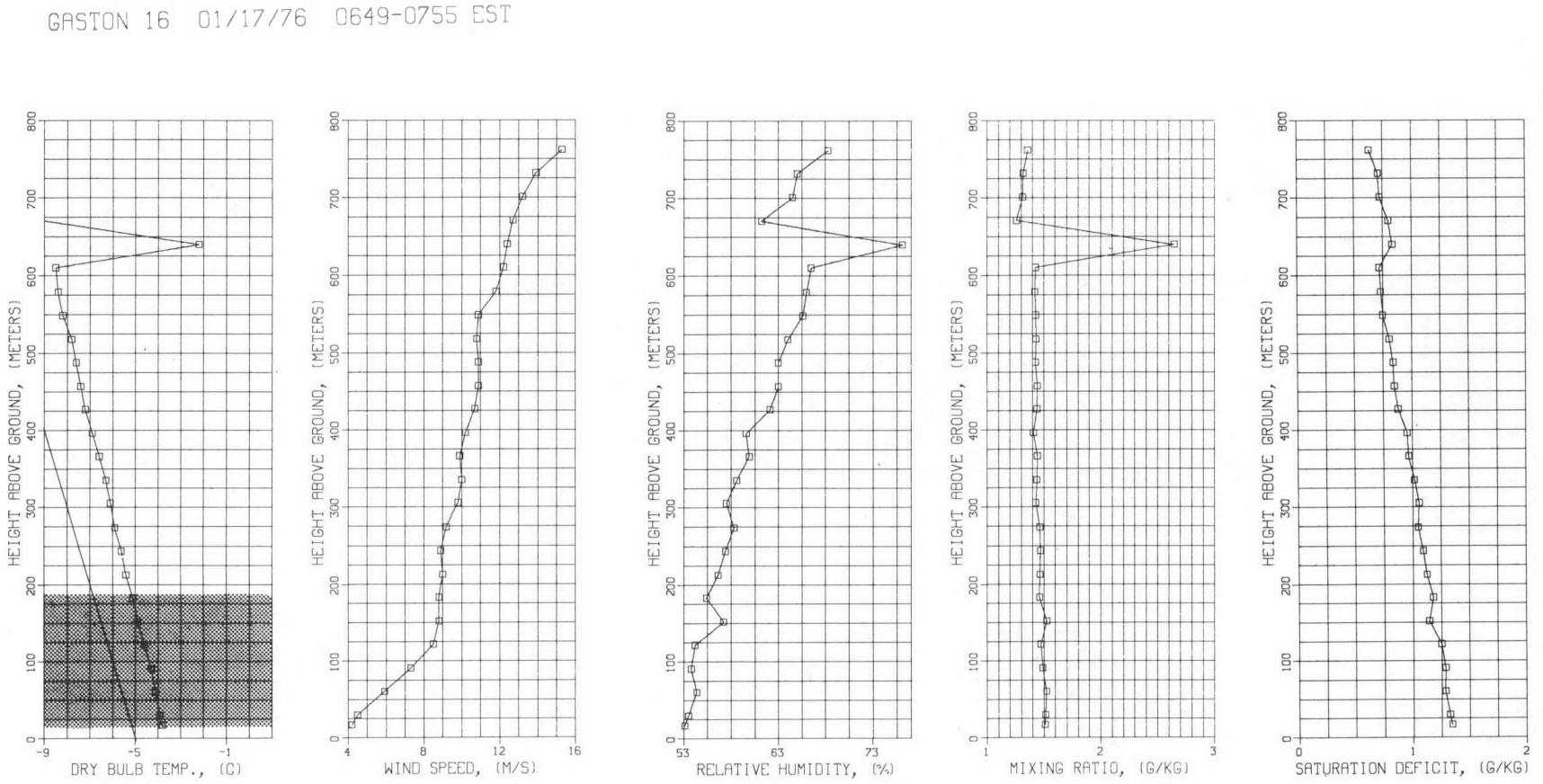

Figure 4-60. Ambient profiles of measured dry-bulb temperature, wind speed and relative humidity along with associated profiles of mixing ratio and saturation deficit . . . Gaston Case 16. 1/17/76 (0649-0755 Hrs.).

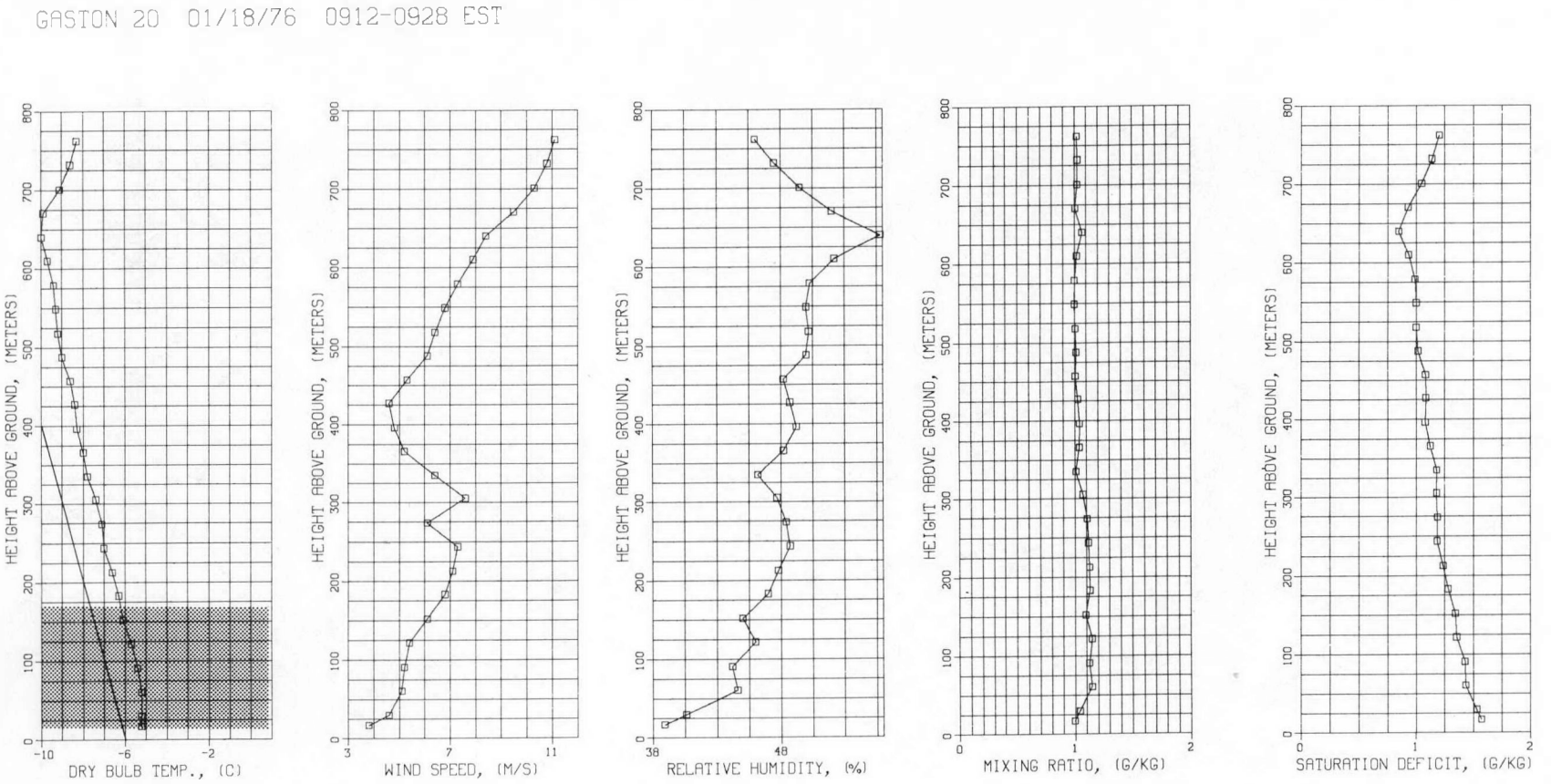

Figure 4-61. Ambient profiles of measured dry-bulb temperature, wind speed and relative humidity along with associated profiles of mixing ratio and saturation deficit . . . Gaston Case 20. 1/18/76 (0912-0928 Hrs.).

saturation deficit penalizes rise overprediction in this case. The Slawson-Wigley model greatly underpredicts the plume following its usual behavior for moderate ambient properties. The ANL model prediction is quite impressive in this case; however, we have previously seen that its performance tends to be good under moderate ambient conditions. (At least the addition of mechanical-draft tower downwash effects and plume merging logic has not changed that desirable behavior.)

Another deep inversion layer case follows, case 14 of Figure 4-56, with moderate winds and moderate to large saturation deficits (2-3 gm/kg). The wind direction makes this case nearly exactly cross-flow. The ANL model prediction is again superior, with the usual relationships between predictions of the three models. The ANL model-predicted-trajectory lies a little above the observed trajectory, suggesting that the downwash-produced force assumed is somewhat too weak here.

All three models underpredict case 15 in Figure 4-56. The observed plume volume seems somewhat too large in view of the large ambient saturation deficit, the moderate windspeeds (but low near the tower, reducing downwash effects), and isothermal stratification. Again the ANL model gives the best prediction.

Another impressive ANL model prediction follows for case 16 in Figure 4-59; here, the wind direction is closer to in-line, windspeeds are moderate, saturation deficits are moderate and ambient stratification is neutral. Again, for the Orville model, the tendency toward rise overprediction is severely penalized by neutral air aloft having decreasing saturation deficit with height.

A very similar case appears in case 20 of Figure 4-59 which concludes the Gaston field data comparisons, and all comments of the preceding case apply.

STATISTICS OF PERFORMANCE OF MODELS TESTED WITH ABOVE FIELD DATA

Figures 4-62 through 4-65 present summary plots of the performance of the ANL, KUMULUS, and Orville Models in terms of visible plume length and rise for the Neurath and Amos field data. Observed visible plume length or visible plume rise are plotted on the abscissa of each graph whereas corresponding predicted values are plotted on the ordinate of each graph. Each "x" refers to one set of our 26 field data cases.

The ANL summary plots (Figures 4-62 and 4-63) show very good plume rise, predictions in most cases with a tendency to underpredict plume rise when observed

values for plume rise are large. ANL predictions of visible plume length are good also with a tendency for underprediction for plumes with large observed values for length as seen in Figure 4-63. The KUMULUS Model (Figure 4-64) shows a wide scatter for visible plume length predictions, but most of the cases are underpredicted. Plume rise predictions are very good except there is a trend towards underprediction for plume rise for cases with large observed values for plume rise. The Orville Model (Figure 4-65) shows fair results for predicting visible plume length with many underpredicted values. Visible plume rise predictions are good for Orville with an inclination to predict higher rises than observed.

Figures 4-66 through 4-68 are the performance summary plots of the ANL, Slawson-Wigley, and Orville Models for the 10 Benning Road field data cases. The ANL Model performs well in predictions of both visible plume length and rise. The tendency for the model to underpredict is evident again. The Slawson-Wigley Model (Figure 4-67) shows very poor results for both visible plume length and rise. All of the final values for this model reveal underpredictions. Figure 4-68 shows excellent predictions for visible plume length and rise for the Orville Model. This is not surprising because the Orville Model was calibrated using the Benning Road data sets.

Figures 4-69 to 4-71 present the summary plots for the ANL, Slawson-Wigley, and Orville Models for the Gaston field data cases. The ANL Model (Figure 4-69) visible plume length and rise predictions are excellent with all but one case within a factor of 2. The Slawson-Wigley Model does very well in predicting visible plume rise, but very poorly for visible plume length predictions as seen in Figure 4-70. The visible plume length predictions for the Orville Model (Figure 4-71) are fair. Visible plume rise predictions are better with a strong tendency for overpredicting final plume rise.

Tables 4-1 to 4-3 present some relatively simple statistical indices of model performance for the Amos, Neurath, Benning Road, and Gaston field data. These indices are all based on the ratio of the predicted to observed length and height of the visible plume, which is denoted by ρ. Excluded from the averages are those cases in which $\rho_i > 5$ or $\rho_i < 0.2$ so as to minimize the impact of poor predictions. Instead we have tabulated the number of cases that are within a factor of 5. Also tabulated is the number of times the prediction falls within a factor of 2 (and 2.5 for visible plume length). In interpreting these values,

one should note the total number of cases used in the table. The ρ_i distribution is further characterized by its range, its arithmetic mean, and 10 raised to a power equal to the average of the absolute values of the logarithms of ρ_i's. This latter average was used since it handles overprediction and underprediction equally and since it weighs values of ρ_i near 1 more heavily than those far from 1. These simple statistical measures are not the only sensible choices, but do give important insight.

Table 4-1 includes performance statistics for five multiple-source models other than the three used in this report in order to get a better view of the whole modeling field. Table 4-1 includes the data cases from Neurath and Amos; Table 4-2 is based on the Benning Road data cases; and Table 4-3 reviews results for the Gaston data cases.

It can be seen from these three tables that the ANL Model is overall the superior model even though it has the tendency to underpredict visible plume rise. The KUMULUS Model is good also, but it does need some improvement when it comes to predicting visible plume length. We feel that the ANL Model has shown comparative success due to the improved merging methodology and downwash formulation incorporated into the model.

REFERENCES

1. L.D. Kannberg. Plumes from Three and Four Cooling Towers. IN: METER Annual Report for 1978. Department of Energy. Oak Ridge National Laboratory. Oak Ridge, Tennessee.

2. Miroslav Gregoric. An Experimental Investigation of Merging Buoyant Jets in a Crossflow. Masters Thesis. Oregon State University. Corvallis, Oregon. 1979.

3. W. Caspar and H. Scharrer. Measurements of the Atmospheric Conditions and Observation of the Cooling Tower Plume. IN: Studies on a Natural Draft Wet Cooling Tower. VDI Report. Vol. 15. No. 5. Ed. G. Ernst. pp 57-69. July, 1974.

4. M.L. Kramer, D.E.Seymour, M.J. Butler, R.N. Kempton, P.J. Brennan, J.J. Conte, and R.G. Thomson. John E. Amos Cooling Tower Flight Program Data December 1974-March 1975. American Electric Power Service Corporation. 1976.

5. M.L. Kramer and D.E. Seymour. John E. Amos Cooling Tower Flight Program Data December 1975-March 1976. American Electric Power Service Corporation. Environmental Engineering Division. Canton, Ohio. 1976.

6. J.H. Meyer, T.W. Eagles, L.C. Kohlenstein, J.A. Kagan and W.D. Stanbro. Mechanical-Draft Cooling Tower Visible Plume Behavior: Measurements, Models, Predictions. Presented at "Cooling-Tower Environment - 1974" Symposium under sponsorship of United States Atomic Energy Commission. March 4-6, 1974. University of Maryland.

7. P.R. Slawson, T.L. Crawford, C.H. Goodman and E.R. Champion. Observations of the Mechanical-Draft Cooling Tower Plumes at Plant Gaston (Data Report). Environmental Fluid Mechanics Group. Department of Mechanical Engineering. University of Waterloo; and Southern Company Services Inc. Birmingham, Alabama. February 1979.

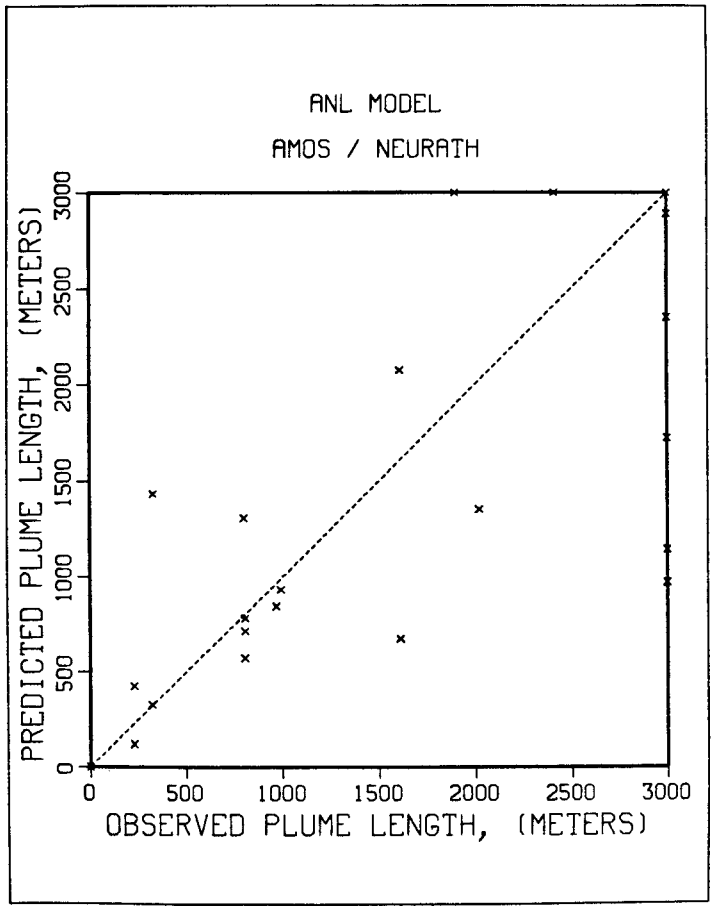

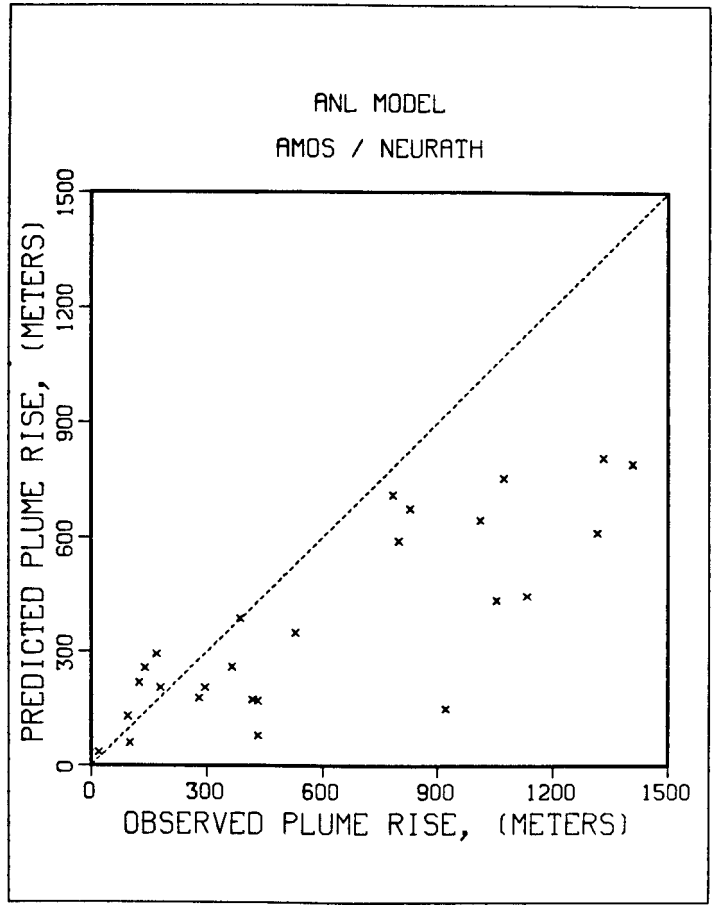

Figure 4-62. Comparison of ANL model predictions of visible plume length and rise to 26 sets of visible plume data for multiple natural-draft cooling towers at Neurath and Amos.

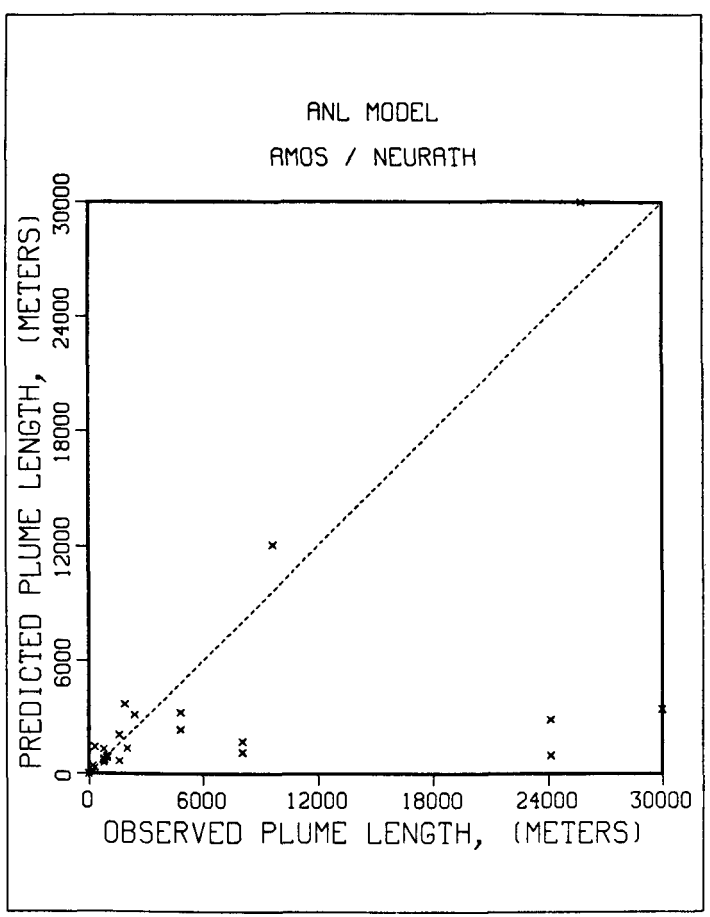

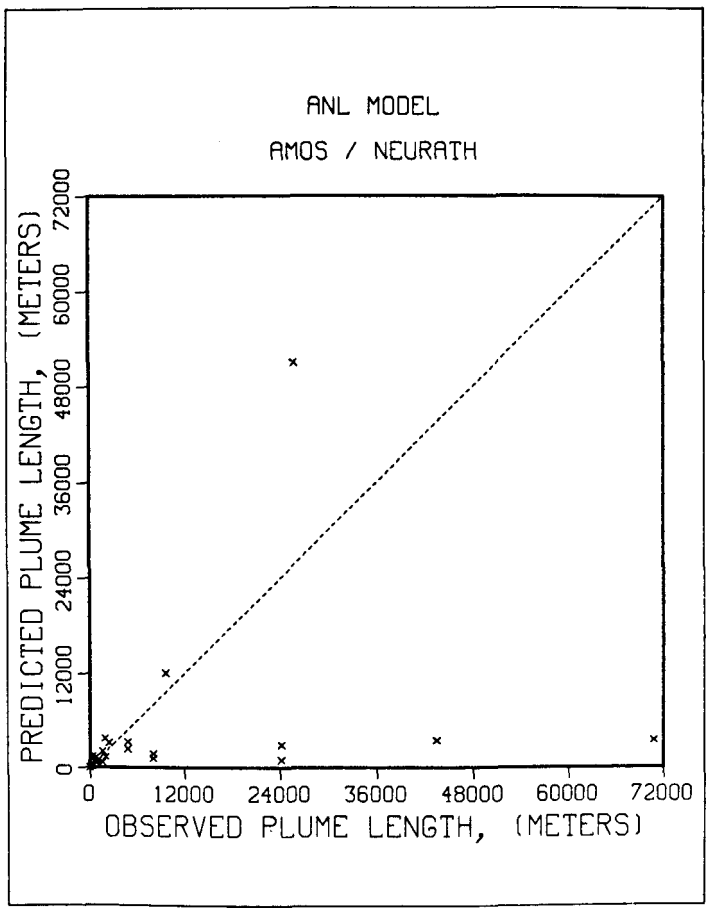

Figure 4-63. Comparison of ANL model predictions of visible plume length to 26 sets of visible plume data for multiple natural-draft cooling towers at Neurath and Amos.

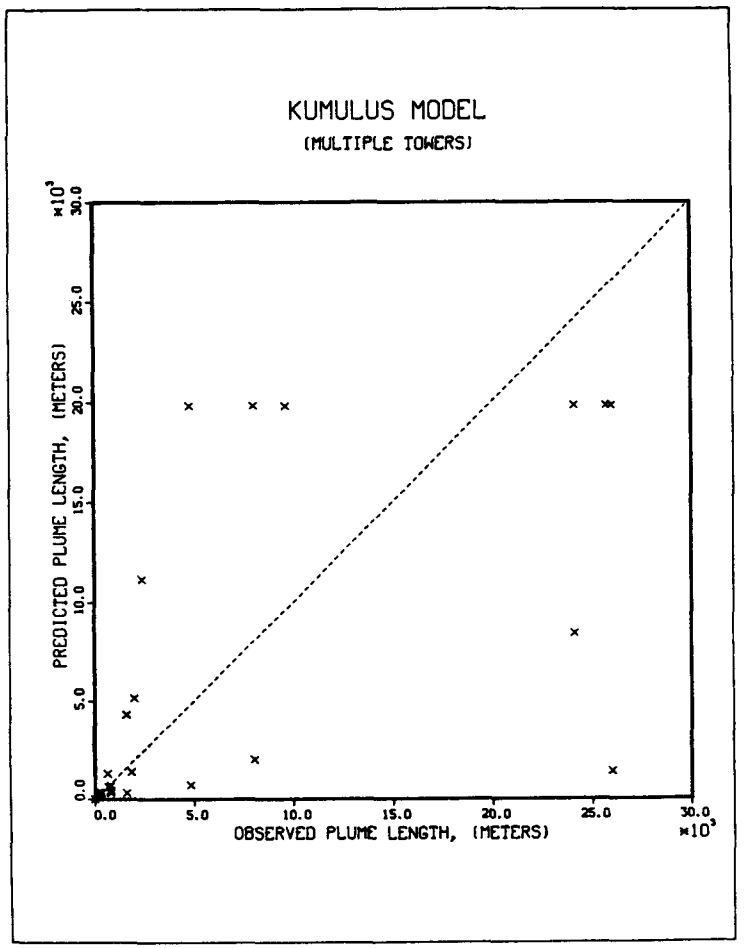

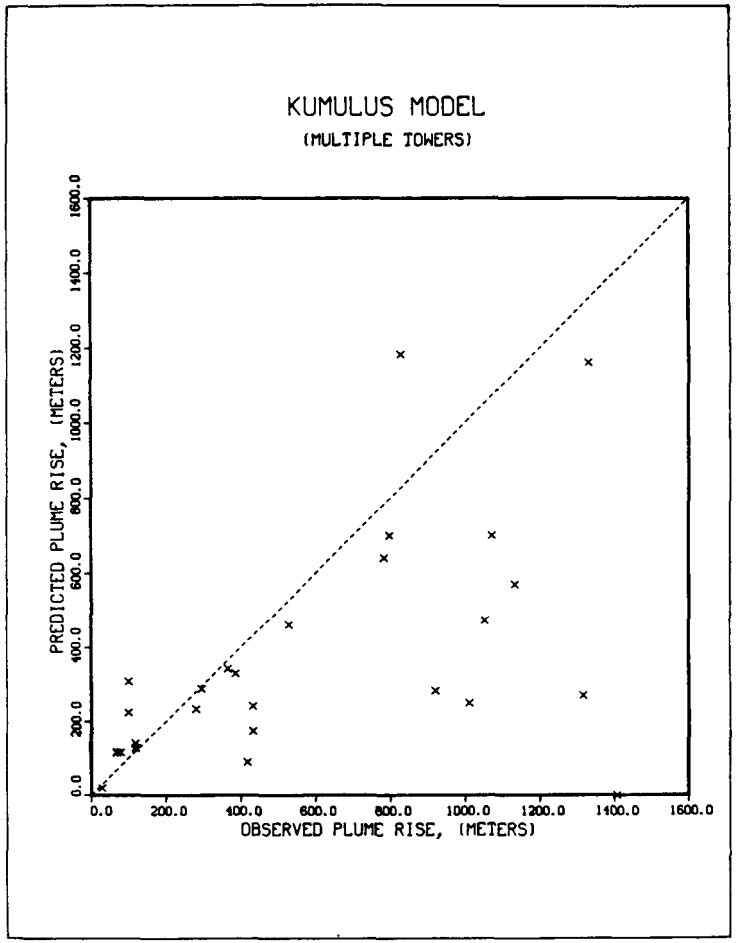

Figure 4-64. Comparison of KUMULUS model predictions of visible plume length and rise to 26 sets of visible plume data for multiple natural-draft cooling towers at Neurath and Amos.

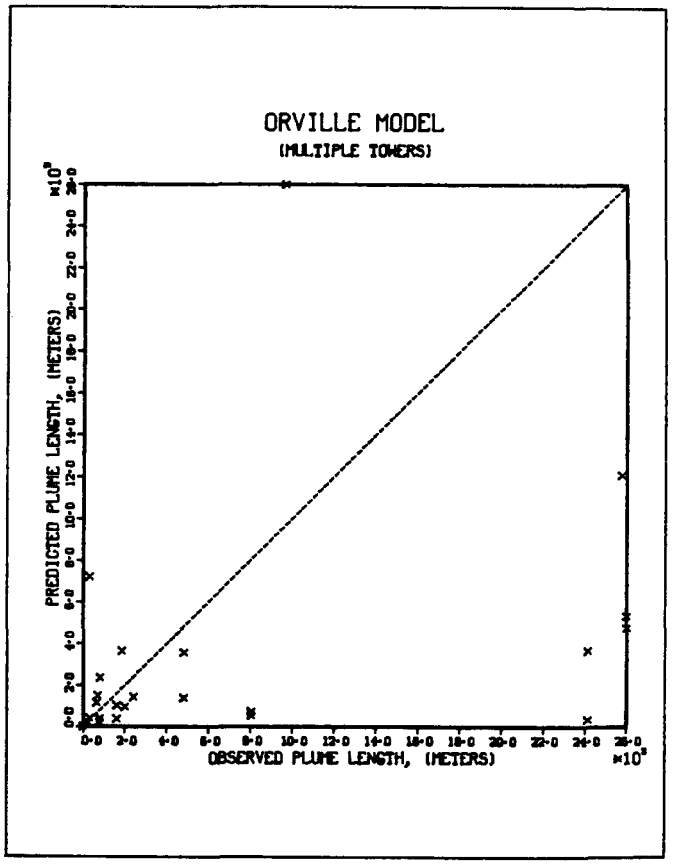

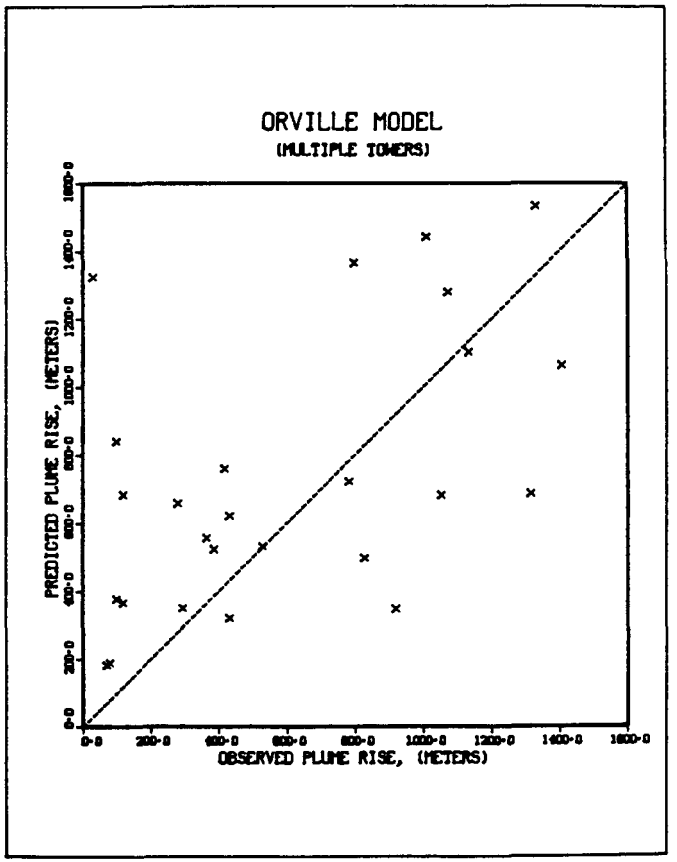

Figure 4-65. Comparison of Orville model predictions of visible plume length and rise to 26 sets of visible plume data for multiple natural-draft cooling towers at Neurath and Amos.

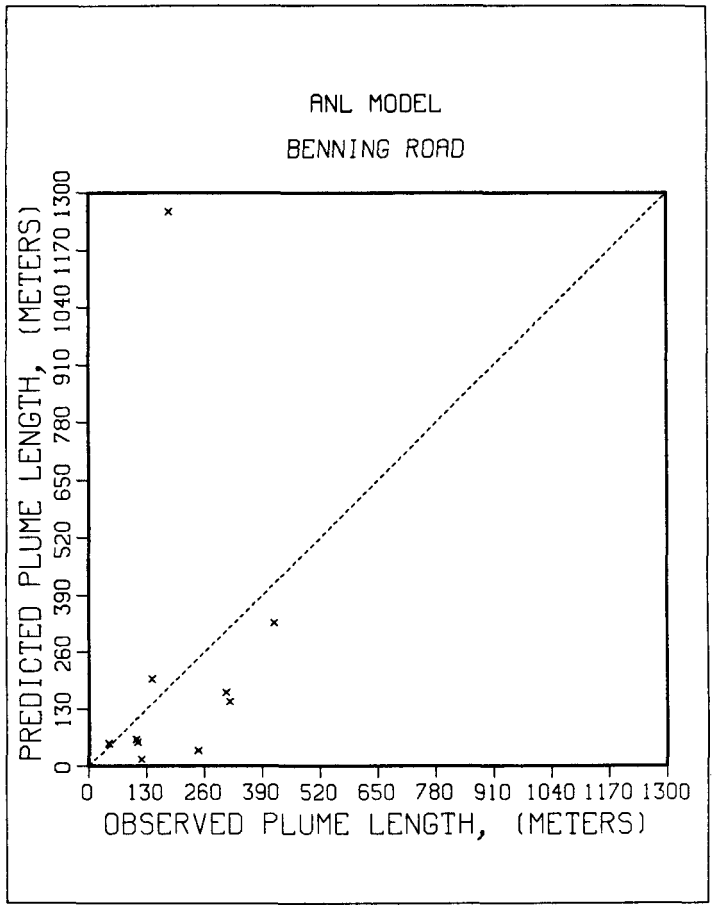

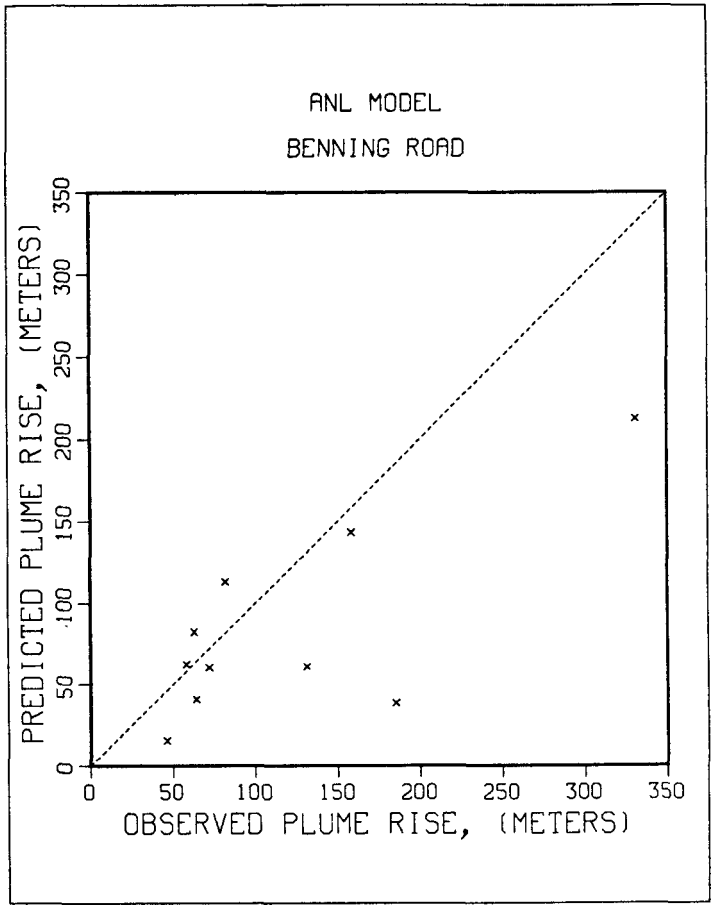

Figure 4-66. Comparison of ANL model predictions of visible plume length and rise to 10 sets of visible plume data for a single mechanical-draft cooling tower at Benning Road.

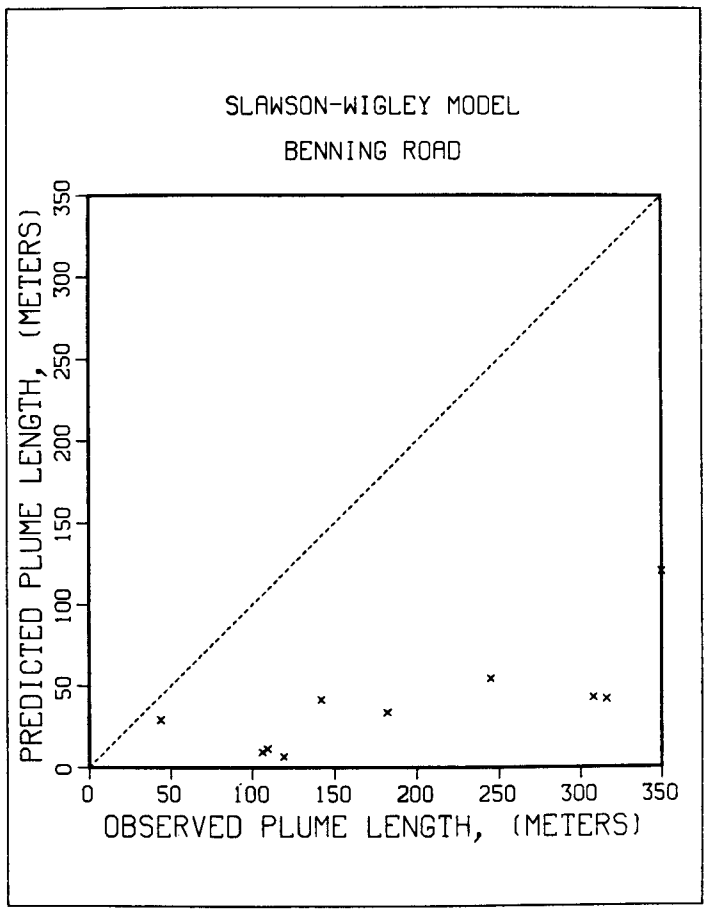

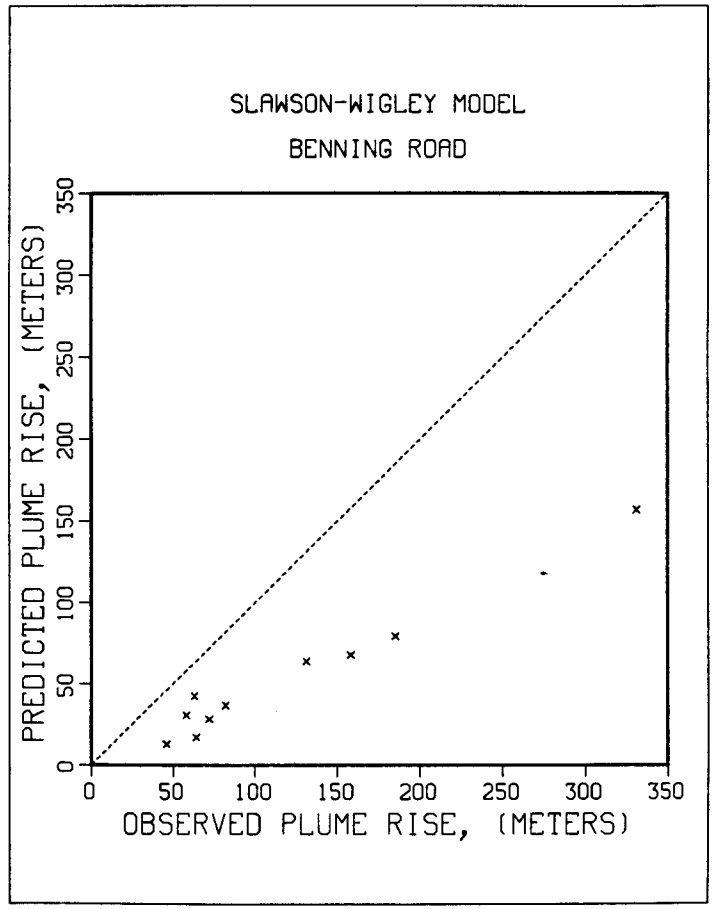

Figure 4-67. Comparison of Slawson-Wigley model predictions of visible plume length and rise to 10 sets of visible plume data for a single mechanical-draft cooling tower at Benning Road.

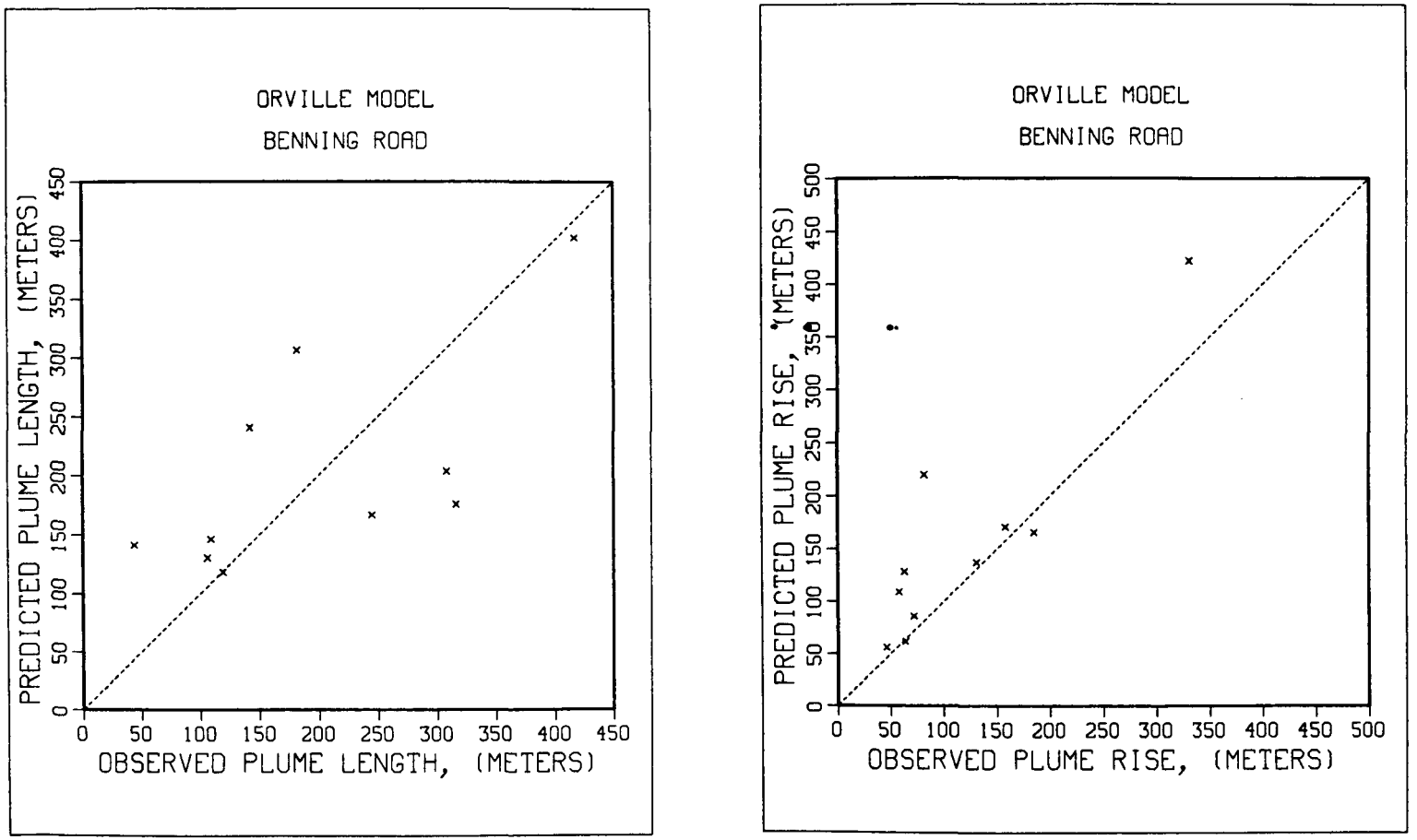

Figure 4-68. Comparison of Orville model predictions of visible plume length and rise to 10 sets of visible plume data for a single mechanical-draft cooling tower at Benning Road.

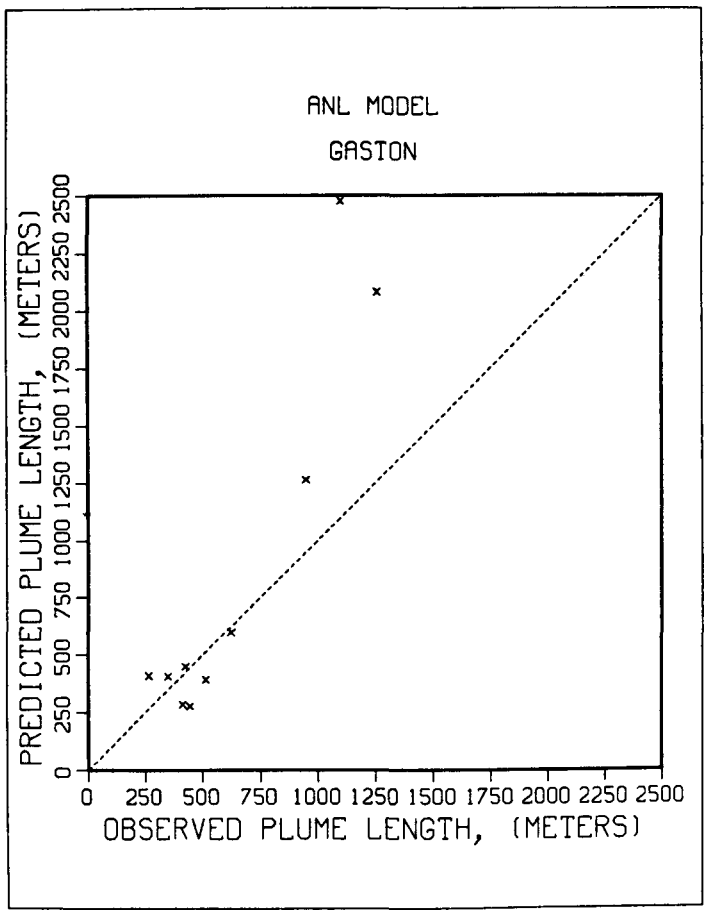

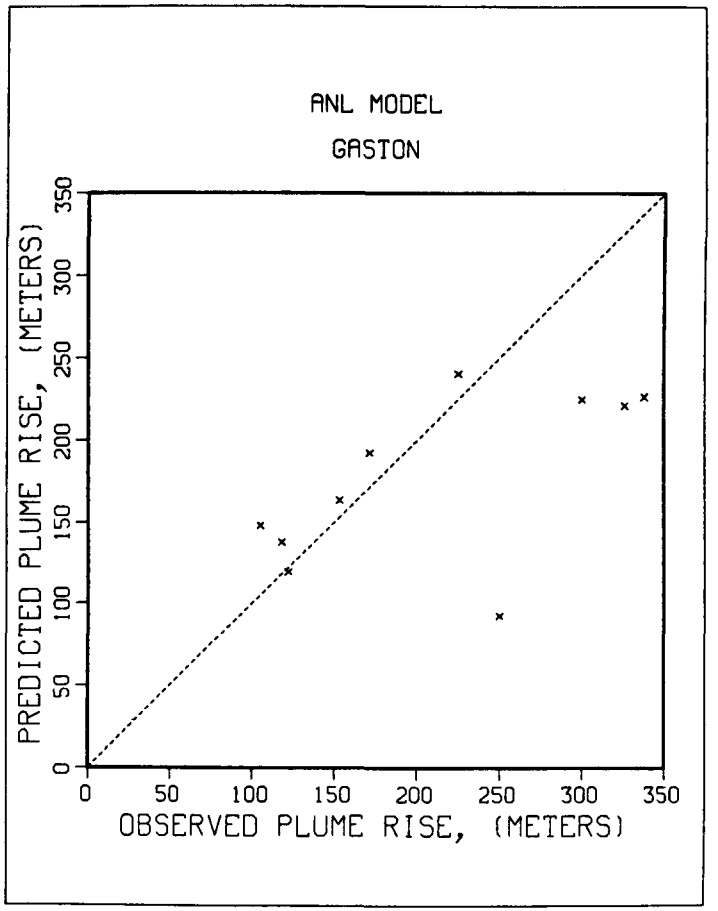

Figure 4-69. Comparison of ANL model predictions of visible plume length and rise to 10 sets of visible plume data for multiple mechanical-draft cooling towers at Gaston.

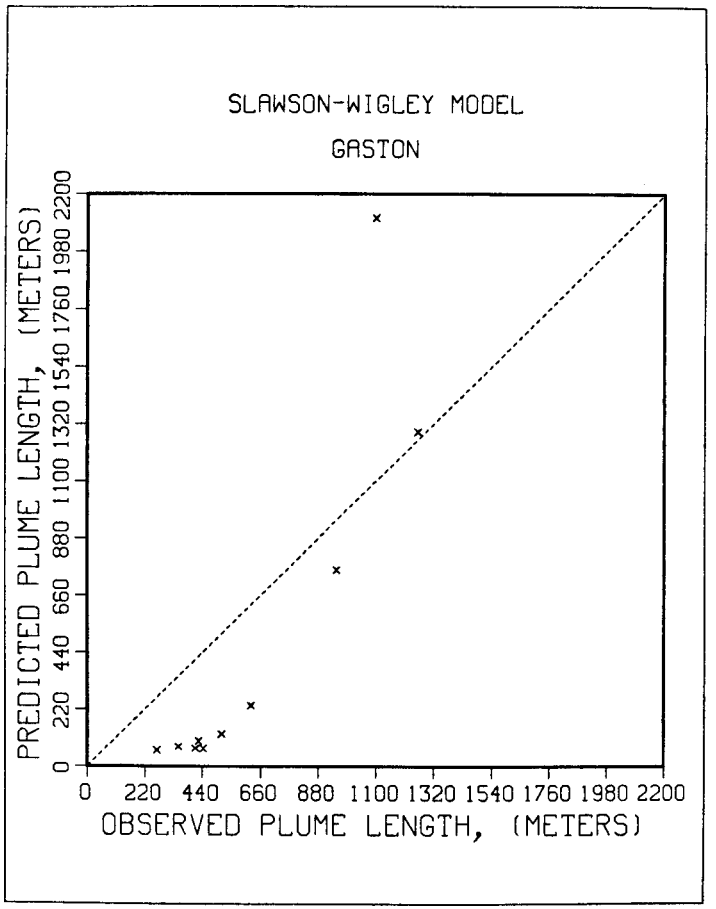

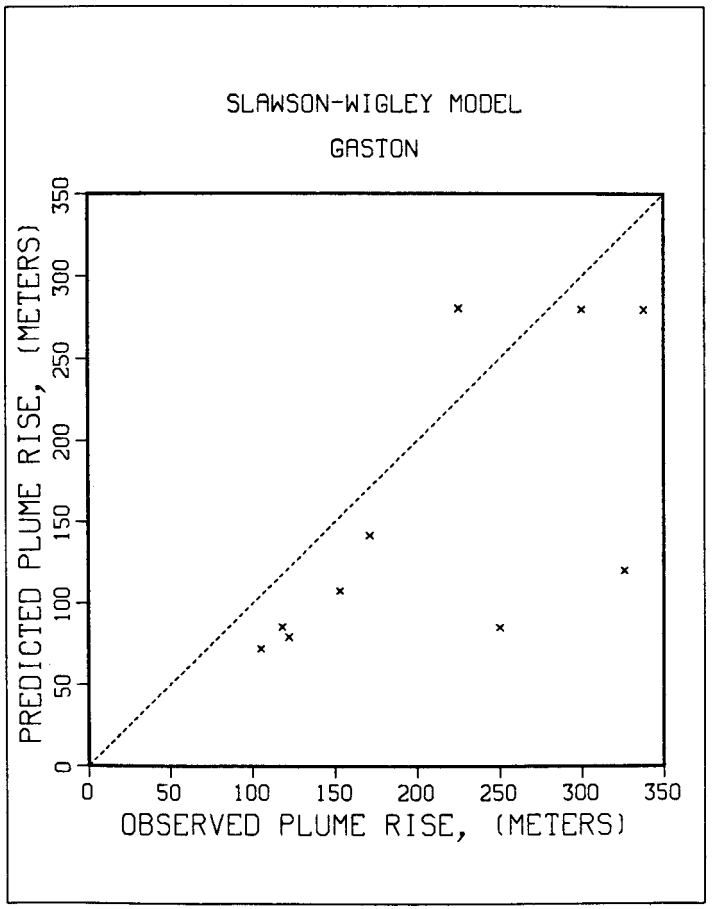

Figure 4-70. Comparison of Slawson-Wigley model predictions of visible plume length and rise to 10 sets of visible plume data for multiple mechanical-draft cooling towers at Gaston.

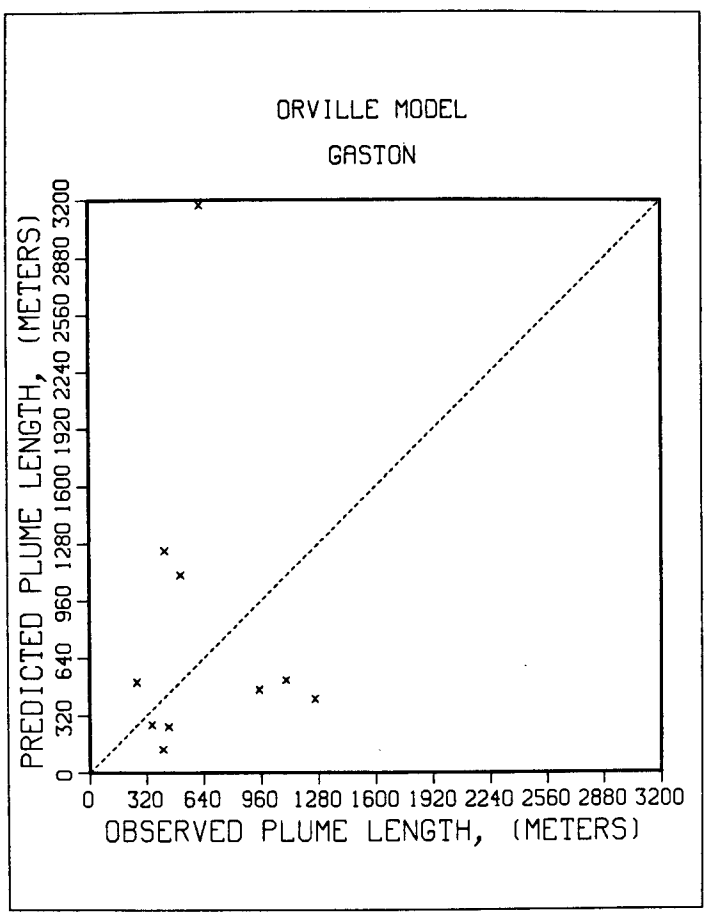

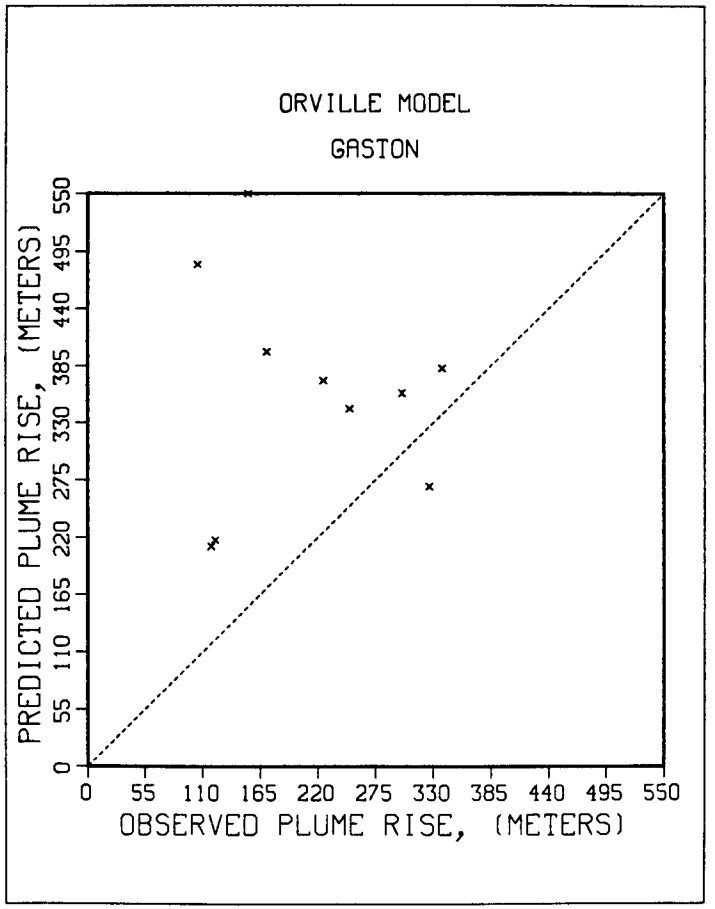

Figure 4-71. Comparison of Orville model predictions of visible plume length and rise to 10 sets of visible plume data for multiple mechanical-draft cooling towers at Gaston.

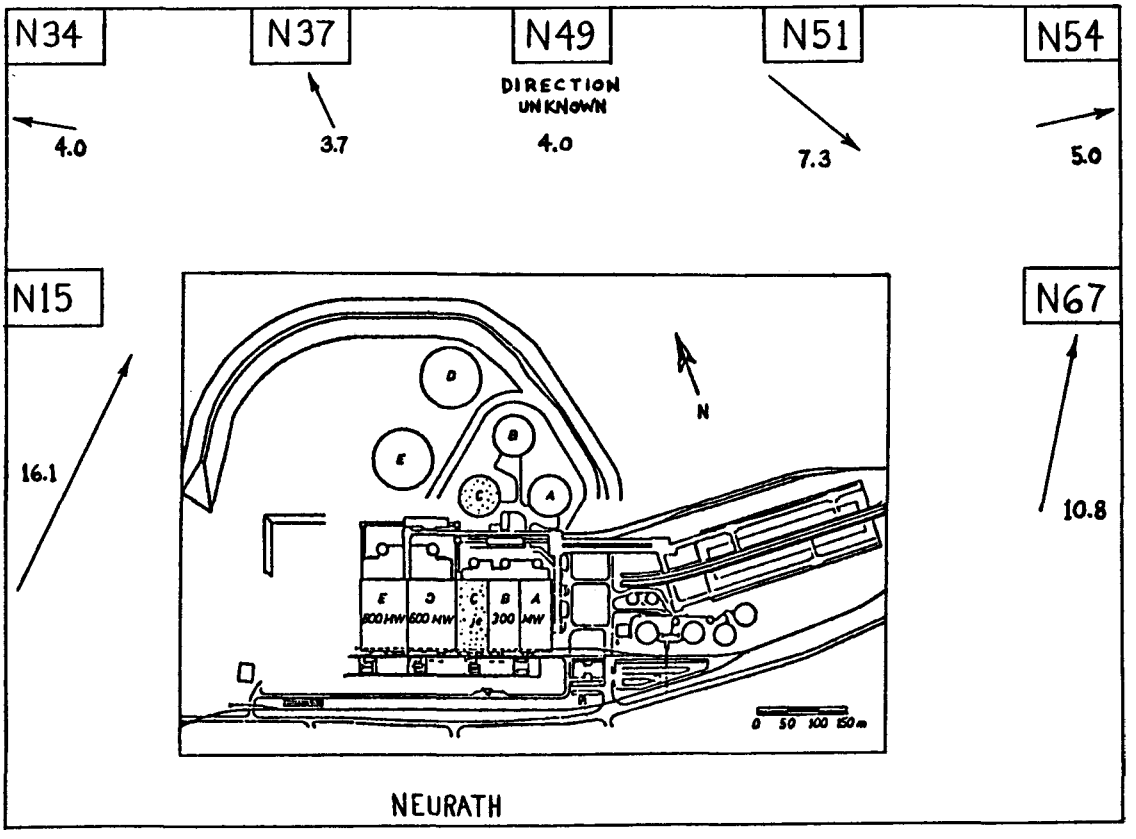

Figure 4-72. Layout of the Neurath site along with magnitude and direction of the wind at tower top for each of our 7 Neurath data cases.

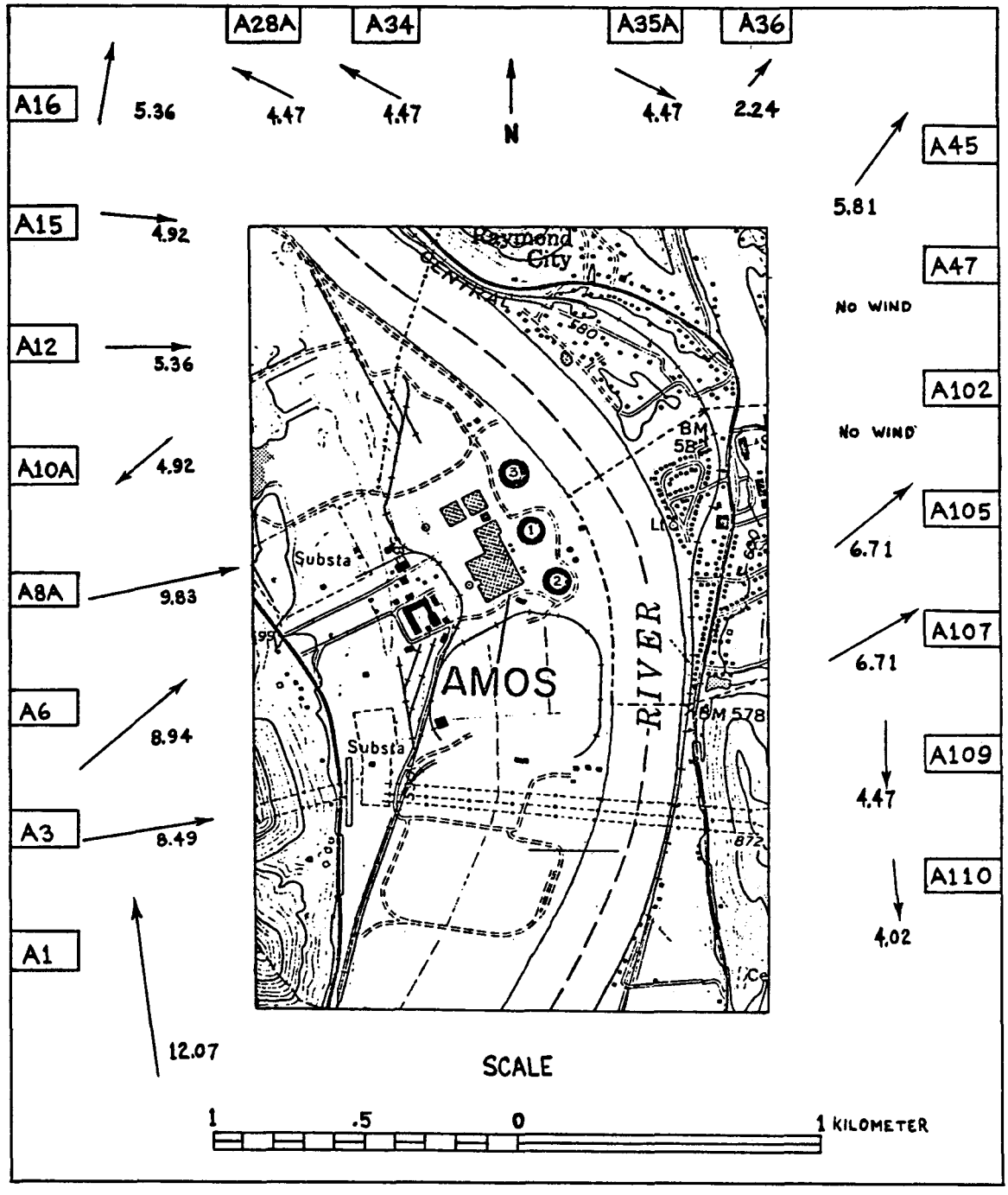

Figure 4-73. Layout of the Amos site along with magnitude and direction of the wind at tower top for each of our 19 Amos data cases.

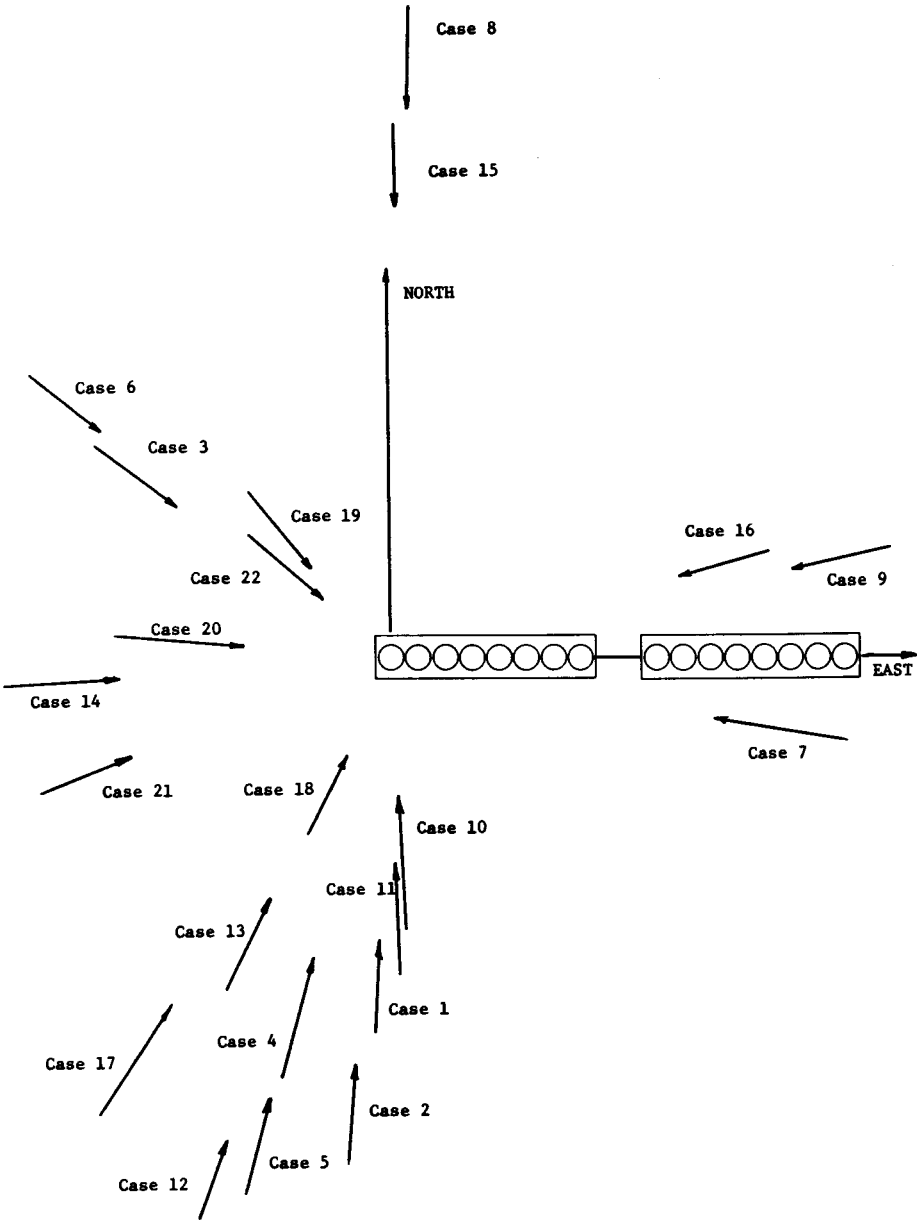

Figure 4-74. Layout of the Benning Road towers with wind direction at tower top for our 22 Benning Road data cases.

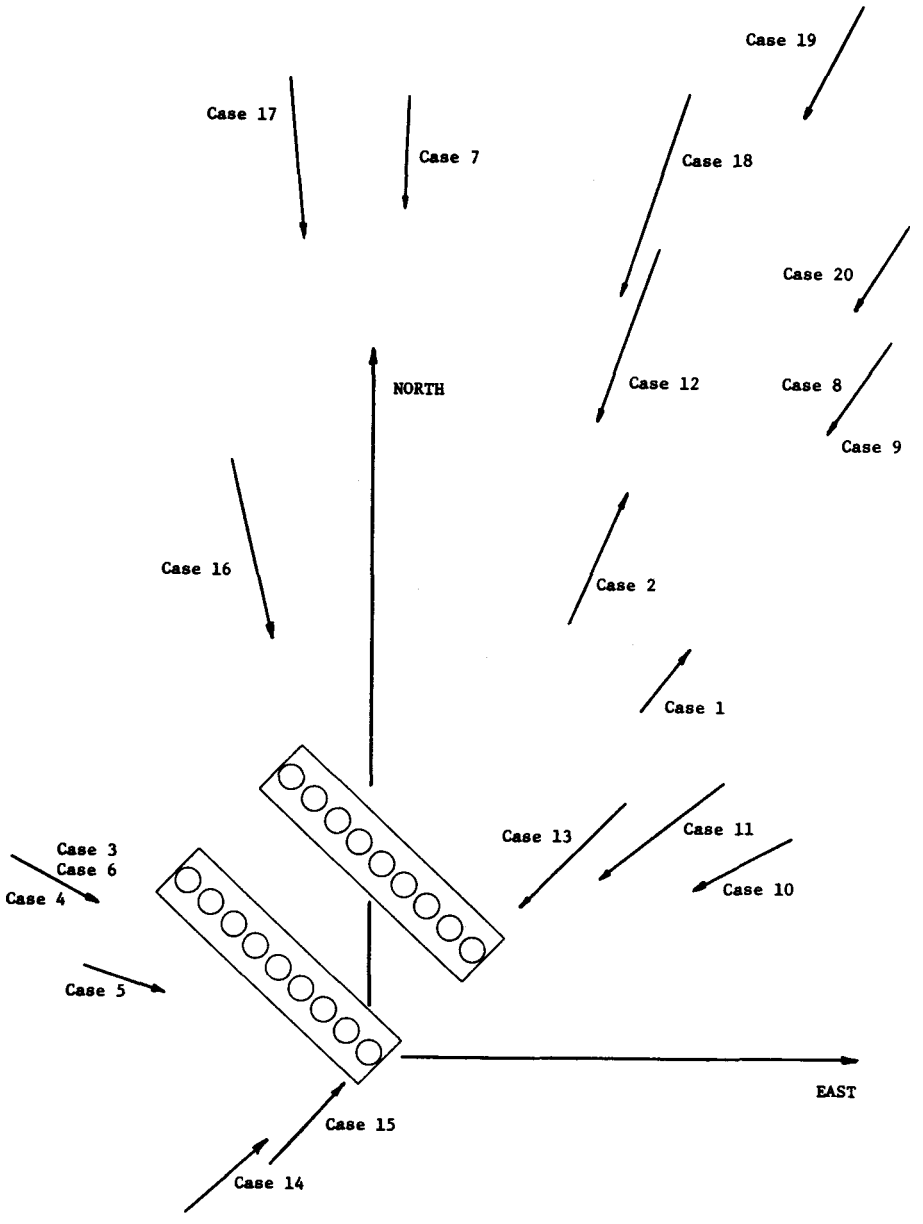

Figure 4-75. Layout of the Gaston towers with wind direction at tower top for our 20 Gaston data cases.

Table 4-1

Performance statistics for eight multiple-tower models for predictions of visible-plume rise and length for Neurath and Amos

	Model	Range of ρ_i	N_2	N_5	N_F	$\bar{\rho}$	σ_1	ρ_2	σ_2
Visible Plume Rise	Hanna	0.24-5.50	19	25	0	1.17	0.63	1.51	0.15
	Slawson-Wigley	0.12-3.27	13	20	0	0.98	0.71	1.71	0.16
	ORFAD	0.44-3.73	0	3	23	2.07	1.34	2.58	0.11
	Lee(NUS)	0.19-7.25	19	24	0	1.10	0.50	1.56	0.14
	Orville	0.38-66.25	18	25	0	1.59	1.06	1.72	0.18
	Calabrese-Halitsky-Woodard (Pickard-Lowe-Garrick Inc.)	0.23-2.31	9	17	9	0.92	0.62	1.84	0.21
	KUMULUS	0.21-1.81	19	25	1	0.83	0.42	1.64	0.21
	ANL	0.16-1.84	19	24	0	0.87	0.47	1.63	0.11

	Model	Range of ρ_i	N_2	$N_{2.5}$	N_5	N_F	$\bar{\rho}$	σ_1	ρ_2	σ_2
Visible Plume Length	Hanna	0.08-3.03	9	9	11	13	1.05	0.69	1.54	0.18
	Slawson-Wigley	0.01-2.46	5	8	13	0	0.80	0.67	2.24	0.19
	ORFAD	14.42-39.46	0	0	0	23	0.0	0.0	1.0	0.0
	Lee(NUS)	0.0-1.20	2	2	7	6	0.48	0.39	2.89	0.27
	Orville	0.02-21.83	11	14	18	1	0.93	0.67	1.84	0.19
	Calabrese-Halitsky-Woodard (Pickard-Lowe-Garrick Inc.)	0.03-1.06	7	7	10	9	0.69	0.29	1.67	0.23
	KUMULUS	0.03-4.61	10	13	23	1	1.34	1.20	2.17	0.20
	ANL	0.04-4.34	17	19	21	0	1.19	0.88	1.60	0.19

Notes: ρ_i is defined as the ratio of predicted to observed (either length or height as indicated)
N_2 is the number of times the prediction is within a factor of 2, i.e., $0.5 < \rho_i < 2.0$
$N_{2.5}$ is the number of times the prediction is within a factor of 2.5 i.e., $0.4 < \rho_i < 2.5$
N_5 is the number of times the prediction is within a factor of 5, i.e., $0.2 < \rho_i < 5.0$
N_F is the number of failures of the model in 26 data sets
σ_1 is the standard deviation of the ρ_i distribution
σ_2 is the standard deviation of the $|\log \rho_i|$ distribution

Table 4-2.

Performance statistics for the ANL Model as compared to the Slawson-Wigley Model and the Orville Model for prediction of visible plume rise and visible plume length for the ten Benning Road data cases

	Model	Range of ρ_i	N_2	N_5	N_F	$\bar{\rho}=\frac{1}{n}\sum\rho_i$	σ_1	$\rho_2 = 10^{1/n\sum\lvert\log\rho_i\rvert}$	σ_2
Visible Plume Rise	ANL	0.21-1.38	7	10	0	0.78	0.39	1.69	0.21
	Slawson-Wigley	0.27-0.67	2	10	0	0.44	0.12	2.34	0.12
	Orville	0.89-2.68	8	10	0	1.43	0.58	1.38	0.14

	Model	Range of ρ_i	N_2	$N_{2.5}$	N_5	N_F	$\bar{\rho}=\frac{1}{n}\sum\rho_i$	σ_1	$\rho_2 = 10^{1/n\sum\lvert\log\rho_i\rvert}$	σ_2
Visible Plume Length	ANL	0.13-6.91	5	7	7	0	0.77	0.37	1.62	0.10
	Slawson-Wigley	0.06-0.66	1	1	4	0	0.37	0.20	2.99	0.21
	Orville	0.58-3.21	9	9	10	0	1.30	0.78	1.51	0.14

Notes:
- ρ_i is defined as the ratio of predicted to observed (either length or height as indicated)
- N_2 is the number of times the prediction is within a factor of 2, i.e., $0.5 < \rho_i < 2.0$
- $N_{2.5}$ is the number of times the prediction is within a factor of 2.5 i.e., $0.4 < \rho_i < 2.5$
- N_5 is the number of times the prediction is within a factor of 5, i.e., $0.2 < \rho_i < 5.0$
- N_F is the number of failures of the model in 10 data sets
- σ_1 is the standard deviation of the ρ_i distribution
- σ_2 is the standard deviation of the $|\log \rho_i|$ distribution

Table 4-3.

Performance statistics for the ANL Model as compared to the Slawson-Wigley Model and the Orville Model for prediction of visible plume rise and visible plume length for the ten Gaston data cases

	Model	Range of ρ_i	N_2	N_5	N_F	$\bar{\rho}=\frac{1}{n}\sum\rho_i$	σ_1	$\rho_2 = 10^{1/n\sum \lvert\log \rho_i\rvert}$	σ_2
Visible Plume Rise	ANL	0.37-1.41	9	10	0	0.93	0.31	1.33	0.12
	Slawson-Wigley	0.34-1.25	8	10	0	0.73	0.26	1.52	0.15
	Orville	0.82-4.59	7	10	0	2.03	1.19	1.85	0.21

	Model	Range of ρ_i	N_2	$N_{2.5}$	N_5	N_F	$\bar{\rho}=\frac{1}{n}\sum\rho_i$	σ_1	$\rho_2 = 10^{1/n\sum \lvert\log \rho_i\rvert}$	σ_2
Visible Plume Length	ANL	0.62-2.25	9	10	10	0	1.20	0.51	1.41	0.10
	Slawson-Wigley	0.17-1.92	3	3	8	0	0.63	0.60	2.62	0.26
	Orville	0.32-5.08	3	6	9	0	1.10	0.96	2.18	0.13

Notes:
- ρ_i is defined as the ratio of predicted to observed (either length or height as indicated)
- N_2 is the number of times the prediction is within a factor of 2, i.e., $0.5 < \rho_i < 2.0$
- $N_{2.5}$ is the number of times the prediction is within a factor of 2.5 i.e., $0.4 < \rho_i < 2.5$
- N_5 is the number of times the prediction is within a factor of 5, i.e., $0.2 < \rho_i < 5.0$
- N_F is the number of failures of the model in 10 data sets
- σ_1 is the standard deviation of the ρ_i distribution
- σ_2 is the standard deviation of the $|\log \rho_i|$ distribution

Table 4-4.

Tower configurations and dimensions

Kannberg towers

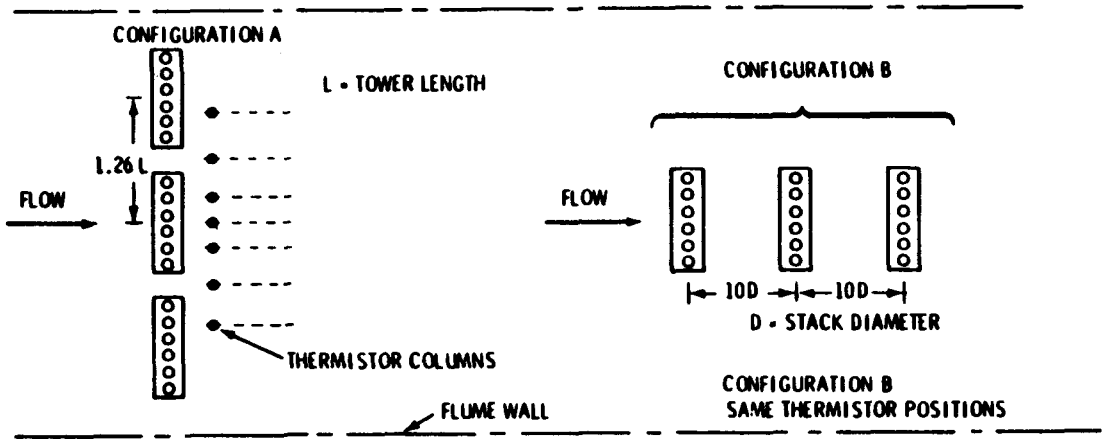

A single tower can be seen in Table 3-1.

Gregoric towers

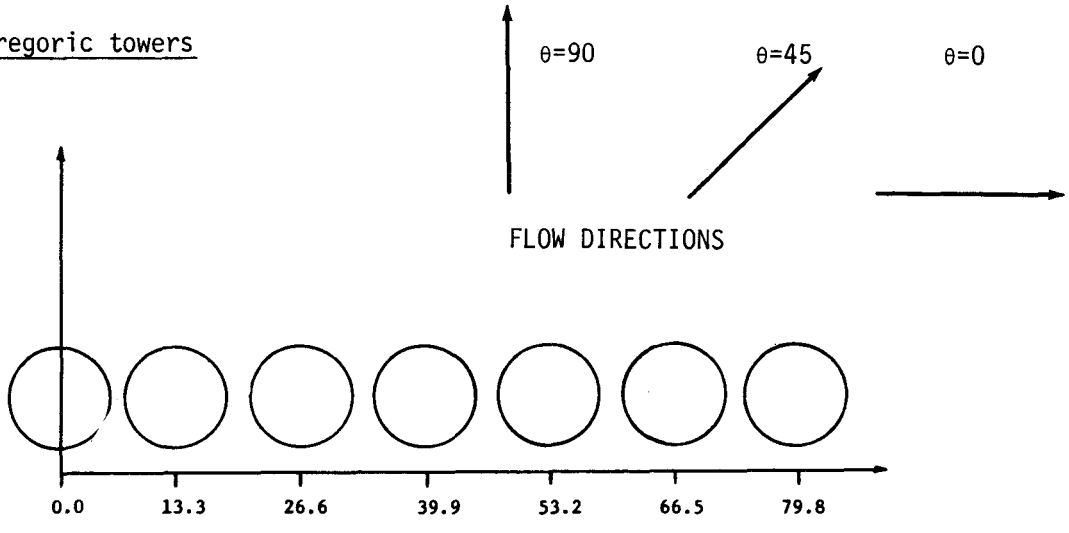

Table 4-4. (continued)

Benning Road towers

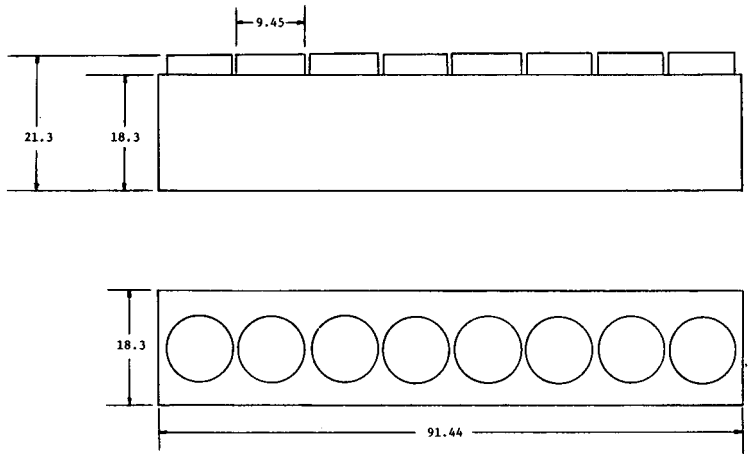

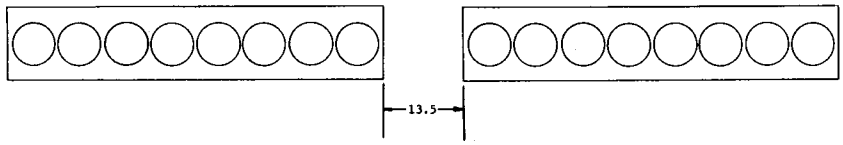

Center-to-center spacing between cells: 10.9 meters

Table 4-4. (continued)

Gaston towers

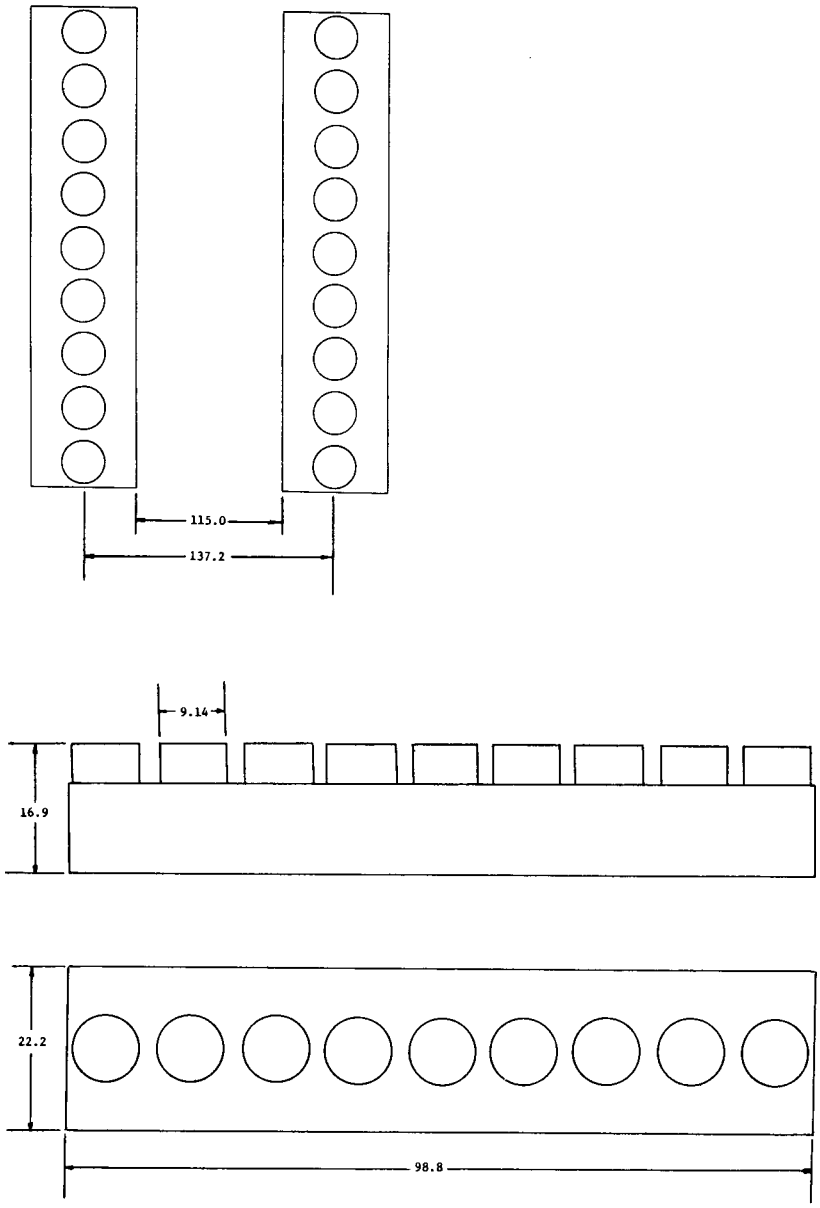

Center-to-center spacing between cells: 11.0 meters